

Dynamics of a vortex ring in a rotating fluid

Citation for published version (APA):

Eisenga, A. H. M. (1997). *Dynamics of a vortex ring in a rotating fluid*. [Phd Thesis 1 (Research TU/e / Graduation TU/e), Applied Physics and Science Education]. Technische Universiteit Eindhoven.
<https://doi.org/10.6100/IR492965>

DOI:

[10.6100/IR492965](https://doi.org/10.6100/IR492965)

Document status and date:

Published: 01/01/1997

Document Version:

Publisher's PDF, also known as Version of Record (includes final page, issue and volume numbers)

Please check the document version of this publication:

- A submitted manuscript is the version of the article upon submission and before peer-review. There can be important differences between the submitted version and the official published version of record. People interested in the research are advised to contact the author for the final version of the publication, or visit the DOI to the publisher's website.
- The final author version and the galley proof are versions of the publication after peer review.
- The final published version features the final layout of the paper including the volume, issue and page numbers.

[Link to publication](#)

General rights

Copyright and moral rights for the publications made accessible in the public portal are retained by the authors and/or other copyright owners and it is a condition of accessing publications that users recognise and abide by the legal requirements associated with these rights.

- Users may download and print one copy of any publication from the public portal for the purpose of private study or research.
- You may not further distribute the material or use it for any profit-making activity or commercial gain
- You may freely distribute the URL identifying the publication in the public portal.

If the publication is distributed under the terms of Article 25fa of the Dutch Copyright Act, indicated by the "Taverne" license above, please follow below link for the End User Agreement:

www.tue.nl/taverne

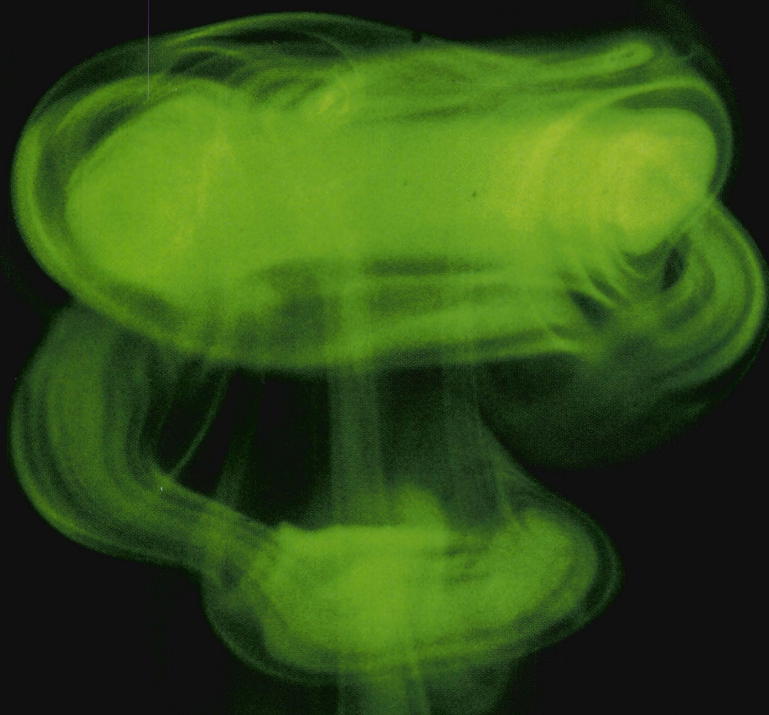
Take down policy

If you believe that this document breaches copyright please contact us at:

openaccess@tue.nl

providing details and we will investigate your claim.

Dynamics of a Vortex Ring in a Rotating Fluid



Menno Eisenga

Dynamics of a Vortex Ring in a Rotating Fluid

by A.H.M. Eisenga

Menno Eisenga
Fluid Dynamics Laboratory
Eindhoven University of Technology
P.O. Box 513
5600 MB Eindhoven
The Netherlands

Cover photography by Erwin Ensink: distorted vortex ring in a rotating fluid

CIP-DATA LIBRARY TECHNISCHE UNIVERSITEIT EINDHOVEN

Eisenga, Alphons Hubert Menno

Dynamics of a vortex ring in a rotating fluid / by Alphons Hubert Menno
Eisenga. - Eindhoven : Technische Universiteit Eindhoven, 1997. - Proefschrift. -
ISBN 90-386-0547-1

NUGI 812

Trefw.: roterende stroming

Subject headings: rotational flow / vortices

Dynamics of a Vortex Ring in a Rotating Fluid

PROEFSCHRIFT

ter verkrijging van de graad van doctor aan
de Technische Universiteit Eindhoven, op gezag
van de Rector Magnificus, prof.dr. M. Rem,
voor een commissie aangewezen door het College
van Dekanen in het openbaar te verdedigen op

dinsdag 27 mei 1997 om 16.00 uur

door

ALPHONS HUBERT MENNO EISENGA

geboren te Maastricht

Dit proefschrift is goedgekeurd door de promotoren:

prof.dr.ir. G.J.F. van Heijst

en

prof.dr.ir. M.E.H. van Dongen

WOORD VOORAF

In dit proefschrift staan de resultaten vermeld van het onderzoek dat ik de afgelopen jaren heb uitgevoerd in het kader van mijn promotie. Het woord 'ik' in de vorige zin wekt misschien de gedachte op dat ik vier jaar lang ergens in mijn eentje heb zitten spelen met wervelingen en nu de resultaten hier presenteer. Het tegendeel is waar. Veel mensen hebben bijgedragen aan het onderzoek dat uiteindelijk geleid heeft tot dit proefschrift. Graag wil ik deze mensen hiervoor bedanken.

Dit promotie-onderzoek is mogelijk gemaakt door GertJan van Heijst, waarvoor ik hem zeer dankbaar ben. Dankzij hem ben ik ook in contact gekomen met een aantal mensen die een belangrijke bijdrage hebben geleverd aan dit onderzoek. First I want to thank Roberto Verzicco (Università di Roma "La Sapienza") for the pleasure collaboration we had last years that resulted in two detailed studies on the motion of a vortex ring in a rotating fluid. He has developed the numerical codes that were used in the simulations, which were very useful for this research. His stimulating help has contributed significantly to the results described in this thesis. Verder wil ik Paul van Enkevort bedanken die tijdens zijn afstudeeronderzoek, en enkele maanden daarna, zeer vele experimenten heeft uitgevoerd. Vaak was hij degene die dagen bezig was een nieuwe opstelling op te bouwen en liet dan vervolgens mij het eerste wervelingetje afschieten. I would like to thank Shura Gourjii to provide the numerical code to perform the simulations with Dyson's model and his assistance in the study of the coaxial motion of vortex rings and vorton rings. I am grateful to Gianni Pedrizzetti for providing his numerical code to perform three-dimensional vorton ring simulations. Verder heeft het enthousiasme van Slava Meleshko voor de beweging van wervelingen mij voortdurend gestimuleerd in dit onderzoek. Ik kreeg van hem altijd meer artikelen dan ik kon verwerken, zodoende ligt er nog een stapel klaar voor rustigere tijden.

Jan van Dijk, Jos Mettler, Frank Toonen en Tony Vandeweyer ben ik dankbaar voor de bijdrage die zij aan dit onderzoek hebben geleverd tijdens hun stage. Jullie vragen hebben mij vaak aan het denken gezet.

Verder wil ik mijn kamergenoten Marcel Beckers, Johan van de Konijnenberg, Oscar Velasco Fuentes en Pauline Vosbeek bedanken voor de fijne tijd die we samen hebben gehad en de hulp en steun bij het oplossen van kleine en grote problemen tijdens het onderzoek. Jos van Geffen, bedankt voor de lekkere koffie en de gezelligheid iedere ochtend.

Jan van Asten wil ik bedanken voor het maken van maar liefst twee werveling generatoren. Voor de verdere technische ondersteuning van de laboratorium experimenten ben ik Harm Jager, Eep van Voorthuisen en Jan Willems dankbaar. Al lieten de wervelingen zich vaak moeilijk fotograferen, het is toch gelukt om ze te 'vangen': Erwin, bedank! Een voorbeeld van zo'n foto is te zien op de voorzijde van dit proefschrift. Gert van der Plas ben ik dankbaar voor zijn hulp als de computers niet deden wat ik graag wilde dat ze deden. Ruben Trieling wil ik bedanken voor de zeer nuttige software om experimentele data te analyseren. Ion Barosan was

altijd direct bereid te helpen als ik vragen had met betrekking tot de software om numerieke simulaties te visualizeren, waarvoor mijn dank. Herman Clercx wil ik bedanken voor het oplossen van storingen in het computernetwerk en voor het gebruik van zijn 'rekenkracht' om enkele zware numerieke simulaties uit te voeren.

Ik wil prof. M.E.H. van Dongen, prof. F.T.M. Nieuwstadt en prof. V.V. Meleshko bedanken voor het lezen van dit proefschrift en het plaatsen van kritische opmerkingen die me op het laatste moment nog even goed aan het denken hebben gezet. GertJan, bedankt voor het snel en zorgvuldig nalezen van de tekst en het opsporen van vele type- en spelfouten.

Ik wil mijn lieve vrouw Yvonne bedanken die ervoor gezorgd heeft dat ik ook nog een ander leven had dan alleen maar onderzoek doen. Zij was 's avonds als ik thuiskwam vaak in staat om mijn gedachten binnen enkele minuten om te zetten van wervelingen naar alledaagse dingen. Lieve meid, al dreigden de wervelingen in de laatste weken alsnog onze huiskamer binnen te komen, zet het raam maar open dan gaan ze vanzelf weer naar buiten. Mijn ouders wil ik bedanken voor de goede zorg gedurende mijn studie en het eerste gedeelte van het promotie-onderzoek.

In het laatste stadium van het onderzoek, tijdens het schrijven van dit proefschrift, hebben vele mensen mij enorm gesteund en ik ben daar iedereen hartelijk dankbaar voor.

MENNO EISENGA

Eindhoven, 7 april 1997

*Hoe simpel lijkt de eenvoud,
hoe complex kan die zijn.*

(Yvonne)

CONTENTS

1	General introduction	3
2	Characteristics of vortex rings	7
2.1	Introduction	7
2.2	Theory of steady vortex rings	8
2.2.1	Equations for axisymmetric flows	8
2.2.2	Models of inviscid vortex rings	9
2.2.3	Potential flow associated with thin-core vortex rings	12
2.2.4	Some effects of viscosity	15
2.3	Description of laboratory experiments	16
2.3.1	Experimental apparatus	16
2.3.2	Generation of vortex rings	17
2.3.3	Data processing of dye-visualized experiments	18
2.3.4	Data processing of particle experiments	21
2.4	Results of laboratory experiments	23
2.4.1	Description of a dye visualization experiment	23
2.4.2	Vortex ring characteristics from dye visualizations	24
2.4.3	Vortex ring characteristics from particle experiments	26
2.5	Conclusions	35
3	Vortex ring moving along the axis of a rotating fluid	37
3.1	Introduction	37
3.2	Experimental set-up	38
3.3	Numerical set-up	39
3.3.1	Equations of motion and numerical scheme	39
3.3.2	Run parameters and convergence checks	40
3.4	Results	42
3.4.1	Matching numerical simulations with laboratory experiments	42
3.4.2	Preliminary flow visualizations	46
3.4.3	Low rotation regime	50
3.4.4	High rotation regime	61
3.4.5	A three-dimensional simulation	69
3.5	Conclusions	70

4	Vortex ring moving perpendicular to the axis of a rotating fluid	73
4.1	Introduction	73
4.2	Experimental set-up	74
4.3	Numerical set-up	76
4.3.1	Equations of motion and numerical scheme	76
4.3.2	Initial configuration and convergence checks	77
4.3.3	Scaling of the experiment	78
4.4	Results	80
4.4.1	Flow visualizations	80
4.4.2	Curved trajectory of vortex ring	82
4.4.3	Vorticity dynamics in horizontal plane of symmetry	85
4.4.4	Three-dimensional flow structure	94
4.5	Conclusions	100
	Appendix A	102
5	Analysis of two models for leapfrogging vortex rings	105
5.1	Introduction	105
5.2	Dyson's model	105
5.3	Vorton model	108
5.4	Connection between Dyson's model and the vorton model	112
5.5	Numerical simulations	115
5.6	Conclusions	119
6	Summary of conclusions	121
	References	123
	Samenvatting	127
	Curriculum Vitae	128

1

GENERAL INTRODUCTION

Vortex rings are best known as the thin rings of smoke that are formed by blowing gently a gust of smoke; the thick smoke of a cigar is excellent for this purpose. Taking a close look at the structure of this flow, it is seen that the smoke inside the ring-shaped core rotates around the core. As a consequence of this intrinsic swirling flow the vortex ring propagates by its own self-propelling mechanism, in a direction normal to the plane of the ring. Vortex rings can be observed in several practical circumstances, although they are not always visible or just appear accidentally. A drop of water falling in a glass of water generates a vortex ring propagating downwards, but this vortex ring is invisible unless the water drop is dyed, e.g. by some milk. Occasionally, a vortex ring can also be observed in the puffs of steam from the chimney of a steam locomotive or a steam boat, rising several tenth of meters with a diameter expanding to more than one meter. Very large vortex rings are the typical mushroom-shaped cloud observed in an explosion or a volcano eruption. A very harmful kind of vortex ring structure, especially a hazard to aircraft, is a microburst, which occurs when a downdraft of dense air suddenly falls to Earth and spreads outward along the Earth's surface with a horizontal extent of several kilometers (Fujita, 1981). Recently, it has been observed that dolphins can create vortex rings very consciously by slamming their fins and visualize them by breathing small air bubbles in the ring core (Marten *et al.* 1996). Also by blowing air from their blowholes the dolphins can create vortex rings and sometimes they are observed to swim through the rings in a playful way.

These are just a few examples of more or less natural circumstances in which vortex rings appear. It is nice to notice that vortex rings are used or have been attempted to use in several technological applications. For example, vortex rings have been suggested as a means for extinguishing gas and oil well fires (Akhmetov *et al.* 1990) and cavitating vortex rings, produced by exciting cavitating jets, have been used for underwater cleaning and rock cutting (Chahine & Genoux 1983). In addition, vortex rings have been proposed to transport industrial wastes to high altitudes (Turner 1960) and, recently, the US Army Research Laboratory conducts a research to the feasibility of using high velocity ($\simeq 200$ m/s) ring vortices for non-lethal riot control at stone throwing ranges ($50 \simeq 100$ m).

It should be stressed that it is not because of these practical examples that vortex rings have been studied so extensively for more than one century. The attention for vortex rings is initiated by the work of Helmholtz (1858) on general vorticity dynamics and Kelvin's theory of vortex ring atoms (Thomson 1867*b*). In the last three decades the vortex ring has been the subject of many fundamental studies. A vortex ring is commonly considered to be an

elementary vortical structure that, although it has a simple symmetric structure, possesses many properties that apply also to more complicated three-dimensional vortices. Due to the axisymmetric stable nature of vortex rings their flow structure can be analyzed in detail and they are easily generated experimentally.

A few examples of studies in which vortex rings are used to gain insight in basic vorticity mechanisms are mentioned here. The interaction of two vortex rings involves many important processes related to vorticity dynamics, like deformations of the vortex core, vorticity cancellation and merging, change of the topology of vortex lines and intense vortex stretching. Several kinds of interaction of vortex rings have been studied, among which the periodical leapfrog motion of two coaxially interacting vortex rings placed in tandem is a classical example (see Yamada & Matsui 1978 for an experimental demonstration of this interaction). The collision of two inclined vortex rings fusing into one big ring (see e.g. Schatzle 1987) has been studied to gain insight in the reconnection mechanism by which the topology of vortex lines changes due to viscous processes. The reconnection mechanism is also an important process in the dynamics of magnetic flux tubes in plasma's and of quantized vortices in superfluid helium. Insight in specific features of the dynamics of coherent vortices (e.g. hairpin vortices) in turbulent boundary layers (an overview of which is given in Robinson, 1991) is acquired by investigation of the impact of a single vortex ring with a solid wall (see Walker *et al.* 1987 and Verzicco & Orlandi 1996*b* for overviews).

In most studies the vortex ring is generated in a fluid at rest. It is obvious that in an ambient shearing flow the vortex ring is deformed according to the local shearing rate (Meng 1978). In general a shearing background flow consists of both a straining and a rotational component. To study these effects separately, the vortex ring is best examined in a fluid containing only one of these two components. In this thesis the effect of the rotation of an ambient flow on the propagation and dynamics of a vortex ring is examined.

Flows affected by a background rotation appear in many practical circumstances. Geophysical flows in the atmosphere and ocean are, among buoyancy effects due to stratification, dominated by the rotation of the Earth. Also flows in turbomachinery and cyclone separators are just a few examples in which the main background swirl is dominant. A very important feature in these flows is the anisotropy, as variations in the flow motion along the rotation axis are prohibited when the rotation is sufficiently strong. In a bounded region this means that the flow motion along the rotation axis is suppressed and the main flow evolves into a two-dimensional motion in a plane normal to this axis. In addition, the energy of the flow is transferred to larger scales, resulting in the formation of large coherent vortices typical of two-dimensional turbulence.

Flows with a uniform background rotation are best examined relative to a corotating frame of reference. The relative flow in such a rotating system is then affected by Coriolis forces which are imposed by the system rotation and tend to deflect all motion in a plane normal to the rotation axis in a direction opposite to the sense of rotation of the system. In terms of vorticity, the background rotation represents a permanent present uniform vorticity field directed along the rotation axis, that interferes with the vorticity of the relative fluid flow. This background vorticity acts as a persisting source by which relative vorticity can be induced in regions of the relative flow that are initially in irrotational motion. As a consequence, flows relative to a rotating system are commonly endowed by relative vorticity. The mechanisms by which relative vorticity is induced and the interaction between the induced vorticity and the vorticity of the main relative flow are processes that are of significant importance in the

dynamics of rotating flow systems. Elementary insight in these processes is indispensable to gain a proper comprehension of the evolution of such rotating flows.

To study these processes in detail a relative flow has to be considered with a well-defined initial structure. A vortex ring is for this purpose an excellent candidate. The structure of a vortex ring is compact, robust and symmetric and the vortex lines form closed circles around the axis of symmetry. Owing to the initial 'simple' structure of a vortex ring the analysis of the development of the flow can be pursued in detail, yielding a thorough insight in the induction and dynamics of relative vorticity in rotating systems.

The main part of this thesis concerns a study of the evolution of a vortex ring that is generated in a fluid in uniform rotation. Basically, two cases can be distinguished. In the first case the vortex ring is initially directed along the axis of rotation and in the second case the ring is directed perpendicular to this axis. Both cases are studied separately, revealing flow patterns that are specific for either case. The development of the flow depends on the rotation rate of the system. The appropriate dimensionless parameter is the Rossby number that measures the relative importance of inertial forces to Coriolis forces. This parameter is defined by $Ro = U/2\Omega\mathcal{L}$, where U and \mathcal{L} are typical velocity and length scales of the relative flow, respectively, and Ω is the angular velocity of the rotation. For low rotation rates ($Ro \gg 1$) the relative flow is slightly perturbed by the background rotation, while for small Ro -values ($Ro \ll 1$) the background rotation dominates the flow motion. For different rotation rates the formation and propagation of vortex rings have been examined, showing a different evolution of the flow for low and high rotation rates.

The investigations are based on both laboratory experiments and numerical simulations that are used as complementary tools. For the laboratory experiments a vortex ring generator was designed and tested to check its reproducibility to generate vortex rings with repeatedly the same characteristics for definite injection parameters. These tests and characterizations have been performed for a vortex ring generated in a fluid at rest and the results are discussed in chapter 2. The propagation of a vortex ring in a rotating fluid is investigated in the next two chapters, the case that the vortex ring is directed along the axis of rotation is considered in chapter 3 and the case of the vortex ring fired perpendicular to the rotation axis in chapter 4. In these studies numerical simulations have been helpful in order to get a complete picture of the flow evolution. Special care has been taken to ensure that the simulations mimic the laboratory experiments in the same range of flow parameters.

In the final chapter a study is presented that is completely different from the previous ones. In this study a comparative analysis has been performed between two inviscid flow models describing the coaxial interaction of two vortex rings. One of these models, the vorton model (Novikov 1983), was originally supposed to be suitable for studying the motion of a vortex ring in a rotating fluid. Before doing this, however, this model has been subjected to a thorough analysis, because many drawbacks are inherent to this model. The analysis is based on the classical leapfrogging motion and provides insight in the drawbacks of the vorton model in relation to the Dyson model (Dyson 1893) that is better founded physically.

The study in chapter 3 has already been published (see Verzicco *et al.* 1996) in a somewhat condensed version. Chapters 4 and 5 have been submitted for publication. The main conclusions of the investigations presented in this thesis are summarized in chapter 6.

2

CHARACTERISTICS OF VORTEX RINGS

2.1 Introduction

This chapter describes experimental investigations of the flow structure of vortex rings generated in a fluid at rest. The vortex rings were created by injection of fluid through a circular orifice on top of a cylindrical box. This generation technique is well known and has already been used in previous studies (see e.g. Maxworthy 1972; Glezer 1988). The characteristic flow parameters of the produced vortex rings are affected by the mechanism of fluid injection and the configuration of the vortex ring generator. Therefore, comparison of ring parameters of vortex rings produced in different experimental arrangements is often very difficult. One of the parameters of the fluid injection that is difficult to fix in most vortex generator designs is the time evolution of the injected fluid slug. For convenience, one commonly assumes a uniform flow profile of the fluid injection, but it has been shown by Didden (1977) that for different injection flow profiles the ring parameters were not the same.

For the experiments presented in this thesis a very simple vortex ring generator has been constructed in which the fluid injection was provided by several syringes that are pressed by a step-motor driven traversing system. Although the amount of injected fluid and the mean injection velocity could be well established, the shape of the injection profile was just approximately uniform. Since no experience was available with this new design, the vortex ring generator and injection mechanism had to be tested first to check whether the created vortex rings have repeatedly the same characteristic ring parameters. To measure these parameters two kinds of flow visualization techniques were used. Visualizations with dye provided a clear insight in the formation and subsequent evolution of the vortex ring and whether the flow field is laminar or turbulent is obviously inferred. In addition, a method was developed to deduce from these dye visualizations values for the characteristic ring parameters. In the second visualization technique the velocity field induced by the vortex ring is measured by tracking the motion of small tracer particles. In these experiments the specific structure of the vortex ring flow is measured from which the various ring parameters can be deduced. Both visualization techniques have been used as complementary tools to gather a complete characterization of the produced vortex rings. The experimental set-up and data processing techniques are described in section 2.3 and the results of the experiments are presented in section 2.4.

Because of the steady structure of vortex rings theoretical models are commonly based on inviscid flow assumptions. In section 2.2 several vortex ring models are presented, which

are well-known from literature. In most of these models the vortex ring is assumed to have a simple (ideal) structure and an expression is derived for the velocity of propagation of the vortex ring in terms of the dimensions of the ring and the strength of the vortex. The effects of viscosity in real fluids on the structure of vortex rings are briefly discussed. The chapter ends with a summary of the main conclusions (section 2.5).

2.2 Theory of steady vortex rings

2.2.1 EQUATIONS FOR AXISYMMETRIC FLOWS

In this section the specific equations describing axisymmetric rotational flows will be introduced and discussed. These equations can be derived from the general equations for three-dimensional fluid motion (see Batchelor 1967), which are reduced due to the symmetry of the flow field. Such axisymmetric flows are conveniently described in cylindrical coordinates (r, ϕ, z) , where the axial z -axis is parallel to the axis of symmetry. Axisymmetry of the motion implies $\partial/\partial\phi = 0$.

Relative to cylindrical unit vectors $\mathbf{e}_r, \mathbf{e}_\phi$ and \mathbf{e}_z the velocity vector \mathbf{u} has components u_r, u_ϕ and u_z , respectively. Here, the azimuthal velocity component u_ϕ describes a swirling motion around the symmetry axis. The radial and axial velocity components can be expressed in terms of the Stokes stream function ψ , defined as:

$$u_z = \frac{1}{r} \frac{\partial \psi}{\partial r}, \quad u_r = -\frac{1}{r} \frac{\partial \psi}{\partial z}. \quad (2.1)$$

Using this definition the mass-conservation equation for incompressible fluid flow, which for axisymmetric flows reduces to:

$$\nabla \cdot \mathbf{u} = \frac{\partial u_z}{\partial z} + \frac{1}{r} \frac{\partial (r u_r)}{\partial r} = 0, \quad (2.2)$$

is automatically satisfied.

In examining flows containing regions of rotating fluid, the *vorticity* vector $\boldsymbol{\omega}$, defined by $\boldsymbol{\omega} = \nabla \times \mathbf{u}$, is an important quantity, measuring the local rate of rotation of fluid elements. For axisymmetric flows without swirl ($u_\phi = 0$) this vorticity vector has only a non-zero azimuthal component, given by:

$$\omega_\phi = \frac{\partial u_r}{\partial z} - \frac{\partial u_z}{\partial r} = -\frac{1}{r} \left(\frac{\partial^2 \psi}{\partial z^2} + \frac{\partial^2 \psi}{\partial r^2} - \frac{1}{r} \frac{\partial \psi}{\partial r} \right). \quad (2.3)$$

The vorticity equation, describing the evolution of the vorticity in time, is obtained by taking the curl of the Navier-Stokes equation (Batchelor 1967). For an axisymmetric swirl-free flow in an incompressible viscous fluid this vorticity equation is written as:

$$\frac{D(\omega_\phi/r)}{Dt} = \nu \left(\nabla^2 \omega_\phi - \frac{\omega_\phi}{r^2} \right), \quad (2.4)$$

where ν is the kinematic viscosity of the fluid. The material derivative $D/Dt \equiv \partial/\partial t + (\mathbf{u} \cdot \nabla)$ denotes the rate of change in time of a quantity (here ω_ϕ/r) when following the motion of the fluid. For an inviscid fluid, the right-hand side of equation (2.4) vanishes and for each fluid element ω_ϕ/r is thus a conserved quantity. In steady inviscid flows ($\partial/\partial t = 0$), the fluid

flows along a pattern of steady axisymmetric streamsurfaces, which are commonly presented by streamlines in a meridional cross-section of the flow. As a consequence, the ratio ω_ϕ/r is constant along the individual streamlines. This means that the following functional relation is satisfied, where the capital Ψ is used to denote the stream function of a *steady* flow.

$$\frac{\omega_\phi}{r} = f(\Psi), \quad (2.5)$$

where $f(\Psi)$ is, in general, an arbitrary function that determines the structure of the axisymmetric flow. The shape of this function for a vortex ring is discussed in the next subsection.

Another important quantity is the *circulation*, which indicates the strength of a vortex. For general three-dimensional flows the circulation around a closed curve C is defined as the line integral of the velocity field along this curve. When the region occupied by the fluid volume is singly-connected and C is a reducible curve in this region, Stokes' theorem can be applied and the line integral of the velocity field can be written as a surface integral of the vorticity over an open surface A bounded by the curve C :

$$\Gamma \equiv \oint_C \mathbf{u} \cdot d\mathbf{s} = \iint_A (\boldsymbol{\omega} \cdot \mathbf{n}) dA, \quad (2.6)$$

where $d\mathbf{s}$ denotes a material line element along the curve and \mathbf{n} is the unit normal to A . For a material curve C that moves with the flow of an ideal fluid* the circulation around C is invariant. This is known as Kelvin's circulation theorem. For viscous fluids the circulation is only invariant as long as there is no viscous diffusion of vorticity across the curve C .

For axisymmetric flows the circulation is usually determined around a curve, which lies in a meridional plane ($\phi = \text{constant}$) and passes along the axis of symmetry and encircles the flow on one side of this axis once. For flows in an infinite domain, in which the velocity field vanishes at infinity, the curve can be closed at infinity and the circulation is given by the integral of the axial velocity component along the z -axis:

$$\Gamma = \int_{-\infty}^{\infty} u_z dz. \quad (2.7)$$

2.2.2 MODELS OF INVISCID VORTEX RINGS

A vortex ring in an ideal fluid at rest at infinity has an axisymmetric ring-shaped structure. The vorticity is concentrated in the core of the ring, there is no swirling motion along the core and the vortex lines[†] are closed circular loops. Such a vortex ring propagates due to its self-induced motion in a direction perpendicular to the plane of the ring, without changing in size or shape.

To describe the structure of the vortex ring mathematically, cylindrical coordinates (r, ϕ, z) are used, with the z -axis coinciding with the centreline of the ring and oriented in the direction of propagation. The velocity field induced by the vortex ring can be written in terms of a Stokes stream function ψ (see equation (2.1)) and the vorticity in the core has only a non-zero azimuthal component. Relative to a frame moving with the ring the flow field is steady and a relation of the form of equation (2.5) applies to the vorticity distribution in the vortex core.

Several theoretical models for steady inviscid vortex rings have been proposed in the literature, since the celebrated works of Helmholtz (1858) and Thomson (1867b; 1869) on vortex

*An ideal fluid is an inviscid incompressible fluid with uniform density.

†A vortex line is a line in the fluid, whose tangent is everywhere parallel to the local vorticity vector.

motion. In these models the vorticity distribution in the core and the shape ∂A of the boundary of the core are assumed to have simple structures. These models are all solutions of the following general problem, which assumes that the vorticity is prescribed inside the vortex core and vanishes outside (Fraenkel 1970):

$$\frac{\partial^2 \Psi}{\partial z^2} + \frac{\partial^2 \Psi}{\partial r^2} - \frac{1}{r} \frac{\partial \Psi}{\partial r} = \begin{cases} -r^2 f(\Psi) & \text{inside } \partial A \\ 0 & \text{outside } \partial A, \end{cases} \quad (2.8)$$

subject to the following conditions: 1) continuity and differentiability of Ψ across the boundary ∂A ; 2) $\Psi = \text{constant}$ on ∂A ; 3) $\Psi + \frac{1}{2}Ur^2 \rightarrow 0$ as $r^2 + z^2 \rightarrow \infty$, where $-U$ denotes the upstream velocity at infinity in the moving frame of reference. Existence proofs which demonstrate that solutions of this problem exist without necessarily prescribing the exact form of $f(\Psi)$ have been discussed in Benjamin (1976). For vortex rings the possible function space consists of those functions $f(\Psi)$ which are non-decreasing, positive for $\Psi > \Psi_c \geq 0$ (i.e. inside the vortex core) and zero for $\Psi \leq \Psi_c$ (i.e. outside the vortex core). Here the streamline $\Psi = \Psi_c$ coincides with the boundary of the vortex core, which is usually connected and separated from the z -axis, like a torus.

In many theoretical models on steady vortex rings the vorticity distribution in the core is assumed to be linear, hence $f(\Psi) = k = \text{constant}$. This class of vortex rings is called the 'Norbury-Fraenkel' family (Norbury 1973) and includes the complete range from thin-core vortex rings to Hill's spherical vortex (Hill 1894; Batchelor 1967). In such a spherical vortex the vorticity is distributed over a sphere of radius R_H . The boundary of this vortex coincides with the streamline $\Psi_c = 0$, because it intersects the z -axis where $\Psi = 0$ is stated. The boundary conditions for the stream function on the surface of the sphere determines the self-induced velocity U_H of this vortex, which is proportional to the slope in the linear vorticity distribution:

$$U_H = \frac{2R_H^2 \omega_\phi}{15 r}. \quad (2.9)$$

Perhaps the most well-known member of the NF-family is the thin-core vortex ring with ring radius R and vorticity concentrated in a small circular core with core radius a . For such vortex rings the vorticity distribution in the core can be assumed to be uniform, at least to first order in a/R . An expression for its self-induced velocity of propagation U has first been given by Thomson (1867a)[†]:

$$U = \frac{\Gamma}{4\pi R} \left[\ln \frac{8R}{a} - \frac{1}{4} + \mathcal{O}\left(\frac{a}{R}\right) \right], \quad (2.10)$$

where Γ denotes the circulation around the core of the vortex ring. This equation is known as Kelvin's formula[‡] for the translation velocity of a vortex ring. Although he did not give a proof, it can for instance be derived from a consideration of the impulse and the kinetic energy of the flow. This derivation is given by Saffman (1970), who showed that the same method can be used to generalize equation (2.10) to steady rings in which the vorticity ω_ϕ in the core is given by a distribution that is, to leading order, a function $\omega_o(s)$ of the distance s from the centre of the core:

$$\omega = \omega_0(s) \left[1 + \mathcal{O}\left(\frac{a}{R}\right) \right]. \quad (2.11)$$

[†]The original equation in Thomson's letter was without the $\mathcal{O}(a/R)$ correction.

[‡]Sir William Thomson was honoured in 1892 and his full name became Sir William Thomson, Baron Kelvin of Largs.

The $\mathcal{O}(a/R)$ term accounts for the deviation of the vorticity distribution in the core from the axisymmetric profile $\omega_o(s)$ owing to the curvature of the vortex ring. It suffices here to give only the result of this mathematical derivation, which clearly shows how the propagation speed depends on the vorticity distribution in the circular core:

$$U = \frac{\Gamma}{4\pi R} \left(\ln \frac{8R}{a} - \frac{1}{2} + \int_0^a \frac{\hat{\Gamma}(s)^2}{s} ds \right) + \mathcal{O} \left(\frac{\Gamma a}{R^2} \ln \frac{a}{R} \right), \quad (2.12)$$

where

$$\hat{\Gamma}(s) = \frac{2\pi}{\Gamma} \int_0^s s' \omega_0(s') ds' \quad (\Gamma = 2\pi \int_0^a s \omega_0(s) ds) \quad (2.13)$$

is the normalized circulation around a circle of radius s with centre at the core and $\hat{\Gamma}(a) = 1$. Here, a denotes the radius of the circular core with all vorticity contained in this region. For example, if the vorticity distribution in the core is uniform, hence $\omega_\phi \approx kR = \text{constant}$ for a thin core in solid-body rotation, the integral term in equation (2.12), which will be denoted by the symbol \mathcal{J} , equals $\mathcal{J} = 1/4$ and equation (2.10) is retrieved. In fact, this value yields a lower bound for \mathcal{J} , which increases if the vorticity, for given a , is concentrated closer to the core centre at $s = 0$. For non-uniform vorticity distributions given by equation (2.11) an effective core radius a_e is defined in Saffman (1978) by:

$$a_e = a e^{\frac{1}{4} - \mathcal{J}} \quad \text{or} \quad a_e = 8R e^{-(\tilde{U} + \frac{1}{4})}, \quad (2.14)$$

where $\tilde{U} = 4\pi UR/\Gamma$ is a commonly used parameter that depends only on the circulation distribution in the core and the ratio a/R . Obviously, the translation speed of the vortex ring is given by equation (2.10) when a is replaced by a_e .

Another method to obtain equation (2.10) has been used by Fetter (1974). It is based on the following general kinematical equation for the velocity field induced at a point \mathbf{x} by a localized vorticity field in an unbounded ideal fluid (see Batchelor 1967):

$$\mathbf{u}(\mathbf{x}) = -\frac{1}{4\pi} \int_V \frac{\boldsymbol{\omega}(\mathbf{x}') \times (\mathbf{x}' - \mathbf{x})}{|\mathbf{x}' - \mathbf{x}|^3} dV'. \quad (2.15)$$

Here, \mathbf{x}' denotes a point in the region V' that contains the vorticity. For an axisymmetric swirl-free flow this vector equation can be reduced to a scalar equation, where the Stokes stream function is given as an integral of ω_ϕ over the cross-section of the core:

$$\psi(r, z) = \frac{1}{2\pi} \int \sqrt{r'r'} \omega_\phi(r', z') dr' dz' \left[\left(\frac{2}{k} - k \right) K(k) - \frac{2}{k} E(k) \right], \quad (2.16)$$

where $K(k)$ and $E(k)$ are the complete elliptic integrals of the first and second kind, respectively, and:

$$k^2 = \frac{4rr'}{(r+r')^2 + (z-z')^2}. \quad (2.17)$$

Fetter (1974) uses an asymptotic expansion of these complete elliptic integrals to determine an analytical expression for the stream function near a thin circular core. The self-induced velocity of the vortex ring follows then from the condition that the boundary of the core coincides with a streamline, thus there is no flow out of the core. If the vorticity distribution in the core is again assumed uniform, equation (2.10) results.

Despite these mathematical derivations, it is also possible to provide a more physical explanation for the self-induced velocity of a thin-core vortex ring by considering the force balance acting on the curved vortex. In simple terms it is proposed that adding curvature to a straight vortex filament leads to an increase in the velocity on the ‘inside’ of the curve and a related reduction of the pressure. Oppositely, at the ‘outside’ of the curve the velocity decreases and the pressure is increased. The resulting pressure force is equivalent to a tension of the curved vortex and is directed toward the ring centre. In the absence of an additional external flow this force has a tendency to shrink the vortex ring. This shrinking would reduce the vortex ring’s impulse, being proportional to the square of the ring radius (Batchelor 1967, p. 522). The fluid impulse, defined as the resultant force impulse required to generate the flow of the vortex ring from rest, is a conserved quantity in an infinite flow domain (Batchelor 1967, p. 520). Therefore, an additional force is required to keep the ring radius constant and the flow steady. This counter force is provided by a Kutta lift force, generated by the external flow that encounters the vortex ring as it propagates through the surrounding fluid. A complete derivation for the propagation velocity based on this approach is given in Moore & Saffman (1972) (see also Saffman 1992).

2.2.3 POTENTIAL FLOW ASSOCIATED WITH THIN-CORE VORTEX RINGS

In this section the irrotational (potential) flow induced outside the core of the vortex ring is investigated. Part of this flow is carried with the vortex ring and forms an ‘atmosphere’ (Thomson 1867*b*) attached to the vortex. To determine this flow equation (2.16) is used and all vorticity is concentrated in a circular line-vortex with radius R , zero core cross-section, but finite circulation Γ . This means that it is assumed, to first order approximation, that at some distance outside the vortex core the flow is not affected by the distribution of vorticity and the shape of the vortex core. The mathematical description for the stream function of such a circular line-vortex, located at $Z = 0$, has first been given by Helmholtz (1858) and is derived from equation (2.16):

$$\psi(r, z) = \frac{\Gamma\sqrt{Rr}}{2\pi} \left[\left(\frac{2}{k} - k \right) K(k) - \frac{2}{k} E(k) \right], \quad (2.18)$$

where

$$k^2 = \frac{4rR}{(r+R)^2 + z^2}. \quad (2.19)$$

In figure 2.1(*a*) a plot of the streamlines in an azimuthal plane is shown. It is important to emphasize that this plot represents the instantaneous flow associated with a circular line-vortex in a fluid at rest at infinity. Because the core cross-section of this line vortex vanishes, its self-induced velocity is infinite (see equation (2.10)).

As stated above, the flow in the region outside the core of a vortex ring with finite core cross-section is approximated by the flow of a circular line-vortex; the expression (2.18) for the stream function of the circular line-vortex is then adopted only in the flow region outside the vortex core. Vortex rings with finite core cross-section have finite self-induced velocity U and, in a frame moving with the ring, the flow field is steady. A moving frame of reference is simulated by adding a uniform counterflow of velocity $-U$:

$$\Psi = \psi - \frac{1}{2}U r^2. \quad (2.20)$$

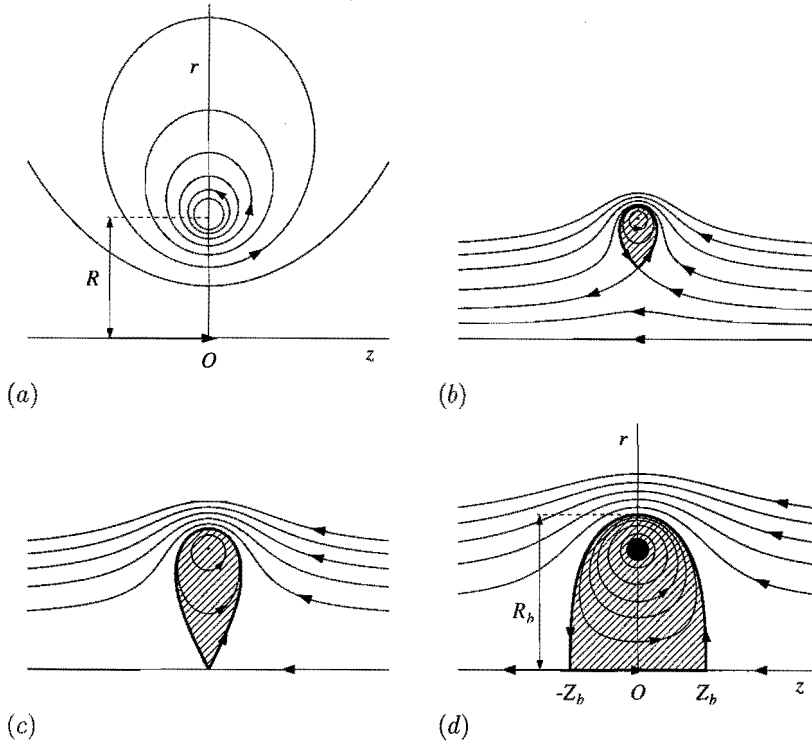


FIGURE 2.1: (a) Instantaneous streamlines in a meridional plane of a circular line-vortex in a fluid at rest at infinity (with equal increments of ψ). (b-d) Patterns of streamlines Ψ of the steady irrotational flow relative to vortex rings with various ratios a/R : (b) $a/R = 0.001$, (c) $a/R = 8 \exp(-2\pi - 1/4)$ and (d) $a/R = 0.1$. The black dots mark the vortical cores and the shaded areas represent the convected vortex atmospheres, which are bounded by the respective separatrices (thick lines). Streamlines are not equidistant in these patterns.

Figure 2.1(b-d) presents plots of the streamlines $\Psi = \text{constant}$ for a number of vortex rings with different core cross-sections. In all cases the flow is divided in two regions, separated by a specific streamline called the separatrix (denoted by a thick line in the figures). Within this separatrix streamlines form closed loops along which fluid is advected steadily with respect to the vortex ring. This region of fluid that encloses the core of the vortex ring and is transported with it is called the vortex *atmosphere*. As seen in figure 2.1 this atmosphere can have various shapes, depending on the size of the core. For thin cores the atmosphere consists of a small volume of fluid surrounding the vortex core and has an open structure with a counterflow of environmental fluid near the ring centre (figure 2.1b). For thick cores the atmosphere reaches to the axial centreline and forms a closed blob of convected fluid, without counterflow at the centre (figure 2.1d). In this case two stagnation points appear where the separatrix intersects the ring axis.

To classify the distinctive atmosphere shapes the axial velocity at the ring axis is determined as induced by a circular line-vortex. Using equation (2.1) to derive this velocity

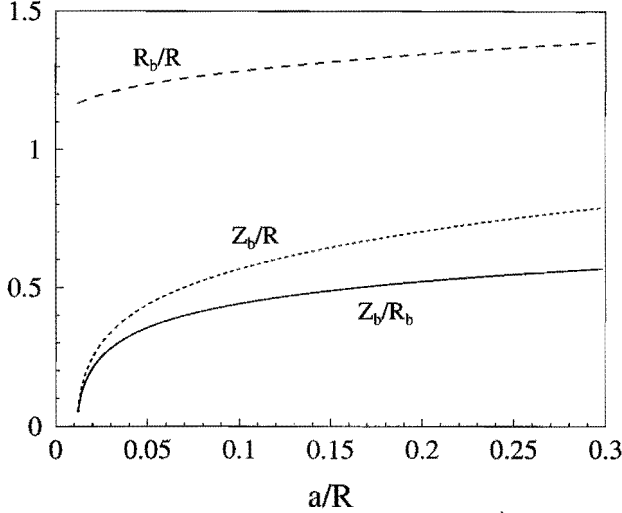


FIGURE 2.2: Scaled dimensions Z_b/R (dotted line) and R_b/R (dashed line) of a blob-shaped atmosphere as a function of a/R . The ratio Z_b/R_b of these sizes is denoted by the solid line.

component from the stream function (2.18) it is found that at $r = 0$ (the axis of symmetry):

$$u_z(r = 0, z) = \frac{\Gamma R^2}{2(z^2 + R^2)^{3/2}}. \quad (2.21)$$

Depending on the core size of the vortex ring, which central axial flow is approximated by this expression, the ring velocity U has different values; these determine the axial positions $z = \pm Z_b$ of the stagnation points in the flow, according to the condition:

$$u_z(r = 0, Z_b) - U = 0. \quad (2.22)$$

For small U (thick cores) two stagnation points appear, between which the expression on the left-hand side in (2.22) is positive. For large U (thin cores) this expression is negative definite and stagnation points are absent. The intermediate case in which there is only a single stagnation point at $Z_b = 0$ is plotted in figure 2.1(c). In this case $U = u_z(0, 0) = \Gamma/2R$ and substitution of Kelvin's formula (2.10) for U yields the related relative core radius $a/R = 8 \exp(-2\pi - 1/4) \simeq 0.01163$.

Returning to the closed-blob atmosphere (figure 2.1d), the dimensions of the shaded area are characterized by the distance $2Z_b$ between the stagnation points and the radial extension R_b of the separatrix. Relative to the ring radius R , the scaled dimensions Z_b/R and R_b/R depend only on the relative core radius a/R . Condition (2.22) can be used to obtain an analytical expression for Z_b/R as a function of a/R . Since the stream function vanishes at the separatrix, the scaled radial dimension R_b/R is given by the condition $\Psi(R_b/R, z = 0) = 0$, which is solved numerically as a function of a/R . In figure 2.2 these two relations are shown, as well as their ratio Z_b/R_b . This third relation is important, because it can be obtained very easily from laboratory experiments (see subsection 2.3.3).

It is emphasized that this technique to determine the atmosphere dimensions only applies to vortex rings with a closed-blob atmosphere. For the ring-shaped atmosphere the stream

function does not vanish at the separatrix; the separatrix is now defined by a self-intersecting streamline with an associated stagnation point below the ring core. This stagnation point is located where the axial velocity at the r -axis ($z = 0$) vanishes and this position depends on the ratio a/R . By localizing this stagnation point and computing the corresponding streamline the separatrix of the flow is obtained, as plotted in figure 2.1(b).

2.2.4 SOME EFFECTS OF VISCOSITY

In the inviscid flow models of vortex rings effects of viscosity on the vorticity distribution in the core and the motion of the vortex ring are by definition completely ignored. A vortex ring is assumed to be a steadily propagating coherent structure, whose size and shape do not change in time. Flow visualization experiments of vortex rings (e.g. smoke rings) support this assumption, showing a clearly marked vortical ring which preserves its circular shape and propagates straight ahead.

Although viscous effects seem to play an inferior role in describing the motion of well-developed vortex rings, for the creation of vortex rings the fluid viscosity is crucial. Vortex rings are often formed by pushing a finite amount of fluid through a thin-walled, sharp-edged circular tube. Due to viscous forces a thin boundary layer is then formed at the inner tube wall, which forms a cylindrical vortex sheet that separates at the tube edge and rolls-up into a toroidal vortical core. The vortex ring formation process has been studied in detail by Didden (1979) and some typical features in this process are quoted here for completeness. During the fluid injection the vortex ring gradually grows and starts to move away from the tube edge. The surrounding flow of the growing vortex ring induces a boundary layer near the outer tube wall containing vorticity of opposite sign and part of this counter-rotating fluid is advected into the core of the vortex ring. The total circulation of the vortex ring, mainly resulting from the net vorticity flux through the tube-exit plane, is therefore difficult to predict accurately. After the fluid injection has stopped the induced flow of the evolving vortex ring produces near the tube edge a secondary vortex of opposite circulation with its toroidal axis exactly in the tube-exit plane. The induced flow of this secondary vortex might contribute to a slight decrease of the ring diameter of the main vortex ring as it propagates away from the tube end, although the influence of the tube wall (which can be modeled by a system of mirror-vortices) on this ring contraction is expected to be dominant (Sheffield 1977). For vortex rings created at a circular sharp-edged orifice in a plate instead of at a tube end, this secondary vortex forms a vortex ring that moves freely in opposite direction into the vortex ring generator.

Depending on the generation conditions and hence the Reynolds number of the flow a vortex ring created in this way is either laminar (low Reynolds number) or turbulent (high Reynolds number). Glezer (1988) has studied the conditions for which a vortex ring is either laminar or turbulent. A laminar vortex ring resembles very well a vortex ring in ideal fluid, with a regular core structure propagating steadily and undisturbed through the surrounding fluid. In turbulent vortex rings the core structure is irregular and considerable mixing of fluid between the vortex ring and the environment occurs. Considerable amounts of vorticity and impulse are left behind in a turbulent wake and the propagation velocity of the vortex ring decreases rapidly. Turbulent vortex rings have been studied extensively by Glezer & Coles (1990). Under certain conditions a transition of the laminar flow into a turbulent vortex ring appears, a process that is preceded by growing wavy instabilities on the core of the laminar vortex ring that eventually breaks up. A detailed description of the successive events in such a flow transition is described in Maxworthy (1977).

In this thesis only laminar vortex rings will be considered, which remain laminar in the observational domain. Because these laminar vortex rings are created at relatively low Reynolds number[†] ($Re_o = 480$), viscous effects may not be negligible completely. Effects of viscosity on the flow of laminar vortex rings have been studied by Maxworthy (1972) and the main features are summarized here. Due to viscosity the vorticity in the vortical core is spread out and is diffused over the region of fluid that is transported by the vortex ring. Near the ring centre vorticity of opposite sense is cancelled by cross-diffusion, leading to a reduction of the circulation of the vortex ring. In addition, vorticity is diffused over the boundary of the convected fluid volume into the outer irrotational flow. Part of this surrounding fluid with newly acquired vorticity is entrained at the rear of the vortex ring and part of the diffused vorticity is lost in the wake. By this entrainment of environmental fluid the vortex ring slightly grows in size and the impulse of the vortex ring has to be shared over an expanding fluid volume. All these effects contribute to a gradual slowing-down of the motion of the vortex ring. A laminar vortex ring in a real fluid thus does not have a perfect steady structure that moves on forever; however, the slow-down of the vortex ring occurs on a viscous time scale much longer than typical time scales of the motion (e.g. the time for one eddy turnover or the time in which a distance equal to the ring size is covered.)

2.3 Description of laboratory experiments

2.3.1 EXPERIMENTAL APPARATUS

In the laboratory experiments, vortex rings were created by pushing a finite amount of fluid through a sharp-edged circular orifice cut in a thin plate. This plate was the lid of a cylindrical box (henceforth referred to as the vortex ring generator) with a closed bottom. The vortex ring generator was held up in a two-pronged fork that was fixed to a vertical stand (figure 2.3 gives a sketch of a perspective view of the experimental set-up). The construction was so that the vortex ring generator could rotate relative to the fork in order to create vortex rings propagating in different directions. For the experiments described in this chapter the generator was directed as shown in figure 2.3 to create vortex rings propagating vertically upwards. Fluid injection was provided by two long reinforced plastic tubes connected to the generator by water taps. The stand holding the vortex ring generator was placed in a corner of an experimental tank and the plastic tubes were guided outside the tank. The set-up was constructed so that the vortex ring generator was now at the centre of the tank.

The experimental tank was a glass container of horizontal dimensions 60×60 cm and 100 cm height. It was filled with clear tap water to a level of 50 cm in most of the experiments. The tank was put on a table. Anticipating to the experiments described in the next chapters a ‘rotating’ table was used, i.e. a table that can rotate with a prescribed angular velocity around a vertical axis. For the present experiments, however, the table was not rotating.

The injection of fluid was controlled by a stepmotor-driven traversing system, which could push the pistons of a series of syringes simultaneously in a prescribed way. This system was placed outside the tank on the table. An equal number of syringes was connected to each of the long plastic tubes by several 3-way joints.

[†]The Reynolds number Re of the flow can be defined in different ways. In terms of the injection conditions $Re_o = U_o R_o / \nu$, where U_o is the mean injection velocity, R_o the radius of the orifice and ν the kinematic viscosity of the fluid.

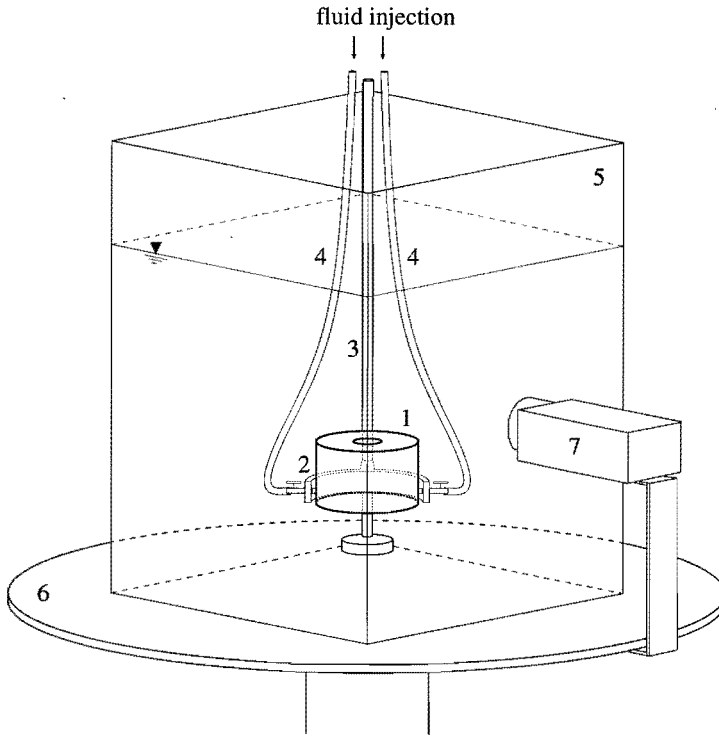


FIGURE 2.3: Perspective view of the experimental set-up. The vortex ring generator consists of a cylindrical perspex box 1 with a circular orifice on top; it was held up in a fork 2 fixed to a vertical stand 3. Fluid injection was provided by plastic tubes 4. The set-up was placed in an experimental tank 5 put on a table 6. The experiments were recorded from a side view by a video camera 7.

All experiments were recorded by either a video camera or a photo camera, mounted on the table to record a side view of the vortex rings (see figure 2.3). The vortex rings were illuminated by a light sheet directed vertically through the centreline of the orifice of the vortex ring generator. Since the experiments were performed relative to a black background in a darkened laboratory environment, only the cross-sectional flow of the vortex ring is then observed. Two identical slide projectors have been used to produce the light sheet. A light sheet can easily be created by cutting a small slit in a black slide and focusing the slide projector. The projectors were mounted at some distance above the experimental set-up and directed downwards, so that both light sheets coincide. The width of the light sheet used was about 5 mm, as for smaller sheets the intensity of the light in the sheet was insufficient.

2.3.2 GENERATION OF VORTEX RINGS

In the experiments a finite amount of fluid was pushed through the orifice of the vortex ring generator by pressing the syringes for a short time. At the sharp edge of the orifice a vortex sheet was then created which rolled up to form a vortex ring. The volume of the

injected fluid and the injection velocity was controlled by the stepmotor-driven traversing system which pushed the pistons of the syringes. The volume of the fluid injected depends on the displacement of the pistons in the syringes as well as on the diameter of each piston and the total number of syringes used. If the pistons of N syringes were displaced by a distance L_s with a mean velocity \bar{U}_s , a comparative column of fluid of length L_o was pushed through the orifice with mean velocity U_o . On account of the incompressibility of the fluid the following relations between these parameters can be derived:

$$L_o = NL_s \left(\frac{D_s}{D_o} \right)^2 \quad (2.23)$$

$$U_o = N\bar{U}_s \left(\frac{D_s}{D_o} \right)^2, \quad (2.24)$$

where D_s and D_o denote the diameter of each piston and the orifice, respectively.

In the experiments orifices with diameters $D_o = 2.0, 3.0, 4.0$ and 5.0 cm were used and pistons with diameter $D_s = 2.54$ cm ($= 1$ inch). For each orifice a specific amount of fluid had to be injected in order to obtain a steadily propagating laminar vortex ring. Too much injected fluid resulted in a jet, while there was no freely moving vortex ring if insufficient fluid was injected. Also the velocity of injection had to be large enough, otherwise the vortex immediately coalesced to a blob of fluid without a definite coherent structure. If the fluid injection is too rapid a transition appears and the laminar ring becomes turbulent (see e.g. Glezer 1988). Therefore, a proper combination of the parameters L_s , \bar{U}_s and N had to be found for each orifice; this was done empirically.

In most of the experiments reported here an orifice with diameter $D_o = 4.0$ cm was used, although the 3.0 cm orifice could be used equally well. Vortex rings produced with the 2.0 cm orifice were too small to examine the small scales appearing in the experiments with background rotation (which are described in the next chapters). On the other hand, the fluid injection system was incapable of injecting at a sufficient flow rate to produce well-structured vortex rings on the relatively large 5.0 cm orifice.

2.3.3 DATA PROCESSING OF DYE-VISUALIZED EXPERIMENTS

Two methods have been used to visualize the flow field of the vortex ring. In one of these methods the flow is visualized by dye, while in the other method small tracer particles are used. The discussion of this second method will be given in the next subsection.

In the dye visualization experiments natrium-fluorescein dye was used, which gives the water a bright yellow-green colour. This dyed fluid clearly contrasts with the ambient undyed fluid, which appears black because of the dark background. In the preparation of these experiments the generator, plastic tubes and syringes were filled with dyed water and all air bubbles were released from the circuit. After closing the orifice with a thin metal plate to avoid mixing, the tank was filled with clear tap water. Before starting the experiment this plate was carefully removed in horizontal direction. This was done by pulling a wire that was fixed to the plate and guided outside the tank by several pulleys.

To calibrate dimensions in the video images of the experiments a recorded image of a well-defined uniform grid has been used. This grid was put in the plane of the light sheet, where the experiments were recorded later, and was carefully removed before starting the experiment. The grid consisted of a set of equidistant horizontal and vertical lines with 0.5 cm grid spacing.

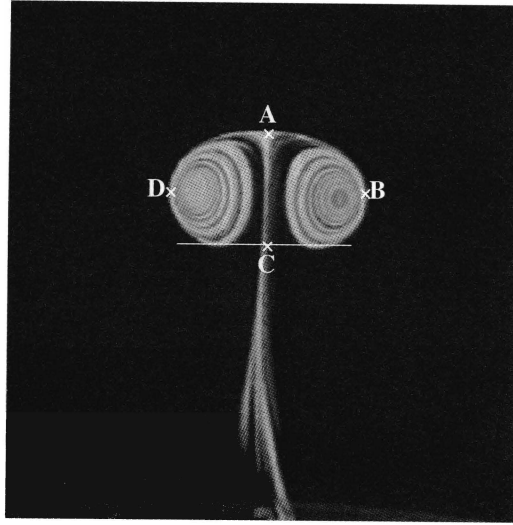


FIGURE 2.4: Cross-sectional view of a fully-developed vortex ring. The region of transported fluid (the vortex ‘atmosphere’) is clearly indicated by the dyed fluid. The dimensions of this blob are obtained by measuring the positions of the points A, B, C and D.

Experiments with dye-visualization were performed to obtain a clear qualitative picture of the evolution of the flow and to trace the propagation of the vortex ring. In several studies on vortex rings (see e.g. Maxworthy 1977; Didden 1979) dye is injected only near the orifice edge, i.e. in the region of the flow where vorticity is created. In these studies dye is thus primarily used to mark the vortical core of the vortex ring. However, in the experiments reported in this thesis all injected fluid is dyed. When the vortex ring has been developed completely the dyed fluid then marks the region of flow that is transported by the vortex ring.

It was mentioned in subsection 2.2.3 that a ‘vortex atmosphere’ exists, consisting of a closed region of irrotational flow surrounding a thin-core vortex ring in an ideal fluid. This region is bounded by a surface, called the separatrix. It was shown that the shape and dimensions of this separatrix depends on the ratio of the core radius a to ring radius R . Based on this observation, a method is proposed to obtain approximate values for these ring parameters from the dimensions of the dyed fluid blob that is observed in flow visualization experiments (see figure 2.4). This method is referred to as the ‘vortex atmosphere method’ and provides a way to obtain some quantitative information about the vortex ring characteristics from dye-visualization experiments.

It might seem cumbersome to determine the ring radius in this way, since a direct method is to measure the distance between the spiral centres in figure 2.4. However, the positions of these centres are usually difficult to define, because diffusion of dye blurs the spiraling structure near the core centre. In contrast, the vortex atmosphere is marked by a definite boundary and its dimensions can be measured accurately.

To demonstrate the application of this method figure 2.4 shows a video image of a cross-sectional view of a fully-developed vortex ring. The roll-up of fluid in the vortex cores on either side is visualized by spiraling sheets of dyed fluid, the sense of rotation is counter-clockwise in the left core section and clockwise in the right core section. The blob of fluid that is convected

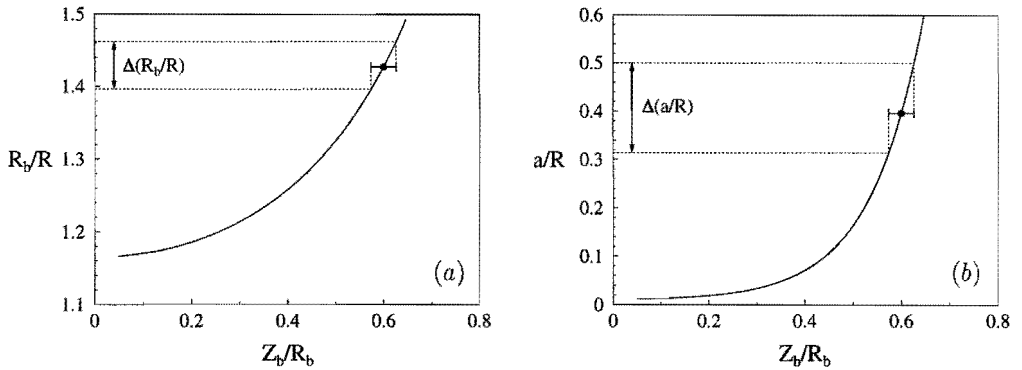


FIGURE 2.5: Ratios R_b/R (a) and a/R (b) plotted as a function of the ratio of the atmosphere dimensions Z_b/R_b .

with the vortex ring clearly contrasts with the dark background. The lateral dimension $2R_b$ of this ‘atmosphere’ is determined by measuring the distance between points **B** and **D** at the lateral edges. The axial length $2Z_b$ is given by the distance between **A** and **C**. The location of point **A** at the front stagnation point can be accurately determined from the video image. At the rear, however, ambient fluid is being entrained and the stagnation point, which denotes the rear edge in the inviscid flow model, is now absent. The location of point **C** is then obtained approximately by drawing a line through the rear edges of the dyed cores, as indicated in figure 2.4. From the ratio Z_b/R_b the parameter a/R can be determined graphically by reading the appropriate graph in figure 2.2. This value for a/R is then used in turn to determine the ratio R_b/R , yielding a value for R .

For convenience the relevant curves of figure 2.2 have been replotted in figure 2.5, but now the ratios R_b/R and a/R are plotted as a function of the parameter Z_b/R_b . The accuracy of the measurement of the lateral coordinates of **B** and **D** is of the order of one pixel in the video image, implying an absolute error in $2R_b$ of 0.7 mm. Due to the approximate method to measure the axial coordinate of **C** the absolute error in $2Z_b$ is larger, of the order of 1 mm. The resultant inaccuracy in the ratio Z_b/R_b is indicated by an error bar in figure 2.5(a), where the values $2R_b = 5.5$ cm and $2Z_b = 3.3$ cm have been used which are typical for the experiments described in this thesis (see subsection 2.4.2). The related inaccuracy in R_b/R is read graphically as indicated in figure 2.5(a), yielding a relative error in R of $\pm 3.5\%$. Similarly, the inaccuracy in a/R is read from figure 2.5(b), which shows a considerable larger relative error (of the order of $\pm 20\%$) in the obtained value for this parameter due to the steeper slope of the curve.

It is thus concluded that this method is suitable to determine the ring radius within a few percent, although only a rough estimation is obtained for the relative core radius. A better accuracy for this parameter should not be aimed at with this ‘vortex atmosphere’ method. In this method it was assumed that the vorticity is concentrated uniformly in a thin-core vortex ring. In real viscous vortex rings, however, the vorticity is spread out over a thicker core region by viscous diffusion. In that case a characteristic core size can be defined, in which most of the

vorticity is concentrated. Various definitions are possible, but this problem will be discussed later (see subsection 2.4.3).

Another important parameter that characterizes the flow of a vortex ring is the circulation Γ around the vortex core. This parameter is deduced from the measured velocity U of the vortex ring. This velocity is determined from the axial distances travelled by the centre of the vortex ring in fixed time intervals. The position of the ring centre is located at the midpoint between points **B** and **D** in figure 2.4. To obtain from this measured value of U an estimation for the ring circulation Γ , Kelvin's formula (2.10) is used, giving the ring velocity of an ideal thin-core vortex ring in term of the ring parameters Γ , R and a . Substituting the measured values for U , R and a/R in this equation yields a value for Γ of the experimental vortex ring. Although the parameter a/R has been obtained with a large inaccuracy, the logarithmic dependence in Kelvin's formula reduces the contribution of this inaccuracy to the relative error in Γ to 7%. Taking also into account the inaccuracies in R and U yields a total relative error in the obtained value for Γ of 15%.

In this way one may derive a quantitative measure of the circulation of a vortex ring from dye-visualization experiments, although the obtained value merely gives an indication of its order of magnitude. To determine the circulation more accurately the velocity field (or even vorticity field) of the vortex ring has to be measured. For this, experiments were performed in which the flow is visualized by small tracer particles. This method will be discussed in the next subsection.

2.3.4 DATA PROCESSING OF PARTICLE EXPERIMENTS

Another way to visualize the flow is by following the motion of small tracer particles that are passively advected by the flow. The length of the path travelled by a particle in a short time interval gives an appropriate estimation for the local flow velocity. Usually, many particles are used that are homogeneously distributed over the fluid, yielding the momentary velocity field of the complete flow.

For these experiments small white particles of $100 \sim 250 \mu\text{m}$ diameter have been used, commercially available as *Optimage seeding powder*. These particles are polycrystalline in structure, giving them a light scattering efficiency approximately five times greater than latex spheres. Therefore, the minuscule particles are clearly observed as bright dots if illuminated sufficiently. Despite the reported specific gravity $\rho_p = 1.0 \pm 0.02 \text{ gr/cm}^3$ of the particles (being assumedly of the same density as the water in the tank at room temperature), they appeared to sink to the bottom of the tank during the experiments. In order to maintain an approximately homogeneous distribution of particles for the time experiments were carried out a homogeneous salt-water solution with an increased density ($\rho \simeq 1.0325 \text{ gr/cm}^3$) had to be used. Unfortunately, another undesirable phenomenon was encountered. The fluid in the tank did not achieve a state of rest, but a continuous slow flow was maintained. Probably, by evaporation of fluid near the free surface a layer of larger density is created underneath this surface. Due to buoyancy forces this layer is unstable, starts to sink and drives the observed flow. To overcome this problem a thin film of clear tap water has been supplied at the water level, which prevents evaporation of the underlying salt-water. In addition, the tank was closed with a transparent foil.

Before the experiments were started, the particles were added to the fluid in the tank and in the vortex generator. Again a light sheet was used to illuminate only a planar cross-section of the flow. When a vortex ring was created the particles were clearly observed to be advected

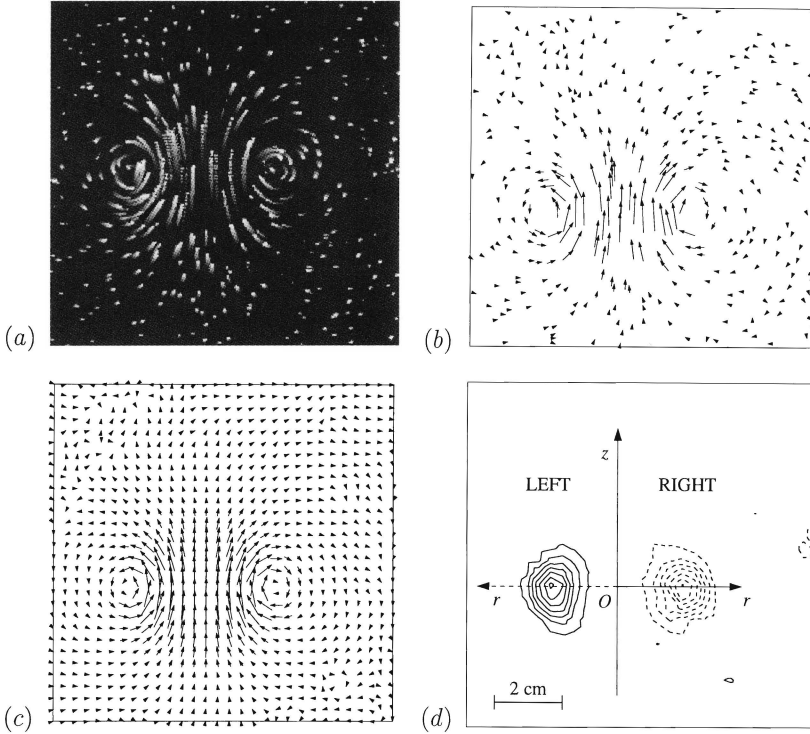


FIGURE 2.6: (a) Traces of particles indicate the flow field of the vortex ring in a cross-sectional plane. (b) Velocity field measured at the momentary positions of the tracer particles. (c) Interpolation of the velocity field on a uniform 30×30 grid from which the component of the vorticity normal to the plane is calculated. (d). Solid contour lines denote positive vorticity (anti-clockwise rotation) and dashed lines denote negative vorticity (clockwise rotation). Experimental parameters: $D_o = 4.0$ cm, $L_o = 2.4$ cm and $U_o = 2.4$ cm/s.

with the evolving flow field. To trace the motion of the particles during the experiment images containing the history of the motion of the particles are very useful. Such images are provided by a module of the software package *DigImage*; an example of such an image is shown in figure 2.6(a). In this way an impression of the development of the flow field was obtained already during the performance of the experiments. All experiments were recorded on video tape for later processing.

The software package *DigImage* was used to track the succeeding positions of the particles from the video images recorded on tape. The path travelled by individual particles is obtained by locating the particles in each video frame and matching corresponding particles in successive frames. The sample frequency of these frames was 25 Hz and each particle was followed over at least 5 successive frames in order to determine its pathlength accurately. From these data the velocity field of the flow at the momentary positions of the particles is calculated. A typical example of a vector plot of this velocity field, measured from a well-developed vortex ring, is shown in figure 2.6(b). For more information on this 'Particle Tracking' technique the reader is referred to Dalziel (1992).

For post-processing purposes, this randomly distributed velocity field is interpolated on a grid of 30×30 points, using a spline interpolation technique which is described in Nguyen Duc & Sommeria (1988). In figure 2.6(c) the interpolated velocity field is shown that corresponds to the measured velocity field in figure 2.6(b). Numerical differentiation of this velocity field yields the component of the vorticity normal to this plane, as shown in figure 2.6(d). It is important to notice that this method only measures the components of the velocity field in the cross-sectional plane that is illuminated by the light sheet. Fortunately, in the experiments the velocity field of the axisymmetric vortex ring is parallel to this plane. The normal vorticity component that is calculated represents thus the vorticity in the core of the vortex ring.

Axisymmetric flows are commonly described relative to a cylindrical coordinate system (r, ϕ, z) with the z -axis directed along the axis of symmetry. To locate these axes in the measured flow field the positions of the core centres in the vorticity contour plot (figure 2.6d) are measured. The ring centre in the middle of both core centres is then the origin of this coordinate system with the z -axis directed perpendicular to the line joining both core centres. The r -axis is then directed from the ring centre through one of both core centres (see figure 2.6d).

For an exactly axisymmetric vortex ring the structure of the flow on both sides of the symmetry axis is the same and it should be sufficient to examine only the flow on one side of this axis. However, the accuracy of the measurements can be checked by comparing the data on both sides. The measured flow region will thus be divided in a left-hand side and a right-hand side and the r -axis is directed through the left or the right core section, respectively.

Relative to both cylindrical coordinate systems the velocity field has components u_z and u_r in axial and radial direction, respectively, and the azimuthal vorticity ω_ϕ is given in terms of these velocity components according to equation (2.3). Note that ω_ϕ has the same sign in both core sections, although their sense of rotation is opposite in a cross-sectional view.

2.4 Results of laboratory experiments

The laboratory experiments that are described in this section have been performed to determine the characteristics of the vortex rings that are generated. To test the reproducibility of the vortex ring generator, the characteristics of four vortex rings, generated by identical fluid injections, are compared. The data are deduced from dye visualization experiments by application of the vortex atmosphere method, as previously described in subsection 2.3.3. The correctness of this method is checked by comparing the obtained ring parameters with corresponding results from a similar particle experiment. In addition, these particle experiments provide a detailed insight in the structure of the flow field of a vortex ring.

2.4.1 DESCRIPTION OF A DYE VISUALIZATION EXPERIMENT

For a proper comprehension of the discussion of the results presented in the next subsections a sequence of images, grabbed from the recorded video tape, is presented first to show the generation and propagation of a vortex ring as observed in the dye visualization experiments. At the sharp edge of the orifice (which is located at the bottom line just outside the images) the injected dyed fluid separates and rolls-up into the vortical core of the vortex ring. During roll-up ambient clear fluid is entrained in the core of the vortex, as indicated by the spiraling structure of sheets of alternating dyed and undyed fluid (see figure 2.7a). As time proceeds the vortex ring develops into a steadily propagating vortex structure (figure 2.7b-d) that moves along a straight path and continues its motion even outside the limited window of figure 2.7(d).

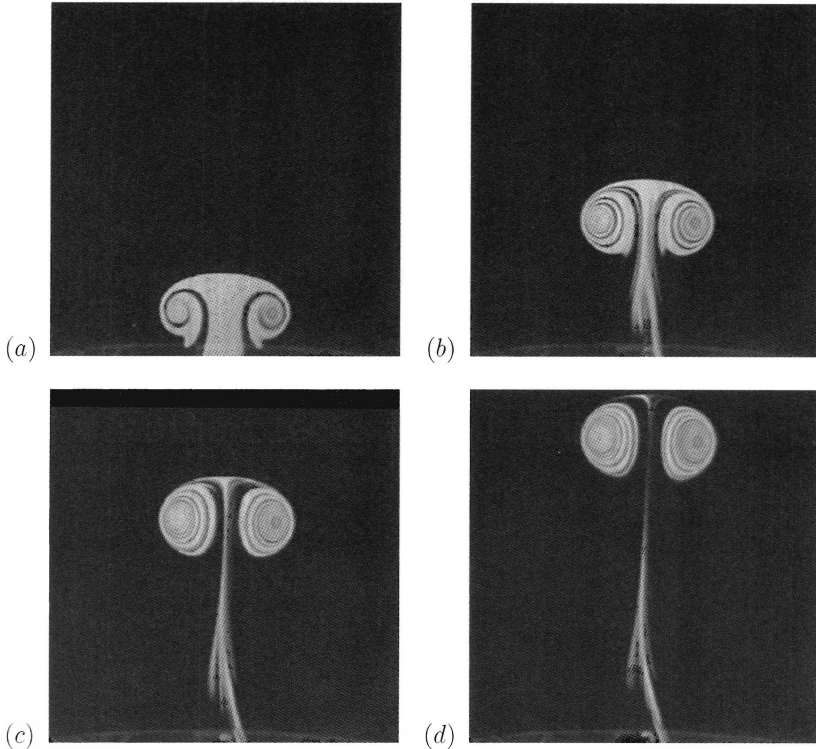


FIGURE 2.7: Cross-sectional view of the evolution of a laminar vortex ring visualized by injecting dyed fluid: (a) $t = 3.3$ s, (b) $t = 6.7$ s, (c) $t = 10$ s and (d) $t = 13.3$ s after start of the fluid injection. Experimental parameters: $D_o = 3.0$ cm, $L_o = 3.0$ cm and $U_o = 4.3$ cm/s.

Not all injected fluid is transported by the vortex ring, a slender tail of dyed fluid is left behind. By entrainment of undyed ambient fluid into the ring centre from the rear of the vortex the dyed region of the vortex ring acquires a torus-like shape. Nevertheless, the region of fluid transported by the vortex ring (i.e. the vortex atmosphere) still has a closed-blob shape (see section 2.2.3), since the flow field along the ring axis is in the same direction as the velocity of propagation of the vortex ring. The stagnation point in front of the vortex ring is clearly observable in figure 2.7(d).

In all experiments reported here the flow of the vortex rings was laminar over the entire trajectory recorded and also remained laminar until the vortex ring reached the free surface of the fluid.

2.4.2 VORTEX RING CHARACTERISTICS FROM DYE VISUALIZATIONS

The four experiments that are described in this subsection were all carried out with the same generation parameters. A series of 6 syringes was used in the traversing system, which were pushed simultaneously over a length of $L_s = 1.0$ cm with an average speed of $\bar{U}_s = 1.0$ cm/s. Dyed fluid was pressed through the orifice of the vortex ring generator with diameter $D_o = 4.0$ cm. According to the slug-model (see equation (2.23) and (2.24)) this means that a comparative

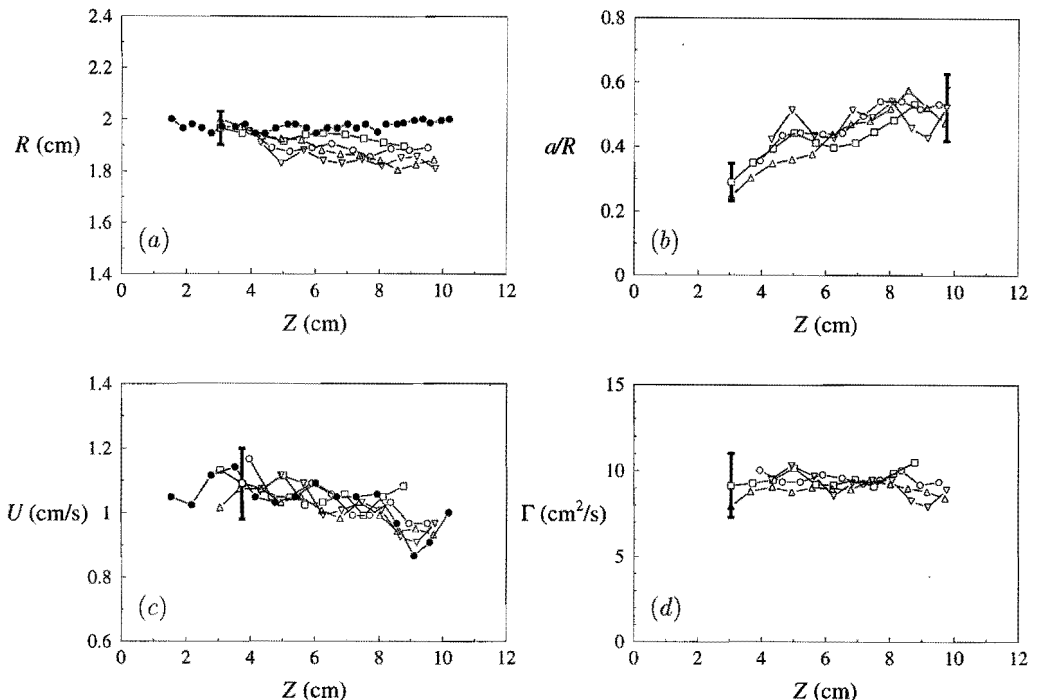


FIGURE 2.8: Evolution of ring characteristics of four vortex rings generated under identical injection conditions: (a) ring radius, (b) relative core radius, (c) velocity of propagation and (d) circulation. For each experiment a different marker has been used (markers at $\Delta t = 0.3$ s). The ring characteristics were obtained by application of the vortex atmosphere method and the inaccuracy in the data that results from this method (see section 2.3.3) is denoted by error bars. In figure (a) and (c) filled circles denote data of an additional experiment, in which the ring radius was directly measured from the distance between the core centres. Experimental parameters: $D_o = 4.0$ cm, $L_o = 2.4$ cm and $U_o = 2.4$ cm/s.

cylindrical column of fluid of length $L_o = 2.4$ cm with mean velocity $U_o = 2.4$ cm/s is injected through the orifice. The Reynolds number of the flow, defined in terms of these injection parameters, is then $Re_o = U_o R_o / \nu = 480$, where $R_o = 2.0$ cm is the radius of the orifice and ν is the kinematic viscosity of the water, being $\nu = 0.01$ cm²/s at room temperature.

In figure 2.8 the obtained ring characteristics are plotted as a function of the axial distance Z travelled by the vortex ring. The data of the four experiments are distinguished by different markers; each marker labels in all plots the same experiment. Data has only been acquired after the vortex ring has been almost completely formed at a distance of about $Z = 3$ cm from the orifice. The mean inaccuracy of the data is denoted in each plot by an error bar and is directly related to the vortex atmosphere method used to deduce the data (for a discussion of the respective accuracies see subsection 2.3.3). The variations of the data of different experiments is very well bounded by these accuracy intervals for all ring parameters. This indicates that the vortex ring generator is able to reproduce, by a fixed fluid injection,

vortex rings whose characteristics are (within the limitations of the data acquisition method) repeatedly the same.

In figure 2.8(a) the evolution of the ring radius shows, on the average, a slight decrease from an initial value of $R = 2.0$ cm to a final value of $R = 1.9$ cm. The relative core radius clearly increases from $a/R = 0.3$ to $a/R = 0.5$ (see figure 2.8b), indicating a widening of the vortex core probably by viscous diffusion of vorticity. The velocity of propagation of the vortex ring decreases slightly from $U = 1.1$ cm/s to just below 1 cm/s, which agrees with the observed growth of the vortex core (according to Kelvin's formula (2.10)). The circulation that is calculated from all these data is approximately constant ($\Gamma \approx 9$ cm²/s, see figure 2.8d).

In figure 2.8a and 2.8c data from an additional experiment have been added, denoted by filled circles. Only this experiment was suitable to measure the ring radius directly from the distance between the core centres. In spite of the other four experiments the ring radius now is approximately constant over the entire axial range examined, even tending to increase from $Z = 8$ cm. The initial values of the ring radius, obtained with the vortex atmosphere method, do agree with these directly measured values, implying that the vortex atmosphere method provides plausible results. The apparent decrease of the ring radius in some of the previous experiments results, however, from a misinterpretation of the measured lateral size of the vortex ring. This size underestimates the true lateral size, because in these experiments the vortex ring moved slowly out of the illuminating light sheet. There is one experiment (denoted with open squares in figure 2.8a), where this trouble does not occur and the ring radius agrees very well with the directly measured ones.

2.4.3 VORTEX RING CHARACTERISTICS FROM PARTICLE EXPERIMENTS

In this subsection we discuss the results of a particle experiment in which a vortex ring was created with the same generation parameters as in the previous dye-visualization experiments. The vortex ring thus has the same ring characteristics and the results of both kind of experiments are complementary. In this particle experiment the velocity field of the vortex ring is measured from which the vorticity distribution in the core is deduced. The velocity and vorticity fields taken from this experiment are presented in figure 2.6, and they show globally the flow field of a well-established vortex ring; the data were taken approximately 6 seconds after fluid injection was started and the vortex ring had travelled a distance of $Z = 6$ cm from the generator orifice.

The structure of the flow and the vortex core is resolved in detail in plots of the velocity and vorticity components along specific axes through the vortex core. These profiles are used to determine the characteristic vortex ring parameters, which are subsequently compared with their corresponding values obtained with the vortex atmosphere method. Since this latter method is based on ideal flow assumptions, its applicability and the reliability of its results can then be verified.

Another important characterization of steadily propagating vortex rings is the relation between the vorticity in the core and the Stokes stream function relative to a frame moving with the ring (see equation (2.5)). This relation will be derived from the measured velocity field. Unfortunately, neither theoretical predictions nor accurate results of previous measurements of this relation for realistic vortex rings are available from the literature; in theoretical inviscid models simple relations are often assumed. Only a comparison with numerical simulations of viscous vortex rings is possible.

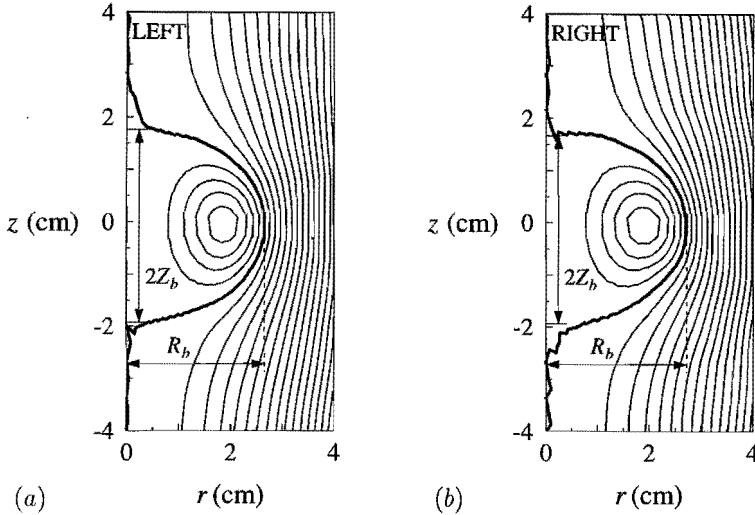


FIGURE 2.9: Streamline pattern in the cross-section of the vortex ring on the left (a) and the right (b) side of the axis of symmetry, respectively. The thick line denotes the separatrix ($\Psi = 0$) that demarcates the fluid region transported with the vortex ring. Experimental parameters: see caption figure 2.8.

Stream function of vortex ring

The Stokes stream function ψ of the vortex ring has been computed by numerical integration of the interpolated velocity field (figure 2.6c) using the condition that $\psi = 0$ at the axis of symmetry. To render the flow relative to the vortex ring moving with instantaneous velocity U , this stream function has to be reduced by a term $\frac{1}{2}UR^2$. The contour lines of the resulting stream function Ψ are shown in figure 2.9 for the flow on both sides of the ring in the cross-sectional view.

The streamline pattern is almost the same on both ring sides and is obviously similar to the pattern shown in figure 2.1(b) for the flow of a vortex ring with a core of uniform vorticity and considerable size. The flow is separated in two regions by the streamline $\Psi = 0$ which is called the separatrix (denoted by a thick line in figure 2.9). Unfortunately, due to small inaccuracies in the calculation of the stream function the contour line $\Psi = 0$ does not properly join the axis of symmetry. In the region enclosed by this separatrix streamlines are closed curves which are approximately circular at the centre of the vortex core. Fluid captured in this region is transported by the vortex ring and constitutes the atmosphere of the vortex ring. The radial and axial extension of the separatrix are deduced from figure 2.9, giving $R_b = 2.7$ cm and $2Z_b = 3.6$ cm. These values agree reasonably well with the dimensions of the dyed fluid region (previously inferred from dye-visualization experiments), which at this moment in the ring evolution has dimensions $R_b = 2.8$ cm and $2Z_b = 3.3$ cm, respectively; the difference in axial length results from the inaccuracy to localize the rear stagnation point in the dyed fluid images. Outside this transported fluid region in which approximately all vorticity of the vortex ring is concentrated the flow is similar to the irrotational flow around a steadily moving oblate spheroid in an inviscid fluid; the fluid in this region is just deflected

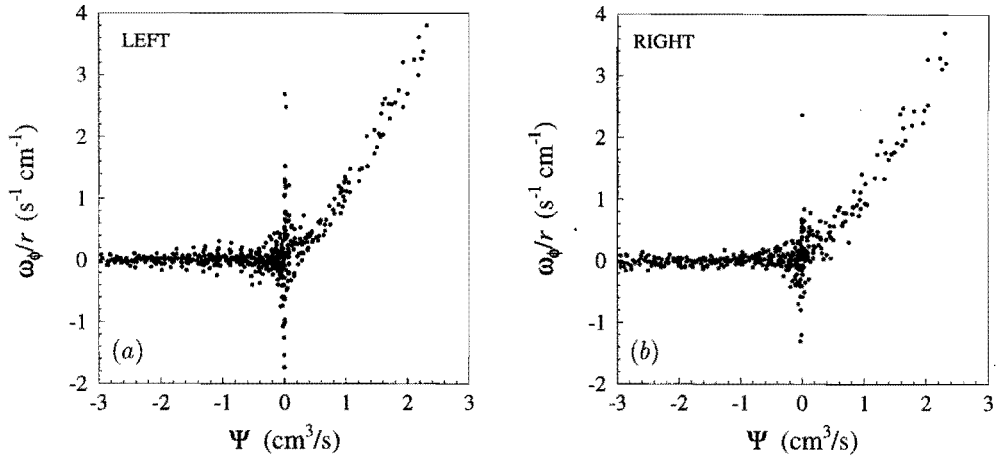


FIGURE 2.10: Scatter plots of ω_ϕ versus Ψ . Data are gathered from all grid points on the left-hand (a) and the right-hand (b) side of vortex ring cross-section, respectively. Experimental parameters: see caption figure 2.8.

by the passing vortex ring.

Both the vorticity and the stream function of the flow have been calculated on a 30×30 grid from the interpolated velocity field. By calculating the quantity ω_ϕ/r at each grid point and plot this value as a function of the local value of Ψ for all grid points, a scatter plot is obtained (see figure 2.10) from which the functional relation $\omega_\phi/r = f(\Psi)$, typical for steady inviscid axisymmetric flows, might be inferred. Both scatter plots show a similar pattern consisting of several branches that correspond to distinct flow regions. The horizontal branch ($\omega_\phi \approx 0$) corresponds to the irrotational flow outside the vortex ring. The vertical branch ($\Psi \approx 0$) with considerable positive and negative values for ω_ϕ/r results from grid points near the axial centreline of the ring, where for small r errors in ω_ϕ are intensified in values for ω_ϕ/r . Some of the data with small positive ω_ϕ/r correspond to grid points at the edge of the vortical core near the separatrix. The curved branch with $\Psi > 0$ consists of data points located in the vortical region of the vortex ring, the maximum vorticity values are located in the core centre. Only for steady inviscid flow these data are expected to coincide exactly to a single curve. As inferred from previous dye-visualization images, the flow of the well-developed vortex ring is approximately steady and viscous effects act only over large time scales. Therefore, an appropriate functional relation between ω_ϕ/r and Ψ is expected to exist. Despite the scatter in the data that results mainly from measurement inaccuracies all data coalesce in a narrow band, which suggests a functional dependence that is close to (but not exactly) linear.

A similar relationship has been found from numerical simulations of vortex rings (Shariff *et al.* 1994). By computing the vorticity and stream function on a sufficiently fine grid the scatter in the data is reduced and a clearly marked curve results, consisting principally of two branches. There is a horizontal branch with $\omega_\phi = 0$, which corresponds to the irrotational flow outside the vortex ring, while the vortical flow in the vortex ring is characterized by a nonlinear increase of ω_ϕ/r versus Ψ . Towards the core centre this curve seems to have a constant slope, approximately. It has to be remarked that this steady vortex structure results from an evolution of an initially unsteady vortex ring with a Gaussian vorticity profile in the

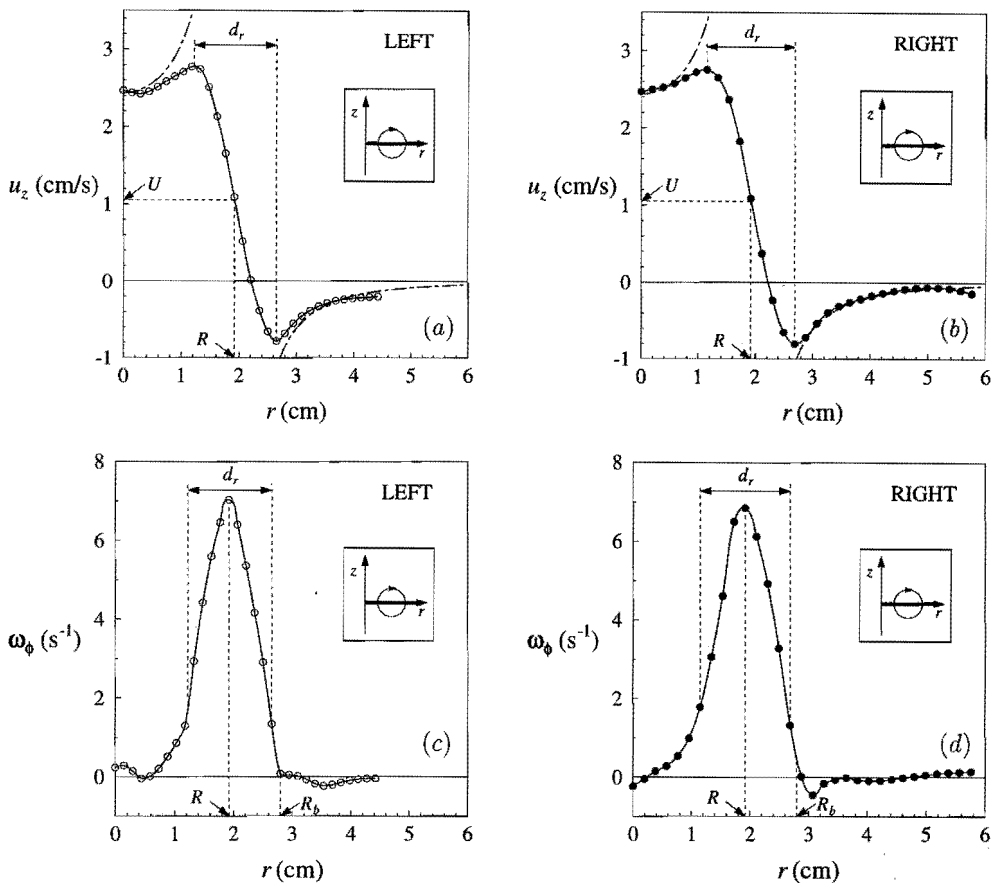


FIGURE 2.11: Profiles of the axial velocity u_z along the radial axes ($z = 0$, see inset drawings) through the left core section (a) and the right core section (b). The dashed-dotted line denotes the potential flow of a comparable circular line-vortex. Corresponding profiles of the vorticity ω_ϕ are plotted in (c) and (d), respectively. Experimental parameters: see caption figure 2.8.

core. How the relation $\omega_\phi/r = f(\Psi)$ for steady vortex rings is affected by the initial vortex generation conditions is still unknown.

Profiles along line through ring centre and vortex core

Profiles of the flow field along the r -axis ($z = 0$) ranging from the ring centre through the centre of the vortex core will now be examined. Along this axis the velocity field of the vortex ring is in axial direction (see figure 2.6c). In figure 2.11 profiles of u_z and ω_ϕ along this axis are plotted for both the left and right core sections, respectively.

Starting from the ring centre (at $r = 0$) the axial velocity initially increases up to a maximum value near the edge of the vortical core (see figure 2.11a,b). Inside the core the velocity drops and reaches a minimum negative value near the outer core edge. Outside the core the axial velocity increases again and vanishes at large distance from the vortex. The correspond-

ing vorticity profiles show a peak in the vorticity at the core centre (at $r = R$) around which most of the vorticity is concentrated. Near the ring centre the vorticity decreases more gradually and vanishes at $r = 0$. Towards the outer edge of the core the vorticity drops rapidly and vanishes outside the vortex; the boundary of the fluid volume of the vortex ring is denoted in the plots by R_b , determined from the dye-visualization experiments. The asymmetry in the vorticity distribution is related to two effects. According to equation (2.5), in a steadily propagating inviscid vortex ring the vorticity of each fluid element varies proportional to r as it moves around the core along a fixed streamline. In addition, successive streamlines are closer for $r > R$ than for $r < R$ (see e.g. figure 2.1*d*).

A measure of the diameter of the core is difficult to infer unambiguously from the vorticity profiles, because vorticity is spread over the complete fluid region of the vortex ring. However, the axial velocity profile displays two clear extrema and the distance d_r between them can be used to indicate the characteristic diameter of the vortical core*. The axial velocity at the core centre equals the propagation velocity U of the vortex ring.

An impression of the inaccuracy in the obtained data can be deduced from a comparison of the profiles through the left and right core sections. Both the axial velocity profile and the vorticity profile are very similar in either core section, although near the ring centre and outside the vortex small deviations are observed. In the vortex core the profiles are very similar; but just in this region the data have to be taken with great care, since the measurements of the velocity field do not resolve this flow region properly (see figure 2.6*b*). The smooth profiles in the core centres are merely a consequence of the interpolation of the measured data. Nevertheless, similar velocity and vorticity profiles have been measured previously in experiments performed by Didden (1977), using a different technique (Laser-Doppler Velocimetry) to measure the velocity field of laminar vortex rings.

From the profiles in figure 2.11 several of the characteristic parameters of the vortex ring are deduced. The radial position of the vorticity maximum is on both ring sides the same and yields for the ring radius $R = 1.95$ cm. The corresponding axial velocity gives the vortex ring propagation speed $U = 1.05$ cm/s; again the same value is obtained on both ring sides. For the core diameter d_r values of 1.4 cm and 1.5 cm are found for the left and right core section, respectively, yielding for the ratio of core radius $a_r = \frac{1}{2}d_r$ to ring radius $a_r/R = 0.37$. All these values agree quite well with the data obtained with the vortex atmosphere method from the dye-visualization experiments (compare with data at $Z = 6$ cm in figure 2.8).

In the vortex atmosphere method it was assumed that all vorticity of the vortex ring is concentrated in a thin circular core with uniform distribution and vanishes outside this core. From the measured vorticity profile in figure 2.11(*c, d*) it is obvious that this assumption is not satisfied in the experiments with real viscous vortex rings and that vorticity is spread over the entire moving fluid volume. Another assumption used in the vortex atmosphere method was that the velocity field outside the thin core can be approximated by the potential flow of a circular line-vortex of zero core size.

For such a circular line-vortex an analytical expression for the axial velocity component along the radial axis through the vortex core can be derived from its stream function given in equation (2.18). To plot this velocity profile both the ring radius and circulation have to be specified. For comparison with the experiments a ring radius $R = 1.95$ cm is taken. The

*This definition has also been used by Sullivan *et al.* (1973) and Maxworthy (1977); another definition for the core diameter as the distance over which the axial velocity profile in the core is approximately linear, has been used by Didden (1977).

appropriate circulation follows by matching the axial velocity at the ring centre, given by $u_z^0(0) = \Gamma/2R$ (see equation (2.21), with the measured axial velocity $u_z \approx 2.43$ cm/s, yielding $\Gamma = 9.5$ cm²/s. In figure 2.11 the axial velocity profile of the circular line-vortex is denoted with a dashed-dotted line. Near the ring centre and outside the vortex it asymptotes the measured profile, but in the vortical core the velocity fields are quite different: the infinite velocity at a core of zero size is replaced by a continuously decreasing profile in a core of finite size. At the boundary $r = R_b$ (denoted in figure 2.11*c, d*) of the fluid volume transported with the vortex ring the potential flow of the circular line-vortex approximates the measured velocity very well. Other sections of this boundary are located further from the vortex core and the potential flow approximation is even better. Therefore, the assumption in the vortex atmosphere method that the flow at this boundary can be represented by a potential flow is acceptable.

Profiles along line through core centre parallel to axis of symmetry

In this subsection profiles along a line through the core centre at $r = R$ directed parallel to the z -axis are discussed. The velocity field along this line is mainly in radial direction, at least near the vortex core where the flow is approximately circular (see figure 2.6*c*). In figure 2.12 the profiles of u_r and ω_ϕ through the left and right core sections are plotted. The velocity profiles show a symmetric distribution with an approximately linear increase of the velocity in the core and extremal values near the core edges. The vorticity is again concentrated in a narrow peak. On both ring sides the profiles are very similar, minor differences indicate the measurement inaccuracies.

For comparison, the radial velocity of the potential flow of a circular line-vortex is added in these profiles as denoted by the dashed-dotted lines. This velocity field is calculated using the same ring parameters R and Γ as in the profiles in figure 2.11(*a, b*). Outside the core region the potential flow approaches the measured velocity field very well. Deviations appear just near the velocity extrema in the measured profiles, from where the distributed vorticity in the core accounts for a continuous variation of the velocity in the core.

In previous studies (Sallet & Widmayer 1974; Didden 1977) the radial velocity profiles have been used to define the core diameter in terms of the distance between the velocity extrema, as indicated in figure 2.12(*a, b*). For both core sections a core diameter $d_z = 1.33$ cm is found, which is slightly smaller than the core size $d_r \approx 1.5$ cm derived from the axial velocity profiles. Didden (1977) prefers the definition d_z for the core diameter, because the corresponding velocity extrema are sharper and the diameter is determined more accurately. Another preference for this definition is that d_z is measured at fixed radial distance r from the axis of symmetry and both the velocity and vorticity distributions are symmetric. In radial direction, the asymmetric vorticity and velocity distributions are not suitable for a proper definition of the core size: the vorticity is different at the opposite core edges, because at the core boundary which coincides with a streamline ω_ϕ/r is fixed.

In comparing various measures of the typical core size of a non-uniform vorticity distribution, the effective core radius a_e has been defined to denote the core radius of an equivalent vortex ring with uniform vorticity distribution in the core and the same propagation velocity. Substituting $R = 1.95$ cm, $\Gamma = 9.5$ cm²/s and $U = 1.05$ cm/s in the second equation of (2.14) an effective core radius $a_e = 0.81$ cm is calculated. As deduced from figures 2.12(*c, d*) the vorticity is still about 30% of its maximum where the distribution has width $2a_e = 1.62$ cm. On the other hand, about all vorticity is contained in a region of size $2a = 3.0$ cm and $2a = 3.3$ cm

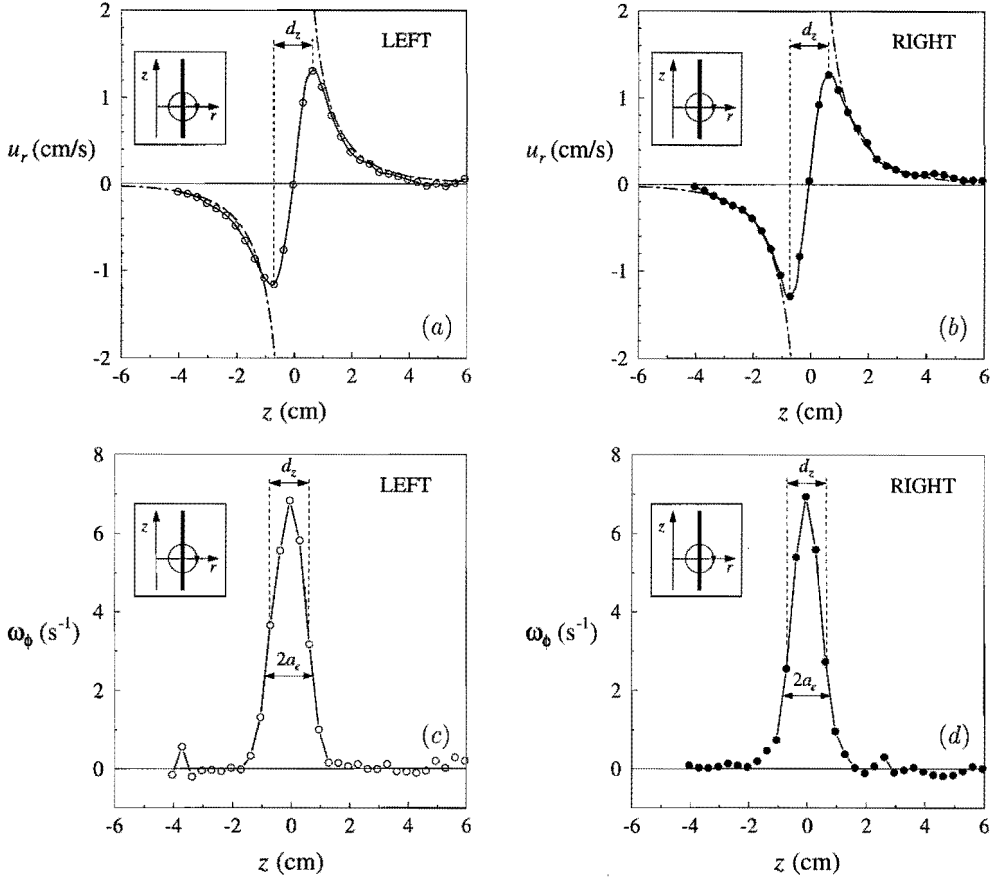


FIGURE 2.12: Profiles of the radial velocity u_r along a line parallel to the z -axis at $r = R$ (see inset drawings) through the centre of the left core section (a) and the centre of the right core section (b), respectively. The dashed-dotted line denotes the potential flow of a comparable circular line-vortex. Corresponding profiles of the vorticity ω_ϕ are plotted in (c) and (d), respectively. Experimental parameters: see caption figure 2.8.

for the left and right core section, respectively. Substituting these results in the first equation of (2.14) yields $\mathcal{J} = 0.87$ and $\mathcal{J} = 0.96$, respectively, which is almost four times the value for a uniform core.

The velocity extrema in figure 2.12(a, b) have the value $|u_r| = 1.3$ cm/s. From this maximum velocity the circulation Γ_c contained within the central core part with diameter d_z is calculated, using the approximation $\Gamma_c \approx \pi d_z |u_r|$ which assumes circular flow inside the core. The value $\Gamma_c = 5.4$ cm²/s is about 60% of the total circulation Γ of the vortex ring, a similar value for this ratio of circulations has been found by Maxworthy (1977). This implies that, although the major part of the vorticity is concentrated in an approximately circular core with core diameter d_z , the vorticity present in the rest of the fluid volume of the vortex ring contributes significantly to the total circulation and hence the propagation speed of the vortex ring.

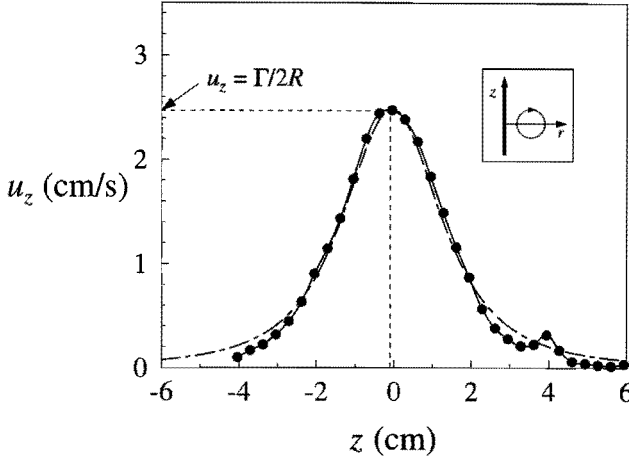


FIGURE 2.13: Profile of the axial velocity u_z along the axis of symmetry ($r = 0$, see inset drawing). The dashed-dotted line denotes the potential flow of a comparable circular line-vortex. Experimental parameters: see caption figure 2.8.

Profile along axis of symmetry

Along the axis of symmetry of the vortex ring ($r = 0$) the flow is in axial direction and the integral of u_z along this axis gives the circulation of the vortex ring (see equation (2.7)). The measured profile of u_z along z is shown in figure 2.13. The velocity has a maximum at the ring centre ($z = 0$) of $u_z = 2.47$ cm/s, which is approximately equal to the mean injection velocity $U_o = 2.4$ cm/s in the generator orifice. The velocity decreases in both directions along the z -axis symmetrically; the small hump at $z = 4$ cm just results from a mistaken particle trace.

The velocity field is measured over a limited axial range ($z_1 \leq z \leq z_2$, with $z_1 = -4.0$ cm and $z_2 = 5.9$ cm). To calculate from these data the circulation of the vortex ring an extrapolation of the measured profile is necessary. For vortex rings in ideal fluid the velocity varies as $u_z \sim 1/z^3$ for $z^2 \gg R^2$. With this approximation the velocity profiles can be extrapolated and the circulation is given by:

$$\Gamma = \int_{z_1}^{z_2} u_z dz + \frac{1}{2} [u(z_2)z_2 - u(z_1)z_1], \quad (2.25)$$

where the integral is computed numerically from the data. The integral yields a value of 8.8 cm²/s, the extrapolations contribute 0.3 cm²/s and thus the total circulation is $\Gamma = 9.1$ cm²/s.

In figure 2.13 the dashed-dotted line denotes a fit of the measured data, which is based on equation (2.21) that gives the equivalent flow of a circular line-vortex. For this fit the parameters $R = 1.95$ cm and $\Gamma = 9.7$ cm²/s has been used (the maximum in the fit has been shifted slightly towards $z = -0.05$ cm). The maximum velocity of the fit is given by $u_z = \Gamma/2R = 2.49$ cm/s, which agrees with the measured maximum. As shown in figure 2.13 the potential flow fit represents the measured data very well; only far from the ring the measured velocity decays faster. As a consequence, the circulation related to this fit is an overestimation for the vortex ring circulation.

Evolution of ring parameters from particle experiments

All of the above presented profiles were taken at a fixed time when the vortex ring has been well-developed. To gain insight in the evolution of the flow and the resolution of the measurements of the velocity field, profiles at successive time steps have been examined. To characterize the flow evolution the variation in time of the ring parameters, which are deduced from these profiles, is determined. It was seen in the previous paragraphs that some of the parameters could be obtained in several ways, but it turns out that not all of these methods are suitable for general application, since the flow field near the vortical core is not always properly resolved (grid spacing $\Delta z = 0.3$ cm, $\Delta r = 0.15$ cm). The methods that have been used to deduce the ring parameters at each moment can be described as follows. The ring radius R is given by the mean radial distance of the respective vorticity peaks on either ring side from the ring axis (cf. the profiles in figure 2.11*c, d*). The propagation velocity U follows from the axial distance travelled by the ring centre in time. The ring centre is located where the axial velocity along the ring axis has its maximum value (cf. the profile in figure 2.13). The circulation Γ of the vortex ring is computed numerically from all the axial velocity data along this axis (equation (2.25), including the contribution from the extrapolation of the data to infinity. For comparison, the total circulation contained in the measured flow regions on either ring side has been computed. Using definition (2.6), this circulation Γ_A is obtained either from numerical integration of the velocity field along the boundary of the considered flow region A or from numerical integration of the vorticity field over the surface of A . The mean value from both ring sides have been used. The size of the vortex core is characterized by the radius $a_z = \frac{1}{2}d_z$ deduced from the distance between the peaks in the radial velocity profiles (cf. profiles in figure 2.12), or by the effective core radius a_e . The latter is calculated from the previously determined values for R , U and Γ . Also for the core radii the mean values from both ring sides have been used.

In figure 2.14 the obtained values for the ring parameters are plotted as a function of the distance z travelled by the ring centre from the generator orifice. For comparison with results from previous dye visualization experiments the same ranges have been used in these plots as in figure 2.8. Error bars denote the measurement inaccuracies. The variations of R are confined to the limits of the measurement accuracy and for the whole trajectory a mean value $\bar{R} = 1.95$ cm can be assigned to the radius of the vortex ring. Similarly, the apparent decrease in U has to be interpreted carefully, because of the considerable inaccuracies in the data. The mean velocity of propagation equals $\bar{U} = 1.04$ cm/s. The mean values for both ring parameters agree very well with the results from the dye visualization experiments (figure 2.8*a, b*), although in a number of these latter experiments the radius and velocity seemed to decrease. However, the variations in the ring radius and propagation velocity are too small to infer a definite increase or decrease from both kinds of experiments.

Also the relative core radius a_z/R displays some variations around a mean value of 0.4. The relative effective core radius a_e/R increases gradually between the values 0.3 and 0.4. Note that due to the logarithmic dependence on the relative core radius in Kelvin's formula (2.10), small deviations in the obtained values for U , R and Γ cause large deviations in the calculated values for a_e/R . In a way the ratio a_e/R can be compared with the relative core radius a/R determined with the vortex atmosphere method from the dye visualization experiments, since both ratios are related to Kelvin's formula for the vortex ring propagation velocity. Both ratios display an increase, starting from the same initial value of 0.3, but eventually a/R exceeds a_e/R (cf. figure 2.8*b*). Nevertheless, it seems that the vorticity is being spread over an

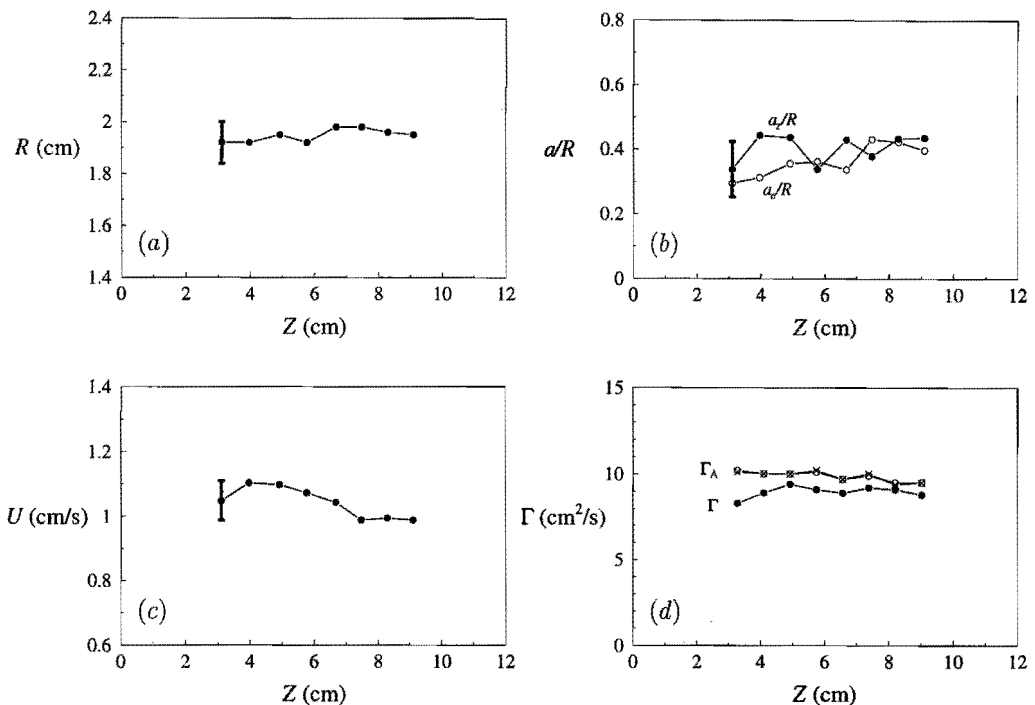


FIGURE 2.14: Evolution of vortex ring parameters from a particle experiment (a) ring radius, (b) relative core radii a_z/R (filled circles) and a_e/R (open circles), (c) velocity of propagation and (d) ring circulation Γ (computed along axis of symmetry) and total circulation Γ_A of the flow (computed from surface integral, crosses, and from line integral, open circles) (markers at $\Delta t = 0.82$ s). Experimental parameters: see caption figure 2.8.

extending region by diffusion; on the other hand, the central core part (radius a_z), which is approximately in solid-body rotation, does not exhibit a definite growth.

The circulation Γ (mean value $\bar{\Gamma} = 9.0 \text{ cm}^2/\text{s}$) of the vortex ring is systematically lower than the total circulation Γ_A (mean value $\bar{\Gamma}_A = 9.9 \text{ cm}^2/\text{s}$) on either ring side. On the other hand, computing the total circulation either from the surface integral of the vorticity field or from the line integral of the velocity around the boundary of the measured flow domain yield approximately the same values. Apparently, there is some small residual flow outside the vortex ring, which contributes to the total circulation. Despite the differences between $\bar{\Gamma}$ and $\bar{\Gamma}_A$, both mean values agree very well with the scattered data for the ring circulation obtained in the dye visualization experiments (figure 2.8d).

2.5 Conclusions

The experimental set-up has been tested and it was found that the vortex ring generator is able to produce repeatedly vortex rings with identical ring characteristics. This is convenient, because it allows comparison of results of distinct experiments, since two different kinds of

injection parameters:	ring parameters:
$R_o = 2.0$ cm	$\bar{R} = 1.95$ cm
$U_o = 2.4$ cm/s	$\bar{U} = 1.04$ cm/s
$L_o = 2.4$ cm	$\bar{a}_z = 0.8$ cm
$Re_o = 480$	$\bar{\Gamma} = 9.0$ cm ² /s

TABLE 2.1: Injection parameters at the generator orifice and related time-averaged values for the ring parameters of the well-developed vortex ring.

flow visualizations were used. In the dye visualization experiments the flow region that is transported by the vortex ring is clearly marked by dye, indicating a laminar flow structure. From the dimensions of this vortex atmosphere the ring radius and core radius are derived, according to the introduced vortex atmosphere method. By substitution of these parameters and the measured ring speed in Kelvin's formula (2.10) for the propagation velocity, the circulation of the vortex ring can be computed. Although this vortex atmosphere method and Kelvin's formula are based on inviscid flow assumptions, the obtained ring parameters agree very well with corresponding values derived from particle experiments.

In these particle experiments the velocity field of the flow has been measured from the motion of passively advected particles. Interpolation to a regular grid and subsequent numerical differentiation of the velocity field yields the vorticity distribution in the vortex core. The flow structure is best examined by plotting profiles of the vorticity and velocity components along specific lines through the vortex ring. From these profiles the various ring parameters have been deduced. Unfortunately, the measured resolution of the flow is not very high inside the core, where the velocity is large and the particle paths cannot be tracked properly. Nevertheless, appropriate values have been obtained for the various ring parameters. Some of the ring parameters could be determined in different ways and all methods yielded similar results.

The experiments reported here were performed with fixed generation conditions on an orifice with diameter $D_o = 4.0$ cm. The appropriate generation parameters, which produce a steadily propagating laminar vortex ring, have been determined empirically. Similar experiments have been performed with smaller orifices, yielding proportionately comparable results. Anticipating to the experiments described in the next chapters, where vortex rings are created in a rotating fluid and small-scale structures are induced, most of the experiments have been performed with the 4.0 cm orifice producing relatively large vortex rings. The steadiness of the evolving vortex rings was inferred from observations of the dyed flow pattern and from measurements of the characteristic ring parameters. It was found that, within the accuracy of the measurement techniques, these parameters have approximately fixed values over the complete trajectory of the vortex ring that is examined. These values are conveniently arranged in table 2.1 and the related injection parameters at the generator orifice are included.

3

VORTEX RING MOVING ALONG THE AXIS OF A ROTATING FLUID

3.1 Introduction

A wide variety of flows of technical or geophysical interest involves the presence of swirl or rotation. Swirling flows in combustion chambers, turbines and cyclone separators are only a few examples among many. Also large-scale geophysical flows on the rotating Earth's surface are, to a larger or smaller extent, affected by the background rotation.

Flow systems subjected to a background rotation are commonly studied relative to a frame of reference rotating with the main fluid flow. The vorticity of the flow relative to the rotating system is then affected by the uniform vorticity imposed by the background rotation. In fact, the background vorticity serves as a permanent source that induces relative vorticity in the fluid flow. As a result, flows with a background rotation are hardly ever free of relative vorticity and the development of the flow is governed by vorticity dynamics.

The mechanisms of relative vorticity induction in rotating flow systems are best studied by considering a relatively simple and well-known initial flow structure. A number of studies about the effect of a background rotation on coherent structures, which are oriented so that the system vorticity is either parallel or antiparallel to the mean relative vorticity, are available in literature (e.g. Tritton 1992; Métais *et al.* 1995). In contrast, much less analysis has been performed when the system vorticity is *orthogonal* to the mean vorticity. The flow of a vortex ring oriented parallel to the axis of a uniformly rotating fluid belongs to this latter configuration and is considered in this chapter.

Very few works are available on vortex rings with swirl. The studies by Moffatt (1988) and Turkington (1989) were focused on finding steady solutions of the Euler equations, without investigating whether or not vortex rings with swirl were stable. Virk *et al.* (1994) focused more on the dynamics of vortex rings with helical vortex lines, showing that the presence of an azimuthal flow, regardless of how it is created, slows down the propagation of the vortex ring. They provided evidence that a secondary vortex structure, oppositely-signed with respect to the primary vortex, is created ahead of the ring. In that paper, however, the vortex ring was initially assigned with a prescribed azimuthal vorticity profile and circular cross-section; the azimuthal flow was then imposed by specifying the 'degree of polarization'. Although very interesting, this initial condition is very difficult, if not impossible, to be created in a laboratory experiment. On the other hand, the vortex ring in a rotating fluid is relatively simple to produce experimentally and probably closer to practical applications.

The aim of the present work is to investigate, by laboratory experiments and direct numerical simulations, how the presence of a background rotation affects the formation and the evolution of vortex rings generated by pushing a finite amount of fluid through a sharp-edged circular orifice. In this case the generated vorticity field results from the interaction between the roll-up of the thin vorticity layer released at the orifice-edge and the uniform background rotation. The result is that the vortex rings have swirl self-generated by the flow dynamics. Results have shown that the ring behaviour with respect to the rotation can be essentially divided into two regimes: 'low' and 'high' rotation. In the former case the vortex ring forms in the same way as it forms without background rotation and the induced relative motion causes minor changes in the ring dynamics. As the rotation rate increases the changes become more pronounced until the effects of the rotation dominate the flow. It will be shown that in the 'high' rotation regime the vortex ring hardly forms and the energy of the flow is radiated away through inertial waves. An explanation for this behaviour is given.

Finally, in laboratory experiments the flow was sometimes observed to depart from axisymmetry. Three-dimensional numerical simulations have shown that this was due to a possible small initial misalignment between the axis of rotation and the direction of translation of the vortex ring.

3.2 Experimental set-up

For a detailed description of the experimental set-up and the production of vortex rings the reader is referred to the previous chapter (see section 2.3). Merely the main features of the experimental arrangement and the adjustments to perform experiments in a rotating fluid are summarized here.

The schematic drawing of the experimental set-up is shown in figure 3.1. Vortex rings were created by injecting during a short period of time a finite amount of fluid through a sharp-edged orifice on top of a cylindrical reservoir, henceforth called the vortex ring generator. This vortex ring generator was placed at the centre of an experimental tank with the orifice centreline directed vertically upwards. The tank was filled with water to a height of about 50 cm. The set-up was put on a rotating table and was aligned so that the orifice centreline coincided with the rotation axis of the system. The angular velocity of the table could be adjusted between $\Omega = 0.06 \text{ s}^{-1}$ and $\Omega = 1.0 \text{ s}^{-1}$. Before the experiments were started the water in the tank had to spin-up for about one hour until a state of uniform rotation was established.

In the experiments vortex rings propagated vertically upwards, parallel to the axis of the rotating system. The vortex rings were illuminated by a thin light sheet produced by slide projectors fixed on top of the rotating set-up. The light sheet was directed vertically downwards through the centre of the generator orifice. In this way a cross-sectional view is obtained of the propagating vortex rings. The flow was recorded by a video camera mounted on one side of the rotating table. A frame grabber was used to grab from the video tape snapshots of the evolving flow at fixed time steps.

Two kinds of flow visualization experiments were carried out. Visualizations consisting of injection with dyed fluid were useful to observe the main features of the flow and to discern subsequent stages in the flow evolution. More quantitative information about the velocity and vorticity field was obtained by using small tracer particles which are passively advected by the flow. For more information about the techniques to deduce from these particle paths the

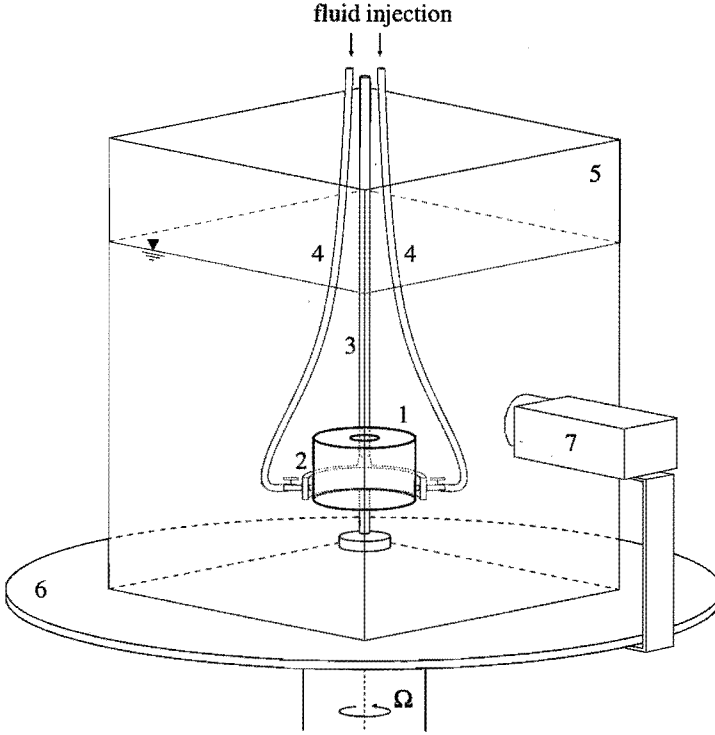


FIGURE 3.1: Perspective view of the experimental set-up. The vortex ring generator consists of a cylindrical perspex box 1 with a circular orifice on top; it was held up in a fork 2 fixed to a vertical stand 3. Fluid injection was provided by plastic tubes 4. The set-up was placed in an experimental tank 5 put on a rotating table 6. The experiments were recorded from a side view by a video camera 7.

velocity and vorticity fields of the flow the reader is again referred to section 2.3.

3.3 Numerical set-up

3.3.1 EQUATIONS OF MOTION AND NUMERICAL SCHEME

The time-dependent Navier-Stokes equations, written in terms of velocity and pressure, for an incompressible viscous fluid have been integrated numerically. The fluid in which the flow evolves is subjected to a uniform background rotation with rotation vector $\boldsymbol{\Omega} = \Omega \mathbf{k}$, \mathbf{k} being the unit axial vector and Ω the rotation rate. The relative flow in the rotating system satisfies the Navier-Stokes and continuity equations:

$$\begin{aligned} \frac{D\mathbf{u}}{Dt} \equiv \frac{\partial \mathbf{u}}{\partial t} + (\mathbf{u} \cdot \nabla) \mathbf{u} &= -\nabla p - \frac{1}{Ro} \mathbf{k} \times \mathbf{u} + \frac{1}{Re} \nabla^2 \mathbf{u}, \\ \nabla \cdot \mathbf{u} &= 0, \end{aligned} \quad (3.1)$$

with $D/Dt \equiv \partial/\partial t + \mathbf{u} \cdot \nabla$ the material derivative operator. The pressure p is the reduced pressure, which includes the potential of the centrifugal force. The equations have been written in dimensionless terms by choosing suitable velocity U and length \mathcal{L} scales, to be specified later. The Reynolds and Rossby numbers are then defined as $Re = U\mathcal{L}/\nu$ and $Ro = U/2\Omega\mathcal{L}$, respectively, where ν is the kinematic viscosity of the fluid.

In order to obtain a closer comparison between dye-visualization experiments and numerical simulations, the motion of a passive scalar has been simulated. The evolution of the concentration C of such a tracer is given by the equation:

$$\frac{DC}{Dt} = \frac{1}{ReSc} \nabla^2 C, \quad (3.2)$$

where Sc is the Schmidt number, defined as the ratio between the kinematic viscosity ν and the scalar diffusivity κ .

The equations have been written in a cylindrical coordinate system, with the axial direction aligned with \mathbf{k} , and discretized by second-order finite-difference schemes on a staggered grid. Details of the numerical method can be found in Verzicco & Orlandi (1995; 1996a) and only the main features are summarized here. In the three-dimensional case, in the limit of $\nu \rightarrow 0$, the energy is conserved and this holds in the discretized equations. The system of equations is solved by a fractional-step method with the viscous terms computed implicitly and the convective terms explicitly; the large sparse matrix resulting from the implicit terms is inverted by an approximate factorization technique. At each time step the momentum equations are provisionally advanced using the pressure at the previous time step, giving an intermediate non-solenoidal velocity field. A scalar quantity Φ is then introduced to project the non-solenoidal field onto a solenoidal one. The large band matrix associated with the elliptic equation for Φ is reduced to a tridiagonal matrix using trigonometric expansions in the axial direction. The pressure is related to the scalar Φ . The third-order Runge-Kutta scheme, described by Verzicco & Orlandi (1996a), is used to advance the equations in time.

Finally, in cylindrical coordinates (r, ϕ, z) the equations are singular at $r = 0$. The advantage of using staggered quantities is that only the radial component of the momentum equation needs to be evolved at the centreline ($r = 0$), and for this component the evolution of the quantity $q_r = ru_r$ is calculated instead of u_r , since the former quantity clearly vanishes on the centreline.

3.3.2 RUN PARAMETERS AND CONVERGENCE CHECKS

There are many quantities that are usually chosen to render the evolution equations nondimensional. For vortex rings it is common to take the toroidal radius and the self-induced translation velocity as length scale and velocity scale, respectively. When the background rotation is added, however, depending on the magnitude of the rotation, the characteristics of the vortex ring change, and it will be shown that, for the highest rotation rates, the vortex ring does not form at all. In these cases the above quantities are not defined and the meaning of the nondimensional parameters becomes unclear. The same problem is encountered if the circulation of the vortex ring is used instead of the self-induced velocity. Within this scenario, it is more convenient to use quantities related to the vortex ring generation. Although these parameters are only indirectly related to the final vortex structure, on the other hand, they are always well defined. In the present case, the radius of the orifice ($R_o = D_o/2$) from which the fluid is ejected and the centreline ejection velocity (U_o) have been chosen as length and

velocity scales, giving the time scale R_o/U_o and the nondimensional parameters $Re = U_o R_o/\nu$ and $Ro = U_o/2\Omega R_o$. In the following, all dimensionless quantities are given in terms of an appropriate combination of the scales R_o and U_o .

Once the scaling quantities are fixed, the run parameters can also be defined. The simulations have been performed in an axisymmetric domain of dimensions $L_r = 5$ and $L_z = 8$ in the radial (r) and axial (z) directions, respectively. The spatial discretization was uniform in z with grid spacing $\Delta z = 0.031$ using 257 grid points, while a non-uniform grid was used in r to achieve a fine resolution close to the edge of the orifice, where a thin vorticity layer rolls up initially. A coarser grid was used near the external cylindrical boundary in order to minimize the number of grid points in a dynamically passive region. The analytical transformation for the radial coordinate is

$$r = L_r r_1(\eta) \cdot r_2(\eta), \quad (3.3)$$

with

$$r_1(\eta) = \frac{L_m \tanh(\beta\eta)}{L_r \tanh(\beta\eta_m)}, \quad r_2(\eta) = \frac{1}{r_1(1)} + \left(1 - \frac{1}{r_1(1)}\right) \frac{\tanh(\alpha(\eta - 1))}{\tanh(\alpha(\eta_m - 1))},$$

where η is the radial computational variable uniformly spaced between 0 and 1. By using the values $L_r = 5$, $L_m = 1$, $\eta_m = 0.39$, $\alpha = \beta = 3$ and 129 grid points a grid spacing of $\Delta r = 0.024$ is obtained near the axis, $\Delta r = 0.017$ near the orifice edge and $\Delta r = 0.1$ in the region of the external boundary where a free-slip boundary condition has been imposed.

The time integration of the equations was performed with a constant time step $\Delta t = 0.02$, which yielded a value of the stability parameter (CFL) always below unity.

Since the formation and the evolution of a vortex ring is a ‘space developing flow’, inflow and outflow boundary conditions have to be assigned in the axial direction. At the inlet ($z = 0$), for $0 \leq r \leq R_o (= 1)$ an axial velocity profile $U_z(r)$ is prescribed that is modulated by a time dependence $f(t)$ in such a way to reproduce the injection of fluid through the orifice of the experimental apparatus. $U_z(r)$ is specified by:

$$U_z(r) = U_o \frac{\tanh[(R_o - r)/\delta]}{\tanh[R_o/\delta]}, \quad (3.4)$$

where δ is a measure of the initial vorticity thickness of the inflow velocity profile for which $\delta = R_o/20$ has been used. The function $f(t)$ increases first from 0 to 1 in a time $\tau_1 = 0.1$, according to the symmetrical profile $f(t) = 3(t/\tau_1)^2 - 2(t/\tau_1)^3$. After this short acceleration phase, the flow injection is constant ($f(t) = 1$) for a time $\tau_2 = 1.0$. The deceleration phase at the end of the injection is prescribed by the same (but reversed) profile as in the initial acceleration phase and $f(t)$ decreases from 1 to 0 in a time $\tau_3 = \tau_1 = 0.1$. The total injection time is thus $\tau = 1.2$ that corresponds to a dimensional time of one second, according to the dimensional values of R_o and U_o used in most of the experiments (see subsection 3.4.1). For $z = 0$ and $R_o < r \leq L_r$ all velocity components are set to zero. Identical inflow conditions have been used for the passive scalar concentration C to simulate the flow visualization experiments in which dyed fluid is injected through the orifice.

Boundary conditions at the outlet are very important in space developing flows. In the present simulations, it is imposed that the velocity components and the passive scalar are convected out of the domain according to the relation:

$$\frac{\partial Q_c}{\partial t} + u_c \frac{\partial Q_c}{\partial z} = 0, \quad (3.5)$$

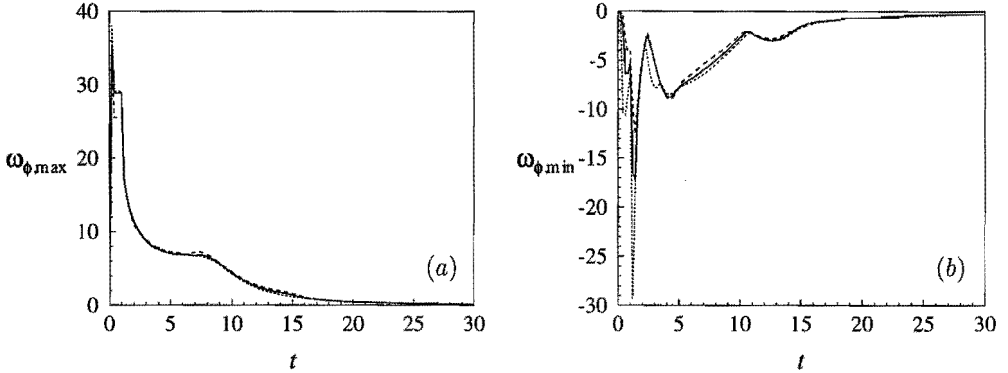


FIGURE 3.2: Time evolution of the maximum (a) and the minimum (b) azimuthal vorticity ω_ϕ during a vortex-ring simulation with $Re = 480$ and $Ro = 1.33$: 385×257 (dotted line), 257×129 (solid line) and 193×97 (dashed line) grid points in axial and radial direction, respectively.

with Q_c the convected quantity and u_c the convection velocity. In the numerical code this velocity is fixed to $u_c = 0.6$; it has been checked, by preliminary simulations, that the results are quite insensitive to the value of u_c .

All axisymmetric simulations have been performed using a grid of 257×129 in the axial and radial directions, respectively. The grid independence of the results has been checked by repeating one typical simulation with a coarser (193×97) and a finer grid (385×257) and comparing the results. For this comparison the run parameters were $Re = 480$ (used for almost all simulations) and $Ro = 1.33$, since it has been observed that for such high rotation rates small vorticity structures are created. The comparison is shown in figure 3.2 for the peak values of the azimuthal vorticity ω_ϕ and the different calculations show a satisfactory agreement for $t > 4$.

Although the hypothesis of axisymmetry was used for most of the numerical experiments, some full three-dimensional simulations were performed (see subsection 3.4.5). Due to computer limitations* a satisfactory azimuthal resolution could not be achieved maintaining the grid of the axisymmetric cases. A good compromise was to reduce the axial and radial extension of the computational domain to 6 and 3.75 and the grid to 193×97 , therefore without changing the radial and axial spatial resolution. This solution allowed to use 49 grid points in the azimuthal direction, which was found sufficiently fine to resolve the scales of the flow.

3.4 Results

3.4.1 MATCHING NUMERICAL SIMULATIONS WITH LABORATORY EXPERIMENTS

In most of the laboratory experiments described here the same fluid injection parameters were used as in the experiments without background rotation described in the previous chapter (see section 2.4). A cylindrical slug of fluid of length $L_o = 2.4$ cm is injected with mean injection velocity $U_o = 2.4$ cm/s through an orifice with diameter $D_o = 4.0$ cm. For the experiments the value of Re was thus fixed at $Re = U_o R_o / \nu = 480$, with $\nu = 0.01$ cm²/s the

*A DEC-Alpha workstation with 128 Mb RAM has been used for these simulations.

kinematic viscosity of water at room temperature. If other injection parameters are used these are specified explicitly.

In order to be able to distinguish the effects of the rotation, the main features are summarized of the evolving vortex ring at $Re = 480$ in *absence* of rotation ($\Omega = 0$), which will be considered as the ‘reference case’. Results of laboratory experiments of such vortex rings are presented in the previous chapter, section 2.4. Several characteristic parameters of the vortex rings have been measured and their evolution is shown in figures 2.8 and 2.14. In this subsection the results of numerical simulations of vortex rings are discussed, which will be used to mimic the laboratory experiments. The vortex rings are generated by the flow injection profile specified in section 3.3 and the subsequent evolution of the flow is computed numerically. In correspondence with the experiment, the Reynolds number of the flow is taken $Re = 480$. The characteristic ring parameters, which are derived from these simulations, are compared with the respective parameters obtained from the laboratory experiments. A proper agreement between these ring parameters is aimed at in order to obtain dynamically similar flows.

The characteristic parameters of the vortex rings in the numerical simulations are determined as follows. The ring radius R and the axial distance Z travelled by the vortex ring are given by the radial and axial coordinates, respectively, of the core centre positioned at the maximum of the azimuthal vorticity ω_ϕ in the core. The velocity of propagation U is calculated from numerical differentiation of Z with respect to time. The circulation Γ of the vortex ring is computed from the surface integral of ω_ϕ over the (r, z) -plane in the computational domain.

The variations of these parameters as a function of the distance Z travelled by the vortex ring are plotted in figure 3.3 by dashed lines. After an initial unsteady stage in which the vortex ring is formed, all flow quantities relax to approximate constant values, indicating a steadily propagating vortex structure. Data obtained from laboratory experiments with $Re = 480$ are added in figure 3.3. For a proper comparison, these data have been scaled relative to R_o and U_o . In the numerical simulation the velocity of propagation and the circulation of the developed vortex ring are both about 50% smaller than in the experiment. Also the radius of the ring is slightly smaller. This is an enormous mismatch between the experiment and the simulation, which has to be clarified and, if possible, reduced by adjustment of the initial conditions in the simulation.

To understand the deficiency in U and Γ , consider the evolution of the axial flow along the symmetry axis. Figure 3.3(d) shows the profiles of the axial velocity u_z along the z -axis, both during the flow injection ($t = 1$) and for the fully-developed vortex ring ($t = 7$). In the numerical simulation the maximum of this profile at $t = 1$ drops considerably and at $t = 7$ it is almost half its initial value $U_z(0) = 1$. On the other hand, in the laboratory experiment this drop does not happen and the maximum in the profile remains approximately equal to the mean injection velocity. It has been found that the velocity drop in the numerical simulation occurs during the deceleration phase of the flow injection. Similar to the impulsive pressure force that initiates the flow during the acceleration phase of the fluid injection, there is an opposite pressure force during the final deceleration phase, when the injection velocity at the orifice retards as prescribed. Note that this pressure force extends over the whole computational domain and thus affects the entire flow. As a result, a vortex ring develops that propagates at a reduced speed and proportionally smaller circulation. One can imagine that in the simulation the flow is generated by a piston that closes the orifice opening when

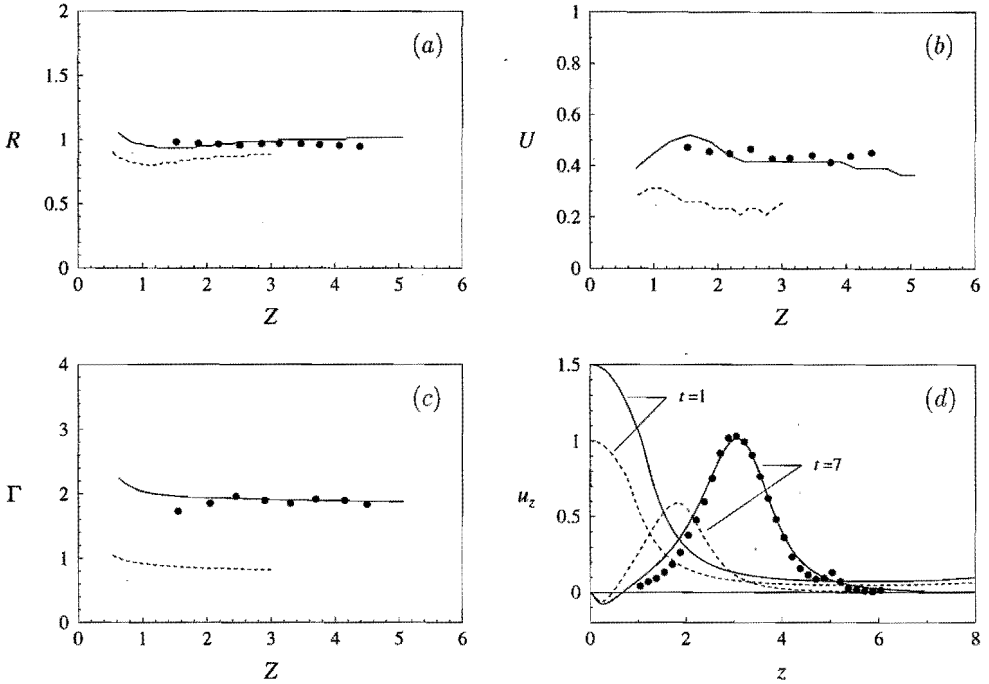


FIGURE 3.3: Evolution of characteristic ring parameters obtained from two numerical simulations with maximum injections $U_z(0) = 1.0$ (dashed lines) and $U_z(0) = 1.5$ (solid lines), respectively ($Re = 480$); (a) ring radius R , (b) propagation velocity U , (c) circulation Γ and (d) profiles of the axial velocity u_z along the z -axis ($r = 0$) (d); near the end of injection ($t = 1$) and when the vortex ring has been fully-developed ($t = 7$). Markers denote experimental data ($Re = 480$): R and U obtained from dye-visualization experiment (cf. data in figure 2.8a, c plotted by open square markers; markers at $\Delta t = 0.36$); data for Γ computed from line integral of u_z along z -axis (cf. data in figure 2.14d plotted by filled circles; markers at $\Delta t = 1$); axial velocity profile in figure (d) measured from particle experiment at $t = 7$. Experimental parameters: $D_o = 4.0$ cm, $L_o = 2.4$ cm and $U_o = 2.4$ cm/s.

the fluid injection is stopped*. In the laboratory experiment, however, the orifice remains open and, after the forced fluid injection, the flow through the orifice opening continues for a short time in absence of a retarding adverse pressure force. Of course, on account of the incompressibility of the fluid this outflow has to be balanced and an opposite flow of ambient fluid into the generator has been observed in the experiments.

Several numerical simulations with different injection parameters $U_z(0)$, τ_1 and τ_2 have been performed to find proper parameters to correct for this different flow injection mechanism, because it has evidently an enormous effect on the subsequent development of the vortex rings. It turns out that increasing the maximum injection velocity $U_z(0)$ with 50% is sufficient to compensate the 50% deficiency in U and Γ . The results of the simulation with $U_z(0) = 1.5$

*A vortex ring approaching a no-slip wall at a right angle increases in size (Walker *et al.* 1987). In the present case, however, the vortex ring propagates away from a no-slip wall after the 'piston' has closed the orifice opening and the ring radius decreases, as seen in figure 3.3(a).

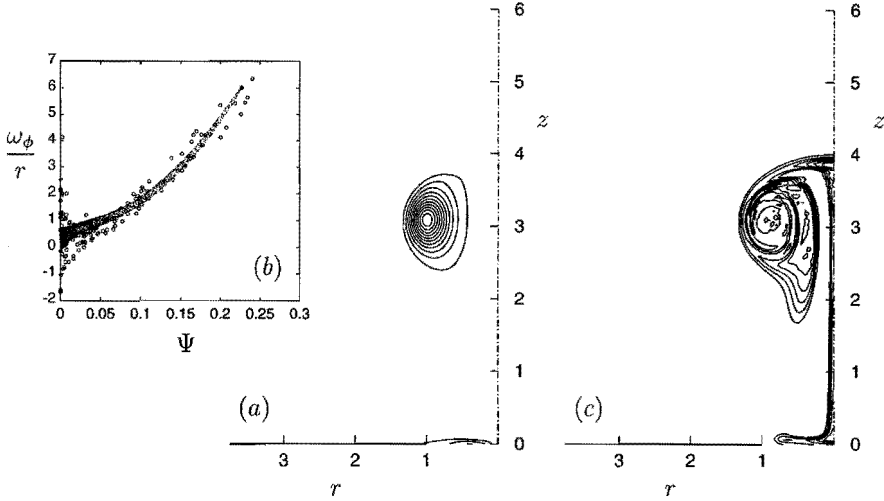


FIGURE 3.4: (a) Contour plot of azimuthal vorticity at $t = 7$, no background rotation ($Re = 480$); contour levels at $\Delta\omega_\phi = 0.5$. The inset figure (b) shows corresponding scatter plot of ω_ϕ/r versus stream function Ψ from numerical simulation (dots) and experimental data (circles); experimental parameters: see caption figure 3.3. (c) Contour plot of passive scalar at $t = 7$, $Sc = 10$ (contour increments $\Delta C = 0.25$).

are shown by solid lines in figure 3.3 and they fit the laboratory experiments quite well.

The formation process of the vortex ring in the numerical simulation is completed after the ring has moved several ring radii downstream from the generating orifice. Figure 3.4 shows the azimuthal vorticity ω_ϕ in the fully formed vortex ring at $t = 7$, after travelling about 3 ring radii. The inset (b) of this figure shows a scatter plot of ω_ϕ/r versus stream function Ψ , data computed at all grid points in the vortex core ($\Psi > 0$). The stream function of the flow is determined relative to a frame moving with the vortex ring. All data coincide in a narrow branch, typical for an axisymmetric flow in almost steady inviscid equilibrium[†]. Experimental data are added, showing a very good agreement with the simulation.

From the results of the numerical simulation with $U_z(0) = 1.5$ in figure 3.3 the following values are read for the ring parameters of the fully-developed vortex ring at $Z = 3$: ring radius $\bar{R} = 0.98$, translation velocity $\bar{U} = 0.42$ and circulation $\bar{\Gamma} = 2.10$, giving for the Reynolds numbers defined in terms of the ring parameters $Re_{\bar{R}} = \bar{U}\bar{R}Re \simeq 200$ and $Re_{\bar{\Gamma}} = \bar{\Gamma}Re \simeq 1000$. To give an idea of the thickness of the ring, a ‘speed-effective core size’ a_e (Saffman 1978; see also section 2.2 of this thesis) is computed, i.e. the core size of the uniform vorticity ring which matches the speed of the present ring. From the formula for the translation velocity of vortex rings (Thomson 1867a):

$$\bar{U} = \frac{\bar{\Gamma}}{4\pi\bar{R}} \left(\ln \frac{8\bar{R}}{a_e} - \frac{1}{4} \right), \quad (3.6)$$

the value $a_e/\bar{R} = 0.53$ is calculated, comparable to the experimental values (see figure 2.14).

Figure 3.4(c) shows a plot of the passive scalar distribution in the (r, z) -plane, obtained for $Sc = 10$. This value is certainly far below the Schmidt number of dye in liquids, which

[†]The reader is referred to section 2.2 in which the theory of axisymmetric inviscid flows is considered.

is typically $\mathcal{O}(500 - 1000)$. Due to resolution problems, however, such values are too large for the numerical simulations. The aim is to partially account for the difference in diffusivity between the vorticity and the passive scalar to study its effects. It should be noted that even though a relatively low Schmidt number has been used for the simulations, the passive scalar in figure 3.4(c) looks slightly under-resolved. However, this is not a problem for the dynamics since the scalar is only a passively convected quantity that does not interact with the flow dynamics which, in contrast, is very well resolved. It is also stressed that the low Schmidt number used in these simulations prevents the passive scalar field from forming those spiraling patterns like in figures 3.5 and 3.6. Verzicco & Orlandi (1995) performed simulations at $Sc = 100$ and they observed spirals like those of flow visualizations; however, in that case only the initial formation of the vortex ring was simulated and a very fine spatial discretization could be achieved. In the present study, in contrast, the evolution of the vortex ring is considered during a larger time and hence a larger computational domain is needed. The same spatial resolution used by Verzicco & Orlandi (1995) in such a large domain would require a very large number of grid points, which is beyond the present computing capabilities.

For times larger than $t = 7$, the ring only undergoes a slow viscous decay, translating with a velocity that decreases in time ($\bar{U} \simeq 0.36$ at $t = 18$) due to viscous effects. The vortex ring gradually grows until $\bar{R} = 1.05$ at $t = 18$. At $t = 20$ the vortex ring leaves the computational domain.

Finally, by comparing the ring parameters computed above with data given in Shariff *et al.* (1994), it can be concluded that this vortex ring is stable to azimuthal perturbations[†] and this further justifies the axisymmetric nature of most of the simulations.

Concludingly, in absence of rotation the considered vortex rings with $Re = 480$ develop within a distance of a few ring radii into a steadily propagating and stable axisymmetric vortex structure. Furthermore, proper conditions have been found to initiate the numerical simulations in order to produce vortex rings with similar characteristics as in the laboratory experiments. In the following subsections the motion of such a vortex ring is considered in case it propagates parallel to the axis of a uniform background rotation. Due to this rotation relative motion is induced in the rotating frame of reference, interfering with the vortex ring and the resulting flow is rather complicated. To give an impression of this perturbed flow, pictures of dye-visualization experiments will be presented first.

3.4.2 PRELIMINARY FLOW VISUALIZATIONS

Before getting into the quantitative description of the results, it is helpful to show a couple of dye visualizations of the evolution of the vortex ring in a background rotation. Similar flow visualization experiments of a vortex ring in a fluid without rotation have been performed and are presented in the previous chapter (see figure 2.7). A comparison of the observed flows with and without background rotation is useful in order to appreciate the differences in the

[†]The computation of the stability parameters implies also the determination of a_1 , the 'inner core radius' with maximum tangential velocity. In addition, Saffman (1978) gives an estimate of the self-induced rate of strain σ due to the curvature of the vortex ring (which drives the instabilities) and he defines a related Reynolds number Re_S :

$$\sigma = \frac{3\Gamma}{16\pi R^2} \left[\ln \frac{8R}{a_e} - \frac{17}{12} \right], \quad Re_S = \frac{\sigma a_1^2}{\nu}.$$

By direct numerical simulations Shariff *et al.* (1994) found the critical value $Re_S \simeq 18$ while the present calculations are in the range $Re_S \simeq 10.5$, which is below the region of growing azimuthal instabilities.

flow dynamics that are induced by the system rotation.

Figure 3.5 presents a sequence of photographic recordings of a dye visualization experiment of a vortex ring in a rotating fluid. In this experiment the rotation rate Ω of the system is relatively low ($Ro = 10$). In contrast, figure 3.6 shows the evolution of a vortex ring in a fluid that rotates faster ($Ro = 4.8$). Initially, in both cases a vortex ring is created in the same way as in the case of no rotation (cf. figure 2.7*a*). However, when the vortex ring creation is almost complete, a small depression is observed in the frontal side of the vortex atmosphere (figures 3.5*a* and 3.6*a*). From this region a thin dye layer rolls up into a secondary vortical structure with circulation of opposite sign relative to the circulation of the primary vortex ring. This secondary vortex is then advected by the local flow field of the primary vortex ring, increasing in strength during stretching around the vortical core of the primary vortex ring (figure 3.5*c, d* and figure 3.6*b*). Eventually, the secondary structure is completely shed from the primary vortex while its localized vorticity soon diffuses due to viscosity (figure 3.5*e, f* and figure 3.6*c, d*).

From figure 3.6(*a, b*) it is seen that the shedding of the secondary structure is not completely symmetrical. In the experiment in figure 3.5 the shedding of dye is observed on the left-hand side only. It is suspected that this asymmetry is caused by a small misalignment between the direction in which the vortex ring propagates and the rotation axis of the system. In order to have a better picture of this phenomenon, and to validate this supposition about the cause of this loss of symmetry, a few three-dimensional simulations have been performed and the results are presented in subsection 3.4.5.

In both cases it is observed that the primary vortex ring was severely deformed during the shedding process, but it is still able to re-establish itself as a vortex ring after the shedding. In case of low rotation, this vortex ring then continues its propagation steadily, without any subsequent deformations (note that the dye still indicates a depression at the front), outside the observation area of figure 3.5(*f*) until it reaches the free surface level of the fluid in the tank. At the higher rotation rate, however, a third vortical structure is created ahead of the re-established primary ring (figure 3.6*c, d*), in the same way the secondary vortex was formed earlier (cf. figure 3.6*a*). The shedding process could in principle be repeated (figure 3.6*e*), if the primary vortex were strong enough. Usually, viscosity weakens the vortex ring during the evolution and, after the first shedding, the primary vortex is too weak to shed a new structure. Besides, at this stage the motion loses its approximate axisymmetric structure completely and it is less clear from a two-dimensional view how the flow field evolves three-dimensionally (figure 3.6*e*).

Eventually, after a few rotations of the system when the flow has decayed almost completely, the dye that is left behind shows a pattern of vertically elongated streaks that perform slow vertical oscillations (figure 3.6*f*). This phenomenon is reminiscent of the formation of a 'Taylor column' (Taylor 1921), a typical feature that illustrates the quasi two-dimensional nature of flows in steady slow motion in rotating fluids.

Summarizing the entire process, it is seen that the first effect of the rotation is to form a depression in the front of the vortex ring atmosphere. From this depression, oppositely-signed vorticity develops and eventually rolls up to generate a counter-rotating secondary vortex ring which is shed behind the primary ring. The impulse of the primary ring is reduced by the shedding of fluid in the secondary structure and this loss is evidenced by the shorter distance travelled by the ring (figure 3.6*d*) with respect to the case without rotation (figure 2.7*d*) in the same period of time. When time proceeds, the rings may lose their axisymmetric shape

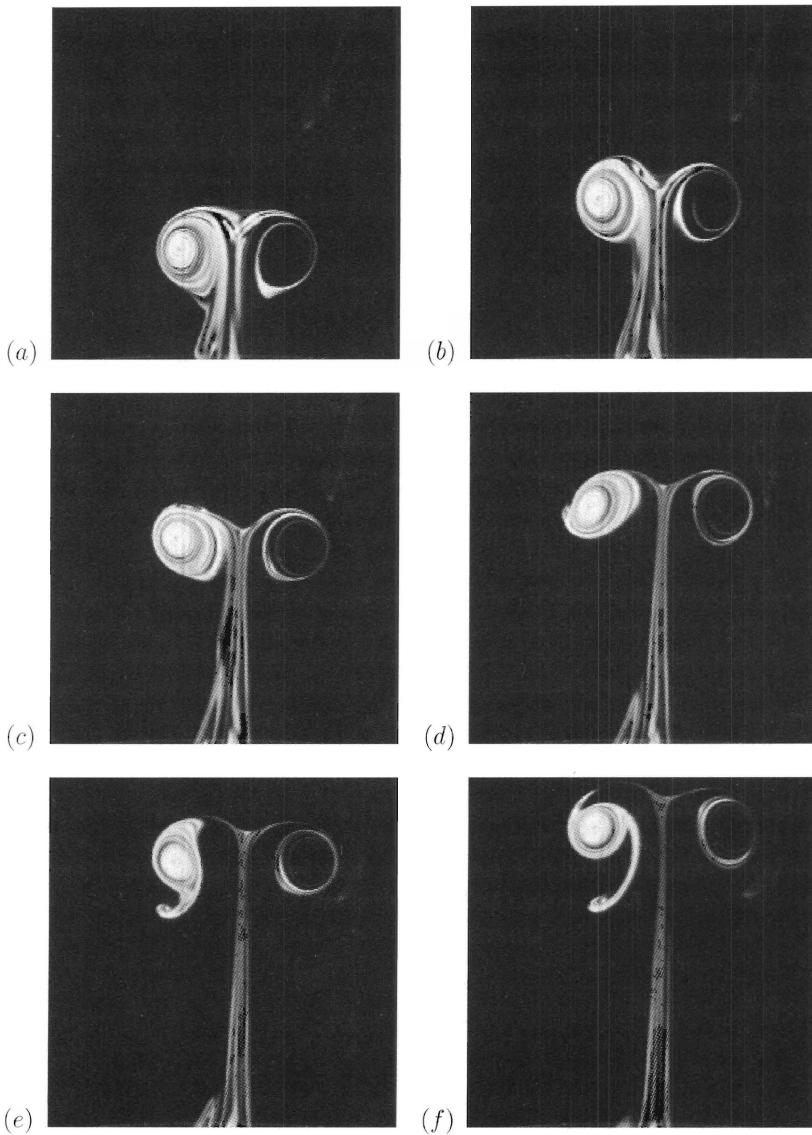


FIGURE 3.5: Cross-sectional (side) view of the evolution of a vortex ring propagating parallel to the axis of a rotating fluid ($Ro = 10$ and $Re = 480$): (a) $t = 7$, (b) $t = 9$, (c) $t = 11$, (d) $t = 13$, (e) $t = 15$ and (f) $t = 17$ after start of the fluid injection. Experimental parameters: $D_o = 4.0$ cm, $L_o = 2.4$ cm, $U_o = 2.4$ cm/s and $\Omega = 0.06$ s $^{-1}$.

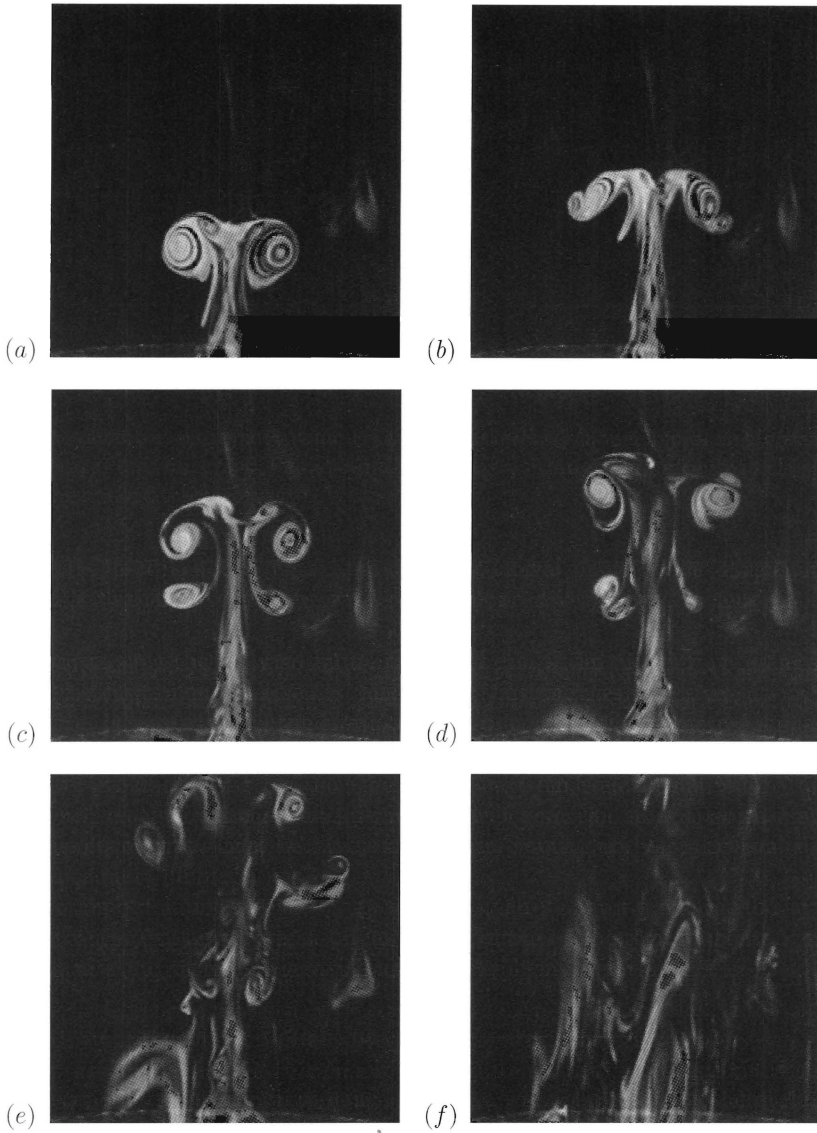


FIGURE 3.6: Cross-sectional (side) view of the evolution of a vortex ring propagating parallel to the axis of a rotating fluid ($Ro = 4.8$ and $Re = 645$): (a) $t = 7$, (b) $t = 10$, (c) $t = 13$, (d) $t = 16$, (e) $t = 23$ and (f) $t = 90$ after start of the fluid injection. Experimental parameters: $D_o = 3.0$ cm, $L_o = 3.0$ cm, $U_o = 4.3$ cm/s and $\Omega = 0.3$ s $^{-1}$.

and the flow shows complex three-dimensional structures. It should be kept in mind that the features described above have been inferred from flow visualizations which merely show the evolution of a passive scalar, which might be different from the evolution of the vorticity field. However, Orlandi & Verzicco (1993) have shown that there is a strong correlation between azimuthal vorticity and passive scalar distributions if the flow remains axisymmetric. On the basis of this observation, it may therefore be expected that at least the gross features of the flow dynamics can be understood from the flow visualizations.

In figures 3.5 and 3.6 it has been seen that the evolution of the vortex ring is strongly influenced by the background rotation. Laboratory experiments and numerical simulations have revealed that the flow dynamics can be roughly divided into two regimes: 'low rotation' and 'high rotation'. In the former regime, the rotation constitutes only a perturbation to the basic flow state, while in the latter the rotation dominates the flow and the vortex ring hardly evolves or even does not form at all. The regimes are separated roughly at $Ro \simeq 2$, although this division is not sharply defined; for intermediate Ro -values flow phenomena are observed that are typical for both regimes. In the next subsection the typical flow evolution of the low rotation regime will be discussed by examining results of numerical simulations and laboratory experiments in a complementary way. The high rotation regime will be addressed in subsection 3.4.4.

3.4.3 LOW ROTATION REGIME

In figure 3.7(a) the trajectory of a vortex ring is shown for the case of a relatively slow background rotation. On the left-hand side results of a dye-visualization experiment with $Ro = 6.0$ and $Re = 480$ are plotted. The filled circles denote the trajectory of the core centre of the primary vortex ring, measured from $t = 2.4$ after start of the fluid injection. The evolution of the flow is similar to the flow visualizations in the previous subsection. At $t = 5.7$ the secondary vortex structure with opposite circulation is observed for the first time, located slightly ahead of the primary ring (see arrows at $t = 5.7$ in figure 3.7a). The subsequent motion of the vortices is affected by their mutual interaction and they can be considered to form an unbalanced vortex ring pair.

The dynamics of pairs of vortex rings has been studied extensively in a number of papers (Gurzhi & Konstantinov 1989; Riley 1993; Weidmann & Riley 1993; recently, Wakelin & Riley 1997). In fact, due to the interaction each vortex ring is advected in the velocity field of the partner vortex ring. This mutually induced motion determines, in addition to the self-induced velocity of the rings, the eventual ring trajectories. In the present case, the secondary (weaker) vortex ring is advected around the core of the primary (stronger) ring. Simultaneously, the primary ring grows in size due to the induced flow of the secondary ring. When the secondary ring is at the outer edge of the primary ring core and the radius R of the primary ring is largest, this induced flow is opposite to the direction of motion of the primary ring and its forward propagation is reduced. In addition, the self-induced velocity of the primary vortex ring is lower, because of the larger ring radius (see equation (3.6)). In figure 3.7(b) the axial distance travelled by the primary vortex ring from the orifice is plotted as a function of time. The temporal slow-down of the vortex ring is observed by the bend in the data around $t = 10$, at the same axial distance from the orifice as the kink in R in figure 3.7(a). After shedding the secondary structure the ring radius of the primary vortex decreases and the vortex ring continues its propagation. A third vortex structure was observed from $t = 8.9$ (figure 3.7a).

The right-hand graph of figure 3.7(a) shows the trajectory of the primary vortex ring

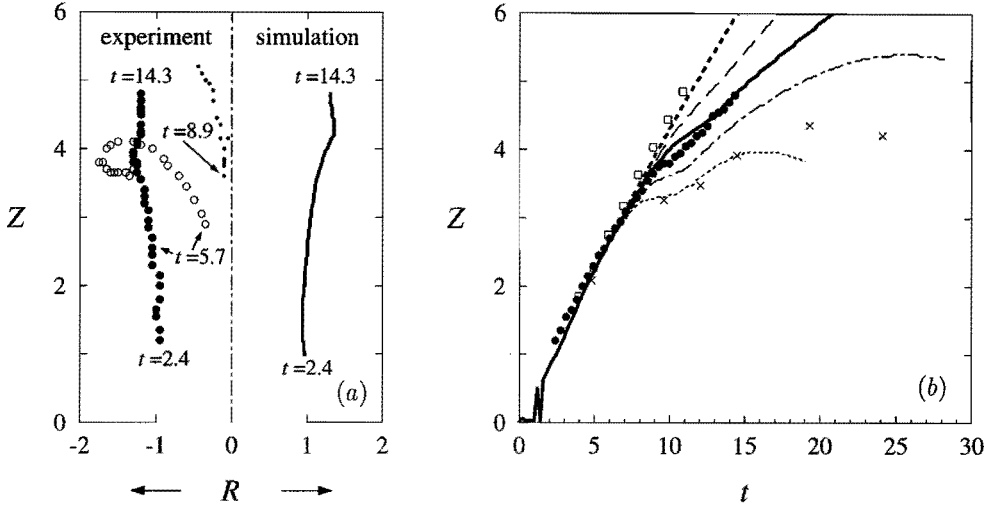


FIGURE 3.7: (a) Trajectory of the core of the primary vortex ring in a rotating fluid obtained from dye-visualization experiment (left-hand side, filled circles) and numerical simulation (right-hand side, solid line), both with $Ro = 6.0$ and $Re = 480$. Trajectories of secondary (open circles) and tertiary (dots) vortex structures are presented only for the experiment. Markers are plotted at $\Delta t = 0.36$; initial and final times of trajectories are given. (b) Time evolution of the axial distance Z travelled by the primary vortex ring from the orifice. Numerical simulations with $Re = 480$ and various Ro are indicated by different lines: $Ro = \infty$ (thick dashed), $Ro = 10$ (long-dashed), $Ro = 6.0$ (thick solid), $Ro = 3.0$ (dashed-dotted) and $Ro = 2.0$ (dotted). Experimental results: $Ro = \infty$ (open squares), $Ro = 6.0$ (filled circles, same experiment as in figure (a)) and $Ro = 2.6$ (crosses); $Re = 480$. Injection parameters for all experiments: see caption figure 3.3.

according to a numerical simulation with the same dimensionless parameters $Ro = 6.0$ and $Re = 480$ as in the experiment and during the same time interval. The trajectory resembles the experimental trajectory very well, covering the same axial distance and showing a similar increase in R . The maximum R -value is attained slightly further away from the orifice, but it is remarked that in the experiment the shedding was not simultaneously on both ring sides. In figure 3.7(b) the time evolution of the travelled distance Z of the primary ring is shown for several values of Ro , including the case without background rotation ($Ro = \infty$). Simulations with $Ro = \infty$ and $Ro = 6.0$ show good agreement with the corresponding experiments. In conclusion, the numerical set-up is well suited to mimic the laboratory experiments also in presence of a background rotation.

From the trajectories in figure 3.7(b) it is seen that the propagation velocity of the vortex ring, given by the slope of the curves, is reduced in a rotating system. At higher rotation rates (small Ro) the vortex ring eventually stops. This stagnation was also observed in flow visualization experiments ($Ro = 2.6$), which showed that at this stage the vortex ring was completely distorted. The maximum vorticity is then no longer located in the vortical core, but in the wake region close to the orifice; presentation of these data is useless and therefore omitted in figure 3.7(b). The slow-down of the vortex ring in a rotating fluid is related to the formation of a layer of oppositely-signed azimuthal vorticity on the front side of the vortex ring (see figure 3.8). The circulation related to the vorticity in this layer contributes to a reduction

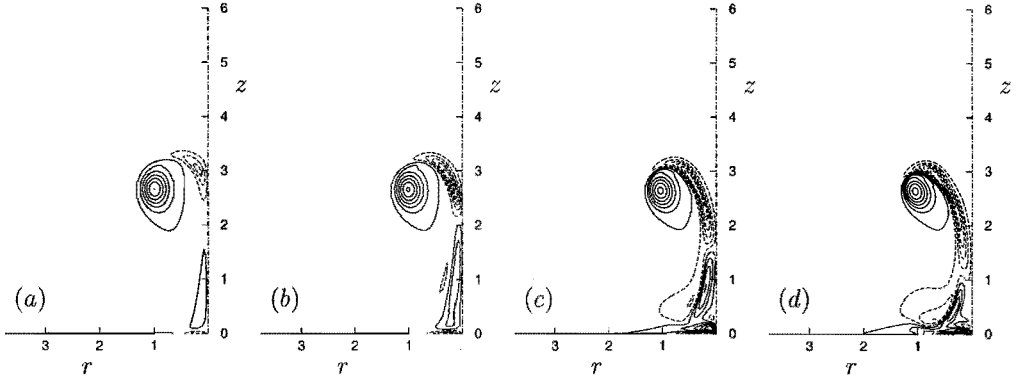


FIGURE 3.8: Contour plots of azimuthal vorticity at $t = 6$, obtained from a numerical simulation with $Re = 480$ and: (a) $Ro = 10$, (b) $Ro = 6.0$, (c) $Ro = 3.0$ and (d) $Ro = 2.0$; vorticity increments $\Delta\omega_\phi = \pm 1.0$, minimum level at $|\omega_\phi| = 0.5$. In this and subsequent similar figures, solid lines denote positive values and dashed lines negative values.

of the net circulation of the vortex ring. As a consequence, the propagation velocity of the vortex ring, being proportional to its circulation, is decreased. The motion of the vortex ring decays also by viscous diffusion of vorticity, although these viscous effects are small compared to the effects induced by the rotation. To see this, consider the simulation with $Ro = \infty$ in figure 3.7(b), in which the decay of the ring speed is solely due to viscosity ($Re = 480$). The minor deviation of this curve from a line with a fixed slope, which would represent the vortex ring trajectory in the inviscid flow limit, gives an estimation of the relatively small viscous slow-down of the vortex ring. In contrast, the curves at finite Ro -values reveal a considerable reduction in the ring velocity imposed by the system rotation. It is seen in figure 3.8 that, as the Rossby number decreases, the oppositely-signed structure strengthens and thus the deceleration of the primary ring is enhanced.

The formation of a secondary vorticity layer has also been observed by particle tracking experiments, and figure 3.9 shows one typical observation. From the particle paths of figure 3.9(a) the velocity field parallel to the cross-sectional plane is computed (figure 3.9b); this field is interpolated on a regular grid by splines (figure 3.9c) in order to facilitate calculation of the component of the vorticity field normal to this plane (figure 3.9d). Although the vorticity shows some low-level noise, the secondary structure with opposite vorticity is clearly discernible on top of the primary ring. Also note the irregular motion at the tail, which was completely absent in the flow without background rotation. From an oblique view (not shown here) a strong azimuthal swirl was observed behind the vortex ring.

To measure this swirling flow, experiments were performed in which the flow in a plane perpendicular to the rotation axis was viewed. For these experiments the illuminating light sheet was directed horizontally through the fluid at a fixed distance of 4 cm above the orifice. Since the main fluid flow is normal to this plane a broad light sheet had to be used in order to trace the minor horizontal motion of the particles. The resulting velocity field gives a qualitative impression of the flow perpendicular to the rotation axis. Figure 3.10(a) shows this velocity field for an experiment with $Ro = 4.0$ at $t = 6$, when the vortex ring has just passed the observational plane and the flow in the tail is viewed. The inward directed flow

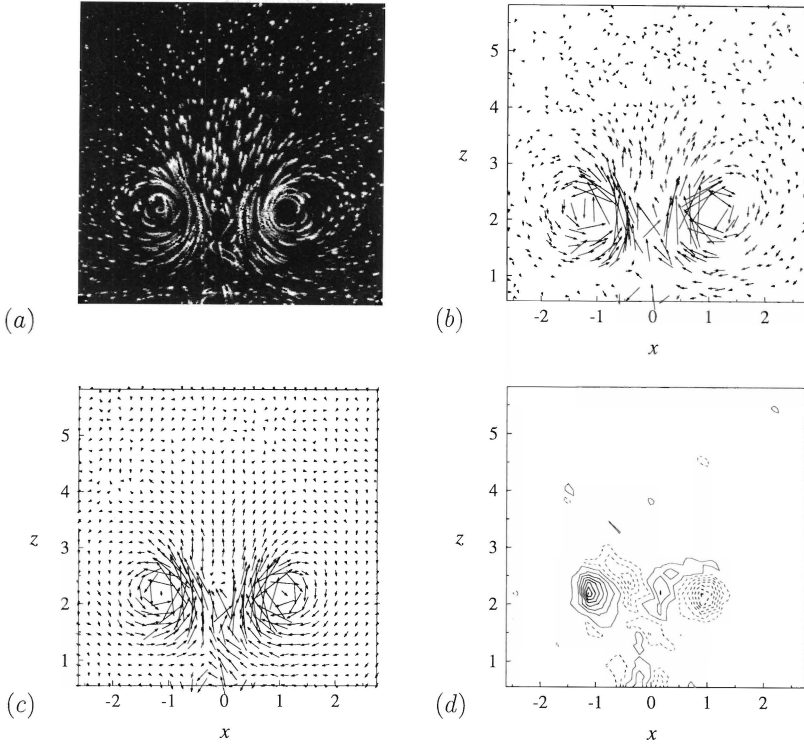


FIGURE 3.9: Results of a particle experiment at $t = 6$ viewing the flow in a cross-sectional plane through the vortex ring centre, parallel to the rotation axis ($Ro = 3.5$ and $Re = 480$): (a) particle trajectories, (b) measured velocity field, (c) interpolated velocity field and (d) component of vorticity field normal to the plane. Injection parameters: see caption figure 3.3, rotation rate $\Omega = 0.17 \text{ s}^{-1}$.

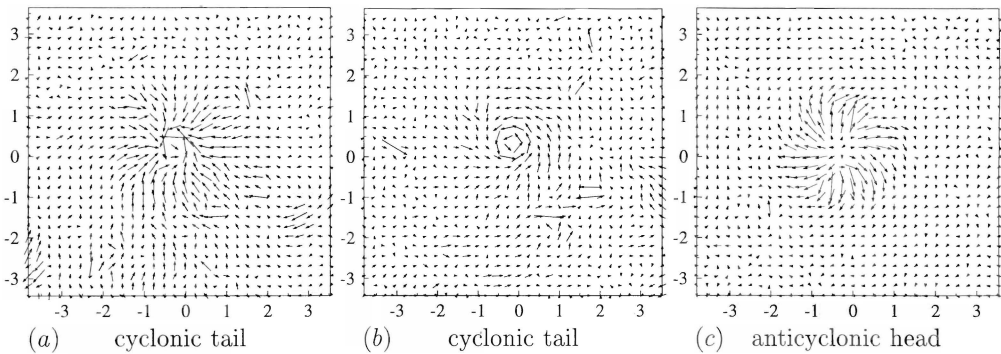


FIGURE 3.10: Results of a particle experiment, presenting the flow velocity in a plane perpendicular to the rotation axis at 4 cm above the orifice opening. Deflection, owing to Coriolis forces, of inward flow behind vortex ring to the right at $t = 6$ (a) leads to cyclonic swirl at $t = 10$ (b); $Ro = 4.0$ and $Re = 480$. Similar deflection of outward flow leading to anticyclonic swirl ahead of vortex ring is weaker, but readily observed for higher rotations ($Ro = 2.9$) at $t = 2.5$ (c). Injection parameters: see caption figure 3.3, rotation rates $\Omega = 0.15 \text{ s}^{-1}$ (a, b), $\Omega = 0.21 \text{ s}^{-1}$ (c).

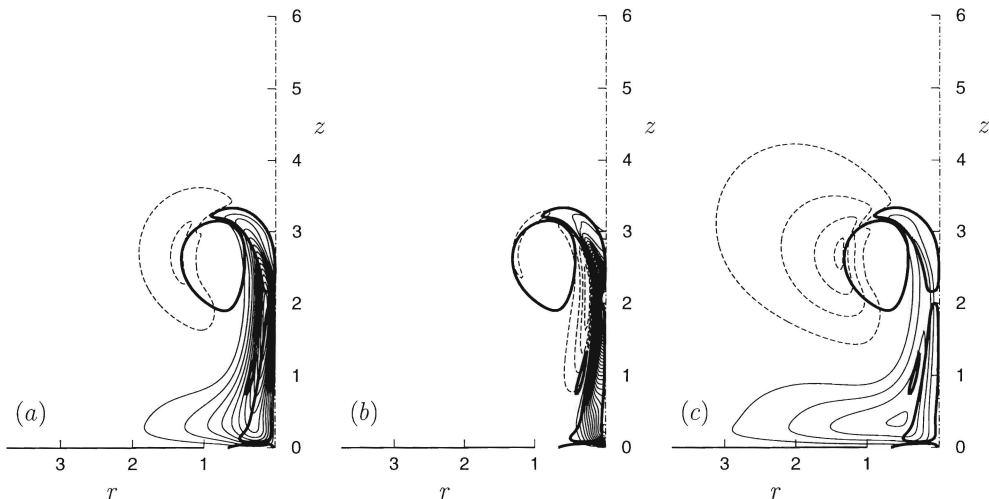


FIGURE 3.11: Contour plots of (a) azimuthal velocity u_ϕ , (b) axial vorticity ω_z and (c) $\xi = ru_\phi$ at $t = 6$, obtained from a numerical simulation with $Ro = 6.0$ and $Re = 480$. Contour increments: $\Delta u_\phi = \pm 0.04$, $\Delta \omega_z = \pm 0.3$ and $\Delta \xi = \pm 0.03$ (solid lines for positive values and dashed lines for negative values). Thick lines in the figures denote boundaries of regions of positive and negative azimuthal vorticity (cf. figure 3.8b), contours at $|\omega_\phi| = 0.5$.

behind the vortex ring is slightly deflected to the right, resulting in a cyclonic[§] swirl at $t = 10$ (b). In the same way the radially outward flow ahead of the vortex ring was measured, revealing also a deflection to the right but not as pronounced as in the tail. The deflection was enhanced by increasing the background rotation and figure 3.10(c) shows the formation of an anticyclonic swirl ahead of the vortex ring at $t = 2.5$ for $Ro = 2.9$.

The generation of this swirling flow in combination with the layer of oppositely-signed azimuthal vorticity on top of the vortex ring leads to a very complicated three-dimensional flow. In laboratory experiments only the flow velocity parallel to some cross-sectional plane can be measured, which is obstructed if there is any flow normal to this plane. This means that only one component of the vorticity field (i.e. normal to the cross-sectional plane) can be determined and this is done with considerable inaccuracies. In contrast, in numerical simulations all flow components are computed simultaneously. Numerical simulations are therefore very useful in order to get a complete picture of the three-dimensional structure of the flow. In the rest of this subsection results of numerical simulations are used to examine and explain the formation of the swirling flow and the oppositely-signed vorticity layer.

Figure 3.11(a) shows the azimuthal velocity u_ϕ in the meridional (r, z) -plane. At the rear of the vortex ring near the symmetry-axis there is a strong swirling flow, in cyclonic direction (positive u_ϕ). In addition, at the outer side of the vortex ring core there is a weak anticyclonic flow (negative u_ϕ). The related axial vorticity ω_z is plotted in figure 3.11(b), showing an axially elongated vortex of finite extent at the symmetry-axis.

To study the three-dimensional structure of the vorticity field and the orientation of vortex

[§]Cyclonic means in the same direction as the rotation of the system, anticyclonic is in opposite direction.

lines it is convenient to introduce the function $\xi(r, z)$, such that:

$$\frac{\partial \xi}{\partial z} = -r\omega_r, \quad \frac{\partial \xi}{\partial r} = r\omega_z. \quad (3.7)$$

According to this definition, in a meridional plane the vector $\omega_r \mathbf{e}_r + \omega_z \mathbf{e}_z$ is tangent to contours of constant ξ [¶]. Hence, $\xi(r, z)$ contours are axisymmetric vortex surfaces on which vortex lines are located. It can easily be shown that the function ξ is given by (see Virk *et al.* 1994):

$$\xi = ru_\phi, \quad (3.8)$$

thus being proportional to the angular momentum of the flow. In all contour plots of ξ presented in this thesis the direction of the vorticity component along the contourlines is in anti-clockwise sense for contours with positive ξ and in clockwise sense for contours with negative ξ .

In figure 3.11(c) contours of constant ξ are shown, corresponding to the azimuthal velocity in figure (a). At the tail of the vortex ring near the symmetry axis the vortex lines are orientated vertically upwards, twisting like right-handed helices around the symmetry-axis, because of the positive azimuthal vorticity. At the centre of the vortex ring this twisting is reversed, because of the layer of negative azimuthal vorticity. Following the contours of constant ξ , the vortex lines diverge from the symmetry-axis and return along the inner side of the toroidal ring core. Evidently, at this stage this axial tail vortex does not overlap with the main core of the vortex ring. At the outer side, however, contour lines of constant ξ intersect the core boundary and the azimuthally directed vorticity in the core is slightly deflected downwards.

To understand the formation of the swirling flow, consider first a vortex ring without rotation, the velocity field of which is shown in figure 3.12. Due to the circumferential flow around the core a parcel of fluid initially located close to the axis at position **A** in figure 3.12 will be transported to a location farther from the axis turning around the front of the ring. In contrast, a parcel initially far from the axis at position **B** in figure 3.12 will be convected toward the axis turning around the rear part of the ring. Note that, because of axisymmetry, any small fluid element in this meridional cross-section of the flow represents in fact a toroidal ring of fluid, centred at the symmetry-axis.

In a rotating system, according to Kelvin's theorem the absolute circulation of the flow is conserved along a material curve that coincides with such a ring of fluid, assuming viscous forces vanish on this curve. The absolute circulation consists of the circulation of the relative flow in the rotating system and the circulation due to the background vorticity 2Ω . This means that along a circle with radius r_c , centred at the symmetry-axis of an axisymmetric flow, the following relation holds:

$$u_\phi 2\pi r_c + 2\Omega \pi r_c^2 = \text{conserved}. \quad (3.9)$$

Hence, wherever there is an outward radial motion (increasing r_c) the azimuthal velocity has to decrease, while it has to increase where the radial motion is directed inward. By this mechanism an azimuthal flow is induced, even if there is initially no swirl relative to the rotating system present. In terms of forces, it is the Coriolis force that has a tendency to

[¶]Compare this definition of ξ with the definition of Stokes stream function ψ (equation (2.1)), the velocity field $u_r \mathbf{e}_r + u_z \mathbf{e}_z$ in the meridional plane being tangent to contours of constant ψ .

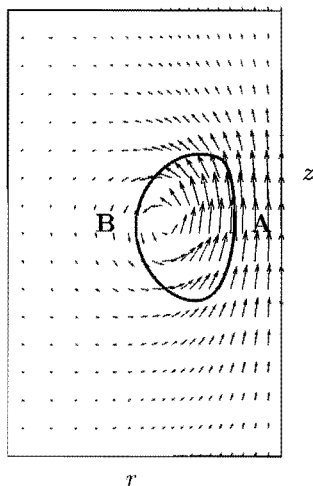


FIGURE 3.12: Velocity vectors and contour $\omega_\phi = 0.5$ sketching boundary of ring core; vortex ring translates upwards ($Ro = \infty$ and $Re = 480$). **A** and **B** are positions of parcels of fluid initially close to and far from the axis, respectively.

deflect all radial motion to the right, parallel to a lateral plane (i.e. a plane normal to the rotation axis), in an anti-clockwise rotating system (positive Ω), thus generating the swirling flow.

For the vortex ring the outward radial motion ahead of the vortex ring induces a negative swirl, while the inward motion behind the vortex ring induces a positive swirl, as already observed in the laboratory experiments (figure 3.10) and in the numerical simulations (figure 3.11a). It has been seen that the negative swirl ahead is weaker than the positive swirl behind the vortex ring. This can now be explained from equation 3.9. An inward radial motion δr , with respect to an initial position r_0 , will be accompanied by an increase of the azimuthal velocity that is larger than the corresponding decrease due to the same displacement δr performed radially outward.

The induction of relative vorticity (figure 3.11b) in a rotating system due to the flow field of a vortex ring can be explained by careful inspection of the relevant components of the vorticity equation in a rotating system. The axial component of this equation is given by:

$$\frac{\partial \omega_z}{\partial t} + (\mathbf{u} \cdot \nabla \omega)_z = (\boldsymbol{\omega} \cdot \nabla \mathbf{u})_z + \frac{1}{Ro} \frac{\partial u_z}{\partial z} + \frac{1}{Re} (\nabla^2 \boldsymbol{\omega})_z, \quad (3.10)$$

where the second term at the right-hand side represents the effect of the system rotation. This term acts as a source term that induces axial vorticity, which is initially absent in the flow field of a vortex ring. Without background rotation, the velocity gradient $\partial u_z / \partial z$ of the axial flow along the symmetry-axis of the vortex ring is positive at the tail and negative ahead of the vortex ring (cf. figure 3.3d). Hence, in the rotating system axial vorticity is induced along this axis, being positive (cyclonic swirl) at the tail and negative (anticyclonic swirl) ahead of the vortex ring. However, the dynamical evolution of the flow is more complicated, because the newly formed axial vorticity is also modulated by self-induced axial stretching and compression behind and ahead the ring, respectively, as represented by the component

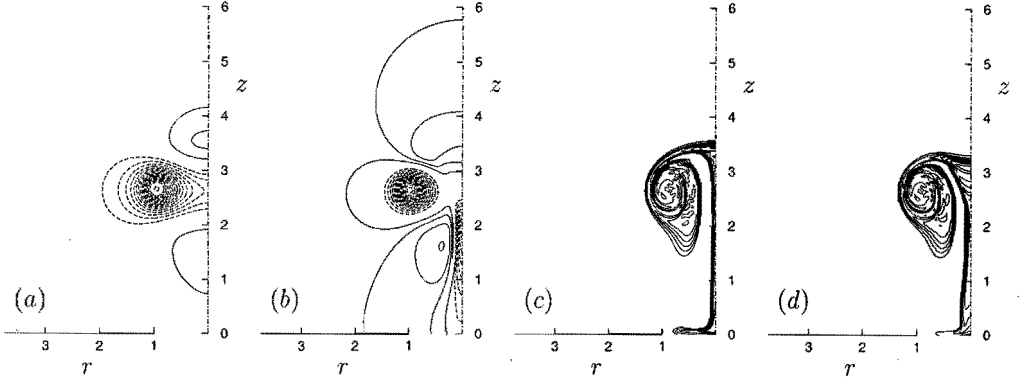


FIGURE 3.13: Contour plots of pressure (*a, b*) and passive scalar (*c, d*) at $t = 6$, obtained from numerical simulations with $Re = 480$ and $Sc = 10$: $Ro = \infty$ (*a, c*) and $Ro = 6$ (*b, d*). Contour increments $\Delta p = \pm 0.03$ (solid lines for positive values and dashed lines for negative values) and $\Delta C = 0.25$.

$\omega_z(\partial u_z/\partial z)$ in the first term on the right-hand side in equation (3.10). Furthermore, ahead of the vortex ring the induced relative vorticity is advected radially outward along the outer edge of the ring core, where the axial stretching rate $|\partial u_z/\partial z|$ of the flow (and thus the induction of axial vorticity) is smaller than near the ring axis. Behind the vortex ring the radially-inward advected flow is subjected to a continuously increasing axial stretching and the induced vorticity is accumulated in an intense axial vortex near the ring axis, the vorticity maximum located slightly below the ring centre (see figure 3.11*b*).

To explain the presence of the layer of negative azimuthal vorticity on top of the vortex ring the azimuthal component of the vorticity equation in a rotating system, given by:

$$\frac{\partial \omega_\phi}{\partial t} + (\mathbf{u} \cdot \nabla \omega)_\phi = (\omega \cdot \nabla \mathbf{u})_\phi + \frac{1}{Ro} \frac{\partial u_\phi}{\partial z} + \frac{1}{Re} (\nabla^2 \omega)_\phi, \quad (3.11)$$

is inspected. Evidently, the induction of relative azimuthal vorticity due to the system rotation is related to axial gradients in the swirl u_ϕ . If one moves upwards along a line parallel to the symmetry axis and passing through the maximum of u_ϕ ($r \simeq 0.2$ in figure 3.11*a*), one first encounters a positive axial gradient of u_ϕ ($\partial u_\phi/\partial z > 0$), whereas further up (above the axial position of maximum ω_z) it becomes negative. According to equation (3.11) this implies a region of positive azimuthal vorticity generation close to the axis behind the ring, while going to the front there is a region of negative azimuthal vorticity generation, consistent with the flow map of figure 3.8(*b*). Furthermore, due to the same gradient in u_ϕ the vertically directed vortex lines near the ring axis are tilted, according to the component $\omega_z(\partial u_\phi/\partial z)$ in the first term on the right-hand side of equation (3.11). This tilting of vortex lines is in the same sense as the induction of azimuthal vorticity by the system rotation. As a result, vortex lines near the ring axis twist around this axis like right-handed helices behind the vortex ring and like left-handed helices near the ring centre.

As a consequence of the strong swirling flow in a tail behind the vortex ring there is a region of relatively low pressure near the ring axis. In figure 3.13 the distribution of the pressure in a vortex ring is shown, both without (*a*) and with (*b*) a background rotation. The low pressure region behind the vortex ring is clearly visible; ahead of the vortex ring

the pressure distribution is almost unaltered by the system rotation, which induces there merely a weak swirl. The axial flow through the ring centre is thus retarded by an adverse pressure gradient. The corresponding passive scalar distributions are shown in figure 3.13(c, d). Without background rotation the front of the ring is concave according to the classical picture (cf. dye-visualization experiments in figure 2.7). In contrast, in the case with background rotation the head of the ring shows a depression, as already seen in the flow visualizations (figure 3.5 and 3.6). This depression indicates that the upward moving fluid along the ring axis is retarded in presence of the low pressure behind the vortex ring and this region of low pressure exerts a suction force that pulls back the vortex ring.

Figure 3.14 presents the development of the flow, showing simultaneously the evolution of the azimuthal vorticity (plotted on left-hand side of each graph) and the passive scalar distribution (plotted on right-hand side). As time proceeds, the interaction with the oppositely-signed structure continues resulting in a radially outward motion of the vortex ring. The diameter of the orifice opening drawn at $z = 0$ can be used as a reference to notice the ring growth. The increase of the radius of the primary ring has already been observed in dye-visualization experiments (see figure 3.7a). It is accompanied by an increase of the vorticity and a reduction of the core cross-section because of vortex stretching. This mechanism increases vorticity gradients considerably and enhances the viscous diffusion.

Evidence of this behaviour is given in figure 3.15(a) where the time evolution of the maximum positive value (positive peak) of the azimuthal vorticity in the flow is shown for several rotation rates; again also the curve for $Ro = \infty$ is included for comparison. The evolution of the minimum negative value (negative peak) of the azimuthal vorticity is shown in figure 3.15(b). For early times $t < 5$, the peaks all have the same value, because the secondary structure is still too weak to influence the core of the vortex ring. The large negative peak around $t \simeq 2$ is created in a thin boundary layer at the wall close to the orifice and its diffusion in time can be estimated from the curve at $Ro = \infty$. Later, when the secondary vorticity layer has formed, the negative peak vorticity is again extreme (figure 3.15b). As the outward radial motion becomes evident the positive vorticities increase, with respect to the case at $Ro = \infty$, due to stretching. Of course, with the stretching, vorticity gradients are also augmented, and the increase of vorticity is followed by a rapid decrease due to diffusion, especially for the higher rotations. Although the secondary structure of negative vorticity is stretched even more than the primary ring as it is wrapped around the latter, its core cross-section is elongated in a very thin layer and viscous diffusion of vorticity dominates vortex stretching (figure 3.14d, e). As a result, the vorticity in the shed structure, which is still observable by the passive scalar, has been diffused completely^{||} (figure 3.14g, h). Eventually, the negative vorticity does not vanish for $Ro = 10$ and $Ro = 6.0$ (figure 3.15b), since a layer of negative vorticity remains attached to the primary vortex ring while it continues its forward propagation (see figure 3.14h-l). Figure 3.16 shows that the anticyclonic swirl, which was restricted to the outer side of the primary ring core at earlier times, extends now over the entire ring core. An azimuthal flow along the core axis reduces the propagation velocity of vortex rings (see Moore & Saffman 1972; Virk *et al.* 1994), hence the induced anticyclonic swirl inside the

^{||}This is a nice example in which the passive scalar, with diffusivity different from the vorticity, suggests the presence of a certain flow structure, while the vorticity has already been diffused. This feature has to be kept in mind when conclusions are drawn from flow visualization experiments: regions of fluid indicated by dye might not have any counterpart in terms of vorticity, although in some cases patterns of spiraling dye are readily observable.

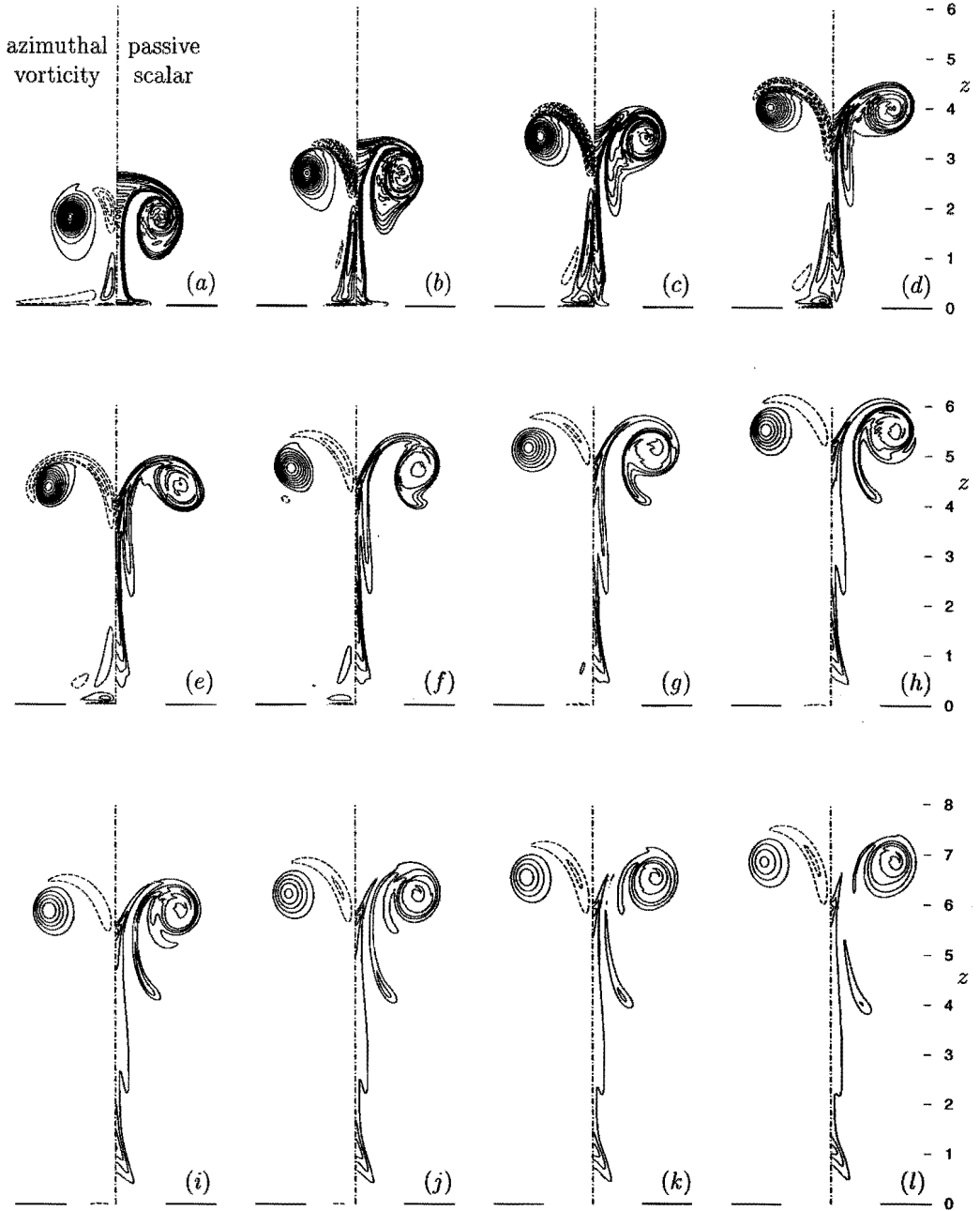


FIGURE 3.14: Pictures showing simultaneously the evolution of azimuthal vorticity (plotted on left-hand side) and passive scalar distribution (plotted on right-hand side) in cross-sectional plane of vortex ring, obtained from a numerical simulation with $Ro = 6.0$, $Re = 480$ and $Sc = 10$: (a) $t = 4$, (b) $t = 6$, (c) $t = 8$, (d) $t = 10$, (e) $t = 12$, (f) $t = 14$, (g) $t = 16$, (h) $t = 18$, (i) $t = 20$, (j) $t = 22$, (k) $t = 24$ and (l) $t = 26$. Contour levels at $\Delta\omega_\phi = \pm 0.5$ and $\Delta C = 0.25$.

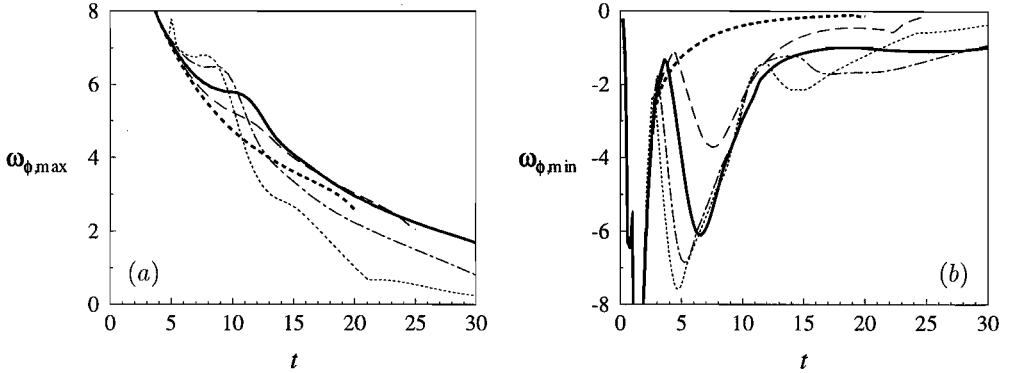


FIGURE 3.15: Time evolution of maximum (a) and minimum (b) azimuthal vorticity, obtained from numerical simulations with $Re = 480$: $Ro = \infty$ (thick dashed), $Ro = 10$ (long-dashed), $Ro = 6.0$ (thick solid), $Ro = 3.0$ (dashed-dotted) and $Ro = 2.0$ (dotted). Note that the primary vortex ring leaves the computational domain at $t = 20$ for $Ro = \infty$ and at $t = 25$ for $Ro = 10$.

ring core contributes to the slow down of vortex rings in presence of a background rotation.

For $Ro = 3.0$ and $Ro = 2.0$ the negative peak shows another oscillation and the layer of negative azimuthal vorticity ahead of the vortex ring is intensified again. Figure 3.17 shows the evolution of the flow at $Ro = 2.0$ ($Re = 480$) and the initiation of a repetition of the shedding process can be observed in figure 3.17(f, g). Note that in this case during the first shedding the primary ring core is severely deformed and, consequently, its vorticity drastically reduced. After the first shedding the positive vorticity is very weak and is further reduced by cross-cancellation with the attached negative vorticity layer (figure 3.17f–i). The vortex ring stops its propagation while its structure is gradually distorted, as seen from the evolution of the passive scalar in figure 3.17(g–l). In this case, the ‘kink’ in the curve in figure 3.15(a) at $t \simeq 21$ indicates that the vortex ring has almost disappeared; the peak vorticity plotted in the figure is then no longer located in the core of the ring, but in the wake region closer to the orifice.

Evidently, for $Ro \simeq 2.0$ the initially created vortex ring is still identifiable for some part of the evolution of the flow; eventually the ring is completely distorted and the vorticity diffused. For lower Ro the ‘kink’ in the curve of maximum azimuthal vorticity moves to the left of the time axis, implying that the vortex ring survives for a shorter time (see also figure 3.2a for the case $Ro = 1.33$). For values of the Rossby number lower than about 1 the rotation effects become dominant from the beginning, and the next section is devoted to study this regime.

All cases presented so far have been computed using a fixed Reynolds number ($Re = 480$), which was the value at which most of the experiments were performed. However, viscous effects play a large role in the flow dynamics and therefore it is important also to examine how the flow changes for increasing Reynolds numbers. Contour plots showing the evolution of the azimuthal vorticity and passive scalar distribution for the case with $Re = 1500$ and $Ro = 6.0$ are shown in figure 3.18 (compare these pictures with those in figure 3.14 with same Ro but lower Re). The first part of the evolution, i.e. the formation of the oppositely-signed structure, is essentially inviscid and simulations performed at different Reynolds numbers have revealed that the features of the flow are the same. However, in the next stage, the evolution is crucially determined by diffusion of vorticity, which is strongly dependent on viscosity. As the

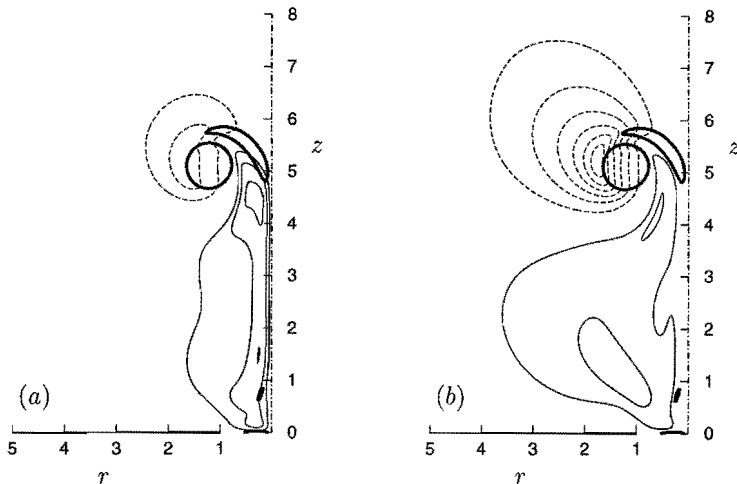


FIGURE 3.16: Contour plots of u_ϕ (a) and ξ (b) at $t = 16$, showing anticyclonic swirl along vortex ring core; results obtained from a numerical simulation with $Ro = 6$ and $Re = 480$. Contour levels at $\Delta u_\phi = \pm 0.04$ and $\Delta \xi = \pm 0.03$ (solid lines for positive values and dashed lines for negative values); thick lines denote boundaries of azimuthal vorticity patches ($|\omega_\phi| = 0.5$).

viscosity is decreased cross-cancellation of vorticity is prevented. Instead of diffusing during the advection around the primary ring, the thin layer of oppositely-signed vorticity rolls-up to form a complete secondary vortex ring that, after being shed, moves in a direction opposite to the primary ring. This secondary ring experiences flow dynamics similar to that described above with the role of positive and negative vorticity reversed and this is readily seen in figure 3.18(*g-l*). After shedding the structure, the primary vortex ring re-establishes and is even strong enough to shed a weak third structure. Remember, that this was also observed in the dye-visualization experiments in figure 3.6.

3.4.4 HIGH ROTATION REGIME

If the Rossby number is further decreased, rotation effects no longer act as just a perturbation of the basic state, but rather they dominate the flow. Figure 3.19 displays a typical experimental flow pattern obtained in the same way as figure 3.9c, but showing completely different phenomena. In particular, the initial roll-up of the injected fluid at the orifice edge is accompanied by a column of fluid pushed ahead of the ring and by oblique wave-like structures confined in thin layers (figure 3.19a). Subsequently, the vortex ring is distorted completely and only the column and the wave structures are left in the field (figure 3.19b-d). In this case, the computation of the azimuthal vorticity field from the flow maps of figure 3.19 does not reveal clear vortex structures, since the large velocity gradients observed in the flow are not resolved properly in the velocity measurements. In addition, the flow is not strictly parallel to the observational plane, hence introducing a lot of noise in the measured velocity field. Therefore, to better understand the vorticity dynamics, numerical simulations have been carried out for the same experimental conditions.

Figure 3.20 shows that immediately after the ejection oppositely-signed vorticity develops (figure 3.20a), partly due to the presence of a no-slip wall and partly, ahead of the ring, due

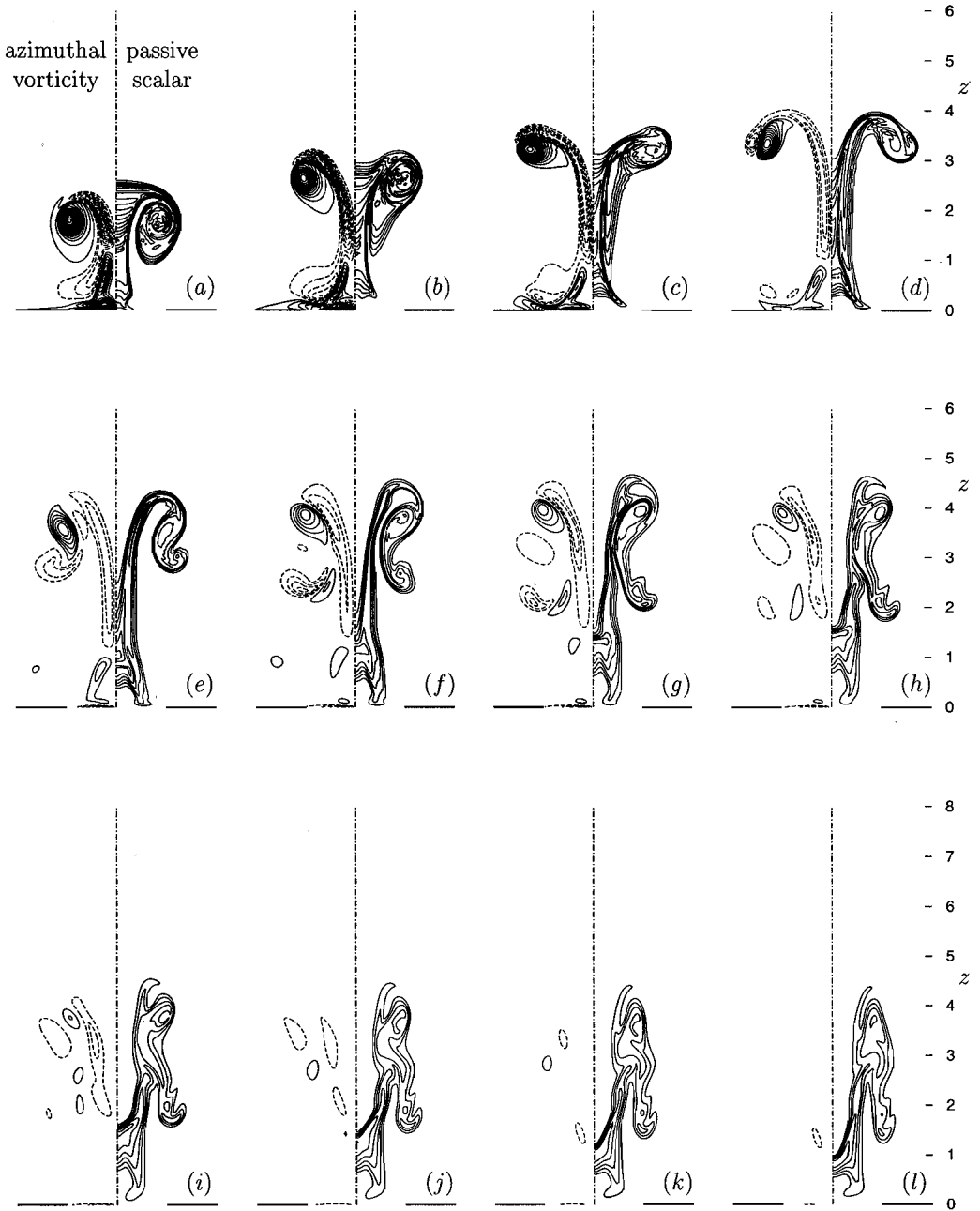


FIGURE 3.17: Pictures showing simultaneously the evolution of azimuthal vorticity (plotted on left-hand side) and passive scalar distribution (plotted on right-hand side) in cross-sectional plane of vortex ring, obtained from a numerical simulation with $Ro = 2.0$, $Re = 480$ and $Sc = 10$: (a) $t = 4$, (b) $t = 6$, (c) $t = 8$, (d) $t = 10$, (e) $t = 12$, (f) $t = 14$, (g) $t = 16$, (h) $t = 18$, (i) $t = 20$, (j) $t = 22$, (k) $t = 24$ and (l) $t = 26$. Contour levels at $\Delta\omega_\phi = \pm 0.5$ and $\Delta C = 0.25$.

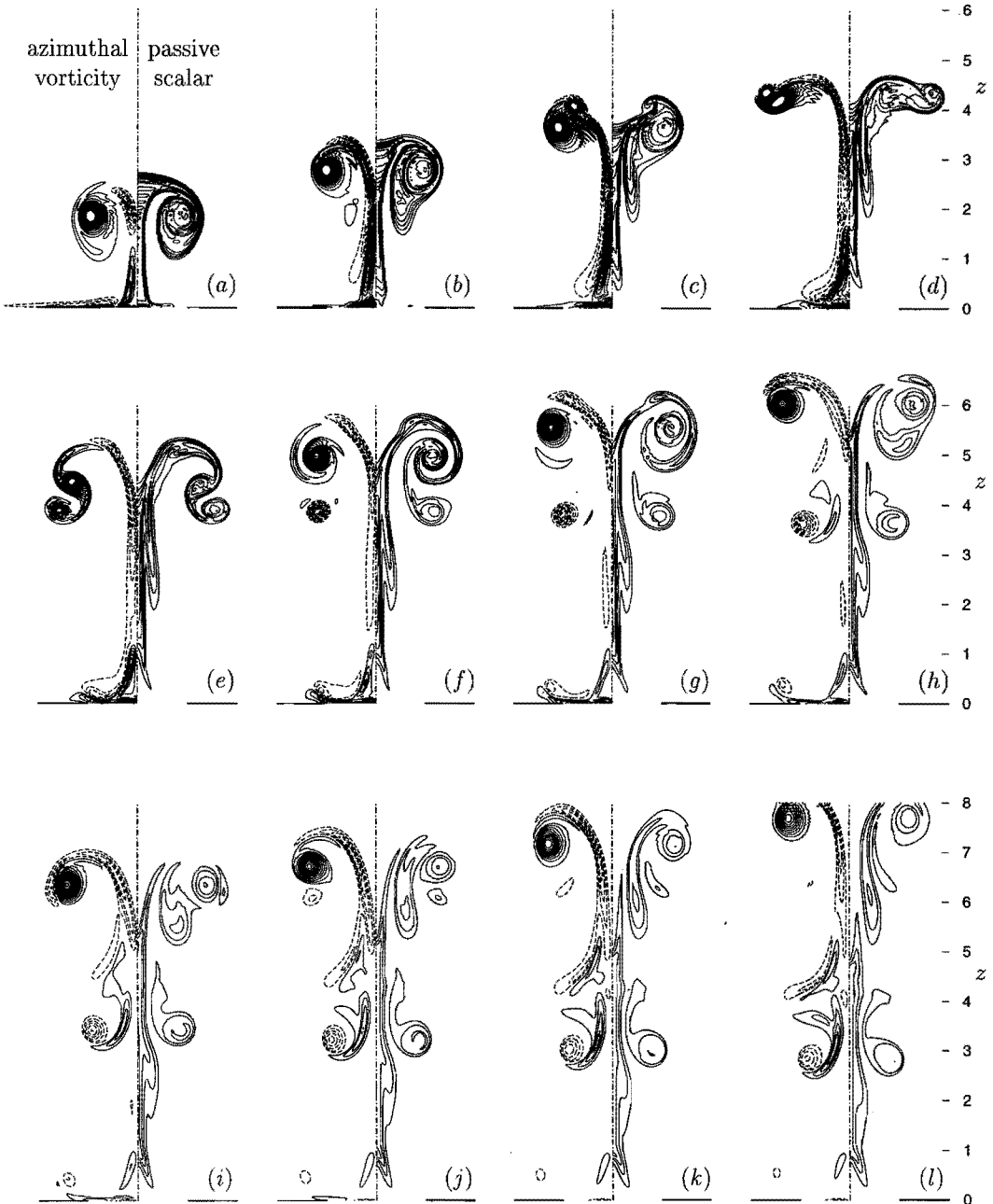


FIGURE 3.18: Pictures showing simultaneously the evolution of azimuthal vorticity (plotted on left-hand side) and passive scalar distribution (plotted on right-hand side) in cross-sectional plane of vortex ring, obtained from a numerical simulation with $Ro = 6.0$, $Re = 1500$ and $Sc = 3.2$: (a) $t = 4$, (b) $t = 6$, (c) $t = 8$, (d) $t = 10$, (e) $t = 12$, (f) $t = 14$, (g) $t = 16$, (h) $t = 18$, (i) $t = 20$, (j) $t = 22$, (k) $t = 24$ and (l) $t = 26$ (vortex ring is leaving the computational domain). Contour levels at $\Delta\omega_\phi = \pm 0.5$ and $\Delta C = 0.25$.

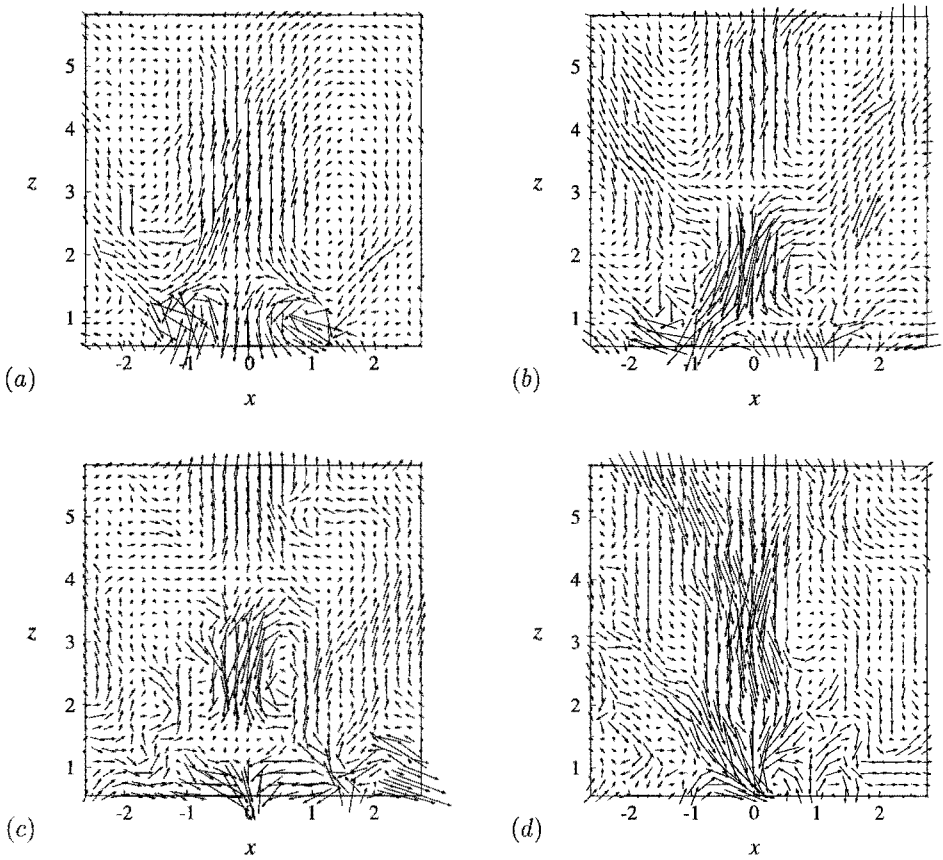


FIGURE 3.19: Interpolated velocity field of a laboratory experiment, showing cross-sectional view of flow generated by injecting a vortex ring at $Ro = 0.6$ and $Re = 480$: (a) $t = 4$, (b) $t = 6$, (c) $t = 8$ and (d) $t = 10$. Injection parameters: see caption figure 3.3, rotation rate $\Omega = 1.0 \text{ s}^{-1}$.

to the mechanism described in subsection 3.4.3. In this configuration, the incipient vortex is shielded by intense oppositely-signed layers and the cross-cancellation becomes dominant (figure 3.20*b, c*). Therefore, the vorticity structures weaken in time until they are completely diffused. Indirect evidence of this behaviour is also given in figure 3.20(*h*) where it is seen that the passive scalar ejected from the orifice does not show any roll-up symptom; but rather it behaves, during the whole evolution, like a column. The peak at the edge of the column demonstrates the flattening of the incipient vortex in figure 3.20(*b, c*).

Similarly as in the experiment, figure 3.20 shows that the high rotation regime introduces oblique shear layers of large axial extension (like those indicated by \mathcal{A} , \mathcal{B} , \mathcal{C} and \mathcal{D} in figure 3.20*d*) that were not evident in the low rotation regime. In course of time shear layers are formed in the region above the radial axis (figure 3.20*a-d*), yielding a pattern of alternating positive and negative vorticity layers. This pattern propagates like a wave in downstream direction, the orientation of the shear layers changing gradually towards the z -axis. Because

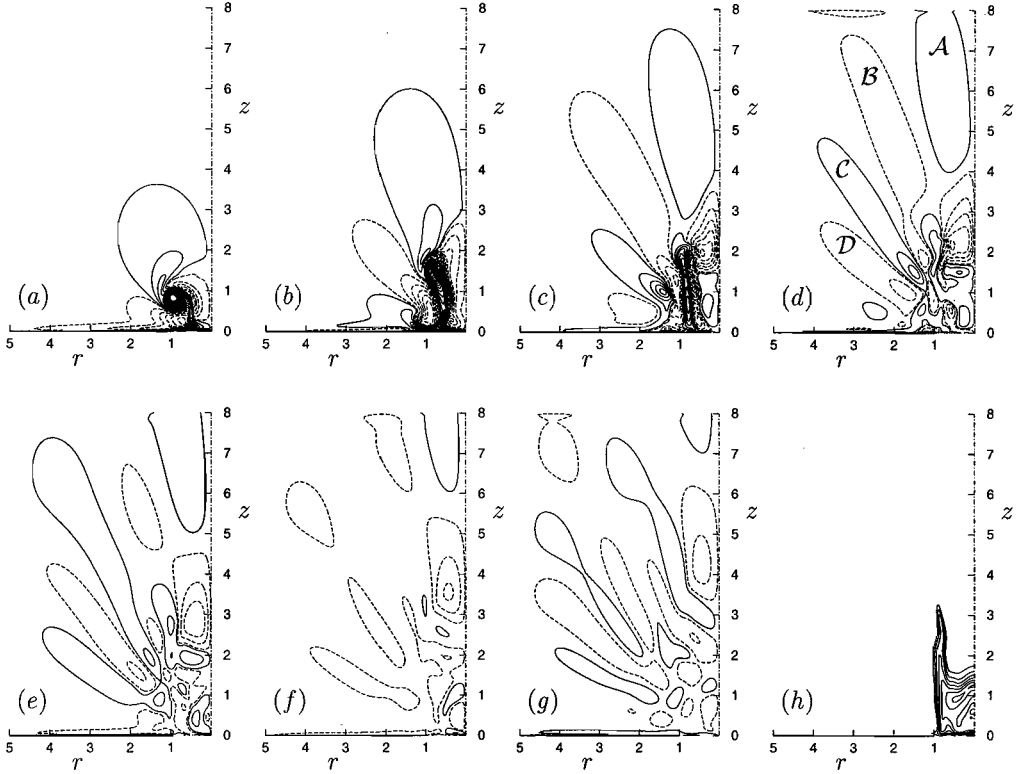


FIGURE 3.20: Contour plots of azimuthal vorticity obtained from a numerical simulation with $Ro = 0.6$ and $Re = 480$: (a) $t = 2$, (b) $t = 4$, (c) $t = 6$, (d) $t = 8$, (e) $t = 10$, (f) $t = 12$ and (g) $t = 14$. Figure (h) shows contour plot of passive scalar at $t = 14$ ($Sc = 10$). Vorticity increments $\Delta\omega_\phi = \pm 0.5$ (minimum vorticity level at $|\omega_\phi| = 0.1$ to show the oblique shear layers; solid lines for positive values and dashed lines for negative values); passive scalar increments $\Delta C = 0.25$.

of the axisymmetry of the flow, these shear layers are directed along conical surfaces around the symmetry-axis. Apparently, the tops of these cones almost coincide at the orifice ($z = 0$) for all shear layers. Note that the oblique flow patterns, which are observed in the experiment, are located between these vorticity layers. This is clearly seen in figure 3.21(a), showing the velocity field parallel to the meridional plane as computed in the simulation, together with contours of the oblique vorticity layers. Furthermore, layers in which the flow is directed towards the symmetry-axis are succeeded by layers with outwardly directed flow. In addition to this flow parallel to the meridional plane a swirl u_ϕ is induced normal to the meridional plane and from figure 3.21(b) it is seen that oblique layers of negative swirl coincide with layers of positive azimuthal vorticity and vice versa. Evidently, the different phases of the travelling wave pattern are distinguished by the main flow direction in the layers, the flow being rotated in successive layers. If a wave passes a fixed point in space, the local velocity \mathbf{u} is deflected parallel to the instantaneous flow layer to the right, i.e. in the direction of the vector $\mathbf{u} \times \mathbf{n}$ (\mathbf{n} is the normal of the layer, pointing in the direction of propagation of the wave). Note that these waves are transversal owing to the incompressibility of the fluid.

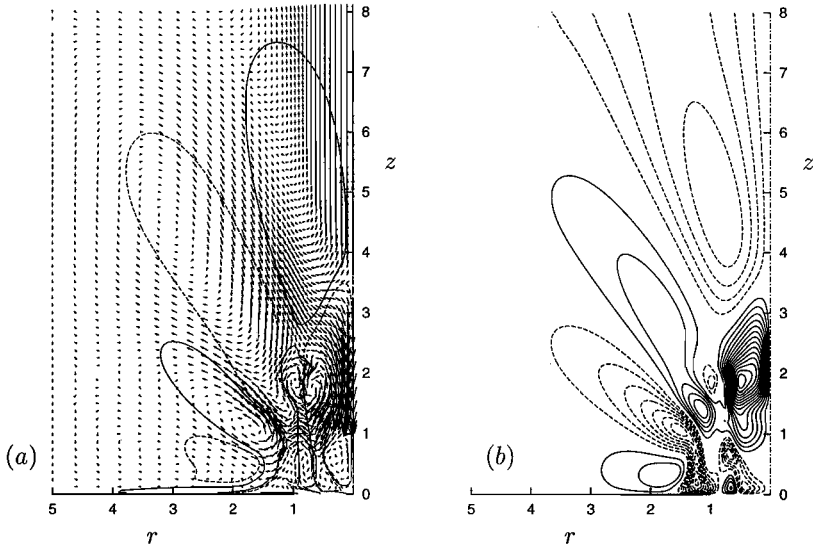


FIGURE 3.21: (a) Vector plot of the velocity field parallel to a meridional plane at $t = 6$, together with contours of azimuthal vorticity ($|\omega_\phi| = 0.1$) indicating the positions of the oblique vorticity layers adjacent to the layers of considerable meridional flow. (b) Contour plot of the azimuthal velocity u_ϕ at same moment (contour increments $\Delta u_\phi = \pm 0.04$; solid lines for positive values and dashed lines for negative values). Results obtained from a numerical simulation with $Ro = 0.6$ and $Re = 480$.

Propagation of inertial waves in a rotating fluid is governed by Coriolis forces and it appears most evident if the flow relative to the rotating system is in slow motion. For such flows the convective inertial forces are small in magnitude compared to the Coriolis forces and the evolution of the flow in time occurs on a time scale of the order of the rotation period Ω^{-1} of the system. To estimate the relative importance of the individual terms in the equations of motion, this time scale is a more appropriate measure than the time scale R_o/U_o , which has been used previously to render the equations of motion (3.1) in dimensionless terms. Using the time scale Ω^{-1} , length scale R_o and velocity scale U_o results in the following dimensionless equations of motion:

$$\frac{\partial \mathbf{u}}{\partial t} + Ro(\mathbf{u} \cdot \nabla)\mathbf{u} = -\nabla p - 2\mathbf{k} \times \mathbf{u} + Ek\nabla^2\mathbf{u}, \quad (3.12)$$

where the Rossby number ($Ro = U_o/\Omega R_o$) now denotes the ratio of the magnitude of convective inertial forces and Coriolis forces. The Ekman number ($Ek = \nu/\Omega R_o^2 = Ro/Re$) measures the relative importance of viscous forces compared to Coriolis forces. Obviously, in weak relative flows ($Ro < 1$) the contribution of the non-linear term $(\mathbf{u} \cdot \nabla)\mathbf{u}$ is small and in the limit $Ro \rightarrow 0$ the equation is linear. This linear approximation for small Ro is not self-evident from the formulation (3.1) of the dimensionless equations of motion used in the simulations; but the inferior role of the non-linear term in the formation of the oblique layers has been verified by performing two simulations at $Ro = \sqrt{2}/2$, one of which with the non-linear terms cancelled out. Typical results are presented in figure 3.22, showing that while the vorticity near the orifice is affected by the non-linear terms, the wave patterns are almost indistinguishable, thus proving that effects of non-linearity are negligible in the far field.

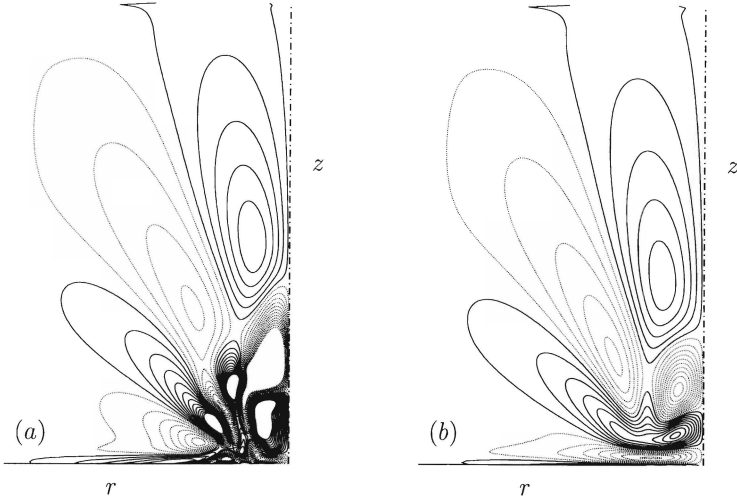


FIGURE 3.22: Contour plots of the azimuthal vorticity at $t = 7$ for $Ro = 0.707$ and $Re = 480$: (a) full Navier-Stokes run, (b) linear run. Vorticity increments $\Delta\omega_\phi = \pm 0.05$.

The inertial wave patterns in the present investigation are somewhat complicated because the source is transient and not a simple oscillation. Greenspan (1968) shows that for linear inertial waves with a single frequency $\omega < 2\Omega$ the governing equation is hyperbolic in its spatial dependence. This implies that discontinuities can occur in the fluid across characteristic surfaces that form cones with definite apex angle. In a cross-sectional view these cones are observed as oblique shear layers with angle:

$$\alpha = \sin^{-1}(\omega/2\Omega) \quad (3.13)$$

relative to the axis of symmetry. A physical interpretation for this expression is obtained by rewriting it as $\omega = 2\Omega \sin(\alpha) = 2\Omega_\perp$, where Ω_\perp denotes the component of Ω normal to the flow layer, along \mathbf{n} . The Coriolis force associated with this projection $\Omega_\perp \mathbf{n}$ has a tendency to deflect the flow parallel to the conical surfaces of the flow layers to the right, i.e. in the direction $\mathbf{u} \times \mathbf{n}$. Since this deflection is at a fixed rate $2\Omega_\perp$ for all velocity magnitudes, a coherent periodical motion is forced with frequency $\omega = 2\Omega_\perp$, as demonstrated by the appearance of inertial waves with the same frequency. Of course, this is just a very simple representation of the flow motion in which the contributions of the component of the Coriolis force along \mathbf{n} , pressure forces and viscous forces are not taken into account. However, in a simple plane wave approximation it can be shown that this normal component of the Coriolis force is balanced by a pressure gradient (see Batchelor 1967, p. 563).

To estimate the angles in figure 3.20 equation (3.13) is rewritten in terms of non-dimensional variables:

$$\alpha = \sin^{-1}(fRo), \quad (3.14)$$

where $f = \omega R_o/U_o$. The problem is that the flow in figure 3.20 is not generated by a periodical forcing which would excite only a single frequency mode (Görtler 1957; Oser 1958). On the contrary, the flow injection is only temporary and the injected flow is transient, exciting a spectrum of many frequencies. What could be done is to focus on one structure (for example

	$\alpha_{0.6}$	$f_{0.6}$	$\alpha'_{0.8}$	$\alpha_{0.8}$	$\alpha'_{0.48}$	$\alpha_{0.48}$
\mathcal{A}	7.5	0.22	10	10	6	6
\mathcal{B}	23	0.65	31	30	18	18
\mathcal{C}	34	0.93	48	48	27	27
\mathcal{D}	51	1.3	—	72	38	39

TABLE 3.1: Comparison of measured (unprimed) and predicted (primed) inclination angles (in degrees) of four successive shear layers at $t = 8$. Values measured from vorticity contour plots ($\alpha_{0.6}$ from figure 3.20(d); $\alpha_{0.8}$ and $\alpha_{0.48}$ from figure 3.23(a, b), respectively). Frequencies $f_{0.6}$, computed from respective angles $\alpha_{0.6}$ at $Ro = 0.6$, are used to predict angles with the same frequencies at different Ro .

that indicated by \mathcal{B} in figure 3.20d) and to measure its angle α_B . Then from equation (3.14) it is possible to compute the corresponding frequency f_B . Since the way of injecting fluid is the same for all cases, and the Rossby number is the only parameter changing, f_B can be used to estimate the angles of the corresponding structures for different Rossby number flows. From figure 3.20(d) with $Ro = 0.6$ the inclination of the structure indicated by \mathcal{B} is $\alpha_{B,0.6} \simeq 23^\circ$, measured with an inaccuracy of $\pm 1^\circ$, from which equation (3.14) yields $f_{B,0.6} = 0.65$. This value has been used to predict the inclination of the corresponding structures formed in the flow at $Ro = 0.8$ and $Ro = 0.48$, obtaining $\alpha'_{B,0.8} = 31^\circ$ and $\alpha'_{B,0.48} = 18^\circ$, respectively. The same angles were measured directly from the flow maps of figure 3.23(a, b) and this yielded $\alpha_{B,0.8} = 30^\circ$ and $\alpha_{B,0.48} = 18^\circ$, which are in good agreement with the predicted values. The same analysis has been performed using the inclinations of the structures indicated by \mathcal{A} , \mathcal{C} and \mathcal{D} in figure 3.20(d) and the agreement between measured and predicted values of α for these cases was as good as in the case for \mathcal{B} . The results are presented in table 3.1.

Looking again at the evolution of the flow in figure 3.20, it is seen that the width of the shear layers and their mutual distances (hence the wavelength of the inertial waves) decrease, in relation to the diminishing sizes of the structures in the transient flow above the orifice. Since the frequencies of the waves depend only on the inclination angle and not on the wavelength, the wave system is dispersive with the long waves travelling fastest. The group velocity of the inertial waves is directed perpendicular to the wave propagation, ‘radiating’ energy along the oblique flow layers.

There is a nice analogy between the characteristic inertial wave pattern observed in a rotating fluid and internal wave patterns in a stratified fluid, although the latter are governed by buoyancy forces. In particular, figure 3.20 shows that as time proceeds the apex angle of the structures tends to diminish in the same way as observed by Stevenson (1973) for transient internal waves in a stratified fluid. In his laboratory experiments, Stevenson (1973) demonstrated that the angle of the internal waves created by an oscillating cylinder tends to decrease down to zero when the forcing stops.

Finally, the limit of very high rotation rates is briefly examined by performing a simulation at $Ro = 0.1$. In this case the predicted angle for the ‘ \mathcal{B} ’ type structure is only 4° , indicating that the shear layers tend to be almost axially aligned. This is in fact a demonstration of the Taylor-Proudman theorem that states that in a flow in slow quasi-steady motion relative to a rotating fluid the velocity field does not vary along the direction of the rotation axis. This theorem can be simply derived by taking the curl of equation (3.12) in the limit $Ro \rightarrow 0$, neglecting variations in time ($\partial/\partial t = 0$) and viscous effects, yielding $\partial \mathbf{u}/\partial z = 0$. This means that fluid particles flow in columns oriented along the rotation axis. Evidence of the appearance

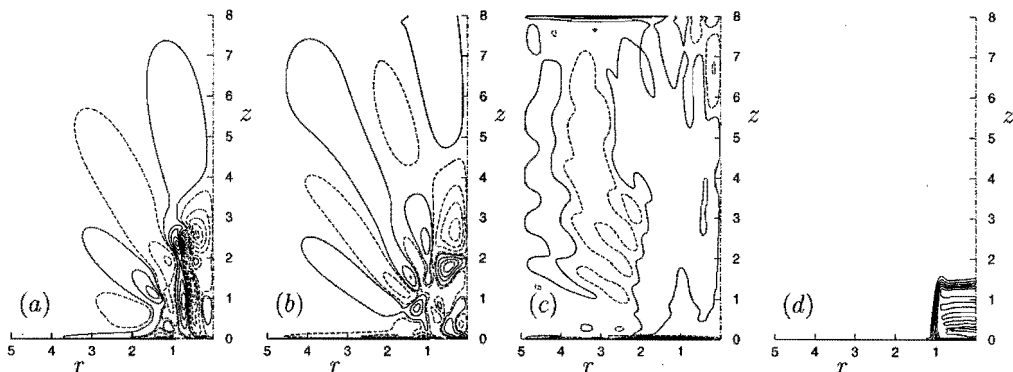


FIGURE 3.23: Contour plots of azimuthal vorticity at $t = 8$, obtained from a numerical simulation with $Re = 480$ and different Ro : (a) $Ro = 0.8$, (b) $Ro = 0.48$, (c) $Ro = 0.1$. (d) Contour plot of passive scalar at $t = 8$ for $Ro = 0.1$. Vorticity increments $\Delta\omega_\phi = \pm 0.5$ (minimum vorticity level at $|\omega_\phi| = 0.1$ to show the oblique shear layers; solid lines for positive values and dashed lines for negative values); passive scalar increments $\Delta C = 0.25$.

of this behaviour in the simulations is obtained from the passive scalar distribution, revealing a columnar structure as seen in figure 3.23(d).

3.4.5 A THREE-DIMENSIONAL SIMULATION

The final point that is discussed is the loss of axial symmetry observed in most of the laboratory experiments (see figure 3.5 and 3.6). In these cases it appeared that the ring developed an asymmetry which led one side of the ring to evolve faster than the other.

One possible explanation is that the vortex ring may have come out of the orifice slightly unbalanced due to asymmetries in the generating device. In the experiments fluid was injected into the vortex ring generator via two taps near the bottom of the generator, already to prevent unbalanced forcing of the fluid injection through the orifice. It has been verified (see figure 2.7 in chapter 2) that the vortex ring generator produces beautiful symmetrical vortex rings in a fluid at rest, without differences in the flow structure on either side of the ring. To exclude that azimuthal perturbations in the initial vortex ring causes the asymmetry in the flow in presence of the background rotation, numerical simulations have been performed in which the vorticity thickness δ (see equation (3.4)) is a function of the azimuthal coordinate, being larger on one side and smaller on the other side of the vortex ring. These simulations are discussed in more detail in Verzicco *et al.* (1996); it suffices to mention that the vorticity differences are diminished by an induced azimuthal flow along the ring core and a uniform-core vortex ring is quickly developed.

Another suggestion about the occurrence of the asymmetry was that the vortex ring was initially not aligned precisely along the axis of rotation. This seems reasonable since it is difficult in the experimental setup to fix the orientation of the vortex ring generator within an accuracy of about $2^\circ - 3^\circ$ and a small deviation yields an angle between the direction \mathbf{j} of propagation of the vortex ring and the orientation \mathbf{k} of the rotation vector. Suppose that the rotation vector forms an angle ε with the axial direction and that the vector lies in the semi-plane $\phi = \phi_0$ (without loss of generality $\phi_0 = 0$ is assumed). Let Ω_r , Ω_ϕ and Ω_z be the components of the rotation vector in the radial, azimuthal and axial direction, respectively,

given by: $\Omega_r = \Omega \cos \phi \sin \varepsilon$, $\Omega_\phi = \Omega \sin \phi \sin \varepsilon$ and $\Omega_z = \Omega \cos \varepsilon$, with Ω the angular velocity of the rotation. If ε is small these relations are simplified to:

$$\Omega_r \simeq \varepsilon \Omega \cos \phi, \quad \Omega_\phi \simeq \varepsilon \Omega \sin \phi \quad \text{and} \quad \Omega_z \simeq \Omega, \quad (3.15)$$

and this means that the effect of the axial rotation remains essentially unchanged while an asymmetric forcing is introduced, pointing for all sections of the vortex ring mainly in the direction $\mathbf{j} \times \mathbf{k}$ (the Coriolis force is proportional to $\mathbf{u} \times \boldsymbol{\Omega}$). Consider for example the flow in the planes $\phi = 0$ and $\phi = \pi$ where $\Omega_\phi = 0$ and $\Omega_r = +\Omega \sin \varepsilon$ and $\Omega_r = -\Omega \sin \varepsilon$, respectively. Only the axial flow component u_z in these semi-planes is affected by the Coriolis force related to the component Ω_r , resulting in an equal but opposite azimuthal** forcing on either side of the ring, and an asymmetry is most likely to occur. Similar examination of the directions of the Coriolis forces (related to the components Ω_r and Ω_ϕ) on the various sections of the initial vortex ring reveals that the core section in the plane $\phi = \pi/2$ is squeezed, the core section in the plane $\phi = -\pi/2$ widens and the core sizes in the intermediate sections change gradually between these extrema. These core deformations become more important if the angle ε increases and in the next chapter the case $\varepsilon = 90^\circ$ will be investigated.

Direct inspection of the flow by three-dimensional numerical simulations has shown that for small ε asymmetries indeed appear (see figure 3.24). Consistent with the flow visualizations, a small initial misalignment of only 3° has a clearly visible effect on the evolution of the flow.

3.5 Conclusions

The main aim of the present chapter has been to study the effects induced by a background rotation on the dynamics of a vortex ring. Since this vortex structure is relatively simple and symmetric its development can be pursued in detail. The analysis has been performed by laboratory experiments and numerical simulations using the two methodologies as complementary tools.

Results have shown that for low rotation rates ($Ro > 2$) the vortex ring is slowed down by the rotation and an oppositely-signed structure forms in front of the vortex ring. For low Reynolds numbers ($Re \simeq 500$) these structures diffuse one into another and the peak vorticity in the ring undergoes a rapid decrease. For higher Reynolds numbers (until $Re \simeq 1500$) part of the diffusion is prevented and the primary ring turns out to be strong enough to elongate the oppositely-signed vorticity in a thin layer. This layer, being unstable, rolls-up to form a secondary vortex ring that propagates in a direction opposite to the primary ring.

Some of the phenomena described for this rotation regime have been observed also by Virk *et al.* (1994) in vortex rings without background rotation but with an assigned swirling flow. This is not surprising, because in their simulations the swirl was not confined to the core of the ring, but it extended to a larger flow region. The same arguments applied to understand the results presented here could therefore be used in the interpretation of their simulations.

For higher rotation rates the scenario changes. In particular, as the thin vorticity layer released from the orifice-edge starts to roll-up, intense oppositely-signed vorticity is generated due to the background rotation. This implies that strong cross-cancellation acts since the beginning, thus preventing the vortex ring to form. At the same time oblique shear layers of large axial extension are generated and they have been identified as features of inertial waves.

**The azimuthal directions in the semi-planes $\phi = 0$ and $\phi = \pi$ are defined in opposite sense!

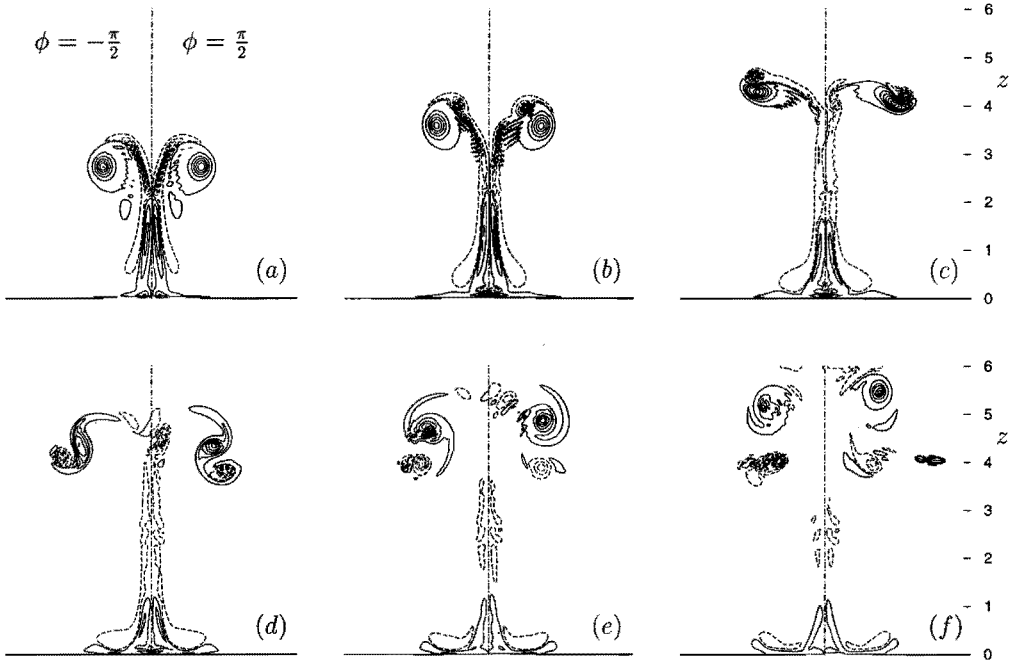


FIGURE 3.24: Contour plots of azimuthal vorticity, obtained from a three-dimensional simulation with $Ro = 6$ and $Re = 1500$: (a) $t = 6$, (b) $t = 8$, (c) $t = 10$, (d) $t = 12$, (e) $t = 14$ and (f) $t = 16$. The initial angle of inclination between the direction of propagation and the rotation vector is 3° ; the rotation vector is oriented in the semi-plane $\phi = 0$ (i.e. pointing slightly towards the reader). The dashed-dotted lines show the direction orthogonal to the orifice. Vorticity increments $\Delta\omega_\phi = \pm 2.0$, minimum level at $|\omega_\phi| = 0.5$ (solid lines for positive values and dashed lines for negative values).

Due to the transient nature of the forcing many frequencies are excited and this usually results in a band of angles γ between the wave patterns and the axis of symmetry. Besides, the angle γ decreased in time; but for a fixed time the dependence of γ on the Rossby number was well described by the relation $\gamma = \sin^{-1}(Rof)$, f being the excitation frequency.

The limit $Ro \approx 2$ between high and low rotation regime has been fixed in this study by observation that for this Rossby number the peak azimuthal vorticity was no longer located in the core of the ring for the whole evolution. It is stressed that this criterion is subjective and has been used mostly for ease of the presentation of the results. In the experiments it has been observed that there is a range of Rossby numbers where different phenomena belonging to both regimes coexist and the flow dynamics is a combination of both.

Finally, in some laboratory experiments the flow field shows some asymmetries in the shedding process of the secondary vortex structure, resulting in a fully three-dimensional flow configuration. Three-dimensional numerical simulations have shown that the reason for this loss of symmetry was a small misalignment between the axis of rotation and the initial direction of propagation of the vortex ring. Even an inclination of a few degrees was sufficient to develop the observed asymmetries.

4

VORTEX RING MOVING PERPENDICULAR TO THE AXIS OF A ROTATING FLUID

This chapter is an adapted version of the paper 'Dynamics of a vortex ring moving perpendicular to a background rotation' by A.H.M. Eisenga, R. Verzicco & G.J.F. van Heijst, submitted to J. Fluid Mech. (1996).

4.1 Introduction

In flows of practical interest that are subjected to a background rotation, the angle between the local relative vorticity and the system rotation covers a wide range of orientations. These flows, consisting of many interacting vortex structures, are generally quite complex and their study is very difficult. However, if the investigation is restricted to study only a single vortex structure with an initially symmetric structure, a profound analysis of the flow dynamics is attainable. Therefore, the motion of a single vortex ring is considered, oriented in a direction *orthogonal* to the rotation vector, hence in a horizontal level. Although this vortex has a 'simple' and well-known structure, all possible orientations between relative vorticity and system rotation are incorporated. A detailed study of this problem can provide substantial insight in the dynamics of complex vortical flows in rotating environments.

Already in the twenties, in one of his celebrated papers Taylor (1921) describes the results of an experiment in which a vortex ring is created in a rotating fluid. The direction of propagation of the vortex ring was perpendicular to the axis of rotation of the fluid. He observed that the vortex ring moved in a curved path relative to the rotating fluid, its path being deflected in clockwise direction if the fluid was rotating anti-clockwise. He performed this experiment in order to demonstrate the difference between two- and three-dimensional motion in a rotating fluid. Among this, he also conducted experiments in which a cylinder and a sphere (with the same density as the fluid) were drawn horizontally through the rotating fluid. As predicted theoretically in previous papers (Proudman 1916; Taylor 1917) the two-dimensional motion generated by the cylinder was not affected by the rotation of the system, and the cylinder moved in a straight line relative to the rotating fluid. For the three-dimensional motion generated by the sphere it was predicted that a net Coriolis force acts perpendicular to the direction of motion, causing the followed path to deviate from a straight line. In analogy to the sphere, the vortex ring was then expected to move along a circular path relative to the rotating system. In the experiments of Taylor, however, no attention was paid to the evolution of the structure of the vortex ring.

It is well-known that the background rotation of the system serves as a source for the production of relative vorticity. In the previous chapter on the motion of a vortex ring along the axis of rotation it was shown that the flow generated by the vortex ring induces relative vorticity that in turn dominates the successive evolution of the flow field. In the case considered in the present chapter, again, due to the rotation a secondary flow is induced by the vortex ring. The structure of the secondary flow is in this case completely different, but the generation and evolution of the flow field can still be studied in detail, because of the symmetric geometry of the vortex ring. Using results of both laboratory experiments and numerical simulations it will be shown that the background vorticity influences the evolution of the vortex ring in a surprising way.

The structure of this chapter is as follows: in the next sections the experimental set-up and the numerical code are briefly described. Then, the combined results of laboratory experiments and numerical simulations will be analysed and discussed in order to provide more physical insight in the observed flow phenomena. Special attention is paid to the structure of the flow in the horizontal cross-sectional plane through the vortex ring centre, which serves as a symmetry plane of the flow. A complete picture of the evolution of the three-dimensional structure of the vortex is obtained from numerical simulations solely. Closing remarks are given in section 4.5. An appendix is added at the end in which the main results of some classical papers (Proudman 1916; Taylor 1917; 1923) are briefly summarized, since these are necessary for the discussion of the curved ring trajectory.

4.2 Experimental set-up

The vortex ring generator used in the present laboratory experiments has already been used in the experiments in the previous chapters and it is described in detail in chapter 2. Only the adjustments to the experimental set-up are mentioned here that were necessary to perform the experiments described in this chapter.

The vortex ring generator, consisting of a closed cylindrical box with a sharp-edged circular orifice on top, could be rotated around a horizontal axis in a fork that was fixed to a stand. In the study in chapter 3 the generator was oriented such that vortex rings were fired vertically upwards. In the experiments presented here the generator was rotated over 90° and the created vortex rings propagated in a horizontal direction. The vortex ring generator was positioned near the centre of a large experimental tank of horizontal dimensions 150×100 cm and 30 cm height (see figure 4.1). The tank was placed on a rotating table, whose angular velocity could be varied between $\Omega = 0.06 \text{ s}^{-1}$ and $\Omega = 1.0 \text{ s}^{-1}$. The centreline of the orifice in the generator was directed towards the centre of the rotating table.

A horizontal light sheet was used to illuminate the cross-section of the vortex ring in a plane through the centre of the orifice. This light sheet was created by a slide projector provided with a black slide with a narrow slit. Two adjacent slide projectors, put on one side of the tank on a platform fixed to the rotating table, created a thin horizontal light sheet spanning a large horizontal area. All experiments were recorded from above by a video camera mounted on a frame attached to the rotating table.

Fluorescein-dye was used to visualize the flow field. The fluid in the vortex ring generator was slightly dyed and the tank was filled with clear tap water to a level of 20 cm, the distance from the orifice centre to the free surface level and the bottom of the tank being 10 cm. To avoid mixing during filling of the tank, the orifice was temporarily closed by a metal plate.

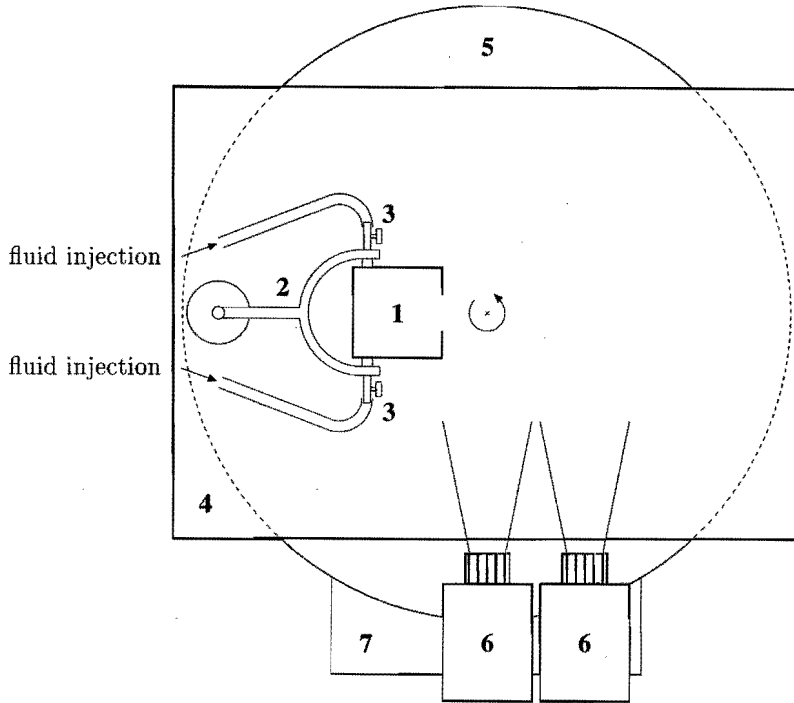


FIGURE 4.1: Schematic top view of experimental set-up. Vortex ring generator 1 is turned in the fork 2 so that vortex rings are fired in horizontal direction. Tubes for fluid injection are connected to the generator by two watertaps 3. The set-up is placed in a tank 4, filled with water, on top of a rotating table 5. The sense of rotation of the table is denoted by an arrow. Two slide projectors 6, put on one side of the tank on a platform 7 fixed to the table, are used to produce a wide light sheet to illuminate the flow in a plane through the vortex ring centre. A video camera (not shown) mounted above the table records a top view of the experiment relative to the rotating system.

Before the experiments were started the water in the tank had to spin-up for about one hour in order to achieve a state of uniform rotation and then the metal plate could be pushed aside carefully.

A vortex ring was created by pushing a finite amount of fluid through the orifice, at the sharp edge of which a vortex sheet rolled-up into a vortex ring. The injection of fluid was controlled by a stepmotor-driven traversing system, pushing a set-up of 6 syringes simultaneously. From previous studies (see chapter 2) it is known that, for an orifice with diameter $D_o = 4$ cm, a fluid injection with slug length $L_o = 2.4$ cm and mean injection velocity $U_o = 2.4$ cm/s at the generator orifice produces a steady laminar vortex ring in a fluid at rest. The characteristics of such a vortex ring have been discussed extensively in chapter 2 and the main ring parameters are given in table 2.1. The same fluid injection parameters were used in the present experiments.

4.3 Numerical set-up

4.3.1 EQUATIONS OF MOTION AND NUMERICAL SCHEME

The flow in a rotating fluid is commonly described relative to axes rotating steadily with the fluid. In a frame rotating with angular velocity $\Omega = \Omega \mathbf{k}$ (with \mathbf{k} the unit vector directed along the axis of rotation) the relative velocity \mathbf{u} of an incompressible viscous fluid satisfies the Navier-Stokes and continuity equations, written as:

$$\begin{aligned} \frac{D\mathbf{u}}{Dt} \equiv \frac{\partial \mathbf{u}}{\partial t} + (\mathbf{u} \cdot \nabla)\mathbf{u} &= -\nabla p - \frac{1}{Ro} \mathbf{k} \times \mathbf{u} + \frac{1}{Re} \nabla^2 \mathbf{u}, \\ \nabla \cdot \mathbf{u} &= 0, \end{aligned} \quad (4.1)$$

with $D/Dt \equiv \partial/\partial t + \mathbf{u} \cdot \nabla$ the material derivative operator. The pressure p is the reduced pressure, which includes the potential of the centrifugal force. These equations have been written in dimensionless terms using the toroidal radius \mathcal{R} and circulation Γ of the initial vortex ring. In terms of these scales the Rossby number is defined as $Ro = \Gamma/2\Omega\mathcal{R}^2$ and the Reynolds number as $Re = \Gamma/\nu$, with ν the kinematic viscosity of the fluid.

In flow visualization experiments passive tracers (e.g. fluorescein dye) are used to infer typical features in the flow development and to track the position of the vortex structure in time. In order to obtain a closer comparison between the results of these flow visualization experiments and numerical simulations, the evolution of the concentration C of such a passively advected tracer is simulated, according to the equation:

$$\frac{DC}{Dt} = \frac{1}{ReSc} \nabla^2 C. \quad (4.2)$$

The Schmidt number Sc is defined as the ratio between the kinematic viscosity ν of the fluid and the diffusivity κ of the tracer.

Equations (4.1) and (4.2) have been written in a Cartesian coordinate system and discretized by centred finite-difference schemes, second-order accurate in space and in time. In the limit of $\nu \rightarrow 0$ the energy is conserved by equation (4.1) and the numerical scheme is such that this holds in the discretized equations. The discretization is uniform in all spatial directions. The numerical method is similar to that described by Orlandi (1990) which has the following features: the discretized equations are solved by a fractional-step method (Kim & Moin 1985) with the viscous terms computed implicitly and the convective terms explicitly. The large sparse matrix resulting from the implicit terms is inverted by an approximate factorization technique. At each time step the momentum equations are provisionally advanced using the pressure at the previous time step, giving an intermediate non-solenoidal velocity field. A scalar quantity Φ is then introduced to project the non-solenoidal field onto a solenoidal one. The large band matrix associated with the elliptic equation for Φ is reduced to a tridiagonal matrix using trigonometric expansions in the periodic directions. The pressure at the new time is also computed from the scalar Φ . The advancement in time of the equations is obtained by a hybrid third-order Runge-Kutta scheme which, owing to its large stability limit ($CFL \leq \sqrt{3}$), allows CPU-time savings.

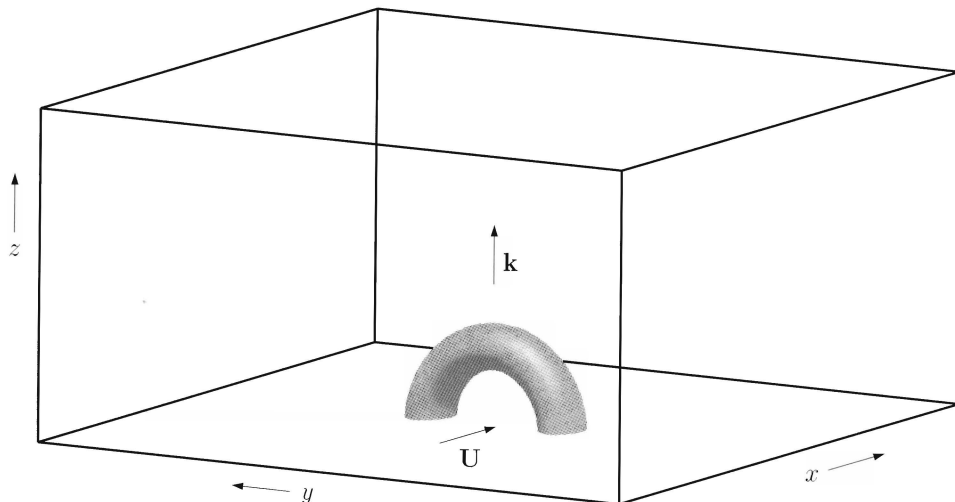


FIGURE 4.2: Perspective view of the computational box and the initial configuration of the vortex ring, which propagation direction \mathbf{U} is oriented orthogonal to the unit vector \mathbf{k} of the rotation. The free-slip boundary conditions at the bottom surface imply the presence of an image vortex below the computational box that completes the vortex ring.

4.3.2 INITIAL CONFIGURATION AND CONVERGENCE CHECKS

The initial flow configuration is shown in figure 4.2 and consists of a vortex ring located at the centre of a computational box. The axial centreline of the vortex ring is oriented parallel to the x -axis and the unit vector \mathbf{k} , denoting the rotation axis, is directed along the z -axis of a Cartesian coordinate system, the vortex ring propagating with velocity vector \mathbf{U} . Laboratory experiments have shown that, even if the rotation is present, the flow field remains symmetric relative to a horizontal plane through the centreline of the vortex ring. To save computational effort it is therefore sufficient to simulate only one half of the vortex ring, the symmetry plane $z = 0$ being the bottom surface of the computational domain. The proper boundary conditions at this side, i.e. vanishing normal velocity component and zero shear stresses (free-slip wall), then imply the presence of an image vortex that completes the vortex ring. Also at the top surface free-slip conditions have been imposed, while periodicity has been assumed at the lateral surfaces.

The domain has been chosen sufficiently large to exclude artificial perturbations of the flow introduced by the periodicity and finiteness of the domain. This is checked by simulations with different box sizes. Furthermore, the number of grid points employed has been submitted to a grid refinement check. For these checks the evolution of the peak values of the vorticity of the flow are examined, the positive and negative peaks of the axial vorticity component ω_z in the plane $z = 0$ can be shown to be representative of the vorticity maxima of the flow. Figure 4.3a shows the time evolution of the positive and negative peak values of ω_z for two simulations with a fine grid $97 \times 97 \times 49$ and a coarse grid $65 \times 65 \times 33$, respectively, in a box with fixed dimensions $8 \times 8 \times 4$ in the x -, y - and z -directions. This check confirms that the finer grid is sufficient to describe the vortex ring evolution. Figure 4.3b shows the results of simulations with three different box sizes and the profiles of ω_z display only a minor dependence on the

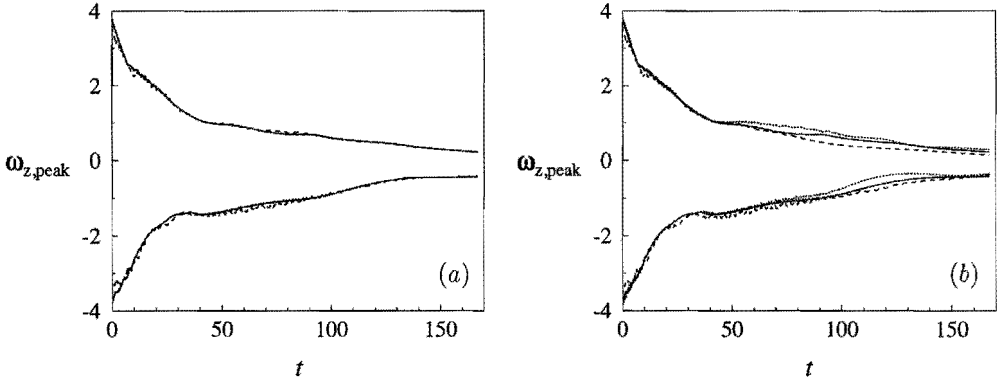


FIGURE 4.3: Time evolution of the positive and negative peak vorticities ω_z in the horizontal symmetry plane $z = 0$ of the flow, obtained from numerical simulations with $Ro = 23$ and $Re = 900$. (a) Grid refinement check with fixed box $8 \times 8 \times 4$: fine grid $97 \times 97 \times 49$ (solid lines) and coarse grid $65 \times 65 \times 33$ (dashed lines). (b) Domain dimensions check: small box $6 \times 6 \times 3$ (dotted lines, grid $65 \times 65 \times 33$), intermediate box $8 \times 8 \times 4$ (solid lines, grid $97 \times 97 \times 49$) and large box $12 \times 12 \times 6$ (dashed lines, grid $97 \times 97 \times 49$).

dimensions of the box. In conclusion, a box with intermediate dimensions $8 \times 8 \times 4$ with a fine grid $97 \times 97 \times 49$ has been employed for the simulations presented in this chapter. Also for the time step size a refinement check was performed and it was mostly taken $\Delta t = 0.1$, according to a CFL number $\leq \sqrt{3}$ as imposed by the stability limit of the time integration scheme.

In this numerical code the initial structure of the vortex ring has to be assigned explicitly. In the previous chapter a different numerical code written in cylindrical coordinates has been used in which the generation and evolution of a vortex ring was simulated as produced experimentally by the ejection of a finite amount of fluid from a circular orifice. In that chapter the initial parameters for the numerical simulations have been adjusted so that they mimic the laboratory experiments very well. Taking advantage that both the experimental set-up and the ring parameters were the same as in the present study, the initial vortex ring obtained in that previous study will be used as initial configuration for the present simulations. More precisely, the vortex structure is used that has been formed at $t = 4$ in a simulation without background rotation performed with the code in cylindrical coordinates. The initial three-dimensional fields necessary to start the numerical simulations with the present code in Cartesian coordinates are then obtained by standard interpolation procedures from the axisymmetric flow field of this initial vortex structure.

4.3.3 SCALING OF THE EXPERIMENT

The scaling of the experiment to the numerical simulation was checked by experiments without background rotation, performed with the present experimental set-up. In these experiments the injection parameters $L_o = 2.4$ cm and $U_o = 2.4$ cm/s were used that lead to the formation of a steadily propagating laminar vortex ring from a 4 cm orifice. Video images of dye experiments taken at successive time steps were used to measure the evolution of the ring radius R and the propagation velocity U in time. The same ring parameters are obtained from a numerical simulation without background rotation, started with the vortex ring described in the previous

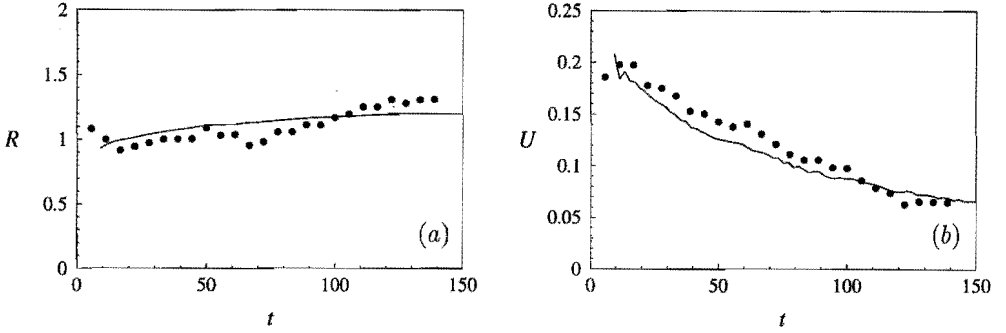


FIGURE 4.4: Evolution of (a) the ring radius R and (b) the velocity of propagation U of a vortex ring without background rotation ($Re = 900$). Experimental data are denoted by markers and results of the numerical simulation by solid lines. Experimental parameters: $D_o = 4.0$ cm, $L_o = 2.4$ cm and $U_o = 2.4$ cm/s. The numerical simulation is started with a vortex ring that has been formed in a preliminary simulation with a different numerical code in a time $t' = 4$. According to the present time scaling, this corresponds to a time $t = 9.2$ during which the vortex ring already has evolved before the actual simulation is started. In the figures the data from the simulation are therefore plotted from $t = 9.2$.

section. The results of both the experiment and the simulation are shown in figure 4.4. In this graph the experimental values of the ring radius and the velocity of propagation have been scaled by a length scale $\mathcal{R} = 1.8$ cm (denoting, approximately, the dimensional value of the initial ring radius) and velocity scale $\mathcal{U} = \Gamma/\mathcal{R} = 5.0$ cm/s, respectively, from which $\Gamma = 9.0$ cm²/s follows. Accordingly, the time axis is scaled by $\mathcal{T} = \mathcal{R}^2/\Gamma = 0.36$ s. These scales are then used to determine the Reynolds number $Re = \Gamma/\nu = 900$ and the Rossby number $Ro(\Omega) = \Gamma/2\Omega\mathcal{R}^2 = 1.4/\Omega$, that are specific parameters for the numerical simulations. Among all parameters only the rotation rate Ω was varied in the laboratory experiments.

While for Re and Ro it was possible to obtain a proper correspondence between simulation and experiments, the same can not be done for the Schmidt number. In fact, the small diffusivity of tracers in liquids yields $Sc \approx \mathcal{O}(500 - 1000)$ which, due to resolution problems, is too large for three-dimensional numerical simulations. Throughout this study a value $Sc = 4$ has been used which, even though considerably lower than the experimental value, accounts for the different diffusivities of vorticity and scalar. This is important when deducing aspects of vorticity dynamics from flow visualizations, since small flow scales observed from the tracer might not exist in terms of vorticity.

It should be stressed that a good agreement between experiments and numerical simulations in absence of background rotation does not imply the same agreement in case the rotation is present. In the latter case, the flow field is affected at any time by the system rotation, also during the injection of fluid and the formation of the vortex ring. This might lead to an initial configuration different from that of the numerical simulations, where the rotation is imposed over an already existing vortex ring formed in absence of rotation. However, in the laboratory experiments only relatively low rotation rates have been used for which it was observed that in the initial stage a vortex ring was formed. Furthermore, comparisons between vortex trajectories and vorticity dynamics of the ring core will be presented showing that the differences in the initial structures are of minor importance for the subsequent flow evolution. This implies that the initial conditions mentioned above can be used also in the rotating cases.

4.4 Results

In order to get a qualitative picture of the flow field images of a flow visualization experiment are presented first. Using the arguments of Proudman (1916) and a simple inviscid model for the motion of a sphere in a rotating fluid, the curved trajectory of the vortex ring in the rotating system can be explained. Flow visualizations are also used as guidelines for the subsequent analysis of the flow by direct numerical simulations, which give a complete three-dimensional view of the structure. Advantage is taken from the symmetry of the flow and important insight in the flow dynamics is gained by analysing the evolution of the flow in the horizontal plane of symmetry.

4.4.1 FLOW VISUALIZATIONS

The sequence of video images presented in figure 4.5 shows the propagation and evolution of the vortex ring. Only a central cross-section of the vortex ring in a horizontal plane normal to the axis of rotation was illuminated by the light sheet. The images were recorded with a video camera fixed on the rotating table, showing the flow field relative to the rotating frame. The table was rotating in anti-clockwise direction with a relatively low angular velocity $\Omega = 0.06 \text{ s}^{-1}$, yielding a Rossby number $Ro = 23$.

From the first image (figure 4.5*a*) it is seen that after injection of the fluid an axisymmetric vortex ring is created. In case of no rotation of the system this vortex ring would propagate along a straight path. However, from the succeeding images of figure 4.5 it is clearly seen that in the present case the path of the vortex ring is curved, the ring being deflected in clockwise direction. Although the vortex ring remains a coherent structure, its shape changes in time and in the cross-sectional views (figures 4.5*b-f*) a gradual change in the size of the dyed cores is observed. In particular, the section of the core part on the inner side of the curved path (henceforth denoted as the 'inner core part') shrinks, while the section of the core part on the outer side (the 'outer core part') expands in time. In oblique views of the flow structure (not shown here) it has been observed that the vortex structure as a whole remains approximately circular during the main part of the motion.

It has to be noted that a small filament of dye crosses along the front of the vortex ring from the outer core part to the inner core part, as can be observed in figure 4.5(*d*). In the same figure a second filament of dye is seen to be shed between the two vortex core parts. This filament is different from the trail behind the vortex ring in figures 4.5(*a*) and 4.5(*b*), which is just fluid not entrained in the vortex ring during the ring's formation. The creation of both filaments in figure 4.5(*d*) will be discussed in more detail in subsections 4.4.3 and 4.4.4, where the results of numerical simulations are examined.

At a later stage in the evolution the vortex ring is slightly twisted (figure 4.5*e*) and a horizontal cross-flow of dye from the outer to the inner core part occurs (figure 4.5*f*). This cross-flow is limited to a narrow band of only a few millimeters thick, located just in the light sheet as observed in an oblique view. After some time, a slowly evolving blob of dyed fluid without any definite structure remains.

Similar features of the ring dynamics have been observed if the Rossby number is decreased, experiments have been performed until $Ro \simeq 8$. Proportional to the rotation rate the curvature of the ring trajectory and the respective squeezing and widening of the core sections are enhanced. The curved trajectory of the vortex ring will be discussed in the next subsection and the gradual change of the core sections in subsection 4.4.3.

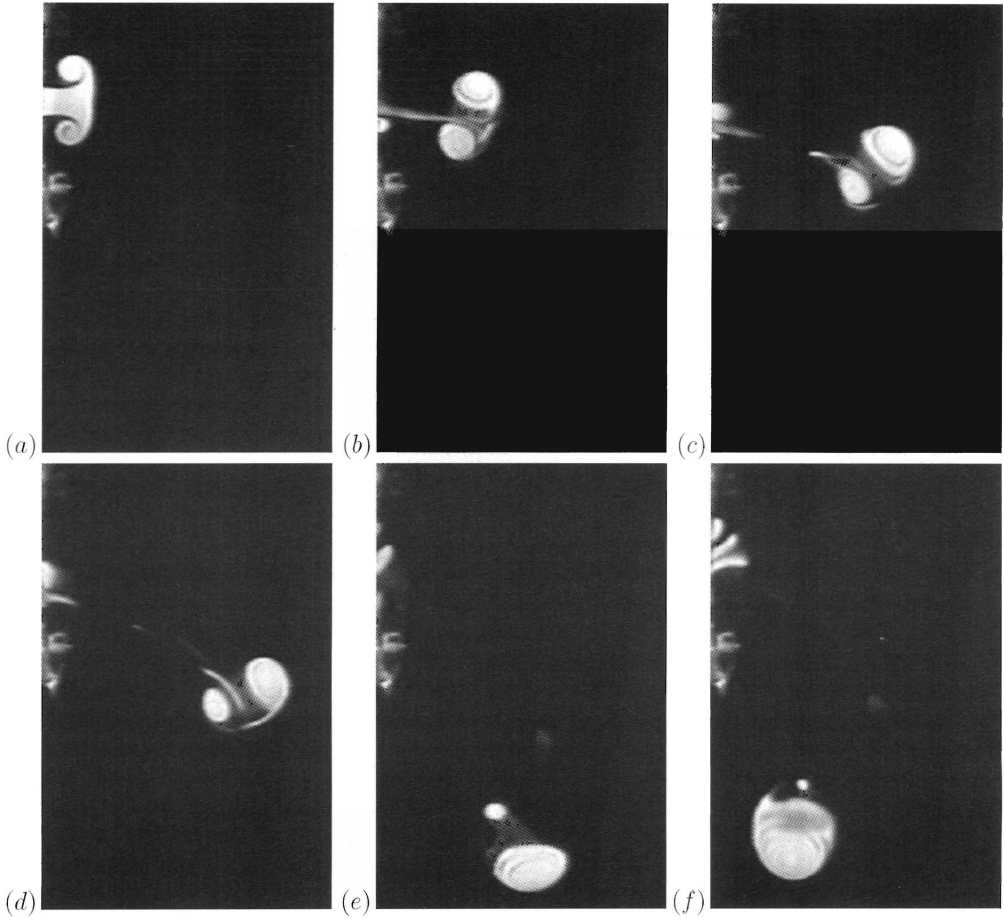


FIGURE 4.5: Cross-sectional (top) view of the evolution of a vortex ring propagating in a plane perpendicular to the rotation axis along a curved path in clockwise direction, i.e. opposite to the sense of rotation of the system ($Ro = 23$ and $Re = 900$): (a) $t = 6$, (b) $t = 17$, (c) $t = 33$, (d) $t = 50$, (e) $t = 117$ and (f) $t = 150$ after start of the fluid injection. Experimental parameters: $D_o = 4.0$ cm, $L_o = 2.4$ cm, $U_o = 2.4$ cm/s and $\Omega = 0.06$ s $^{-1}$.

4.4.2 CURVED TRAJECTORY OF VORTEX RING

To determine the trajectory of the vortex ring the positions of the centres of the visualized core parts have been measured from video images at successive times and these data are plotted in figure 4.6(a). At a few positions in its trajectory the plane of the vortex ring is denoted by dashed lines connecting the corresponding core centres and the direction of propagation of the vortex ring is indicated by arrows. The first part of the curved path is approximately circular and the plane of the vortex ring remains perpendicular to its direction of propagation. At later times, however, this motion is not maintained, the curvature of the path increases and the outer core part seems to lag behind. This situation was viewed in figure 4.5e, where the vortex ring was seen to be twisted. Clearly, the direction of propagation of the vortex ring is at this stage no longer perpendicular to the plane of the vortex ring.

The angle ϕ over which the plane of the vortex ring rotates has been measured as a function of time and the results are plotted in figure 4.6(b). The orientation angle decreases steadily, implying that the vortex ring rotates with a constant angular velocity (in clockwise direction), whose value is obtained from the slope of these data points. Using a linear regression, given by the straight line in figure 4.6(b), a value $\Omega_{v,r} = -0.06 \pm 0.002 \text{ s}^{-1}$ is obtained, which is exactly opposite to the angular velocity $\Omega = 0.06 \text{ s}^{-1}$ of the rotating table in this experiment. This means that relative to the inertial frame of the laboratory the vortex ring maintains a fixed orientation in space.

Figure 4.6(c) shows the gradual decay of the propagation velocity of the vortex ring. This velocity is calculated from the distance travelled by the midpoint between the core centres in fixed time intervals. Figure 4.6(c) shows a kink in the velocity decay around $t = 32 \text{ s}$. Around the same moment there is a strong decrease of the inclination angle θ between the plane of the vortex ring and its direction of propagation (see figure 4.6d). It has been observed from dye-visualization experiments that near the end of the motion the vortex ring is slightly twisted (see figure 4.5e). From figure 4.6d it is seen that this twisting of the vortex ring starts around $t = 32 \text{ s}$. After this moment the vortex ring continues its propagation very slowly, but the twisting and deformations of the structure will inevitably lead to the total destruction of the vortex ring.

A series of experiments have been performed in which different rotation rates Ω were used with the injection parameters for the vortex ring kept fixed. If the table rotates faster the evolution of the flow field has the same features as described above, although the curvature of the trajectory is enhanced (see figure 4.7). Experiments were carried out for four different values of the rotation rate, ranging from $\Omega = 0.06 \text{ s}^{-1}$ to $\Omega = 0.17 \text{ s}^{-1}$ ($Ro = 23$ and $Ro = 8.2$, respectively) and the angular velocity $\Omega_{v,r}$ of the rotating vortex ring was measured in each experiment. The results are summarized in table 4.1, showing that for all experiments the angular velocity of the rotation of the vortex ring is just equal but opposite to the angular speed of the rotating table, indicating that the vortex ring maintains a fixed orientation relative to the inertial frame of the laboratory.

This property of the horizontal motion of a vortex ring in a rotating fluid was already observed by Taylor in a similar experiment (Taylor 1917; 1921). However, Taylor did not report measurements on the curved trajectory nor observations about the deformation of the vortex structure. He performed this experiment merely to demonstrate the analogy with the horizontal motion of a solid sphere in a rotating fluid. According to theoretical predictions, it was expected that the motion of three-dimensional objects in a rotating fluid is affected by the background rotation. For the experiments with the sphere Taylor built an experimental

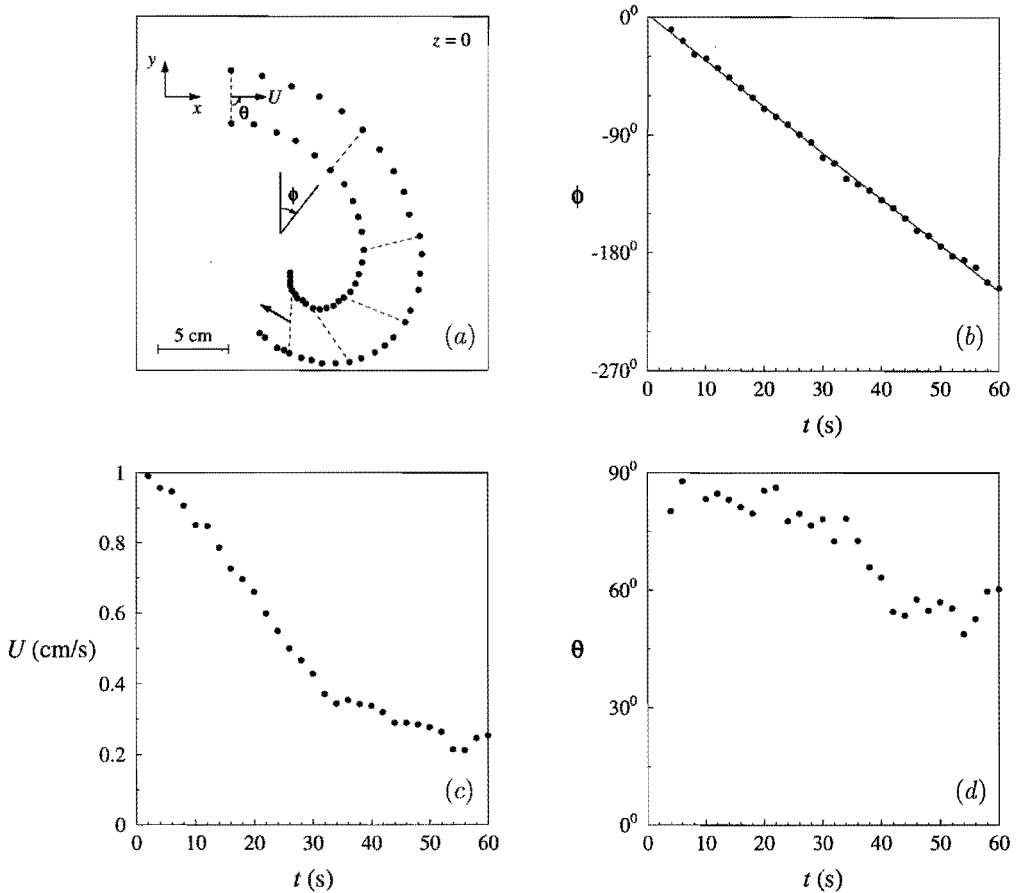


FIGURE 4.6: (a) Trajectory of vortex ring measured from a dye-visualization experiment with $Ro = 23$ and $Re = 900$. Markers denote the positions of the core centres at fixed time intervals $\Delta t = 2$ s (first positions measured at 2 seconds after start of fluid injection); at a few positions, the plane of the vortex ring (dashed lines) and its direction of motion (arrows) are indicated. (b) Rotation ϕ of the plane of the vortex ring in time. (c) Decay of vortex ring propagation velocity U . (d) Variation in time of angle θ between plane of vortex ring and its direction of motion.

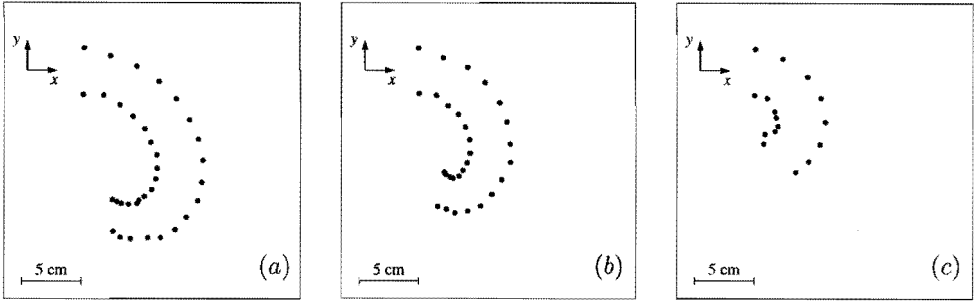


FIGURE 4.7: Ring trajectories measured from laboratory experiments with $Re = 900$ and different rotation rates: (a) $Ro = 16$ ($\Omega = 0.09 \text{ s}^{-1}$), (b) $Ro = 13$ ($\Omega = 0.11 \text{ s}^{-1}$) and (c) $Ro = 8.2$ ($\Omega = 0.17 \text{ s}^{-1}$). In all cases markers are plotted at $\Delta t = 2 \text{ s}$ (cf. figure 4.6a).

Exp.	$\Omega \text{ (s}^{-1}\text{)}$	$\Omega_{v.r.} \text{ (s}^{-1}\text{)}$
1	0.06	-0.06
2	0.09	-0.101
3	0.11	-0.12
4	0.17	-0.17

TABLE 4.1: Rotation rate $\Omega_{v.r.}$ of vortex ring in curved motion for four experiments with different angular velocity Ω of the rotating table (measurement inaccuracy $\Delta\Omega_{v.r.} = \pm 0.002$).

set-up in which a solid sphere could be towed in a horizontal level through a rotating fluid by pulling a wire steadily. A homogeneous sphere was used with the same density as the fluid. The path of the sphere was observed to be deflected to the right relative to a system rotating in anti-clockwise direction.

According to the arguments given by Proudman (1916) (for completeness summarized in appendix A of this chapter) this behaviour can be explained by analysing the balance of the forces acting on the sphere. Consider a homogeneous sphere of mass M with the same uniform density as the fluid. The fluid rotates in anti-clockwise direction with angular velocity Ω . The sphere propagates relative to the rotating system with velocity U in a direction perpendicular to the rotation axis. The balance of all the forces acting on the sphere (Proudman 1916) gives a net force $\frac{3}{2}M\Omega U$ orthogonal to the trajectory of the sphere to the right, deviating the motion of the sphere in clockwise direction.

To determine the acceleration of a sphere in response to an applied force a virtual mass $\frac{1}{2}M$, due to the displacement of the surrounding fluid, has to be added to its real mass M , yielding a total mass $\frac{3}{2}M$ (see Batchelor 1967, p. 453, where this is derived for a sphere moving in a fluid at rest). Supposing that this also holds for the motion of a sphere in a rotating fluid, the acceleration of the sphere due to the force $\frac{3}{2}M\Omega U$ is then given by $a_{\perp} = \Omega U$, in the same direction as the force. This centripetal acceleration causes the sphere to move along a circular path with radius R_c , according to $a_c = U^2/R_c$. Equating the expressions for a_{\perp} and a_c then yields the relation:

$$U = \Omega R_c, \quad (4.3)$$

implying that the angular velocity (U/R_c) of the circular motion of the sphere is just equal to the angular velocity of the rotating table, although the sense of the rotation is opposite.

It should be stressed that this model is derived for the motion of a solid sphere in an ideal rotating fluid, which is quite different from the translating vortex ring in the present experiments. In fact, in the derivation of the model (see appendix A) the pressure force exerted by the surrounding flow on the surface of the sphere* played a crucial role and Proudman (1916) has shown that this force depends on the shape of the solid considered. For example, for a prolate ellipsoid with polar axis parallel to the rotation of the system this pressure force is larger than for a sphere, while for an oblate ellipsoid oriented in the same way it is smaller. A vortex ring transports during its motion a closed blob of fluid, called the vortex ‘atmosphere’ (Thomson 1867*b*; see also chapter 2 of this thesis). The boundary of this vortex ring atmosphere does not have the shape of a simple mathematical object, and the pressure force can not be computed analytically. On the other hand, similar to a sphere (and in contrast to a prolate or an oblate ellipsoid) the vortex ring atmosphere has equal dimensions in vertical and lateral directions orthogonal to the horizontal propagation. Furthermore, the shape of the boundary of the vortex ring atmosphere in the experiments without background rotation (see chapter 2) might reasonably be approximated by a spherical surface. Therefore, the mean pressure force at right angle to the motion of the vortex ring is assumed to be equal to the force exerted on a sphere. The motion of the vortex ring is then given by equation (4.3), which describes a curved path with angular velocity equal but opposite to the rotation rate of the table. Unlike the solid structure of the sphere the shape of the vortex ring atmosphere is subject to deformations resulting from local variations in the pressure force exerted by the surrounding fluid. Deformations of the vortex ring structure affect the evolution of the flow and will be examined in more detail in subsection 4.4.3.

According to equation (4.3) the ring trajectory is circular only if the propagation velocity U is constant. A decaying velocity results in a decreasing value for the radius of curvature R_c , as displayed by the spiral-shaped trajectory in figure 4.6(*a*). The decay of the velocity U results mainly from viscous diffusion of vorticity, but is enhanced by effects of the rotation through the deformation of the vortex structure. Figure 4.8 shows the decrease of the propagation velocity of the vortex ring in experiments with different rotation rates of the fluid. Also the case without background rotation ($Ro = \infty$) is included, for which the velocity decay is solely due to viscous effects. It is seen that with increasing background rotation (decreasing Ro -values) the velocity decay is enhanced and a substantial retardation of the ring speed is imposed by the system rotation. This phenomenon is related to the vorticity dynamics of the vortex structure in the rotating fluid, which will be examined in the next subsection.

4.4.3 VORTICITY DYNAMICS IN HORIZONTAL PLANE OF SYMMETRY

In the previous section the trajectory of the vortex ring was considered and its curvature was explained regardless of the vorticity dynamics. From figure 4.5, however, it is clear that during the evolution significant changes in the vortex structure occur and these are expected to be related to effects of the background rotation. A detailed study of the vorticity dynamics from laboratory experiments is hardly possible because of the three-dimensional nature of the flow. Measurements of the velocity field with the available particle tracking technique (based on tracking the motion of small tracer particles advected with the flow, see chapter 2) were only possible for the flow in the horizontal symmetry plane through the vortex ring centre. However, attempts to measure this velocity field yielded only a global impression of the flow motion in

*The combined Coriolis forces acting on the fluid elements displaced by the moving sphere are responsible for this net pressure force exerted on the sphere’s surface.

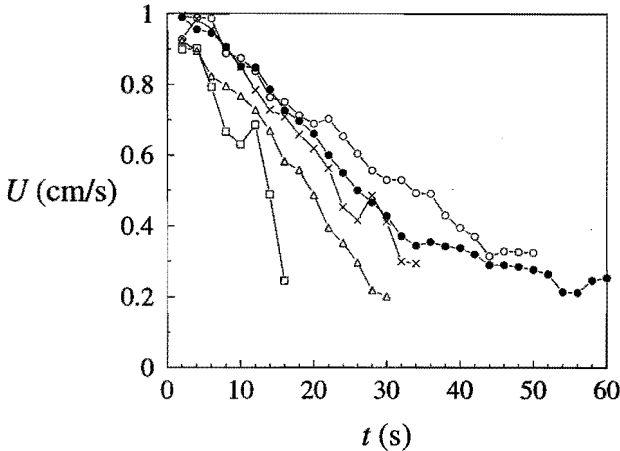


FIGURE 4.8: Decay of propagation velocity of vortex ring as measured from dye-visualization experiments with $Re = 900$ and different rotation rates: $Ro = \infty$ (no background rotation) (open circles), $Ro = 23$ (filled circles), $Ro = 16$ (crosses), $Ro = 13$ (triangles) and $Ro = 8.2$ (squares).

this plane; the derived vorticity fields were too noisy to identify definite vortex structures. In the dye-visualization experiments small-scale structures and tiny filaments were observed, which certainly can not be resolved properly by the particle-tracking facilities. In contrast, by direct numerical simulations the complete three-dimensional structure of the evolving vortex ring can be examined, as well as the flow in any cross-sectional plane. Some aspects of the vorticity dynamics conjectured from dye-visualization experiments have been verified by these numerical simulations and, in addition, a detailed analysis of the three-dimensional vortex structure has been performed.

To check the results of the numerical simulations and the scaling of the experiments, the trajectory of the computed vortex ring has been compared with the ring trajectory obtained from a laboratory experiment with the same parameters. The rotation rate of the system in this laboratory experiment was $\Omega = 0.06 \text{ s}^{-1}$, yielding the values $Ro = 1.4/\Omega = 23$ and $Re = 900$ to be used in the simulations (according to the scaling of the experiment). In numerical simulations the ring trajectories are obtained from the successive positions of the vorticity peaks in the horizontal plane $z = 0$ through the centre of the vortex ring. In figure 4.9 the ring trajectories obtained from the laboratory experiment and corresponding numerical simulation are plotted simultaneously. They show a very nice agreement, taking into account the experimental inaccuracy in the measurement of the positions of the vortex centres from the dyed core patches (see figure 4.5) and the differences between vorticity and passive scalars mentioned in subsection 4.3.3. These results indicate that the numerical simulations mimic the laboratory experiments quite well in presence of the background rotation and they will now be used to examine the effects of the rotation of the system on the vorticity dynamics of the vortex ring.

As a first step in the analysis of the flow dynamics consider the flow in the horizontal cross-sectional plane through the vortex ring centre. This plane is a mirror plane of the motion, since deformations of the vortex ring due to Coriolis forces appear symmetrically in the upper and lower ring half, and this feature already allowed the simulation of only one half of the

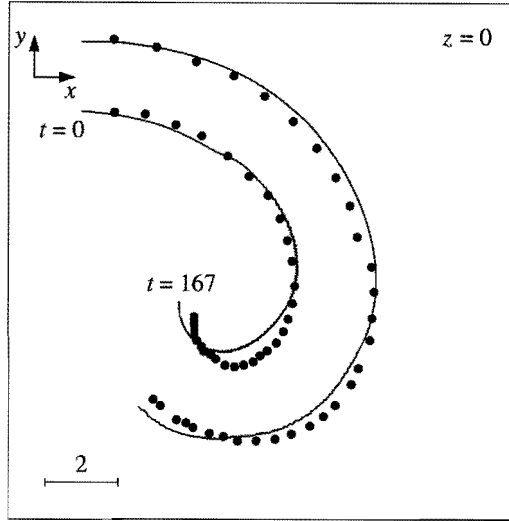


FIGURE 4.9: Ring trajectories measured from the positions of the core centres in the horizontal symmetry plane $z = 0$ ($Ro = 23$ and $Re = 900$). Experimental data are denoted by markers (plotted each $\Delta t = 5.6$) and results of the numerical simulation by solid lines. For experimental parameters: see caption figure 4.5.

vortex ring. As a consequence, the flow in this plane is planar and therefore attractive for a detailed analysis. In addition, the computed structure of the flow in this plane can be compared with the video images from the dye-visualization experiment, in which the flow in the same cross-sectional view was recorded. Relative to the Cartesian coordinates defined in figure 4.2 this planar flow is given by a two-dimensional velocity vector \mathbf{u}_2 in the plane $z = 0$ with components u and v in x - and y -directions, respectively, and the vorticity vector is directed normal to this plane with vertical component:

$$\omega_z = \frac{\partial v}{\partial x} - \frac{\partial u}{\partial y}. \quad (4.4)$$

The two core parts of the vortex ring in this cross-sectional plane have positive and negative vorticity ω_z , respectively.

As already evidenced from the dye-visualizations in figure 4.5, a typical feature of the evolution of the flow in this plane is the variation of the sizes of the core sections, which is opposite for the core parts on the inner and outer side of the curved ring path. It will be shown now that this is a direct consequence of the Coriolis force acting on the flow field of the vortex ring. In the horizontal symmetry plane this force is given by $\mathbf{F}_c = \mathbf{u}_2 \times 2\boldsymbol{\Omega}$ (per unit mass) and is directed orthogonal to the velocity vector \mathbf{u}_2 to the right. Figure 4.10a presents a vector plot of the initial velocity field of the vortex ring in the plane $z = 0$. For each of the velocity vectors a Coriolis force vector is plotted in figure 4.10(b). This Coriolis force vector plot demonstrates the presence of a mean force that deflects the motion of the vortex ring into a curved ring trajectory (in clockwise sense). In addition, the orientations of the individual Coriolis force vectors indicate that the planar flow will be diverged from the outer core part (with anti-clockwise rotation) and converged towards the inner core part. In between the core

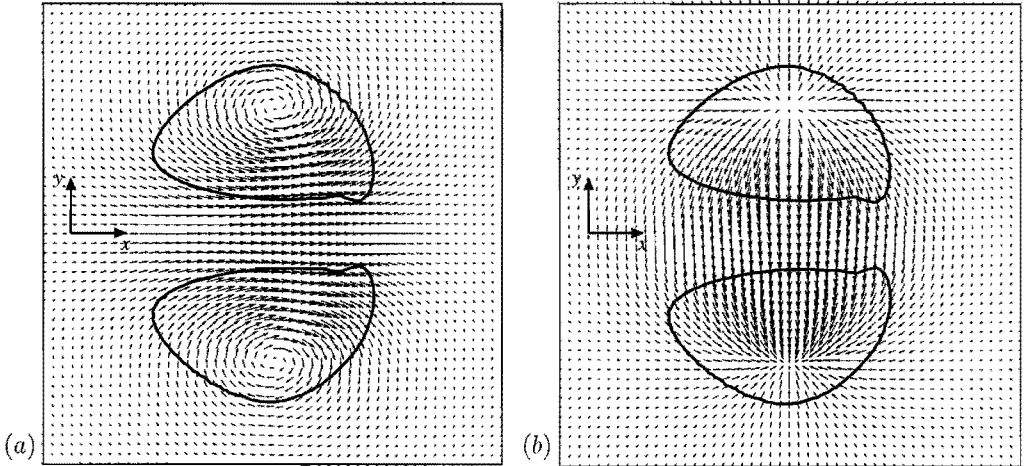


FIGURE 4.10: (a) Velocity vector plot showing the planar flow \mathbf{u}_2 in the horizontal plane of symmetry $z = 0$ of a vortex ring propagating from left to right. Relative to a system in anti-clockwise rotation, with rotation vector pointing along the z -axis, this flow experiences a Coriolis force proportional to $\mathbf{u}_2 \times 2\boldsymbol{\Omega}$. The vector field of this force is plotted in figure (b). The thick solid lines are vorticity contours at $|\omega_z| = 0.1$, which are indicative of the boundaries of the cross-sections of the vortex core.

parts the central axial flow of the vortex ring will be deflected to the right. As a consequence of this opposite forcing the outer core part (with positive ω_z) widens and the inner core part (negative ω_z) is squeezed, as observed previously in the dye-visualizations.

On account of the incompressibility of the fluid, the squeezing of the inner core part of the vortex ring results in a local stretching of the fluid elements in a direction normal to the plane $z = 0$. The opposite happens at the widening outer core part where fluid elements are compressed along the same direction. The evolution of the vertical vorticity component ω_z of the planar flow field is affected by this local stretching and compressing of fluid elements. The relevant vorticity equation is obtained by taking the curl of the Navier-Stokes equation in (4.1), yielding the equation:

$$\frac{D\omega_z}{Dt} = \omega_z \frac{\partial w}{\partial z} + \frac{1}{Ro} \frac{\partial w}{\partial z} + \frac{1}{Re} \nabla^2 \omega_z, \quad (4.5)$$

while the other vorticity components vanish identically in the plane $z = 0$. In this equation w denotes the vertical velocity component that vanishes identically in the plane $z = 0$. The vertical gradient $\partial w / \partial z$ does not vanish and represents the local stretching ($\partial w / \partial z > 0$) and compressing ($\partial w / \partial z < 0$) of fluid elements along the vertical z -axis. According to equation (4.5) the vorticity ω_z changes by self-induced stretching and compression of relative vorticity (first term on right-hand side of (4.5)), induction of relative vorticity from the permanent background vorticity (second term), and viscous diffusion (third term). Since in the present simulation (with $Ro = 23$) the magnitude of the relative vorticity of the vortex ring is much larger than the uniform vorticity Ro^{-1} of the background rotation (both differing initially a factor $\mathcal{O}(70)$), the first term on the right-hand side dominates the second term. Apart from viscous diffusion, the vorticity in the horizontal plane thus changes by self-induced stretching and compression of vortex lines of relative vorticity, which are initially circular lines along the

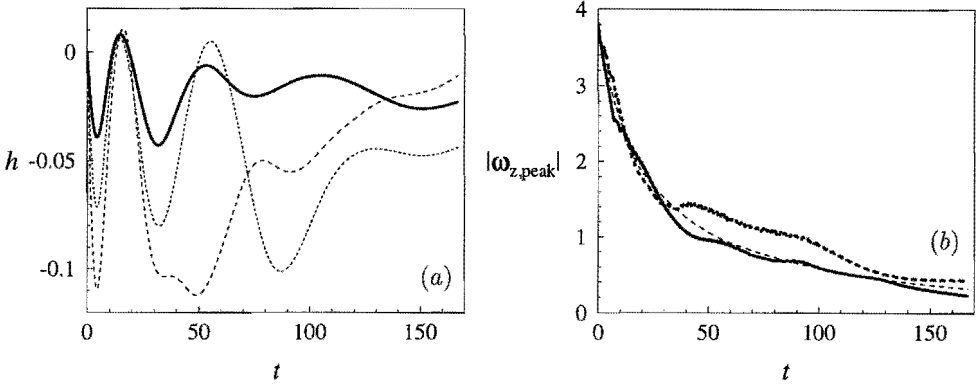


FIGURE 4.11: (a) Time evolution of the helicity h (computed only for the upper ring half) for three different Ro -values ($Re = 900$): $Ro = 23$ (solid line), $Ro = 12.6$ (dotted line) and $Ro = 8.2$ (dashed line). (b) Time evolution of the absolute values $|\omega_{z,peak}|$ of the peak vorticities in both core centres for $Ro = 23$ and $Re = 900$: positive peak (thick solid line) and negative peak (thick dashed line); decay of peak vorticity by viscous diffusion (without background rotation and $Re = 900$) is included for reference (thin dashed line).

toroidal axis of the vortex ring. At the squeezed inner core part vortex lines are vertically stretched and the negative vorticity ω_z in the horizontal plane increases (in absolute sense); at the widened outer core part vortex lines are vertically compressed and the positive vorticity ω_z in the horizontal plane decreases. It is stressed that, although the induction of relative vorticity from the permanent background vorticity is of minor importance in these processes, the rotation of the system affects the vorticity dynamics of the flow indirectly by the opposite forcing of the vertical core parts of the vortex ring owing to Coriolis forces. Note that the induction of relative vorticity ω_z from the background vorticity might become important at later times, when the magnitude of the vorticity in the ring core has been decreased by viscous diffusion, or in simulations with increased background rotation.

The squeezing and widening of the core sections will drive a mass flow from one side of the vortex ring (the squeezed side) towards the other side. An easy way to verify the presence of such a flow is by computing the helicity $h = \int_V \boldsymbol{\omega} \cdot \mathbf{u} dV$ over the volume V of the computational domain. In fact, the mass flow has to follow the toroidal axis of the ring and, since the flow direction is opposite to the vorticity vector, the helicity has to be negative. Of course this is true only because the evolution of only one half of the vortex ring is computed (see figure 4.2); in the complementary ring half the direction of the flow is in the same sense as that of the vorticity and the helicity is positive. The total helicity of the ring is thus zero, as one should expect from the presence of the horizontal symmetry plane. In figure 4.11(a) the time evolution of the helicity of one ring half is shown for several cases with different Ro -values. For all simulations the helicity is on the average indeed negative, although oscillations are exhibited whose amplitudes depend on the Rossby number. These oscillations are due to the opposite squeezing and widening of the vertical ring core parts that, as explained in the previous paragraph, create a differential vorticity along the toroidal axis of the ring and induces, in turn, Kelvin waves (see e.g. Saffman 1992). In figure 4.11(b) the time evolution of the absolute values $|\omega_{z,peak}|$ of the peak vorticities in both core centres are plotted for a

simulation with $Ro = 23$. It shows the alternating differences between the vorticity peak in the outer core part (positive vorticity) and in the inner core part (negative vorticity) before $t \simeq 30$, in agreement to the oscillations in the helicity. The viscous decay of the peak vorticity in a simulation without background rotation is included for reference. After $t = 30$, small oscillations in the peak values are still observable, but now the negative peak exceeds the positive peak in absolute value all the time. Apparently, the stretching of the inner core part is enhanced by a secondary mechanism, but this will be addressed in the next subsection. For the moment, attention is paid to the formation of the Kelvin waves.

The mechanism by which Kelvin waves develop in vortices with variable cross-sections can be summarized as follows: consider a straight vortex with constant circulation Γ , the vorticity $\bar{\omega}$ being uniformly distributed over a circular core with radius a . The tangential velocity u_ϕ in the core is sustained by a radial pressure force directed towards the vortex axis, as expressed in non-dimensional terms by:

$$\frac{\partial p}{\partial r} = \frac{u_\phi^2}{r}, \quad (4.6)$$

according to which the pressure at the core axis is lower than at the core boundary. Suppose this vortex is locally perturbed, hence the core radius is not uniform along the axis of the vortex. On account of the conservation of circulation along the vortex the vorticity in the core is increased in regions where the core is narrow and the vortex rotates locally faster. Following equation (4.6), this enhanced swirling flow induces an additional reduction of the pressure at the core axis. Oppositely, in regions where the core is wide the vorticity is locally reduced and the vortex rotates slower, corresponding to a relatively higher pressure at the axis. This pressure gradient *along* the vortex axis causes an axial flow from wide core sections of high pressure towards narrow core sections of low pressure, thus tending to cancel the local variations of the core size. The restoring effect of this axial pressure force is responsible for the excitation of waves, travelling along the vortex axis.

The propagation of axial waves on rectilinear vortices has first been studied by Thomson (1880) in a linear theory. Recently, in several papers this theory has been extended to more general vortex configurations (see e.g. Moore & Saffman 1972; Lundgren & Ashurst 1989) and the effects of viscosity and non-linear terms have been examined by direct numerical simulations (see e.g. Verzicco *et al.* 1995). For the present study, however, a thorough analysis of these waves is difficult, because of the complexity of the flow and the additional effect of the Coriolis force. It is well-known (Batchelor 1967, p. 555) that also the Coriolis force might act as a restoring force, that tends to eliminate local flow deformations by exciting waves. Therefore, to examine the nature of the observed oscillations in the helicity of the flow a series of simulations have been performed in which the Rossby number was varied. The results of these simulations are plotted in figure 4.11(a). It is clear that initially the period of the oscillations is independent of the Rossby number, which proves that the oscillations are truly Kelvin waves. At later times the oscillation period increases and the increase is not the same for all the cases. As a very simple approach this increase can be explained using the expression for the group velocity $c_g \simeq 0.417 \bar{\omega} a$ of long axisymmetric Kelvin waves on a uniform columnar vortex (see Saffman 1992, p. 231). From this expression it is found that the group velocity of these waves varies proportional to the vorticity in the vortex. As seen in figure 4.11(b), during the evolution of the vortex ring in the rotating environment the vorticity in the ring core decays substantially by diffusion, implying a reduction of the group velocity of the waves and hence an increase in the oscillation period. This is confirmed by figure 4.11(a), although the

increase of the period is not the same for all the cases, since the amount of diffusion depends on the details of the flow structures which change with the Rossby number.

Some details of the complicated vortex dynamics can be reconstructed from the vorticity cross-sections shown in figure 4.12. To better appreciate the deformations occurring in the vortex core, each panel in figure 4.12 is a blow-up of the small region occupied by the vortex ring. To get some feeling for the relative positions of these panels in the trajectory of the vortex ring, insets are provided showing the complete ring trajectory with the instantaneous ring positions denoted explicitly. The shrinking and widening of the core parts, already observed in the dye-visualization experiments, is confirmed by the vorticity contour plots of figure 4.12, even though additional features are observed. In front of the outer core part (positive vorticity ω_z) vorticity filaments are seen to be formed. The filaments are strained towards the opposite core part, upon which they rapidly disappear owing to ordinary diffusion and cross-diffusion with oppositely signed vorticity. A similar formation of filaments was also observed in dye-visualization experiments (figure 4.5d) and is also seen in the contour plots of the passive scalar distribution (figure 4.13). These concentration plots also clearly reveal the continuous accumulation of scalars in the outer core part due to the azimuthal mass flow previously discussed. It is emphasized that the comparison between figures 4.12 and 4.13 is useful to better appreciate analogies and differences between vorticity and passive scalars due to the absence of vortex stretching and the reduced diffusivity of the latter.

The reason for the formation of filaments stripped from the outer core part lies in the strain experienced by the vortex ring during its motion. This is easily verified by inspecting the velocity field of the vortex ring relative to a frame rotating instantaneously with the vortex itself. The construction of such a rotating frame is based on the observation (see subsection 4.4.2) that the vortex ring rotates with a constant angular velocity, opposite to the rotation Ω of the table. The decaying speed U of the vortex ring determines the radius of curvature R_c of the curved trajectory (see equation (4.3)) and the centre of the co-rotating frame is then located at the local centre of curvature.

The flow relative to such a co-rotating frame is shown in figure 4.14 as a velocity vector plot, with the vorticity contours $\omega_z = \pm 0.1$ showing the accompanying deformation of the boundary of the vortex core. The deflection of the relative flow owing to Coriolis forces is clearly seen between the vortex core parts. As a result of this deflection, the stagnation point (marked by a black dot) at the front of the vortex ring is slightly shifted towards the outer core part¹. When this point enters the boundary of the vortex core, a thin filament of vorticity is stripped and advected by the local strain flow, indicated by the adjacent velocity vectors. The position of the shifted stagnation point relative to the vortex ring varies in time, probably due to the presence of the Kelvin waves, and hence the stripping of the vortex core is not continuous, as was also found in the experiment and in the numerical simulation. On the side it is noted that, even though vortex filaments in the front of the ring are preferentially peeled from the outer core part, there are some instants ($t = 33$ and $t = 67$ in figure 4.12) during which filaments are also peeled from the inner core part. These times correspond to the negative peaks of the helicity (figure 4.11a) giving further support to the idea that the oscillations induced by Kelvin waves modify the location of the frontal stagnation point, causing the filament formation to be intermittent.

Similarly to the frontal stagnation point, the stagnation point at the rear of the vortex

¹In absence of the background rotation this stagnation point is located at the central axis of the vortex ring.

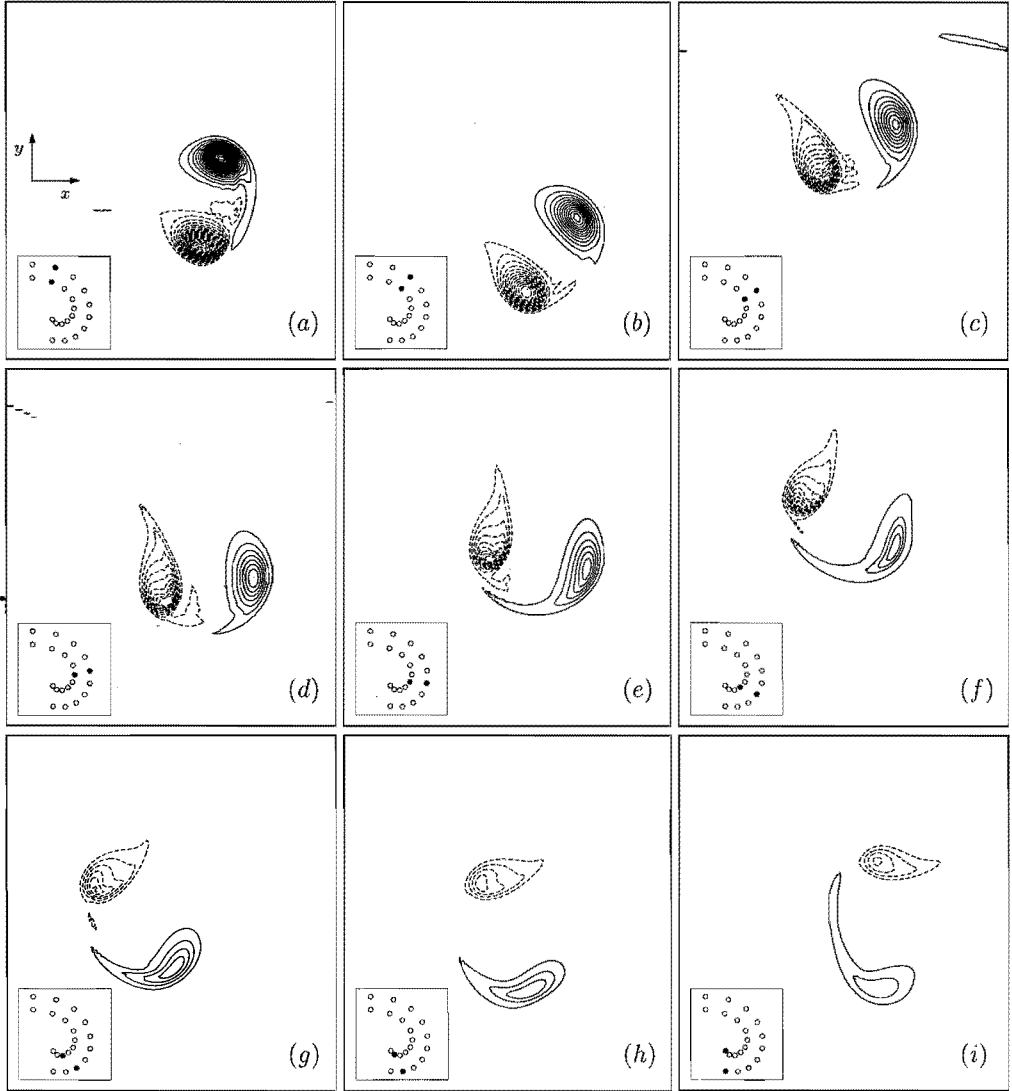


FIGURE 4.12: Contour plots of relative vorticity ω_z in the horizontal symmetry plane $z = 0$ of the vortex ring, obtained from a numerical simulation with $Ro = 23$ and $Re = 900$: (a) $t = 17$, (b) $t = 33$, (c) $t = 50$, (d) $t = 67$, (e) $t = 83$, (f) $t = 100$, (g) $t = 117$, (h) $t = 133$, (i) $t = 150$. Contour increments $\Delta\omega_z = \pm 0.1$, solid lines denote positive values and dashed lines negative values. The insets show the trajectories of the core centres, the instantaneous position of the vortex ring in each panel is denoted by black dots.

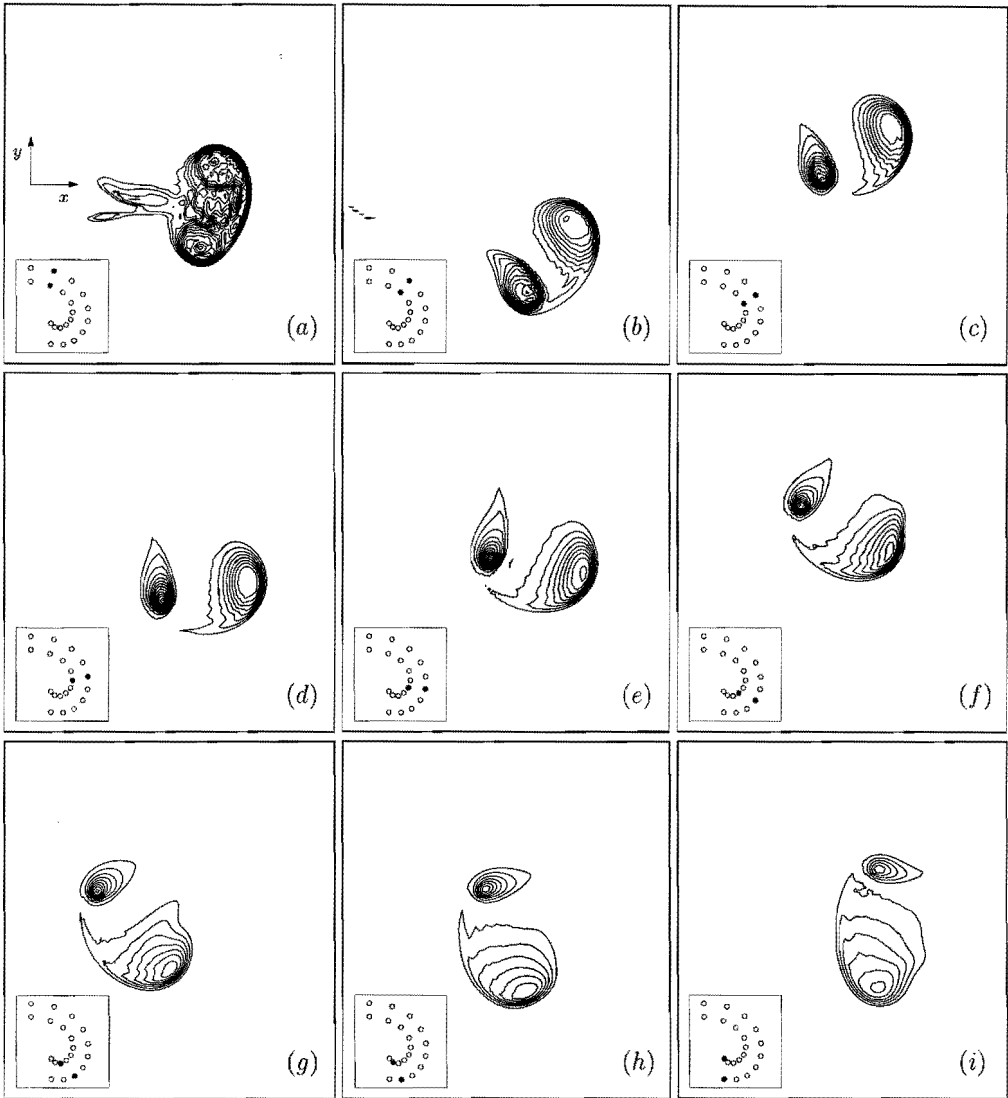


FIGURE 4.13: Contour plots of passive scalar concentration C in the horizontal symmetry plane $z = 0$ of the vortex ring, obtained from a numerical simulation with $Ro = 23$ and $Re = 900$: (a) $t = 17$, (b) $t = 33$, (c) $t = 50$, (d) $t = 67$, (e) $t = 83$, (f) $t = 100$, (g) $t = 117$, (h) $t = 133$, (i) $t = 150$. Contour increments $\Delta C = 0.1$; minimum contour levels: (a-c) $C = 0.25$, (d) $C = 0.2$ and (e-i) $C = 0.15$. The insets show the trajectories of the core centres, the instantaneous position of the vortex ring in each panel is denoted by black dots.

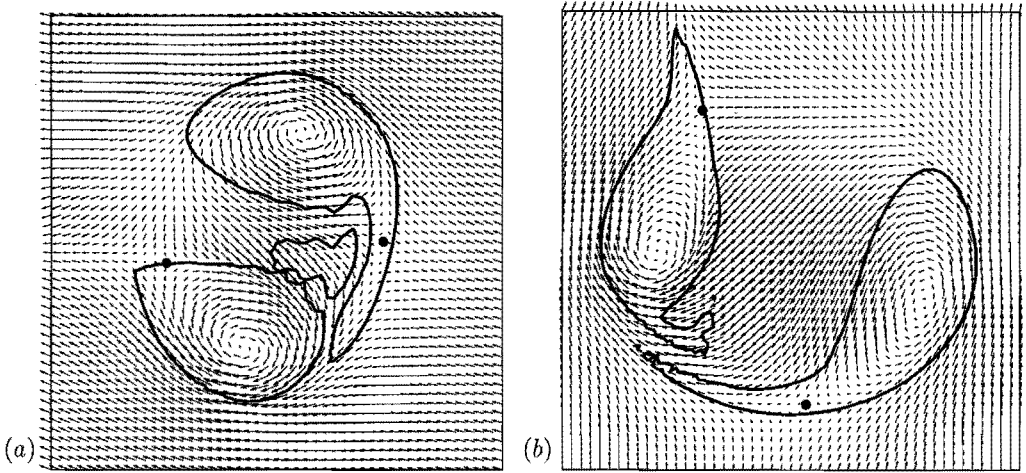


FIGURE 4.14: Velocity vector plots showing the velocity fields at $t = 17$ (a) and $t = 83$ (b) relative to a frame rotating instantaneously with the vortex ring. The positions of the shifted stagnation points are indicated by black dots. Contour lines at $|\omega_z| = 0.1$ show the stripping of vorticity from the boundary of the vortex core ($Ro = 23$ and $Re = 900$, cf. figure 4.12a,e).

ring is also shifted, but in this case towards the inner core part. The deformation of this core part also results from the position of the stagnation point, which in figure 4.14 is located at the border of the core section. The strain flow surrounding the stagnation point then causes the observed elongation of this core part.

The shedding of vortex filaments from the ring core causes the vortex ring to gradually weaken in time until hardly any vorticity is left in the structure ($t = 150$ in figure 4.12). This results in a rapid decrease of the translation velocity U of the vortex ring, faster than solely viscous decay as evidenced in figure 4.8. Also, since the vortex stripping is directly related to the deflection of the flow relative to the vortex ring, this phenomenon will be enhanced when the rotation rate is increased. This is again confirmed by the results of figure 4.8 and by the consequently more strongly curved trajectories of figure 4.7.

4.4.4 THREE-DIMENSIONAL FLOW STRUCTURE

In order to get a complete picture of the ring dynamics, its three-dimensional structure has to be investigated. Since it is difficult to gain insight in the three-dimensional flow from laboratory experiments, the further investigation is mainly based on numerical simulations.

One specific feature, observed from the simulations, is the creation of a secondary vortex that extends as a horizontally elongated tail behind the main vortex ring. This is shown in figure 4.15 by plotting perspective views of vorticity magnitude iso-surfaces. Indeed, a similar structure also appeared in the laboratory experiments (see figure 4.5d) as a thin filament of dye between and behind the dyed core parts, although it was not self-evident from the visualizations that this dye filament indicated the presence of a tail-vortex.

The tail-vortex is located near the centre of the vortex ring, slightly above the mirror plane of the flow and the vorticity in this vortex points away from the vortex ring, according to the sense of rotation indicated in figure 4.15(a). Because of the symmetry of the flow, there is

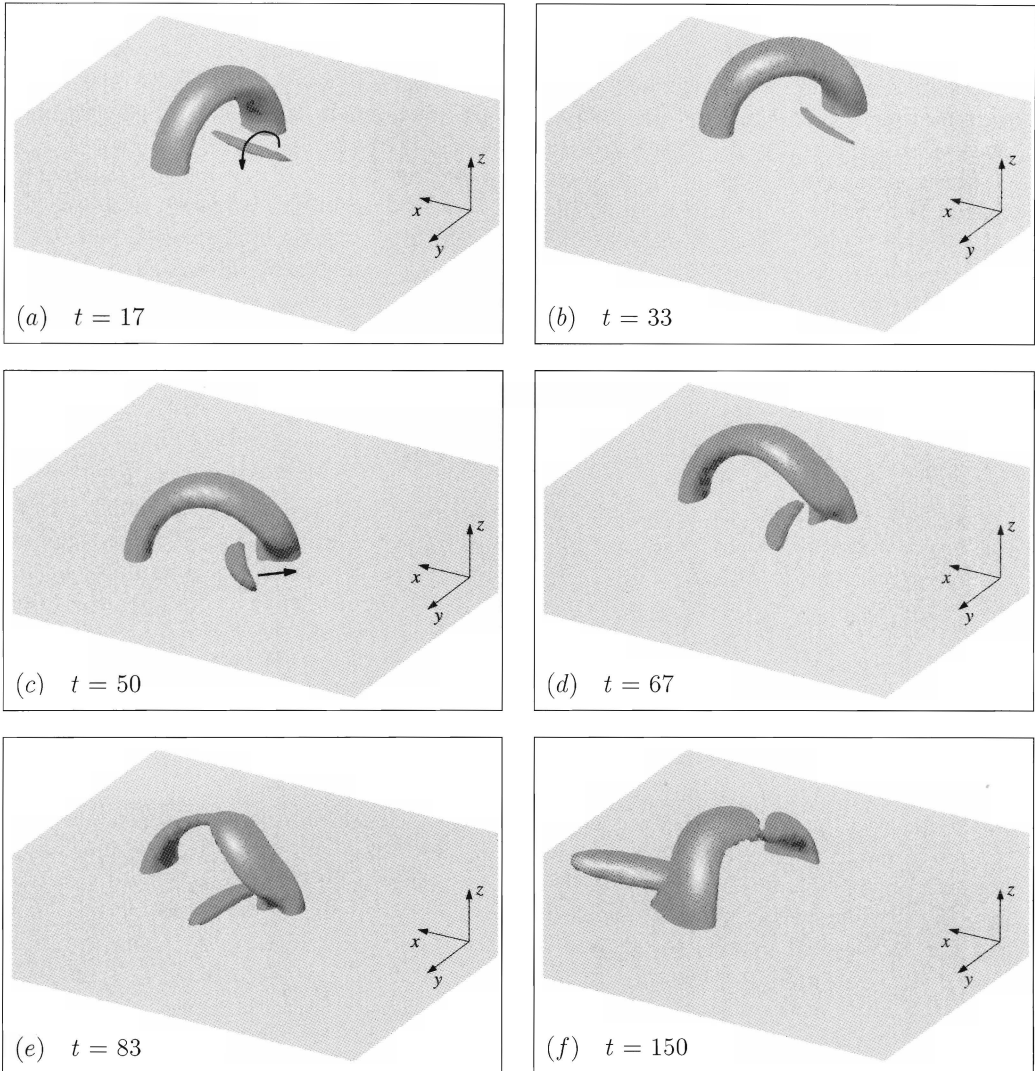


FIGURE 4.15: Perspective views of the evolution of the vortex ring structure as represented by isosurfaces of *relative* vorticity, obtained from a simulation with $Ro = 23$ and $Re = 900$. The curved arrow in figure (a) indicates the sense of rotation in the tail-vortex, which propagates in a horizontal level in the direction of the arrow in figure (c). The vortex ring is mainly viewed from the rear side to show the relative position of the tail-vortex; the initial propagation of the vortex ring is in the direction of the positive x -axis. Isosurfaces $|\omega|$ plotted each moment at half the maximum value $|\omega|_{peak}$.

a similar vortex below the mirror plane with oppositely-signed vorticity and both vortices compose a vortex pair. This vortex pair propagates by mutual propulsion perpendicular to its orientation along the horizontal plane, as indicated in figure 4.15(c). Note that in the horizontal plane $z = 0$ the flow associated with this vortex pair agrees with the deflection of the flow near the centre of the vortex ring observed in figure 4.14a.

The appearance of such a strong vortex pair behind the ring could hardly be expected without the results of the numerical simulation. Once this structure is known, however, it is necessary to explain the mechanism of its formation. The creation of the vortex pair has to result from stretching and tilting of vortex lines. Taking advantage of the initially symmetric structure of the vortex ring, more insight in the tail-formation might be gained by examining the vorticity transport equation attentively. In this analysis also another interpretation will be obtained for the curved trajectory of the vortex ring.

Taking the curl of the Navier-Stokes equation in (4.1) gives the vorticity equation:

$$\frac{D\boldsymbol{\omega}}{Dt} = (\boldsymbol{\omega} \cdot \nabla)\mathbf{u} + \frac{1}{Ro}(\mathbf{k} \cdot \nabla)\mathbf{u} + \frac{1}{Re}\nabla^2\boldsymbol{\omega}. \quad (4.7)$$

The second term on the right hand side acts as an additional source term by which relative vorticity is induced by the permanent rotation of the system. This mainly occurs in regions of the flow where the vertical gradient ($\mathbf{k} \cdot \nabla$) of the velocity field is large. For the present flow this happens in planes where the vorticity in the core is perpendicular to the axis of rotation of the system, i.e. in the vertical plane through the centreline of the vortex ring. Note that in the case of zero background rotation all other terms in equation (4.7) are in balance for an axisymmetric vortex ring, so that any deviation from this structure now primarily results from the term proportional to $1/Ro$.

Consider the flow in the vertical plane through the centreline of the vortex ring, slicing the horizontal parts of the ring core orthogonally. Initially, the flow in this plane is equal to the flow in the horizontal plane $z = 0$ examined in the previous subsection, owing to the axisymmetric structure of the initial vortex ring. One can thus think of the flow as presented in figure 4.10(a) with now the x - and the z -axis oriented horizontally and vertically, respectively. The vorticity in the sections of the ring core points normal to this vertical plane and is thus directed parallel to the y -axis. Since the unit vector \mathbf{k} points along the z -axis (hence $(\mathbf{k} \cdot \nabla) = \partial/\partial z$), the second term on the right hand side of equation (4.7) describes the induction of relative vorticity components ω_x and ω_z at a rate proportional to $\partial u_x/\partial z$ and $\partial u_z/\partial z$, respectively. Direct inspection of the magnitude of the terms $\partial u_x/\partial z$ and $\partial u_z/\partial z$ has shown that the former is dominant (see figure 4.16a,b). Since in the upper half of the vortex ring $\partial u_x/\partial z < 0$ in the main part of the cross-section, the induced axial vorticity component ω_x is negative. Of course, the same (with the gradient sign reversed) occurs in the lower half of the ring, implying the generation of positive ω_x . Near the ring centre these vorticity components strengthen due to self-induced vortex stretching, according to the component $\omega_x(\partial u_x/\partial x)$ in the term $(\boldsymbol{\omega} \cdot \nabla)\mathbf{u}$ on the right-hand side of equation (4.7). The contour plot of $\partial u_x/\partial x$ (figure 4.16c) shows that $\partial u_x/\partial x > 0$ (vortex stretching) at the rear of the vortex ring and $\partial u_x/\partial x < 0$ (vortex compression) at the front side.

Considering now the whole vortex ring one can think of the following mechanism for the formation of the tail-vortices. To explain this it is necessary to introduce the absolute vorticity $\boldsymbol{\omega}_a = \boldsymbol{\omega} + (1/Ro)\mathbf{k}$ of the flow, representing the vorticity relative to an inertial (non-rotating) frame of reference. It can be shown (see Pedlosky 1987, p. 34) that vortex lines of absolute vorticity $\boldsymbol{\omega}_a$ are advected with the flow as material lines (at least in the limit of inviscid

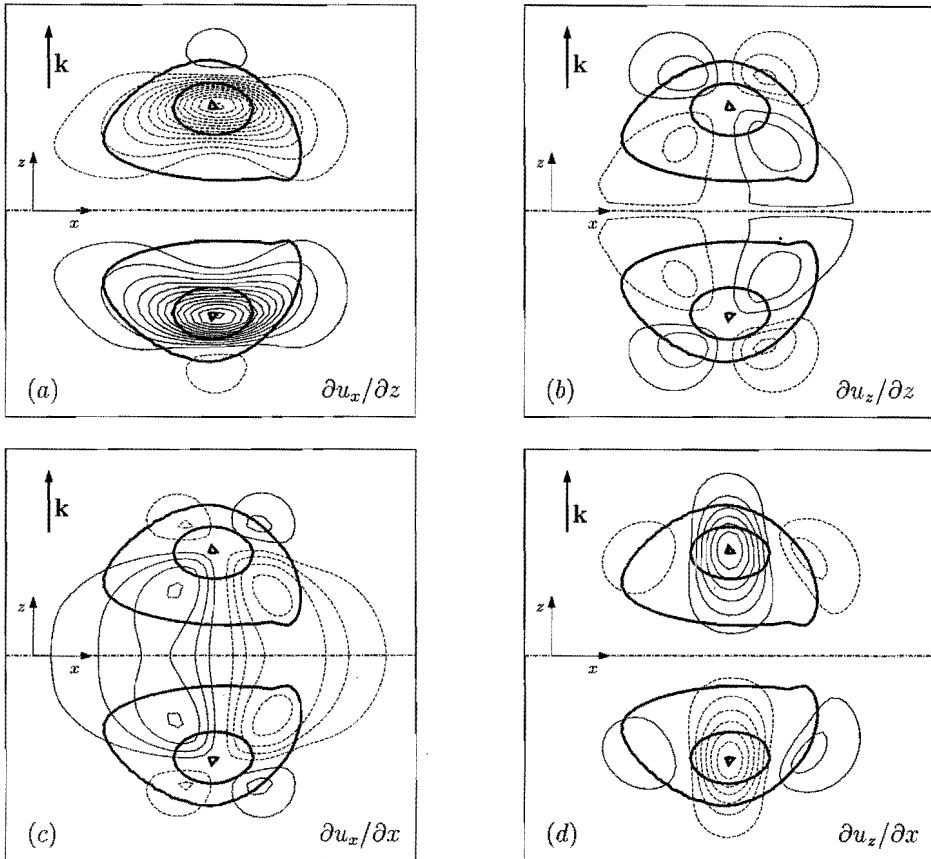


FIGURE 4.16: Contour plots of (a) $\partial u_x / \partial z$, (b) $\partial u_z / \partial z$, (c) $\partial u_x / \partial x$ and (d) $\partial u_z / \partial x$ in the vertical (x, z) -plane through the centre of the initial vortex ring. Solid lines denote positive values and dashed lines negative values, contour increments ± 0.1 . The structure of the ring core is represented by several thick vorticity contour lines (levels $|\omega_y| = 0.1, 1.0$ and 2.0). The chain-dotted line is the trace of the horizontal symmetry plane of the flow on the cross-section of the vortex ring.

flow according to Kelvin's theorem), a property that does not hold for vortex lines of relative vorticity ω . In the present flow, far from the vortex ring there is only the background vorticity due to the ambient rotation, oriented along the z -axis with non-dimensional magnitude $1/Ro$. The corresponding vortex lines of absolute vorticity are thus straight vertical lines. However, those vortex lines passing close to the vortex ring will be tilted according to the local velocity gradients in the flow field of the vortex ring, as shown in figure 4.17. The dominant terms are $\partial u_x/\partial z < 0$ in the upper ring half and $\partial u_x/\partial z > 0$ in the lower half, generating relative vorticity components $\omega_x < 0$ and $\omega_x > 0$, respectively. In the region behind the vortex ring the generation of negative ω_x in the upper ring half means that the vortex lines gain a negative slope and thus are tilted towards the vortex ring centre. Closer to the symmetry plane these tilted vortex lines are intensified by self-induced vortex stretching due to the gradient $\partial u_x/\partial x > 0$ in the flow field at the rear side of the vortex ring. This combination of vortex line tilting, induced by the system rotation, and subsequent self-induced stretching results in the formation of the horizontally elongated tail-vortex in the upper ring half (see figure 4.17*a*). The vorticity in this tail-vortex points in the direction of the negative x -axis. In the lower ring half (not shown in figure 4.17) the tilting of vortex lines behind the vortex ring results in vortex lines with a positive slope (generation of $\omega_x > 0$). One can imagine that these vortex lines are also deflected towards the centre of the vortex ring. In fact, the vortex lines in the upper ring half continue in the lower ring half and the tilting and stretching processes are mirror-symmetric. Subsequent stretching of these tilted vortex lines at the ring centre yields a tail-vortex in the lower ring half with vorticity pointing along the positive x -axis, hence opposite to the vorticity in the tail-vortex in the upper ring half.

As mentioned above, these tail-vortices form a vortex pair propagating towards the vertical core part on the inner side of the ring trajectory (as observed in figure 4.15), where they interfere with the local orthogonal vorticity in this core part. On one hand, the circumferential flow associated with each leg of the vortex pair induces an additional stretching of the vorticity in this core part while, on the other hand, the vortex pair is curved by the main flow of the vortex ring. The increase of stretching induced by this vortex pair further enhances the squeezing of the vortex core and the differential vorticity along the toroidal axis of the vortex ring. As a result of this strong interaction with the tail-vortices the ring core is locally distorted, as seen in figure 4.15*b-e*. This torsion is also reflected by the deformed shape of the negative vorticity contour lines near the core centre in figure 4.12.

It should be noted that in the upper half of the ring the vorticity vector in the tail-vortex points in the opposite direction with respect to the local flow velocity, thus generating additional negative helicity. This contribution is already included in the data of figure 4.11(*a*): the negative helicity has to be attributed partly to the mechanism previously described (see subsection 4.4.3) and partly to the tail-vortex. However, it has been checked by separation of these two contributions that the oscillatory behaviour is entirely due to Kelvin waves and the helicity contribution of the tail is always negative.

Returning to equation (4.7), a proper interpretation of the rotation term can give a different explanation of the curved ring trajectory. By rewriting:

$$\frac{1}{Ro}(\mathbf{k} \cdot \nabla)\mathbf{u} \equiv \frac{1}{Ro}\boldsymbol{\omega} \times \mathbf{k} + \frac{1}{Ro}\nabla(\mathbf{k} \cdot \mathbf{u}), \quad (4.8)$$

it appears that the first term on the right-hand side is a pure rotation of pre-existing vorticity, while the second term is a transformation of background vorticity ($1/Ro$) into relative vorticity due to the gradient of the velocity component parallel to \mathbf{k} . Recalling that \mathbf{k} is oriented in the

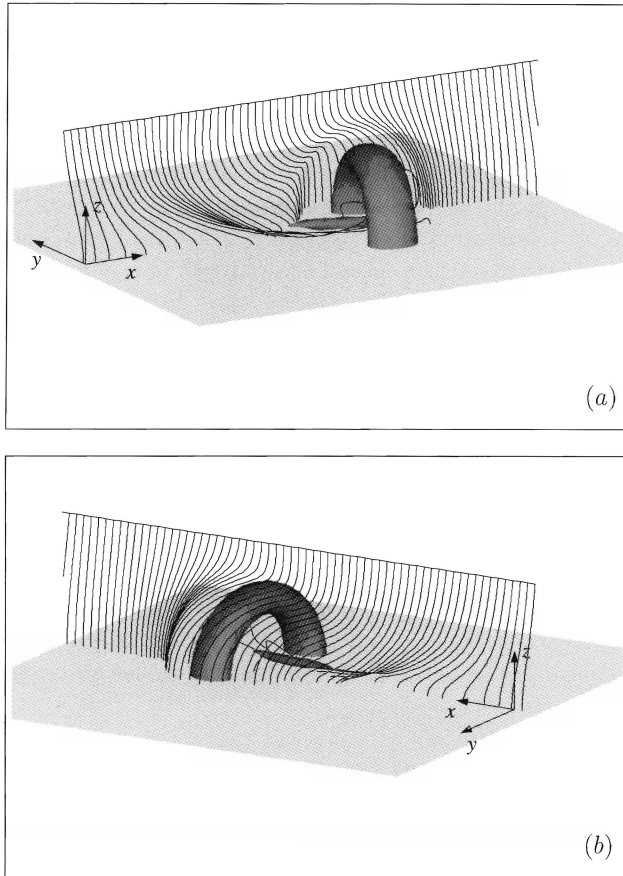


FIGURE 4.17: Two different perspective views taken from the rear side of the vortex ring at $t = 17$ through iso-surfaces of *absolute* vorticity $|\omega_a| = 0.5|\omega_a|_{peak}$ ($Ro = 23$ and $Re = 900$; cf. figure 4.15a). Vortex lines of absolute vorticity are released from a single horizontal line (drawn in the figure) that represents the intersection of the horizontal plane $z = 2$ and the vertical (x, z) -plane through the centre of the initial vortex ring. Far from the vortex ring the vorticity in the vortex lines points vertically upwards; close to the vortex ring vortex lines are tilted and stretched due to local gradients in the velocity field of the vortex ring.

direction of the z -axis the first term on the right-hand side describes a rotation of the vorticity vector ω in the vortex ring core around this axis in clockwise direction. Since this tilting occurs at a rate $1/Ro$, a faster rotation of the ambient fluid will enhance the curvature of the ring trajectory, as confirmed by the results of figure 4.7. Although this approach demonstrates the curved motion of the vortex ring very nicely, the complete picture is more complicated. In fact, the rotation rate depends on the local angle between ω and \mathbf{k} , which varies along the toroidal ring axis. In the vertical parts of the vortex ring ω and \mathbf{k} are either parallel or antiparallel and $\omega \times \mathbf{k}$ vanishes identically. For the horizontal parts of the vortex ring the clockwise rotation around the z -axis means that the vorticity vector pointing initially parallel to the y -axis is gradually turned towards the direction of the x -axis. This tilting is counteracted by the component $(1/Ro)\partial u_z/\partial x$ in the second term on the right-hand side in equation (4.8) as follows. In the horizontal part of the vortex core in the upper ring half the vorticity has initially a negative component ω_y and this is turned into a negative component ω_x by the clockwise ring rotation. The second term in equation (4.8) describes a generation of ω_x at a rate proportional to $\partial u_z/\partial x$. As seen in figure 4.16(d) this gradient is positive in the upper ring half, thus generating positive ω_x that partially opposes the negative ω_x due to the clockwise rotation. As a consequence of these effects the vortex ring does not have a uniform rotation, leading to internal distortion of the vortex structure. Nevertheless, as shown in subsection 4.4.2, the vortex ring propagates with average rotation equal and opposite to the background rotation $1/(2Ro)$ of the system.

Before coming to the conclusions one comment is added to figure 4.15. The vorticity iso-surfaces in this figure have been drawn using for each time half the value of the instantaneous peak vorticity. As can be seen from figure 4.11(b), however, the peak vorticity undergoes a substantial decrease in time owing to ordinary viscous diffusion and to the peeling processes described in subsection 4.4.3. This implies that the vortex ring of figure 4.15 at $t = 150$ is in fact a very weak structure even if it preserves its toroidal topology. This result agrees with the laboratory experiments in which at the end of the ring evolution a compact blob of dyed fluid with hardly any motion was observed.

4.5 Conclusions

In this chapter the dynamics of a vortex ring has been investigated that propagates perpendicular to the axis of a uniformly rotating fluid. The interaction between the permanent vorticity of the rotating fluid and the ring vorticity yields a comprehensive example of the complex dynamics of localized vorticity distributions in rotating flows. Owing to the initially 'simple' structure of the vortex ring, the analysis of the development of the flow can be pursued in detail, yielding a thorough insight in the induction and dynamics of relative vorticity in rotating systems. The investigation was based both on laboratory experiments and on numerical simulations, which were used as complementary tools.

Flow visualization experiments have shown that the vortex ring propagates in the rotating system along a curved path, being deflected clockwise if the system rotates anti-clockwise. A similar behaviour was observed in laboratory experiments by Taylor (1917; 1921), though his experiments were only aimed at demonstrating the analogy with the motion of a solid sphere in a rotating fluid. In Taylor's papers, neither measurements of the ring trajectory nor details on the evolution of the vortex structure were reported. In the present study the ring trajectory has been measured following the dyed core patches in an illuminated cross-section

of the vortex ring. The trajectory has a spiraling shape in the rotating frame, while the vortex ring maintains its orientation with respect to the laboratory frame. Another typical feature of the flow, observed from flow visualizations, is the variation of the size of the core cross-sections: the section along the inner side of the trajectory gradually shrinks while the other section expands in time.

Examination of the velocity field in the horizontal symmetry plane of the flow shows that the flow near the ring centre is strongly deflected, owing to the action of the Coriolis force. Also the flow around the vortex cores is deflected, forcing both core sides oppositely. One side of the core expands while the other side contracts and these processes are accompanied by compression and stretching of vortex lines, respectively. Due to this local forcing of the vortex core inertial waves, similar to Kelvin waves along a rectilinear vortex, are excited, travelling along the toroidal axis of the ring. The increase in time of the period of these waves could be explained applying the theoretical results for the group velocity of Kelvin waves along an infinitely long vortex: the group velocity of these waves is proportional to the vorticity of the vortex. In case of the vortex ring the vorticity decreases mainly by viscous diffusion, resulting in a decaying group velocity and hence longer periods for the wave motion along the ring core. The deflection of the flow around the vortex ring also caused the front and rear stagnation points to be shifted. In particular, the front stagnation point was preferentially moved towards the core part on the outer side of the ring trajectory, while the opposite happened for the rear stagnation point moving towards the inner core part. The local strain around these points led to stripping of vorticity filaments from the vortex ring, thus producing a progressive weakening of the vortex structure up to a complete depletion. This phenomenon is confirmed by the time evolution of the translation velocity of the vortex ring (figure 4.8), which decays in time at a rate faster than in the non-rotating case.

To gain more insight in the evolution of the three-dimensional structure of the vorticity field, the results from the numerical simulations were analysed in detail. It has been proved, by checking the trajectory and velocity of a vortex ring both in a fluid at rest and relative to a rotating fluid, that the numerical simulations mimic the laboratory experiments very well. Furthermore, the evolution of the flow in a horizontal cross-sectional plane through the vortex ring has been compared with the video images obtained from dye-visualization experiments. Despite restrictions to simulate the advection of passive scalars only at disproportionately low Schmidt numbers, the gradual deformations on each vertical core part of the vortex ring were readily reproduced.

A specific feature of the flow, observed by examining the three-dimensional structure of the vortex, is the formation of a horizontally extending vortex pair at the tail. A detailed analysis has shown that this vortex pair is created by turning and stretching of vortex lines gathered by the main vortex ring. This process is initiated by the induction of relative vorticity due to the rotation of the system, but the subsequent evolution into an elongated vortex pair is dominated by the main flow field of the vortex ring. The vortex pair propagates by its self-induced motion in a horizontal level towards the shrinking side of the main vortex ring, increasing there the local stretching and thus enhancing the squeezing of this vertical core part. As a result the vortex core is locally distorted.

Most of the experiments and simulations were performed at a relatively low rotation rate of the system, i.e. $Ro \geq 8$. In these cases the development of deformations on the main vortex structure could readily be followed in time and a thorough analysis of the evolution of the vorticity field was possible. A few simulations have been done with $Ro < O(1)$. The coherent

structure of the vortex ring is then rapidly destroyed by the strongly enhanced stretching and turning of vortex lines. Moreover, induction of relative vorticity is then no longer restricted to a region of the flow close to the vortex ring, but it takes place over the whole flow domain, probably radiating inertial waves. These results, however, cannot be considered as reliable, mainly for two reasons: if inertial waves are radiated the limited size of the computational domain and the periodic conditions on the lateral boundaries could then be no longer suitable to study the preferably unbounded flow field. In addition, as mentioned in subsection 4.3.3, the rotation of the system affects the whole flow evolution, so also the generation of the vortex ring. For the range of Rossby numbers investigated in the present chapter it was known from previous experiments that a vortex ring was formed initially, and therefore an axisymmetric vortex ring could be used as initial condition. In contrast, for higher rotation rates this is not known and it would seem more appropriate to use a numerical set-up as in chapter 3, where the initial vortex structure was generated by injection of a finite amount of fluid through an orifice.

Appendix A

In this appendix the forces are discussed that are exerted on a solid object that propagates perpendicular to the axis of a rotating fluid. Attention is focused to two special cases, i.e. the forces on a solid sphere and on a solid cylinder, respectively. These cases typically illustrate the effect of the rotation of the fluid on either a three-dimensional or a two-dimensional flow. Taylor (1917) discussed the forces that are exerted on the sphere, being responsible for the deflection of the sphere's trajectory from a straight line. The mathematical derivation of the expressions for these forces was performed by Proudman (1916) in a previous paper. For completion of the discussion in subsection 4.4.2 the main results of the mentioned studies are summarized here briefly, emphasizing the difference of the force balance exerted on a cylinder and on a sphere.

Consider a homogeneous solid object (either a cylinder or a sphere) of mass M placed in a fluid that rotates with angular velocity Ω . The object moves steadily in a prescribed motion with velocity U in a direction perpendicular to the rotation vector. In addition to the pressure and viscous forces that are exerted on the object also in case of zero rotation, the object experiences two inertial forces that directly originate from the applied system rotation: 1) a centrifugal force $M\Omega^2 D$ acting through the centre of gravity \mathcal{C} of the object, pointing away from the centre of rotation (D is the distance of \mathcal{C} from the centre of rotation), 2) a Coriolis force $2M\Omega U$ perpendicular to the direction of the velocity U of the centre \mathcal{C} , directed to the right if the rotation of the fluid is anti-clockwise (see figure A.1).

Furthermore, an additional pressure force is exerted by the surrounding flow on the boundary of the object. This net pressure force results from the various inertial forces (i.e. centrifugal and Coriolis forces) related to the system's rotation that act on the flow around the moving object. Expressions for the components of this pressure force had been derived by Proudman (1916) and applied by Taylor (1917). For a vertical cylinder with horizontal cross-sectional area A , extending over the whole fluid depth, these components per unit axial length consist of: 1) a force $M_F\Omega^2 D$ acting through \mathcal{C} towards the centre of rotation and 2) a force $2M_F\Omega U$ acting at \mathcal{C} perpendicular to U to the left (see figure A.1). Here, $M_F = \rho A$ is the mass per unit length of the region of the fluid occupied by the solid object, ρ being the density of the fluid. If the cylinder and the fluid have the same density, all forces that are related to the

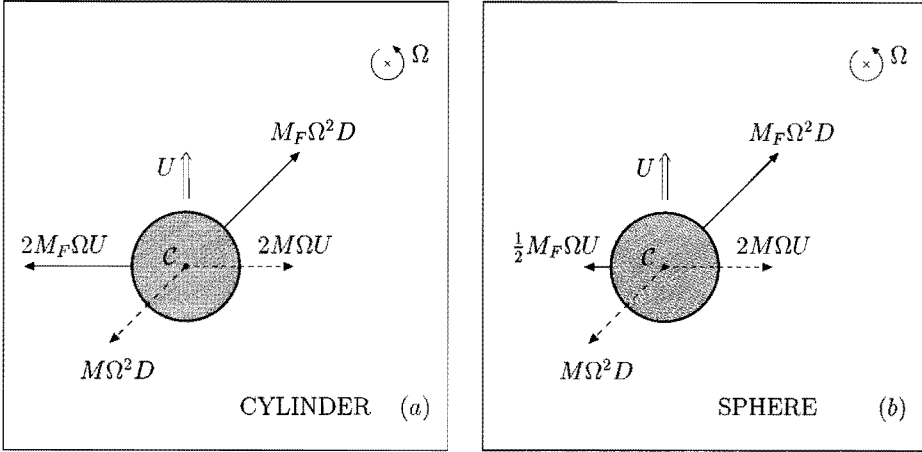


FIGURE A.1: Additional forces exerted on a cylinder (a) and a sphere (b) due to the system's rotation (top view, the centre of rotation is marked by a cross at the top left corner, an arrow indicates the anti-clockwise rotation of the system.) Centrifugal and Coriolis forces (dashed arrows) act at the centre of gravity C of the object, while competing components of fluid pressure forces (solid arrows) are exerted on the solid's surface. For the sphere the resultant force is directed perpendicular to its motion to the right, deviating its path from a straight line. Explanation of the symbols: U is the velocity of the object, M is the mass of the object, M_F is the mass of the fluid region occupied by the object, D is the distance of the centre C of the object from the rotation centre and Ω is the system's rotation rate.

rotation of the system cancel and the cylinder moves along a straight path, as if the rotation were absent.

An important property of any two-dimensional flow (u, v) in a rotating fluid, related to this result, is the possibility to rewrite the components of the Coriolis acceleration $(-2\Omega v, 2\Omega u)$ in the Navier-Stokes equation in terms of the gradient of a scalar function. Describing the 2-D flow by a stream function ψ , defined by:

$$u = \frac{\partial \psi}{\partial y} \quad \text{and} \quad v = -\frac{\partial \psi}{\partial x}, \quad (\text{A.1})$$

the expression $2\Omega\psi$ is found for this scalar function. This implies that a reduced pressure field $p' = p + 2\Omega\psi\rho$ can be defined that, in addition to the centrifugal force, includes also the Coriolis force on the fluid flow. In terms of the pressure p' the Navier-Stokes equation describing the flow relative to a rotating frame of reference reduces to its formulation in an inertial frame and hence the two-dimensional flow in the rotating system is not affected by the rotation.

For a sphere of volume V , however, the flow generated around it is essentially three-dimensional and the forces due to fluid pressure are insufficient to cancel the inertial forces on the sphere. The mathematical derivation of the total pressure force on a sphere is rather complicated and the results obtained by Proudman (1916) will be used, who derived the following expressions for the components of the pressure force: 1) a force $M_F\Omega^2 D$ directed towards the centre of rotation and 2) a force $\frac{1}{2}M_F\Omega U$ perpendicular to U to the left (see figure A.1). In this case $M_F = \rho V$ is the total mass of the region of the fluid occupied by

the solid object, ρ being the density of the fluid. If the sphere and the fluid have the same density, the component of the resultant force perpendicular to the sphere's motion does not vanish and the sphere is compelled to move along a curved trajectory, its path being deflected to the right.

A special situation occurs when the sphere is moved very slowly and the system rotates at a considerable speed. According to Proudman's theorem any slow steady motion relative to the rotating system is then two-dimensional. Experiments performed by Taylor (1923) have shown that also for the sphere a steady two-dimensional flow is established. In fact, he had observed that a cylinder of fluid of the same diameter as the sphere moves with the sphere and acts towards the rest of the fluid as if it were a solid cylinder. Such a cylinder of fluid, accompanying an object moving in a rotating system, is commonly called a 'Taylor column'.

5

ANALYSIS OF TWO MODELS FOR LEAPFROGGING VORTEX RINGS

This chapter is a slightly adapted version of the paper 'Analysis of two models for leapfrogging vortex rings by A.H.M. Eisenga & A.A. Gourjii, submitted to Fluid Dyn. Res. (1996).

5.1 Introduction

The motion of two coaxially interacting vortex rings has been an important subject for investigation within the field of vortex dynamics, since the famous work of Helmholtz (1858). In this paper the 'leapfrog motion' of two identical vortex rings, placed in tandem, was predicted. Experiments by Yamada & Matsui (1978) demonstrate this alternating, periodical motion for two smoke rings. Several models have been derived for describing this phenomenon in inviscid flow (see e.g. Shariff *et al.* (1988; 1989), where a contour dynamics method has been used) and direct numerical simulations of leapfrog motion in viscous flows have been performed (Riley & Stevens 1993). Dyson (1893) has derived a simple model for describing the coaxial interaction of two arbitrary axisymmetric vortex rings in an ideal fluid. In this model the trajectories of the vortex rings can be obtained from two invariants of motion (impulse and energy) without explicit integration of the equations of motion with respect to time.

In this chapter Dyson's model is compared with another more general three-dimensional vortex model, namely the vorton model (Novikov 1983). In this model, a system of vortical singularities (vortons) are used to construct two coaxial interacting vorton rings (Aksman *et al.* 1985). Because of the symmetry of this configuration the equations of motion of the vortons can be written in a formulation similar to the equations of motion in Dyson's model. In this so-called 'axisymmetric vorton model' each vorton ring is assumed to move in the approximately axisymmetric velocity field induced by the other vorton ring. Using corresponding initial conditions, the trajectories of two interacting vortex rings and two vorton rings are obtained by numerically solving the respective equations of motion with respect to time. Comparison of these trajectories provides more insight in the differences between both models.

5.2 Dyson's model

Consider an axisymmetric vortex ring with radius R , moving in an unbounded ideal fluid which is at rest at infinity. The vorticity is uniformly distributed in a thin circular core with radius

a ($a/R \ll 1$) and circulation Γ . Such an isolated vortex ring propagates steadily, without changing in size or shape, due to its self-induced motion in a direction normal to the plane of the ring. The velocity of propagation of the vortex ring is given by (Thomson 1867a):

$$U = \frac{\Gamma}{4\pi R} \left(\ln \frac{8R}{a} - \frac{1}{4} \right). \quad (5.1)$$

In this study the motion of two of such vortex rings, moving along a common axis of symmetry, is considered. The motion of each vortex ring is now affected by the velocity field induced by the other vortex ring. Due to this mutual interaction the ring radii change and the vortex rings either expand in size or shrink. As a consequence, the self-induced velocity of the vortex rings is not constant, and the motion of the system of two vortex rings is thus, generally, unsteady. Hicks (1922) has first discussed the possibility of a steady vortex ring pair. Recently, Gurzhii *et al.* (1994) and Weidman & Riley (1993) have investigated the existence and stability of vortex ring pairs.

Dyson (1893) has derived the equations of motion of two coaxially interacting thin vortex rings in ideal unbounded fluid. In his derivation he assumed that during the interaction the cores of the vortex rings are not deformed and do not overlap. This assumption is valid for situations in which the distance between the cores of the respective vortex rings remains large. The radii of the thin circular cores change in size so as to conserve the vortical volume $2\pi^2 a^2 R$ of the core of each vortex ring. Relative to cylindrical coordinates (r, ϕ, z) , with the z -axis directed along the central axis of the vortex ring, the evolution of the azimuthal vorticity component ω_ϕ in the vortex core is given by:

$$\frac{D(\omega_\phi/r)}{Dt} = 0. \quad (5.2)$$

According to this equation Dyson assumed a vorticity distribution $\omega_\phi/r = \text{constant}$ in the core and $\omega_\phi/r = 0$ outside the core. The self-induced velocity of the vortex ring is then given by equation (5.1), supplemented by an $\mathcal{O}(a/R)$ correction according to variations of ω_ϕ within the vortex core. For thin-core vortex rings this correction term can be omitted. The circulation around the vortex core is conserved according to Kelvin's circulation theorem for inviscid flows.

In figure 5.1 the configuration of two coaxial vortex rings has been drawn schematically in a cross-sectional view. The vortex rings have circulations Γ_1 and Γ_2 and core radii a_1 and a_2 , respectively. The equations of motion, describing the evolution of the ring radii R_1 and R_2 and the axial positions Z_1 and Z_2 of the ring centres, are given by:

$$\begin{aligned} \frac{dR_1}{dt} &= \frac{\Gamma_2 Z_{21}}{2\pi R_1 \{Z_{21}^2 + (R_1 + R_2)^2\}^{1/2}} \left(K(k) - E(k) - \frac{2R_1 R_2 E(k)}{Z_{21}^2 + (R_1 - R_2)^2} \right) \\ \frac{dR_2}{dt} &= \frac{-\Gamma_1 Z_{21}}{2\pi R_2 \{Z_{21}^2 + (R_1 + R_2)^2\}^{1/2}} \left(K(k) - E(k) - \frac{2R_1 R_2 E(k)}{Z_{21}^2 + (R_1 - R_2)^2} \right) \\ \frac{dZ_1}{dt} &= \frac{\Gamma_1}{4\pi R_1} \left(\ln \frac{8R_1}{a_1} - \frac{1}{4} \right) + \\ &\quad + \frac{\Gamma_2}{2\pi \{Z_{21}^2 + (R_1 + R_2)^2\}^{1/2}} \left(K(k) - E(k) - \frac{2R_2(R_1 - R_2)E(k)}{Z_{21}^2 + (R_1 - R_2)^2} \right) \\ \frac{dZ_2}{dt} &= \frac{\Gamma_2}{4\pi R_2} \left(\ln \frac{8R_2}{a_2} - \frac{1}{4} \right) + \end{aligned} \quad (5.3)$$

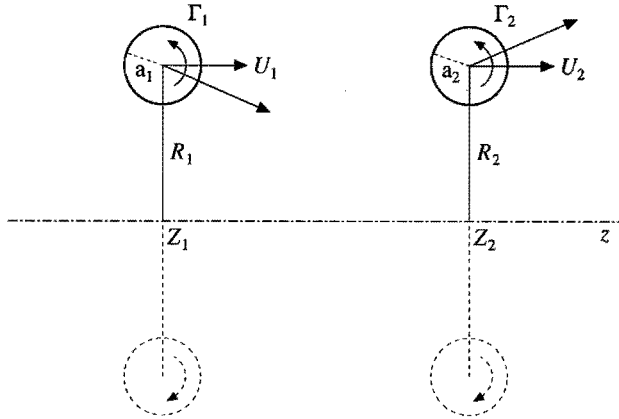


FIGURE 5.1: Cross-sectional view of configuration of two coaxial vortex rings. The horizontal arrows indicate the self-induced velocity U_1 and U_2 , respectively, of the vortex rings and the inclined arrows the subsequent direction of motion affected by the mutual interaction of the vortices.

$$+ \frac{\Gamma_1}{2\pi \{Z_{21}^2 + (R_1 + R_2)^2\}^{1/2}} \left(K(k) - E(k) - \frac{2R_1(R_2 - R_1)E(k)}{Z_{21}^2 + (R_1 - R_2)^2} \right),$$

with $Z_{21} = Z_2 - Z_1$. Here $K(k)$ and $E(k)$ denote the complete elliptic integrals of the first and second kind, respectively, with argument k given by:

$$k^2 = \frac{4R_1R_2}{Z_{21}^2 + (R_1 + R_2)^2}. \quad (5.4)$$

As can be seen from equation (5.3) the motion of the vortex rings is determined by two contributions: the self-induced velocity of the vortex rings in axial direction (see also equation (5.1)) and the mutually induced velocity giving rise to both a radial and an axial velocity component at the location of the vortex cores. Since the equations of motion are derived only to lowest order in a/R , the mutually induced velocity field is identical to the velocity field induced by a circular vortex filament of zero core cross-section, with stream function (see Batchelor 1967, p. 521):

$$\psi(r, z) = \frac{\Gamma\sqrt{Rr}}{2\pi} \left[\left(\frac{2}{k} - k \right) K(k) - \frac{2}{k} E(k) \right], \quad (5.5)$$

where $k^2 = \frac{4rR}{(r+R)^2 + z^2}$.

Hence, as far as the mutual interaction is concerned the vortex rings can be represented by singular vortex filaments.

The equations (5.3) have to be completed with the conditions of constant volume of the vortical cores:

$$\begin{cases} a_1^2 R_1 = \text{constant} \\ a_2^2 R_2 = \text{constant}, \end{cases} \quad (5.6)$$

which are used to prescribe the evolution of the core radii in time.

It can be shown (Dyson 1893; Gurzhii 1988 *et al.*) that the system of equations (5.3) with Γ_1 and Γ_2 constant has two independent invariants of motion:

$$\begin{aligned} P_{z,tot} &= \pi\Gamma_1 R_1^2 + \pi\Gamma_2 R_2^2 \\ &= P_1 + P_2 = \text{constant} \end{aligned} \quad (5.7)$$

and

$$\begin{aligned} E_{tot} &= \frac{\Gamma_1^2 R_1}{2} \left(\ln \frac{8R_1}{a_1} - \frac{7}{4} \right) + \frac{\Gamma_2^2 R_2}{2} \left(\ln \frac{8R_2}{a_2} - \frac{7}{4} \right) + \\ &+ \Gamma_1 \Gamma_2 \sqrt{R_1 R_2} \left[\left(\frac{2}{k} - k \right) K(k) - \frac{2}{k} E(k) \right] \\ &= E_1 + E_2 + E_{1-2} = \text{constant}, \end{aligned} \quad (5.8)$$

which express the conservation of the impulse along the axis of symmetry and the energy of the flow field of the vortex rings, respectively. The total impulse consists of the impulses P_1 and P_2 of the individual vortex rings. The total energy E_{tot} consists of the kinetic energies E_1 and E_2 of the individual vortex rings and a term E_{1-2} related to the interaction between the two vortex rings.

From a theoretical point of view it is noted that the existence of two invariants of motion is sufficient to determine the phase trajectories $R_1(Z_{21})$ and $R_2(Z_{21})$ of the vortex rings without explicit integration of the equations of motion with respect to time. This possibility enables the classification of different types of coaxial interaction of two arbitrary vortex rings (Gurzhii *et al.* 1988; Gurzhii *et al.* 1994). In the present study, however, the trajectories are determined by numerically solving the equations (5.3) with conditions (5.6). The invariants of motion (5.7) and (5.8) are then used to check the accuracy of the numerical integration.

5.3 Vorton model

A vorton (Novikov 1983) is a three-dimensional vortical singularity. It is specified by a position vector \mathbf{x} and an intensity vector $\boldsymbol{\gamma}$, which denote its location and strength, respectively. A system of N vortons can be used to model a three-dimensional flow with vorticity. The vortons are located in the regions with vorticity and their intensity vectors are oriented parallel to the local vorticity field. Each vorton moves with the local velocity field induced by all other vortons. An expression for the velocity field induced by a single vorton has been derived by Novikov (1983).

The velocity of a vorton j , located at position $\mathbf{x}^{(j)}$, is then given by:

$$\frac{d\mathbf{x}^{(j)}}{dt} = \mathbf{u}^{(j)} = -\frac{1}{4\pi} \sum_{\substack{i=1 \\ i \neq j}}^N \frac{(\mathbf{x}^{(j)} - \mathbf{x}^{(i)}) \times \boldsymbol{\gamma}^{(i)}}{|\mathbf{x}^{(j)} - \mathbf{x}^{(i)}|^3}. \quad (5.9)$$

The intensity of a vorton changes due to local gradients in the velocity field:

$$\frac{d\boldsymbol{\gamma}^{(j)}}{dt} = (\boldsymbol{\gamma}^{(j)} \cdot \nabla) \mathbf{u}^{(j)}. \quad (5.10)$$

Equations (5.9) and (5.10) constitute the equations of motion of a system of vortons. For any initial configuration of vortons, the trajectories of the vortons and the evolution of their intensities follow from numerical integration of these equations with respect to time.

In this study the dynamics of continuous vortex rings is simulated using discrete vortons that are arranged in so-called vorton rings. As introduced in Novikov (1983), a vorton ring consists of a system of identical vortons placed tangent to a circle at the vertices of a regular polygon. In such a configuration, the vortons are located at positions $\mathbf{x}^{(i)} = (R \cos \phi^{(i)}, R \sin \phi^{(i)}, Z)$ with intensities $\boldsymbol{\gamma}^{(i)} = \gamma(-\sin \phi^{(i)}, \cos \phi^{(i)}, 0)$. Here, R and Z are the radius and axial position of the ring, respectively, $\phi^{(i)} = 2\pi i/N$ is the azimuthal angle of the i^{th} vorton, N is the number of vortons on the ring and γ is the modulus of the intensity, which is the same for all vortons. For this configuration it can be shown from (5.10) and (5.9) that the intensities of the vortons do not change and the ring itself drifts perpendicular to its plane with velocity:

$$U = \frac{dZ}{dt} = \frac{\gamma}{8\sqrt{2\pi}R^2} \sum_{i=1}^{N-1} \frac{1}{\sqrt{1 - \cos \phi^{(i)}}}, \quad (5.11)$$

which is in fact the axial velocity at the position of one of the vortons on the ring (here the N^{th} vorton has been chosen) due to all other vortons.

In the case of two N -vorton rings moving along a common axis of symmetry, the vorton rings will mutually induce an additional velocity. To calculate the velocity of one of the vorton rings, to equation (5.11) is added the velocity field induced by all vortons constituting the other ring at the position of the N^{th} vorton on the first ring. Two vorton rings have been used with ring radii R_1 and R_2 , respectively, separated by an axial distance $Z_{21} = Z_2 - Z_1$. The moduli of the intensities of the vortons on the rings are γ_1 and γ_2 , respectively. The distribution of vortons over the rings, denoted by the azimuthal angle $\phi^{(i)}$, is initially the same for both rings. After some straightforward calculations, using (5.9), it turns out that for this configuration of vorton rings the azimuthal component of the mutually induced velocity field vanishes, so the initial distribution of vortons over the rings does not change. For the radial and axial components of the velocity of the vorton rings the following equations have been derived:

$$\begin{aligned} \frac{dR_1}{dt} &= -\frac{\gamma_2 Z_{21}}{4\pi} \sum_{i=1}^N \frac{\cos \phi^{(i)}}{[R_1^2 + R_2^2 + Z_{21}^2 - 2R_1 R_2 \cos \phi^{(i)}]^{3/2}} \\ \frac{dR_2}{dt} &= \frac{\gamma_1 Z_{21}}{4\pi} \sum_{i=1}^N \frac{\cos \phi^{(i)}}{[R_1^2 + R_2^2 + Z_{21}^2 - 2R_1 R_2 \cos \phi^{(i)}]^{3/2}} \\ \frac{dZ_1}{dt} &= \frac{\gamma_1}{8\sqrt{2\pi}R_1^2} \sum_{i=1}^{N-1} \frac{1}{\sqrt{1 - \cos \phi^{(i)}}} + \\ &\quad - \frac{\gamma_2}{4\pi} \sum_{i=1}^N \frac{R_1 \cos \phi^{(i)} - R_2}{[R_1^2 + R_2^2 + Z_{21}^2 - 2R_1 R_2 \cos \phi^{(i)}]^{3/2}} \\ \frac{dZ_2}{dt} &= \frac{\gamma_2}{8\sqrt{2\pi}R_2^2} \sum_{i=1}^{N-1} \frac{1}{\sqrt{1 - \cos \phi^{(i)}}} + \\ &\quad - \frac{\gamma_1}{4\pi} \sum_{i=1}^N \frac{R_2 \cos \phi^{(i)} - R_1}{[R_1^2 + R_2^2 + Z_{21}^2 - 2R_1 R_2 \cos \phi^{(i)}]^{3/2}}. \end{aligned} \quad (5.12)$$

The intensity of the vortons on one ring changes due to gradients in the velocity field induced by the vortons on the other ring. Since initially the intensity vectors of the vortons on both rings are all pointed in azimuthal direction, $\boldsymbol{\gamma}^{(i)} = \gamma \mathbf{e}_{\phi^{(i)}}$ (where local cylindrical unit vectors ($\mathbf{e}_{r^{(i)}}$, $\mathbf{e}_{\phi^{(i)}}$, \mathbf{e}_z) have been introduced) and the vortons are symmetrically distributed

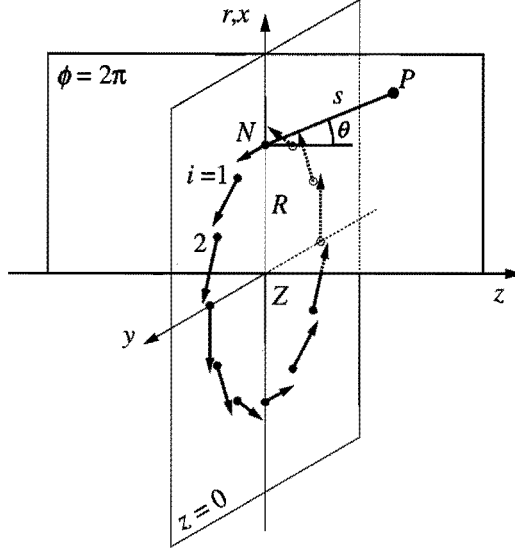


FIGURE 5.2: The position of point P , located in the meridional plane $\phi = 2\pi$, is given by polar coordinates (s, θ) relative to the position of the N^{th} vorton of the vorton ring in the same plane.

over both rings, it can be shown that the orientation of the intensity vectors does not change in time. So, the vector equation (5.10) can be reduced to a scalar equation for the azimuthal component of the intensity vector only. For each of the vortons on a ring with radius R the evolution of γ is the same and can be written as:

$$\frac{D(\gamma/R)}{Dt} = \frac{\gamma}{R^2} \frac{\partial u_\phi}{\partial \phi}, \quad (5.13)$$

where u_ϕ denotes the azimuthal component of the velocity field induced by the other vorton ring. As discussed above, this mutually induced velocity component vanishes at the positions of the vortons, but, in general, azimuthal variations in this component do not vanish. The velocity field induced by a vorton ring is not axisymmetric, because of the discrete distribution of the vortons over the ring. However, far from the vortons on the ring the induced velocity field is approximately axisymmetric and $\partial u_\phi / \partial \phi$ vanishes. The conditions for which $\partial u_\phi / \partial \phi$ is negligibly small will now be examined.

Consider the meridional plane $\phi = 2\pi$ intersecting a vorton ring at the position of the N^{th} vorton, and an arbitrary point P in this plane with polar coordinates (s, θ) relative to vorton N (see figure 5.2). Note that in the case of two vorton rings the position of this point P corresponds to the position of the N^{th} vorton on the secondary vorton ring. After some straightforward derivations based on the general equation for the velocity field induced by a system of vortons (equation (5.9)), the following expression is obtained for $\partial u_\phi / \partial \phi$ as a function of $s' = s/R$ and θ :

$$\frac{\partial u_\phi}{\partial \phi} = U_0 \frac{s' \cos \theta}{N} \sum_{i=1}^N \left(-\frac{\cos \phi^{(i)}}{[s^{(i)}]^3} + \frac{3(1 + s' \sin \theta) \sin^2 \phi^{(i)}}{[s^{(i)}]^5} \right), \quad (5.14)$$

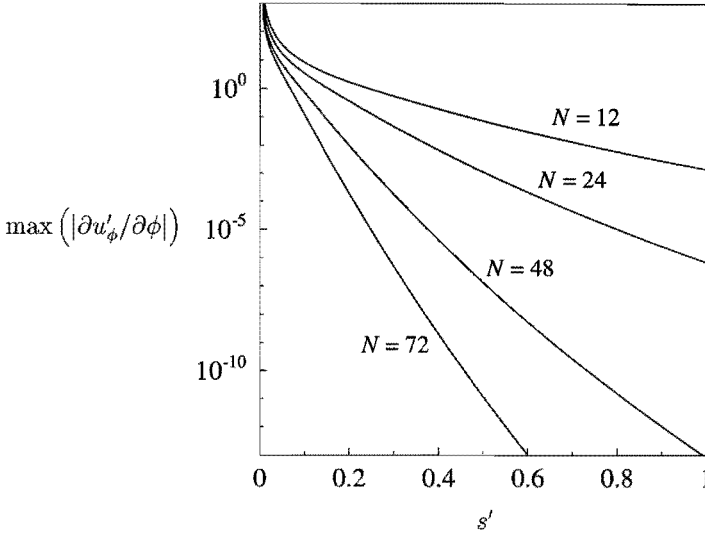


FIGURE 5.3: In this graph the maximum value of $|\partial u'_\phi/\partial\phi|$ as a function of θ is plotted, calculated at various distances s' from the core of several N -vorton rings.

where $s^{(i)} = (s'^2 + 2(1 + s' \sin \theta)(1 - \cos \phi^{(i)}))^{1/2}$ denotes the distance, scaled relative to R , between point P and vorton i on the ring. The characteristic velocity $U_0 = N\gamma/4\pi R^2$ is the axial velocity at the cross-section of the axis of symmetry with the plane of the vorton ring. In terms of the scaled velocity $u'_\phi = u_\phi/U_0$, the value of $\partial u'_\phi/\partial\phi$ has been calculated for each s' as a function of θ ; the maximum $\max(|\partial u'_\phi/\partial\phi|)$ of this function at various distances s' from the ring core* is plotted in figure 5.3. It is obvious that for small values of s' , i.e. near the positions of the vortons on the ring, $|\partial u'_\phi/\partial\phi|$ is large. At larger distances from the ring $|\partial u'_\phi/\partial\phi|$ decreases. The same calculation has been repeated for various numbers of vortons on the ring. At a fixed distance s' from the ring, $|\partial u'_\phi/\partial\phi|$ turns out to be smaller for larger values of N .

So, if the distance between the cores of two vorton rings remains large and if the number of vortons on each ring is sufficiently high, the right-hand side in equation (5.13) is approximately equal to zero. The solution of this equation is a linear relationship between γ and R : $\gamma/R = \mathcal{C} = \text{constant}$. This is an important approximation that is made in the present model, since it implies that the evolution of the intensity follows directly from the evolution of the ring radius and does not need to be calculated explicitly. For both vorton rings this linear relationship is substituted into the equations of motion (5.12) to eliminate γ_1 and γ_2 , using proportionality constants \mathcal{C}_1 and \mathcal{C}_2 instead. These new equations can be integrated numerically to determine the trajectories of the vorton rings. In the next section a choice for \mathcal{C}_1 and \mathcal{C}_2 will be discussed which depends on the connection between the vorton model and Dyson's model.

The equations of motion (5.12) have an invariant, related to the conservation of the total

*The core of a vorton ring is here defined as the circle on which the vortons are located.

impulse along the axis of symmetry, as defined in Winckelmans (1989):

$$\begin{aligned}
 P_{z,tot} &= \frac{1}{2} \sum_{i=1}^{2N} (\mathbf{x}^{(i)} \times \boldsymbol{\gamma}^{(i)})_z \\
 &= \frac{1}{2} N (R_1 \gamma_1 + R_2 \gamma_2) \\
 &= P_1 + P_2 = \text{constant},
 \end{aligned} \tag{5.15}$$

while the components of the impulse in radial and azimuthal direction both vanish. Clearly, the total impulse consists of the sum of the impulses P_1 and P_2 of the individual vorton rings. Generally, the impulse of a system of vortons is not a conserved quantity (see Winckelmans 1989). However, due to the symmetric distribution of the vortons over both rings in the present case, effects of the non-axisymmetry of the flow field, which may cause additional variations in the total impulse, are cancelled.

Since a vorton is a vortical singularity, its self-energy is infinite. To calculate the kinetic energy related to the flow of a system of vortons an expression for the interaction energy between two vortons is derived in Aksman *et al.* (1985). Using this expression, the total energy of a system of vortons is found by summing over all interactions between couples of vortons:

$$E_{int} = \frac{1}{16\pi} \sum_{\substack{i,j=1 \\ i \neq j}} \left(\frac{\boldsymbol{\gamma}^{(i)} \cdot \boldsymbol{\gamma}^{(j)}}{|\mathbf{x}^{(i)} - \mathbf{x}^{(j)}|} + \frac{\boldsymbol{\gamma}^{(i)} \cdot (\mathbf{x}^{(i)} - \mathbf{x}^{(j)}) \boldsymbol{\gamma}^{(j)} \cdot (\mathbf{x}^{(i)} - \mathbf{x}^{(j)})}{|\mathbf{x}^{(i)} - \mathbf{x}^{(j)}|^3} \right). \tag{5.16}$$

This is not an invariant of the motion, because by stretching interaction energy can be transformed into the infinite self-energy of a vorton. For the case of two interacting N -vorton rings the following expression for the total interaction energy can be derived:

$$\begin{aligned}
 E_{tot} &= \frac{N\gamma_1^2}{32\sqrt{2}\pi R_1} \sum_{i=1}^{N-1} \frac{1 + 3 \cos \phi^{(i)}}{\sqrt{1 - \cos \phi^{(i)}}} + \frac{N\gamma_2^2}{32\sqrt{2}\pi R_2} \sum_{i=1}^{N-1} \frac{1 + 3 \cos \phi^{(i)}}{\sqrt{1 - \cos \phi^{(i)}}} \\
 &+ \frac{2N\gamma_1\gamma_2}{16\pi} \sum_{i=1}^N \left(\frac{\cos \phi^{(i)}}{[R_1^2 + R_2^2 - 2R_1R_2 \cos \phi^{(i)} + (Z_1 - Z_2)^2]^{1/2}} \right. \\
 &\quad \left. + \frac{R_1R_2 \sin^2 \phi^{(i)}}{[R_1^2 + R_2^2 - 2R_1R_2 \cos \phi^{(i)} + (Z_1 - Z_2)^2]^{3/2}} \right) \\
 &= E_1 + E_2 + E_{1-2},
 \end{aligned} \tag{5.17}$$

where the first and the second term describe the kinetic energies E_1 and E_2 of the individual vorton rings, respectively, and the last term (E_{1-2}) is related to the interaction between the vorton rings.

5.4 Connection between Dyson's model and the vorton model

In the previous sections two models have been discussed for describing the interaction between two vortex rings. In Dyson's model a single vortex ring is characterized by its ring radius R , relative core radius a/R and circulation Γ . A vorton ring, however, is characterized by its ring radius R , the number of vortons N on the ring and the intensity γ of each vorton. In order to make a comparative analysis between both models additional relations are required to connect

the sets of initial parameters describing a vortex ring and a vorton ring. These relations will be discussed in this section.

It is obvious that in both models the same radius R and axial position Z for the rings is chosen initially. Furthermore, it is demanded that initially the impulse of each vortex ring is equal to the impulse of the corresponding vorton ring. Using equation (5.7) and (5.15) the following initial relation between Γ and γ is found:

$$N\gamma = 2\pi R\Gamma. \quad (5.18)$$

This relation can be interpreted as follows. Initially, each vorton represents the vorticity in the N^{th} part of the volume $V = 2\pi^2 a^2 R$ of the core of a continuous vortex ring with uniform vorticity $\omega_\phi = \Gamma/\pi a^2$. The intensity γ of the vorton is equal to the product of this partial volume $V_p = V/N$ and ω_ϕ , hence $\gamma = V_p \omega_\phi = 2\pi R\Gamma/N$.

In the previous section, the invariant linear relation between γ and R has been discussed in the approximation that the distance between the cores of the vorton rings is large during the motion of the rings. An expression for the proportionality constant can now be obtained from (5.18): $C = 2\pi\Gamma/N$. Only within this linear approximation equation (5.18) holds during the entire motion of the rings and so also its additional interpretation. Furthermore, the evolution of the impulse of vortex rings and vorton rings is now the same, i.e. the impulse is proportional to the square of the instantaneous value of the ring radius in both models.

Finally, it is demanded that the self-induced velocity of each vortex ring is, initially, equal to the self-induced velocity of the corresponding vorton ring. Using equation (5.1) and (5.11) this yields, together with equation (5.18), the following initial relation between the relative core radius a/R and N :

$$\frac{a}{R} = 8 \exp\left(-\frac{1}{4} - \frac{\pi}{\sqrt{2}N} \sum_{i=1}^{N-1} \frac{1}{\sqrt{1 - \cos \phi^{(i)}}}\right). \quad (5.19)$$

For an increasing number of vortons on the ring, the corresponding relative core radius a/R for the vortex ring decreases, implying faster moving rings.

It should be noted that during the interaction of the rings the total number of vortons N on each ring is kept fixed, whereas in Dyson's model the vortical volume $\sim a^2 R$ of each vortex ring is conserved. These different conditions lead to different self-induced velocities of the rings during the interaction. For a vortex ring and a vorton ring both having initially the same radius R^0 and self-induced velocity, the difference in self-induced velocity $U_{\text{vortex}} - U_{\text{vorton}}$ when their radii have been changed to a value R due to the interaction with the respective other ring, is given by:

$$U_{\text{vortex}} - U_{\text{vorton}} = \frac{3\Gamma}{8\pi R} \ln \frac{R}{R^0}, \quad (5.20)$$

where equation (5.18) has been substituted into equation (5.11). Hence, if the rings grow in size ($R > R^0$) the vortex ring moves faster than the corresponding vorton ring. If the rings shrink ($R < R^0$) the vorton ring moves faster. This difference is inversely proportional to the instantaneous value of the ring radius R and thus becomes larger as the radius is decreased.

To complete the analytical examination of both models the mutually induced velocity field between two vortex rings is compared with the mutually induced velocity field between two vorton rings, and the conditions for which these velocity fields are approximately the same are investigated. Consider the velocity field which is induced by a single vortex ring or a vorton

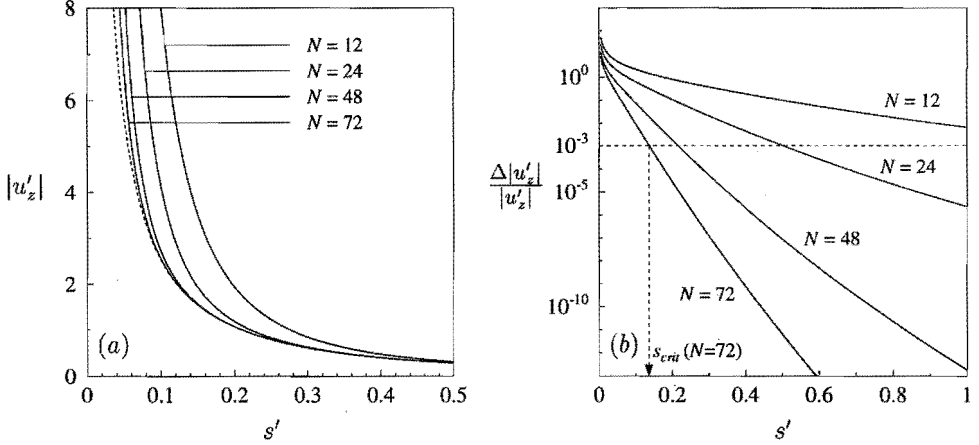


FIGURE 5.4: (a) Comparison of the magnitude of the axial velocity component $|u'_z|$ induced by a circular vortex filament (dashed line) and by a vorton ring (solid lines) in the plane of the ring ($\theta = \pi/2$), as a function of the scaled distance s' from the ring core. For large values of N the curves of the vorton ring approach the curve of the zero-core vortex ring. (b) Relative difference $\Delta|u'_z|/|u'_z| = (|u'_{z,vorton}| - |u'_{z,vortex}|)/|u'_{z,vortex}|$ between the axial velocity induced by a vorton ring $|u'_{z,vorton}|$ and a zero-core vortex ring $|u'_{z,vortex}|$ as plotted in figure (a). The arrow points to the critical distance s_{crit} for a $N = 72$ vorton ring where $\Delta|u'_z|/|u'_z| = 10^{-3}$.

ring, respectively, at a point P with polar coordinates (s, θ) relative to the core of the ring (see e.g. figure 5.2 in the previous section, where the vorton ring can be replaced equivalently by a vortex ring of the same ring radius). In general this velocity field has components u_r and u_z in radial and axial directions, respectively. The velocity field induced by a single ring at an arbitrary point P can be deduced from the equations of motion of two interacting rings by locating point P at the core of a (non-existing) ring 2 and calculating the velocity field induced by ring 1 at P (i.e. $\Gamma_2 = 0$ and $\gamma_2 = 0$ are substituted in the equations of motion (5.3) and (5.12), respectively).

The magnitude $\sqrt{u_r^2 + u_z^2}$ of the velocity field at P has been calculated as a function of the scaled distance $s' = s/R$ of P from the ring core and its angle θ and has been scaled with respect to the characteristic velocity $U_0 = \Gamma/2R = N\gamma/4\pi R^2$. It turns out that, at fixed distance s' , the magnitude of the velocity field induced in P by a vorton ring is larger than for a vortex ring for all angles θ . This difference is maximal for $\theta = \pi/2$, where the radial velocity component is equal to zero. In figure 5.4(a) the magnitude of the axial velocity component $|u'_z|$ at $\theta = \pi/2$ is plotted as a function of s' for vorton rings with various N and also for a vortex ring. In this plot the difference between both models in the induced velocity fields is thus maximal. It is seen that for all N the induced velocity fields of both models approximately coincide for large values of s' , while there is a discrepancy for smaller s' . In figure 5.4(b) the relative difference $\Delta|u'_z|/|u'_z| = (|u'_{z,vorton}| - |u'_{z,vortex}|)/|u'_{z,vortex}|$ has been plotted on a logarithmic scale as a function of s' . From this plot a critical distance s_{crit} can be derived above which $\Delta|u'_z|/|u'_z|$ is negligibly small (e.g. when $\Delta|u'_z|/|u'_z| < 10^{-3}$). This means that for $s' > s_{crit}$ the mutually induced velocity field of both models is approximately the same. From figure 5.4(b) it is seen that for larger values of N this critical distance is

Dyson's model	—	vorton model
$R_1^0 = 1.0$		$R_1^0 = 1.0$
$R_2^0 = 1.0$		$R_2^0 = 1.0$
$Z_1^0 = 0.0$		$Z_1^0 = 0.0$
$Z_2^0 = 2.0$		$Z_2^0 = 2.0$
$a_1^0/R_1^0 = 0.07632$	\Leftarrow	$N_1 = 72$
$a_2^0/R_2^0 = 0.07632$	\Leftarrow	$N_2 = 72$
$\Gamma_1 = 1.0$	\Rightarrow	$\gamma_1^0 = 0.087$
$\Gamma_2 = 1.0$	\Rightarrow	$\gamma_2^0 = 0.087$

TABLE 5.1: Initial parameters for vortex rings (Dyson's model) and vorton rings (vorton model).

smaller. In conclusion, differences in the trajectories of two vortex rings and two vorton rings can be explained entirely by the different self-induced velocity during the motion of the rings (see equation (5.20), if the distance between the cores of the rings is always larger than s_{crit} , which depends on the number of vortons on each ring.

5.5 Numerical simulations

In this section the above described analytical results will be demonstrated by comparing the trajectories of two identical vortex rings with the trajectories of two identical vorton rings, using corresponding initial conditions. The trajectories are obtained by numerical integration of equations (5.3) and (5.12) (in the linear approximation with $\gamma_i/R_i = C_i$ ($i = 1, 2$)) in time using a Runge-Kutta solver with adaptive time step (Hairer *et al.* 1987).

In table 5.1, the initial parameters used in the numerical simulations are summarized. The small index 'o' denotes the initial value for the corresponding parameter, while parameters without this index are fixed during the entire calculation. Each vorton ring consists of 72 vortons. The choice for this number was arbitrary, although a large value is required since then the corresponding relative core radius in Dyson's model satisfies the condition $a/R \ll 1$.

In figure 5.5 the trajectories of the vortex rings (dotted lines) and the vorton rings (solid lines) both exhibit the typical leapfrog motion. Due to the mutually induced velocity field, the leading ring grows in size and the trailing ring shrinks. Since the self-induced velocity of the shrinking trailing ring increases, it passes through the leading ring after which it grows and reduces its self-induced velocity again. After such a single passage, the positions of the rings are interchanged and the complete process is repeated periodically.

Although in both models the global motion is the same, the trajectories differ slightly and after each passage these differences are enhanced. To investigate these differences, it is sufficient to focus on the part of the motion until the moment of the first passage of the rings when $Z_1 = Z_2 \equiv Z^*$ and the ring radii have extreme values. It is obvious from figure 5.5 that this axial position is smaller for the vorton rings than for the vortex rings. This difference can be explained by the different self-induced velocity of vortex rings and vorton rings since their initial identical ring radius is changed due to the mutual interaction (as discussed in section 5.4). As can be seen from the positions of the markers in figure 5.5, before the first passage the axial velocity of the trailing shrinking vorton ring is indeed larger than the axial velocity of the corresponding vortex ring. For the leading growing ring this phenomenon is

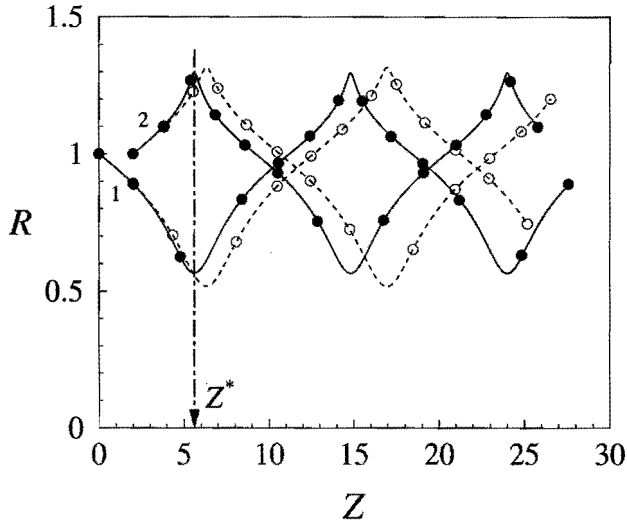


FIGURE 5.5: Trajectories of two identical vortex rings (dotted lines) and of two identical vorton rings (solid lines) in leapfrog motion. Vortex rings and vorton rings have corresponding initial parameters (see table 5.1). The markers denote the positions of the ring cores at fixed time intervals $\Delta t = 5.0$, indicating the motion of the rings in time.

reversed, although the difference in axial velocity is now smaller. Consequently, the passage of the vorton rings is at an earlier time than of the vortex rings. This implies that the axial position Z^* of the passage is smaller for the vorton rings.

Furthermore, since there is less time to the first passage, the increase of the ring radius of the leading vorton ring and the decrease of the ring radius of the trailing vorton ring is smaller at the moment of passage (see figure 5.5). Note that this change in ring radius is entirely due to the mutual interaction between both rings which also could be different for both models since it is given by essentially different expressions (see equations (5.3) and (5.12)). Furthermore, differences in the mutual interaction also affect the axial motion and this has not been mentioned in the discussion above. However, for this simulation it will be shown that differences between both models in the mutually induced velocity fields are negligible, using figure 5.4(b).

The distance $s = \sqrt{(R_1 - R_2)^2 + (Z_1 - Z_2)^2}$ between the cores of the two vorton rings at each moment during the interaction has been checked. This distance is scaled to the instantaneous ring radius of the largest of both vorton rings. The minimal scaled distance s'_{min} , apparently occurring at each moment of passage of the vorton rings, is used to determine the maximal relative difference between the induced velocity fields of the vorton rings and the vortex rings from figure 5.4(b). For the trajectories in figure 5.5 $s'_{min} = 0.566$ has been calculated, which means that $\Delta|u'_z|/|u'_z| = \mathcal{O}(10^{-13})$. Differences between both models in the mutually induced velocity field are thus negligible in this case.

Furthermore, using figure 5.3, it is seen that $|\partial u'_\phi / \partial \phi| = \mathcal{O}(10^{-13})$ for $s'_{min} = 0.566$. The linear approximation in the axisymmetric vorton model, neglecting azimuthal variations in the mutually induced velocity field of the vorton rings, is thus valid for this simulation.

Finally, the minimal unscaled distance s_{min} between the cores of the two vortex rings at

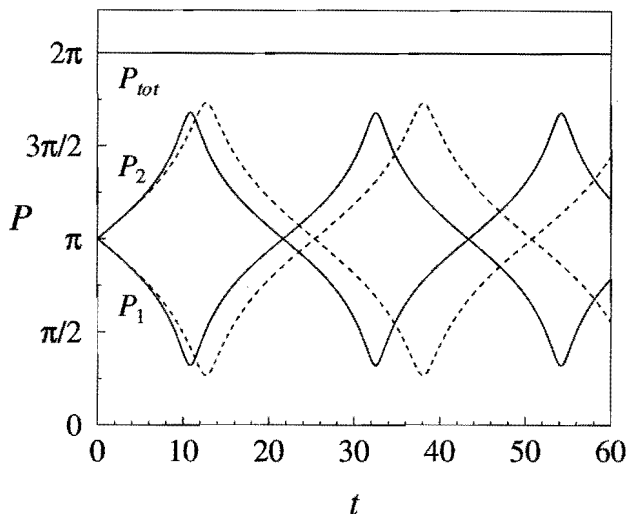


FIGURE 5.6: Variation of impulses P_1 and P_2 of the two vortex rings (dotted lines) and the two vorton rings (solid lines) in time during leapfrog motion. The total impulse $P_{tot} = P_1 + P_2$ is constant in both models.

the moment of passage of the rings has to be checked. In Dyson's model it is assumed that the distance between the cores of the vortex rings remains large in order to prevent core overlap and deformation of the vortex cores. For the present simulation it is found that the sum of the core radii a_1 and a_2 of the respective rings is $a_1 + a_2 = 0.173$ when $s = s_{min} = 0.801$, so this assumption in Dyson's model is satisfied. Furthermore, the maximal relative core radius a/R of the smallest of both rings is at this moment $a/R = 0.205$, which is indeed smaller than unity as required in Dyson's model.

The difference in the trajectories of the vortex rings and vorton rings is reflected in the difference of the impulse and energy of the flow field. In figure 5.6, the impulse of the individual vortex rings and vorton rings is plotted, which varies proportional to the square of the ring radius. From this figure, it is seen that the period of the oscillating motion is indeed shorter for the vorton rings, as was already mentioned above. It is important to notice that the total impulse $P_{tot} = P_1 + P_2$ of both the vortex rings and the vorton rings is constant within a maximal deviation of $3 \cdot 10^{-5}$, which is the accuracy of the numerical integration.

In figure 5.7, the various contributions to the total energy of the flow field have been plotted separately, as given by equations (5.8) and (5.16). Analogous to equation (5.20), an equation can be derived expressing the difference in kinetic energy of a vortex ring and a vorton ring of instantaneous ring radius R , both having initially the same radius R^0 and kinetic energy:

$$E_{vortex} - E_{vorton} = \frac{3\Gamma^2 R}{4} \ln \frac{R}{R^0}. \quad (5.21)$$

Hence, if the ring radius is increased ($R > R^0$), the kinetic energy of a vorton ring is smaller than that of a vortex ring and this difference is proportional to R . Oppositely, if the ring radius is decreased ($R < R^0$) the kinetic energy of a vorton ring is larger. This behaviour is also observed in figure 5.7 and can be explained in terms of inviscid energy dissipation and generation, respectively. As discussed in section 5.3, the kinetic energy of a vorton ring is the

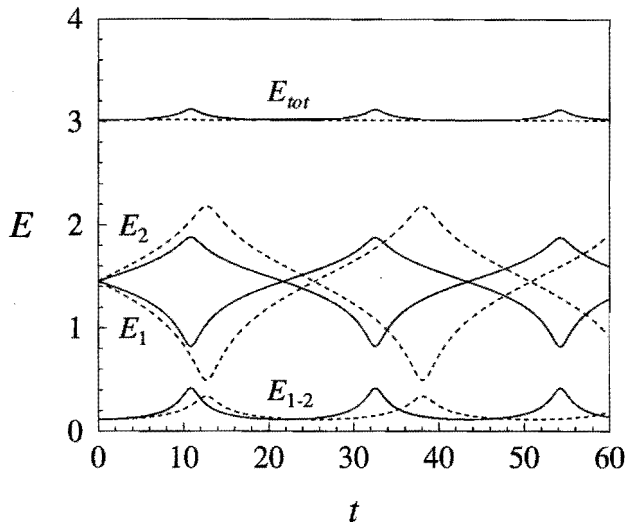


FIGURE 5.7: Variation of self-energies E_1 and E_2 and interaction energy E_{1-2} of the two vortex rings (dotted lines) and the two vorton rings (solid lines) in time during leapfrog motion. In contrast to the Dyson vortex rings, the total energy $E_{tot} = E_1 + E_2 + E_{1-2}$ is not constant for the interacting vorton rings, due to inviscid energy dissipation and generation (as explained in the text).

sum of the interaction energies between all couples of vortons constituting the ring, omitting the infinite self-energy of the individual vortons. As noted by Aksman *et al.* (1985), stretching of the vorton ring can lead to transformation of interaction energy into the infinite self-energy of the vortons, which can be interpreted as inviscid energy dissipation. Similarly, if the vorton ring is compressed interaction energy is released, so dissipated energy can be regained by compression of the vorton ring.

At the moment of passage of the rings the mutual interaction energy E_{1-2} of the vorton rings is larger than that of the vortex rings, because the distance between the cores is smaller, leading to a stronger mutual interaction of the vorton rings. The total energy of the vortex rings is constant within a maximal deviation of $1 \cdot 10^{-5}$. In Dyson's model the total energy is an invariant of the motion, but in the vorton model it is not. For the vorton rings the total energy is not constant, but increases about 3% during the passage of the rings due to inviscid energy generation as discussed above.

Until now, the differences between Dyson's model and the vorton model have been discussed only for one typical example of the coaxial interaction of two identical vorton rings and two corresponding vortex rings ($N = 72$ and $a^0/R^0 = 0.07632$, respectively). For this example, it has been shown that the reduction of the equations of motion of the vorton model (the so-called 'axisymmetric vorton model') to a set of equations analogous to the equations of motion in Dyson's model was valid. This is an important approximation for the vorton model, since it implies that the azimuthal velocity field caused by the discrete distribution of the vortons over the ring is negligible, and the vorton rings interact as continuous axisymmetric vortex structures. To investigate for which values of N the axisymmetric vorton model is a proper approximation, several simulations have been performed in which the value of N has been varied, adapting the relative core radius of the respective vortex rings according to

N	a^0/R^0	s'_{min}	$ \partial u'_\phi/\partial\phi $	$\Delta u'_z / u'_z $	s_{min}	$a_1 + a_2$	$(a/R)_{max}$
12	0.4583	0.611	$2.8 \cdot 10^{-2}$	$5.1 \cdot 10^{-2}$	0.935	1.104	1.702
24	0.2290	0.590	$2.5 \cdot 10^{-4}$	$3.1 \cdot 10^{-4}$	0.868	0.533	0.718
48	0.1145	0.573	$1.3 \cdot 10^{-8}$	$1.0 \cdot 10^{-8}$	0.822	0.261	0.323
72	0.07632	0.566	$5.0 \cdot 10^{-13}$	$3.2 \cdot 10^{-13}$	0.801	0.173	0.205

TABLE 5.2: Comparison of simulations with various N and corresponding a^0/R^0 .

equation (5.19). In table 5.2 some of the results of these simulations have been summarized. In all cases the typical leapfrog motion of the vorton rings and vortex rings was observed, although the trajectories of the rings were slightly different from the previous ones. For example, since the global self-induced velocities of the rings are smaller for decreasing values of N the period of the motion is larger, and the travelled distance of the rings is shorter.

In table 5.2, s'_{min} denotes the minimal scaled distance between the cores of the vorton rings, which is approximately the same for all values of N . The corresponding values of $|\partial u'_\phi/\partial\phi|$ and $\Delta|u'_z|/|u'_z|$ both decrease substantially with increasing number N . However, for $N = 12$ both quantities are of $\mathcal{O}(10^{-2})$, so for this number of vortons the axisymmetric vorton model might not be a proper approximation, and the complete equations of motion of the vorton model have to be used. Examining the last three columns of table 5.2, it is found that for $a^0/R^0 = 0.2290$ (i.e. $N = 24$ in the vorton model), the distance between the vortex cores is relatively small and for $a^0/R^0 = 0.4583$ ($N = 12$), the cores even overlap. The maximal value of the relative core radius $(a/R)_{max}$ is relatively large for the first two cases (even larger than one) and only satisfies the condition $a/R \ll 1$ for the thinnest vortex rings. It is thus concluded that the investigation made in the first part of this section for $N = 72$ was also proper for the case $N = 48$, while for smaller values of N both the axisymmetric vorton model may not be applied and Dyson's model is not valid.

It was seen that the differences between the vorton model and Dyson's model are due to the different self-induced velocities of vorton rings and vortex rings during the interaction. One possibility to diminish this difference is to change the number of vortons on each ring during the motion. To this end, the simulations have been repeated with a complete three-dimensional vorton code developed by Pedrizzetti (1992), in which vortons can be 'divided' or 'fused', depending on the change of their mutual separation $L = 2\pi R/N$. If $L \geq 2^{2/3}L_0$, where L_0 denotes the initial separation of the vortons, an extra vorton is added, while if $L \leq 2^{-2/3}L_0$ a vorton is removed. For the leapfrog simulations, however, it turns out that the distances between the vortons on the rings do not exceed these critical values, and thus also with this code the number of vortons on each ring remains the same. The assumption that the number of vortons on each vorton ring is fixed is thus valid for these simulations.

5.6 Conclusions

In this chapter the relation between two models that can be used to describe the coaxial interaction of two inviscid vortex rings has been analyzed. An axisymmetric vorton model has been derived, an approximation of the complete vorton model in which vorton rings are assumed to induce an axisymmetric velocity field. It was shown that for the simulations of leapfrog motion with $N \geq 48$ this is a valid approximation. In this approximation, the equations of

motion of the vorton model are written in a similar formulation as in Dyson's model, hence making a close investigation of both models possible. For this purpose, relations connecting the initial conditions and parameters for both models have been derived in order to perform similar simulations. It was found that for $N \geq 48$ ($a^0/R^0 \leq 0.1145$) the observed differences in the ring trajectories can be explained entirely by the different self-induced velocity of vortex rings and vorton rings during the motion.

A short note is made about this difference that demonstrates an essential drawback inherent to the vorton model. The velocity of a vortex ring depends on the geometry of the ring core, denoted by the parameter a/R , which varies during expansion and shrinking of the ring radius in order to conserve the volume of the core. A vorton ring does not have an intrinsic core structure and thus an important contribution to the self-induced ring motion is missing in the vorton model.

In this chapter the vorton ring model and the Dyson model were applied to study the coaxial interaction of two identical rings. In principle, the coaxial interaction of two arbitrary rings can be studied and the application of the axisymmetric vorton model to these cases can then be verified. Since it is now known how to relate the characteristics of a vortex ring (i.e. $Z, R, a/R, \Gamma$) and of a vorton ring (Z, R, N, γ) for coaxial interactions, the simulations can also be extended to non-coaxial interactions of vorton rings. Since Dyson's model is not valid in this case, vorton rings might be used to investigate the dynamics of such vortex ring interactions. Of course, for these simulations the complete set of equations of the vorton model have to be used.

Based on the results of the present work a few warnings are given that have to be considered carefully when applying the vorton model to study vortex ring interactions. Due to the discrete distributions of vortons on the ring, the induced velocity field of a vorton ring is not axisymmetric. If two vorton rings come close to each other, the evolution of the vorton intensities is affected by azimuthal variations in the mutually induced velocity field between the vorton rings. Criteria for the distance between the ring cores for which this artificial effect becomes significant are given in the present work. However, local variations in the core structure appearing during vortex ring interactions are not represented by the vorton model. From this it is concluded that relatively weak interactions between vortex rings at sufficiently large mutual distance with only minor variations in the core structure are expected to be modelled properly using vorton rings with fixed number of vortons.

6

SUMMARY OF CONCLUSIONS

In this thesis the dynamics of a vortex ring generated in a fluid in uniform rotation has been studied. The investigation was based both on laboratory experiments and numerical simulations, which were used as complementary tools to examine the evolution of the flow. Because of the initial symmetric structure of the vortex ring the analysis of the flow development could be followed in detail, providing important insight in the dynamics of relative flow motion in rotating fluids. Detailed descriptions of the results and conclusions gathered from this study have already been presented at the end of each chapter and a brief summary of the main conclusions is presented here.

In the first case considered the vortex ring was directed parallel to the rotation axis. It turns out that the flow dynamics of the vortex ring is strongly affected by the presence of the rotation. In particular, as the background rotation increases the propagation velocity of the vortex ring decreases. In addition, a secondary flow structure of oppositely-signed vorticity develops at the front side of the vortex ring and an intense axial vortex is generated along the axis of symmetry. The occurrence of these structures has been explained by the presence of a self-induced swirl flow and by inspection of the extra terms in the Navier-Stokes equations due to the rotation. Asymmetries in the flow observed from flow visualization experiments resulted from a small misalignment between the propagation direction of the vortex ring and the rotation axis, as verified by three-dimensional numerical simulations. If the rotation rate is further increased beyond a critical value, the flow starts to be dominated by Coriolis forces. In this flow regime the impulse imparted to the fluid no longer generates a vortex ring, but rather it excites inertial waves allowing the flow to radiate energy. Evidence of this phenomenon is shown.

In the second case the vortex ring propagated perpendicular to the rotation axis. In the rotating system the vortex ring describes a curved trajectory, turning in opposite sense to the system's rotation. This behaviour has been explained by using the analogy with the motion of a sphere in a rotating fluid. Measurements have revealed that the angular velocity of the vortex ring in its curved trajectory is opposite to the background rotation rate, so that the ring has a fixed orientation in an inertial frame of reference. Consequently, the curvature of the path increases proportional to the rotation rate of the system. The dynamics of the ring vorticity is affected by the background rotation in such a way that the vortex shrinks on one side (where the local relative vorticity in the ring core is opposite to the background vorticity) while the opposite side expands. By this opposite forcing on either side of the ring core inertial waves are excited, travelling along the toroidal axis of the ring core. In addition,

the curved motion of the vortex ring modifies its self-induced strain field, resulting in stripping of vorticity filaments from the ring core. Vortex lines of absolute vorticity, being deflected by the main vortex ring due to induction of relative vorticity, are stretched by the local straining field near the ring centre and form a horizontally extending vortex pair behind the ring. This vortex pair propagates by its self-induced motion towards the shrunk side of the ring core and enhances there the deformations of the ring core. Deflection of vortex lines from the main ring core persists during the whole motion and is responsible for the gradual erosion of the coherent toroidal structure of the initial vortex ring.

Finally, a comparative analysis between Dyson's model and the vorton model provided criteria for which differences in the mutual interaction between vorton rings and vortex rings are negligible. The deviating self-induced velocity of vorton rings during the interaction is inherent to the vorton model, since vortons do not have an intrinsic core structure.

REFERENCES

- AKHMETOV, D. G., LUGOVTSOV, B. A. & TARASOV, V. F. 1980 Extinguishing gas and oil well fires by means of vortex rings. *Combustion, Explosion and Shock Waves* **16**, 490–494.
- AKSMAN, M. J., NOVIKOV, E. A. & ORSZAG, S. A. 1985 Vorton method in three-dimensional hydrodynamics. *Phys. Rev. Lett.* **54** (22), 2410–2413.
- BATCHELOR, G. K. 1967 *An Introduction to Fluid Dynamics*. Cambridge University Press.
- BENJAMIN, T. B. 1976 The alliance of practical and analytical insights into the non-linear problems of fluid mechanics. *Applications of Methods of Functional Analysis to Problems in Mechanics, Lecture Notes in Mathematics* (eds. Germain, P. and Nayroles, B.) **503**, 8–28. Springer.
- CHAHINE, G. L. & GENOUX, P. F. 1983 Collapse of a cavitating vortex ring. *J. Fluids Eng.* **105**, 400–405.
- DALZIEL, S. 1992 *DigImage. Image Processing for Fluid Dynamics*. Cambridge Environmental Research Consultants Ltd.
- DIDDEN, N. 1977 Untersuchung laminarer, instabiler Ringwirbel mittels Laser-Doppler-Anemometrie. *Mitt. aus dem MPI für Strömungsforschung and der AVA* **64**, Göttingen.
- DIDDEN, N. 1979 On the formation of vortex rings: rolling-up and production of circulation. *Z. angew. Math. Phys.* **30**, 101–116.
- DYSON, F. W. 1893 The potential of an anchor ring.—Part II. *Phil. Trans. R. Soc. Lond. A* **184**, 1041–1106.
- FETTER, A. L. 1974 Translational velocity of a classical vortex ring. *Phys. Rev. A* **10** (5), 1724–1727.
- FRAENKEL, L. E. 1970 On steady vortex rings of small cross-section in an ideal fluid. *Proc. Roy. Soc. Lond. A* **316**, 29–62.
- FUJITA, T. T. 1981 Tornadoes and downbursts in the context of generalized planetary scales. *J. Atmos. Sci.* **38**, 1511–1534.
- GLEZER, A. 1988 The formation of vortex rings. *Phys. Fluids* **31** (12), 3532–3542.
- GLEZER, A. & COLES, D. 1990 An experimental study of a turbulent vortex ring. *J. Fluid Mech.* **211**, 243–283.
- GÖRTLER, H. 1957 On forced oscillations in rotating fluids. *5th Midwestern Conf. on Fluid Mech.*, 1–10.
- GREENSPAN, H. P. 1968 *The Theory of Rotating Fluids*. Cambridge University Press.

- GURZHII, A. A., KONSTANTINOV, M. YU. & MELESHKO, V. V. 1988 Interaction of coaxial vortex rings in an ideal fluid. *Fluid Dyn.* **23** (2), 224–229.
- GURZHII, A. A. & KONSTANTINOV, M. YU. 1989 Head-on collision of two coaxial vortex rings in an ideal fluid. *Fluid Dyn.* **24** (4), 538–541.
- GURZHII, A. A., KONSTANTINOV, M. YU. & MELESHKO, V. V. 1994 Ordered and chaotic movement in the dynamics of three coaxial vortex rings. *J. Math. Sci.* **68**, 711–714. Translated from *Teoret. & Prikl. Mekh.* **21**, 100–104 (in Russian).
- HAIRER, E., NØRSETT, S. P. & WANNER, G. 1987 *Solving Ordinary Differential Equations I, Nonstiff problems*. Springer.
- HELMHOLTZ, H. 1858 Über Integrale hydrodynamischen Gleichungen welche den Wirbelbewegungen entsprechen. *J. reine angew. Math.* **55**, 25–55. Translated in English by P. G. Tait (1867): On integrals of the hydrodynamical equations, which express vortex-motion. *Phil. Mag.* **4** **33** (226), 485–512.
- HICKS, W. M. 1922 On the mutual threading of vortex rings. *Proc. R. Soc. Lond. A* **102**, 111–131.
- HILL, M. J. M. 1894 On a spherical vortex. *Phil. Trans. Roy. Soc. A* **185**, 213–245.
- KIM, J. & MOIN, P. 1985 Application of a fractional-step method to incompressible Navier-Stokes equations. *J. Comput. Phys.* **59**, 308–323.
- LUNDGREN, T. S. & ASHURST, W. T. 1989 Area-varying waves on curved vortex tubes with application to vortex breakdown. *J. Fluid Mech.* **200**, 283–307.
- MARTEN, K., SHARIFF, K., PSARAKOS, S. & WHITE, D. J. 1996 Ring bubbles of dolphins. *Scientific American* August 1996, 83–87.
- MAXWORTHY, T. 1972 The structure and stability of vortex rings. *J. Fluid Mech.* **51**, 15–32.
- MAXWORTHY, T. 1977 Some experimental studies of vortex rings. *J. Fluid Mech.* **81**, 465–495.
- MENG, J. C. S. 1978 The physics of vortex-ring evolution in a stratified and shearing environment. *J. Fluid Mech.* **84**, 455–469.
- MÉTAIS, O., FLORES, C., YANASE, S., RILEY, J. J. & LESIEUR, M. 1995 Rotating free-shear flows. Part 2. Numerical simulations. *J. Fluid Mech.* **293**, 47–80.
- MOFFATT, H. K. 1988 Generalized vortex rings with and without swirl. *Fluid Dyn. Res.* **3**, 22–30.
- MOORE, D. W. & SAFFMAN, P. G. 1972 The motion of a vortex filament with axial flow. *Phil. Trans. R. Soc. Lond. A* **272**, 403–429.
- NGUYEN DUC, T. & SOMMERIA, J. 1988 Experimental characterization of steady two-dimensional vortex couples. *J. Fluid Mech.* **192**, 175–192.
- NORBURY, J. 1973 A family of steady vortex rings. *J. Fluid Mech.* **57**, 417–431.
- NOVIKOV, E. A. 1983 Generalized dynamics of three-dimensional vortical singularities (vortons). *Sov. Phys. JETP* **57** (3), 566–569.
- ORLANDI, P. 1990 A numerical method for direct simulation of turbulence in complex geometries. *Annual Research Briefs, 1989. Ames Center for Turbulence Research*, 215–229.

- ORLANDI, P. & VERZICCO, R. 1993 Free vortex rings, analogies and differences between vorticity and passive scalar. In *Vortex Flows and Related Numerical Methods*, (ed. J. T. Beale *et al.*) Kluwer, 303–313.
- OSER, H. 1958 Experimentelle Untersuchung über harmonische Schwingungen in rotierenden Flüssigkeiten. *Z. angew. Math. Mech.* **38**, 386–391.
- PEDLOSKY, J. 1987 *Geophysical Fluid Dynamics*. (second edition) Springer.
- PEDRIZZETTI, G. 1992 Insight into singular vortex flows. *Fluid Dyn. Res.* **10**, 101–115.
- PROUDMAN, J. 1916 On the motion of solids in liquids possessing vorticity. *Proc. Roy. Soc. A* **92**, 408–424.
- RILEY, N. 1993 On the behaviour of pairs of vortex rings. *Q. Jl Mech. Appl. Math.* **46** (3), 521–539.
- RILEY, N. & STEVENS, D. P. 1993 A note on leapfrogging vortex rings. *Fluid Dyn. Res.* **11**, 235–244.
- ROBINSON, S. K. 1991 Coherent motions in the turbulent boundary layer. *Annu. Rev. Fluid Mech.* **23**, 601–639.
- SAFFMAN, P. G. 1970 The velocity of viscous vortex rings. *Stud. Appl. Maths* **49**, 371–380.
- SAFFMAN, P. G. 1978 The number of waves on unstable vortex rings. *J. Fluid Mech.* **84**, 625–639.
- SAFFMAN, P. G. 1992 *Vorticity Dynamics*. Cambridge University Press.
- SALLET, D. W. & WIDMAYER, R. S. 1974 An experimental investigation of laminar and turbulent vortex rings in air. *Z. Flugwiss.* **22**, 207–215.
- SCHATZLE, P. R. 1987 An experimental study of fusion of vortex rings. *Ph.D. thesis* (California Institute of Technology).
- SHARIFF, K., LEONARD, A., ZABUSKY, N. J. & FERZIGER, J. H. 1988 Acoustics and dynamics of coaxial interacting vortex rings. *Fluid Dyn. Res.* **3**, 337–343.
- SHARIFF, K., LEONARD, A., & FERZIGER, J. H. 1989 Dynamics of a class of vortex rings. NASA TM-102257.
- SHARIFF, K., VERZICCO, R. & ORLANDI, P. 1994 A numerical study of three-dimensional vortex ring instabilities: viscous corrections and early nonlinear stage. *J. Fluid Mech.* **279**, 351–375.
- SHEFFIELD, J. S. 1977 Trajectories of an ideal vortex pair near an orifice. *Phys. Fluids* **20**, 543–545.
- STEVENSON, T. N. 1973 The phase configuration of internal waves around a body moving in a density stratified fluid. *J. Fluid Mech.* **60**, 759–767.
- SULLIVAN, J. P., WIDNALL, S. E. & EZEKIEL, S. 1973 Study of vortex rings using a Laser Doppler Velocimeter. *AIAA Journal* **11**, 1384–1389.
- TAYLOR, G. I. 1917 Motion of solids in fluids when the flow is not irrotational. *Proc. Roy. Soc. A* **93**, 99–113.
- TAYLOR, G. I. 1921 Experiments with rotating fluids. *Proc. Roy. Soc. A* **100**, 114–121.
- TAYLOR, G. I. 1923 Experiments on the motion of solid bodies in rotating fluids. *Proc. Roy. Soc. A* **104**, 213–218.

- THOMSON, W. 1867a The translatory velocity of a circular vortex ring. *Phil. Mag.* 4 **33** (226), 511–512. (A letter in the appendix of the translation of Helmholtz (1858) paper.)
- THOMSON, W. 1867b On vortex atoms. *Phil. Mag.* 34 (4), 15–24.
- THOMSON, W. 1869 On vortex motion. *Trans. Roy. Soc. Edinb.* 25, 217–260.
- THOMSON, W. 1880 Vibrations of a columnar vortex. *Phil. Mag.* 5 **10**, 155–168.
- TRITTON, D. J. 1992 Stabilization and destabilization of turbulent shear flow in a rotating fluid. *J. Fluid Mech.* 241, 503–523.
- TURKINGTON, B. 1989 Vortex rings with swirl: axisymmetric solutions of the Euler equations with nonzero helicity. *SIAM J. Math. Anal.* 20, 57–73.
- TURNER, J. S. 1960 On the intermittent release of smoke from chimneys. *Mech. Engng Sci.* 2, 356.
- VERZICCO, R., JIMÉNEZ, J. & ORLANDI, P. 1995 On steady columnar vortices under local compression. *J. Fluid Mech.* 299, 367–388.
- VERZICCO, R. & ORLANDI, P. 1995 Mixedness in the formation of a vortex ring. *Phys. Fluids* 7, 1513–1515.
- VERZICCO, R. & ORLANDI, P. 1996a A finite-difference scheme for three-dimensional incompressible flows in cylindrical coordinates. *J. Comput. Phys.* 123, 402–414.
- VERZICCO, R. & ORLANDI, P. 1996b Wall/vortex-ring interactions. *Appl. Mech. Rev.* 49, 447–460.
- VERZICCO, R., ORLANDI, P., EISENGA, A. H. M., HEIJST, G. J. F. VAN & CARNEVALE, G. F. 1996 Dynamics of a vortex ring in a rotating fluid. *J. Fluid Mech.* 317, 215–239.
- VIRK, D., MELANDER, M. V. & HUSSAIN, F. 1994 Dynamics of a polarized vortex ring. *J. Fluid Mech.* 260, 23–55.
- WAKELIN, S. L. & RILEY, N. 1997 On the formation and propagation of vortex rings and pairs of vortex rings. *J. Fluid Mech.* 332, 121–139.
- WALKER, J. D. A., SMITH, C. R., CERRA, A. W. & DOLIGALSKI, T. L. 1987 The impact of a vortex ring on a wall. *J. Fluid Mech.* 181, 99–140.
- WEIDMAN, P. D. & RILEY, N. 1993 Vortex ring pairs: numerical simulation and experiment. *J. Fluid Mech.* 257, 311–337.
- WINCKELMANS, G. S. 1989 Topics in vortex methods for the computation of three- and two-dimensional incompressible unsteady flows. *Ph.D. thesis* (California Institute of Technology, Pasadena, California).
- YAMADA, H. & MATSUI, T. 1978 Preliminary study of mutual slip-through of a pair of vortices. *Phys. Fluids* 21 (2), 292–294.

SAMENVATTING

Een belangrijk deel van dit onderzoek is gericht op de bestudering van de dynamica van een werveling die zich voortbeweegt in een roterende vloeistof. Vanwege hun relatief eenvoudige vorm worden wervelingen vaak gebruikt om eigenschappen van drie-dimensionale wervelstructuren te bestuderen. In dit proefschrift is de ontwikkeling van een werveling in een roterende vloeistof onderzocht om zodoende een beter inzicht te krijgen in de beweging van wervels in een roterende stroming. Roterende stromingen komen voor in een aantal technische toepassingen, zoals turbines, verbrandingskamers en cyclonen. Bovendien wordt de dynamica van grootschalige wervelbewegingen in de atmosfeer en de oceaan beïnvloed door de rotatie van de aarde. De beweging van wervels in een roterende stroming is over het algemeen zeer gecompliceerd als gevolg van de interactie tussen de rotatie in de wervel en de permanent aanwezige achtergrondrotatie. Door echter gebruik te maken van de symmetrische structuur van een werveling kan de dynamica van een wervel in een roterende stroming grondig onderzocht worden.

Tijdens het onderzoek zijn zowel laboratorium experimenten als numerieke simulaties uitgevoerd. Voor de experimenten was een werveling-generator ontworpen. De wervelingen werden gegenereerd in een perspex tank gevuld met water door middel van injectie van een kleine hoeveelheid vloeistof door een cirkelvormige opening in de generator. De experimentele opstelling was geplaatst op een roterende tafel, waarvan de hoeksnelheid ingesteld kon worden. Numerieke berekeningen, gebaseerd op de Navier-Stokes vergelijkingen, werden uitgevoerd om dit experiment te simuleren. Details van de stroming die moeilijk meetbaar waren konden op die manier alsnog bestudeerd worden, terwijl de numerieke code getest kon worden aan de hand van de experimenten.

Twee gevallen zijn bestudeerd. In het eerste geval werd de werveling parallel aan de rotatie-as gegenereerd. Door de interactie tussen deze primaire wervel en de achtergrondrotatie ontstaat er een secundaire werveling, vlak voor de primaire ring. Door dit proces wordt de primaire werveling sterk gedeformeerd en, afhankelijk van de achtergrondrotatie, volledig afgebroken. In het tweede geval bewoog de werveling loodrecht op de rotatie-as. Nu wordt de baan van de ring afgebogen, en wel precies tegen de draaiing van het systeem in. Ook vervormt de wervelstructuur en wordt deze aan een kant ingeknepen, terwijl de andere zijde langzaam uitdijt. In beide gevallen kunnen de waargenomen verschijnselen verklaard worden door de invloed van de Coriolis-kracht in het roterende systeem.

Bovendien is er onderzoek gedaan naar de overeenkomst tussen twee wiskundige modellen, waarmee de dynamica van wervels bestudeerd kan worden. Beide modellen werden met elkaar vergeleken aan de hand van een klassiek voorbeeld, namelijk de coaxiale interactie tussen twee wervelingen. Gezien de symmetrie van dit probleem kunnen criteria voor toepassing van één van deze modellen, namelijk het omstreden 'vorton' model, afgeleid worden.

CURRICULUM VITAE

Alphons Hubert Menno Eisenga

- 5 april 1968 geboren te Maastricht
- 1980-1986 VWO, Gymnasium β
Henric van Veldeke College te Maastricht
- 1986-1992 studie technische natuurkunde
aan de Technische Universiteit Eindhoven
afgestudeerd in de theoretische natuurkunde
onder begeleiding van prof.dr. D. Lenstra
- 1992-1997 promotie-onderzoek als assistent in opleiding (A.I.O.)
in dienst van de Technische Universiteit Eindhoven

STELLINGEN

behorende bij het proefschrift

‘Dynamics of a Vortex Ring in a Rotating Fluid’

A.H.M. Eisenga, 27 mei 1997

1. Dankzij zijn eenvoudige, symmetrische vorm is een werveling een ideale kandidaat om fundamentele mechanismen te bestuderen die optreden in de dynamica van complexe drie-dimensionale wervelstructuren.

Dit proefschrift, hoofdstuk 3 en 4.

2. Het door Novikov afgeleide vorton-model is slechts beperkt bruikbaar voor de kwalitatieve beschrijving van zwakke interacties tussen drie-dimensionale wervelstructuren.

Dit proefschrift, hoofdstuk 5.

3. Wervelingen: speelgoed voor intelligente zoogdieren.

MARTEN, K., SHARIFF, K., PSARAKOS, S. & WHITE, D.J. Ring bubbles of dolphins. *Scientific American* August 1996, 83–87.

THOMSON, W. 1867 On vortex atoms. *Phil. Mag.* 4 34 (227), 15–24.

Dit proefschrift.

4. In twee artikelen leidt James Clerk Maxwell op verschillende manieren criteria af voor de stabiliteit van een twee-dimensionale stationaire stroming van een ideale vloeistof. De tegenstrijdige resultaten zijn het gevolg van een simpele tekenfout in de afleiding in het eerste artikel.

MAXWELL J.C. ‘Manuscript on the steady motion of an incompressible fluid, 9 May 1855’ en ‘Letter to William Thomson, 15 May 1855’. In *The scientific letters and papers of James Clerk Maxwell* 1, 295–299 en 309–313, Cambridge University Press 1990 (P.M. Harman, editor).

5. In het kader van het (slechts beperkte) anti-rook beleid van de Nederlandse Spoorwegen zou het gepast zijn de toiletten in de moderne intercity-rijtuigen niet aan de zijde van de rokers-compartimenten te plaatsen.

6. Het is ethisch niet geoorloofd mensen direct aan te spreken c.q. te beledigen aangaande hun opvallende lichamelijke uiterlijk, tenzij het de lichaamslengte betreft.

7. Het beschrijven van het ladingstransport in metaal-supergeleider juncties middels de Bogoliubov-vergelijkingen voorspelt een sterke afname van de coëfficiënt voor Andreev-reflectie in deze juncties in aanwezigheid van een storingspotentiala, gemodelleerd door een δ -piek, aan het contactvlak. Indien deze potentiala een eindig, uniform profiel heeft kunnen er bij discrete energieniveaus gelegen in de 'energy gap' van de supergeleider resonanties optreden waarbij deze coëfficiënt juist zeer groot is.

BLONDER, G.E., TINKHAM, M. & KLAPWIJK, T.M. 1982 Transition from metallic to tunneling regimes in superconducting microconstrictions: Excess current, charge imbalance, and supercurrent conversion. *Phys. Rev. B* **25** (7), 4515–4532.

EISENGA, A.H.M. 1992 Charge transport in metal-(insulator)-superconductor configurations. Afstudeerverslag T.U.E.

8. Het geldt als een ongeschreven regel in het openbaar vervoer om, indien er nog voldoende zitplaatsen vrij zijn, niet naast iemand plaats te nemen.
9. Als Nederland zich minder met voetbal zou bezighouden en België meer, zou in beide landen het aantal misdaden afnemen.
10. Er zou een maximumsnelheid ingevoerd moeten worden voor wielrenners die deelnemen aan het openbaar verkeer.
11. Het onderhoud van een klassieke motor is geen routine-werk.
12. In een maatschappij waarin communicatie en computers een steeds belangrijkere rol spelen is een goede communicatie tussen mens en computer van essentieel belang.
13. Het bedenken van stellingen na het schrijven van het proefschrift voelt aan als een flinke kater na een lange nacht.